MMP

Modelling for Materials Processing

Rīga, September 2023

Proceedings of the IX International Scientific Colloquium

# Modelling for Materials Processing

Rīga, September 18-19, 2023

**Organized by**

LATVIJAS UNIVERSITATE
ANNO 1919

Leibniz Universität Hannover

In tradition of the international scientific colloquiums Modelling for Materials Processing held in Riga in 1999, 2001, 2007, 2010 and 2017, and Modelling for Electromagnetic Processing held in Hanover in 2003, 2008 and 2014, the Institute of Numerical Modelling and Institute of Physics of the University of Latvia are organising the next colloquium Modelling for Materials Processing in Riga in September 2023, together with the Institute of Electrotechnology of the Leibniz University Hannover.

The results presented at the colloquium will cover recent numerical and experimental research activities in the field of industrial processing technologies for creating new and alternative materials, materials of highest quality and purity, and new innovative products.

## Scientific Committee



## Local Organising Committee (University of Latvia)



## Editors:


**Dr. A. Brēķis**
**Ms. S. Ščaņicina**

E-mail: mmp2023@lu.lv

## CONTENTS

### Welcome adress

How magnetic field measurements can be applied to characterise flow structures in liquid metals or to monitor electrified industrial processes

*S. Eckert*.....1

MHD effects on the alumina dissolution in aluminium electrolysis cells

*V. Bojarevics*.....2

Multiphysical model experiments for crystal growth from melt

*K. Dadzis, A. Wintzer, I. Tsiapkinis, S. Foroushani*.....3

### MHD technologies I

Innovative NbSi composites: investigation and development of an alloying process using cold crucible induction furnace

*E. Baake, M. Guglielmi, A. Köppen, E. Holzmann, S. Herbst*.....4

Modelling contactless ultrasonic cavitation for industrial scaling

*C. E.H. Tonry, V. Bojarevics, G. Djambazov, K. Pericleous*.....10

Results of 3D simulations of electromagnetic induction pump using electric potential formulation

*N. Jēkabsons, L. Goldšteins, L. Buligins, K. Kravalis*.....11

Electromagnetic control of the direct strip casting process

*V. Dzelme, A. Jakovičs, E. Baake*.....12

Advanced electrode melting for highest purity cast parts

*S. Spitans, H. Franz, B. Sehring, S. Bogner*.....13

## Crystal growth

Simulation of the Growth of Crystalline Silicon fibers for the 3rd Generation Gravitational Wave detectors

*L. Vieira, I. Tsiapkinis, K. Dadzis, R. Menzel*.....19

New open-source software for simulation of thermal stresses and dislocations in crystals during the growth process

*A. Sabanskis, K. Dadzis, A. Wintzer, J. Virbulis*.....20

Validation of high-frequency electromagnetic models for crystal growth applications

*I. Tsiapkinis, A. Wintzer, S. Foroushani, K. Dadzis*.....21

Experimental and numerical investigation of LiBr crystal growth using the CZ method

*K. Kalme, A. Sabanskis, J. Virbulis*.....22

Simulation-driven process development of AlN-single crystal growth by the physical vapor transport method

*M. Hainke, M. Lang, S. Krishna Tangedipelli, Ch. Kranert, J. Friedrich*.....23

## Advanced technologies

Experimental and simulative studies on the electrothermal behavior of carbon fiber resistive heating elements

*N. Sufis, I. Niedzwiecki, A. Nikanorov, E. Baake*.....29

Density-based topological optimization of 3D-printed casts for fracture treatment with FreeFem software

*K. Kokars, A. Krauze, K. Muižnieks, J. Virbulis, J. Oliņš, A. Gutcaits, P. Verners*.....35

Inverse identification of SMC material properties – innovative implementation of flux concentrator losses in numerical design of inductive systems

*I. Niedzwiecki, A. Nikanorov, E. Baake, N. Sufis*.....42

Porous material for gas thermal compression in space conditions. Thermal design aspects

*I. Ušakovs*.....47

Analysis of the heat-exchangers energy efficiency of variable cross section with an inhomogeneous coolant

*S. Sakipova, B. Nussupbekov, K. Shaimerdenova, D. Ospanova, B. Kutum*.....53

**Crystallization**

Directional solidification of silicon: experimental results

*M. Forzan, M. Guglielmi*.....54

Numerical study of the Bridgman directional solidification process of photovoltaic silicon ingot using the power control technique

*B. Hiba, Ab. Nouri, L. Hachani, K. Zaidat*.....60

Pulsed electromagnetic field effects on dendritic solidification in a thin cell

*N. Shevchenko, Q. Bai, A. Kao, S. Eckert*.....70

Incorporating interdependent structural mechanical mechanisms into modelling three-dimensional microstructure solidification

*P. Soar, A. Kao, K. Pericleous*.....76

300 mm silicon mono Czochralski crystals: parameters and conditions for crystal growth

*F. Zobel, P. Dold*.....77

## Numerical MHD

Surface deformations of liquid metal flow in porous media in external uniform magnetic field

*D. Berenis, I. Grants, L. Buligins*.....78

Continuous casting simulation with MAGMASOFT®

*E. Shvydkii, E. Hepp, J. Fainberg*.....84

Influence of external magnetic field on 3D electro vortex flow inside conducting liquids

*M. Al-Nasser, H. Barati, E. Karimi-Sibaki, M. Wu, Ch. Redl, A. Ishmurzin, N. Voller, G. Hackl, A. Kharicha*.....90

Modeling of magnetohydrodynamics in liquid metals with a free surface using OpenFOAM

*V. Giovacchini, S. Mingozzi*.....91

Simulation of melt flow in steel continuous casting considering transient clogging of submerged entry nozzle

*H. Barati, M. Wu M, A. Kharicha, A. Ludwig*.....97

## MHD technologies II

Influence of the rotational component of a submerged entry nozzle jet on the free surface oscillations under the applied DC magnetic field

*A. Vakhrushev, A. Kharicha, E.Karimi-Sibaki, M. Wu, A. Ludwig, G. Nitzl, Y. Tang, G. Hackl, J. Watzinger*.....98

Thermoelectric magnetohydrodynamic control in alloy solidification

*A. Kao, X. Fan, N. Shevchenko, C. Tonry, P. Soar, I. Krastins, S. Eckert, K. Pericleous, P. D. Lee*.....99

Mass transport and solutal convection in a sodium-zinc molten salt battery with liquid electrolyte: comparison of modelling and experiments

*M. Sarma, C. Duczek, W. Nash, N. Weber, T. Weier*.....100

Role of thermoelectromagnetic effect in metal additive manufacturing

*I. Kaldre, V. Felcis*.....101

Modelling azimuthal velocity of liquid metal in a 2D centrifugal separator driven by a travelling magnetic field

*L. Terlizzi, R. Strazdiņš, L. Goldšteins*.....106

**Poster session**

Magnetic field distribution in disc-type electromagnetic pump with permanent magnets

*A. Brēķis, A. Šiško, I. Bucenieks*.....112

Simulation of autothermal reforming of methane in a packed-bed reactor

*V. Dzelme, V. Geza, A. Jakovics, V. Kharitonov, L. Rodin*.....113

Finite element method calculations coupled with circuit simulator

*V. Geza, K. Bolotin*.....114

Optical imaging of MHD bubble flow in a Hele-Shaw liquid metal cell

*A. Jegorovs, M. Birjukovs, A. Jakovics*.....120

Numerical analysis of condensation risk in different multilayer building structures

*B. Jirgensone, A. Jakovics*.....121

The calibration of turbulence model for melt flow in floating zone growth of silicon crystals

*K. Surovovs, S. Stroževs, M. Surovovs, J. Virbulis*.....122

A well coupled multi-scale model of additive manufacturing based on phase field method, cellular automata method and lattice Boltzmann method

*Ling Shi, Jiang Wang, Songzhe Xu,*, Jingjing Li, Chaoyue Chen, Tao Hu, Hari Sundar, Zhongming Ren*.....123

Modelling liquid metal free-surface capillary flow for nuclear fusion applications

*S. Mingozzi, M. Iafrati*.....124

Numerical modelling of feed rod melting dynamics during floating zone silicon crystal growth

*M. Surovovs, J. Virbulis*.....125

Numerical study of heating and melting of metal in industrial direct current electrical arc furnace

*S. Pavlovs, A. Jakovics, A. Chudnovsky*.....126

Improving the Ekibastuz coal quality using "dry enrichment" technology

*K.M. Shaimerdenova, S.E. Sakipova, N.T. Abdirova, A.P. Tussupkhanova, T. Shunkeev*.....132

Power calculation in a 2D axisymmetric centrifugal separator with traveling magnetic field

*R. Strazdiņš, L. Terlizzi, L. Goldšteins*.....133

Ultrasonic Doppler velocimetry for melt flow in model experiments for Czochralski crystal growth

*I. Tsiapkinis, A. Wintzer, S. Foroushani, K. Dadzis*.....134

Influence of surface waves on liquid-to-gas mass transfer in molten silicon

*G. Zageris, V. Geza, S. Pavlovs*.....135

# How magnetic field measurements can be applied to characterise flow structures in liquid metals or to monitor electrified industrial processes

*T. Wondrak, M. Sieger, R. Mitra, J. Schmidtpeter, L. Krause, D. Makarov, S. Eckert*

Inductive measurement techniques are extremely sensitive and thus offer high potential for monitoring flow processes in metallurgy, the chemical industry and process engineering. In particular, they are suitable for the characterisation of multiphase flows, e.g. in the detection of gas bubbles in electrically conductive fluids or the tracking of magnetic particles in flotation. The contactless inductive flow tomography (CIFT) is developed in our laboratory over the last 20 years to visualize three-dimensional velocity fields in liquid metals. The technique is based on precise measurements of small flow-induced perturbations of an applied magnetic field and the subsequent reconstruction of the flow field by solving the associated inverse problem. We will give an overview of diverse modifications of this technique employed for various measuring tasks in different processes specified below.

Contactless Inductive Flow Tomography (CIFT) is based on the precise measurement of very weak induced magnetic fields arising from the fluid motion under the influence of one or several primary excitation magnetic field(s). The simultaneous use of more than one excitation magnetic field is necessary to fully reconstruct three-dimensional liquid metal flows, yet is not trivial as the scalar values of induced magnetic field at the sensors need to be disentangled for each contribution of the excitation fields. Another approach is to multiplex the excitation fields. Here the temporal resolution of the measurement needs to be kept as high as possible. We apply two trapezoidal-shaped excitation magnetic fields with perpendicular direction to each other to a mechanically driven liquid metal flow. The consecutive application by multiplexing enables to determine the flow structure in the liquid with a temporal resolution of about 1 Hz using the existing equipment. This proof-of-principle for a CIFT two-field excitation opens the way for further improvements of the technique that will be delineated in the outlook.

Foam processes are essential in many industrial applications e.g., in froth flotation for material separation. A detailed understanding of foam flows is vital for improvements in process efficiency. X-Ray and Neutron imaging can measure flow fields in foam, but require a complex setup and cannot be performed in-situ. Magnetic particle tracking (MPT) is an alternative approach, that measures the trajectory of a small magnetic tracer particle inside the foam as a representation of its movement. Different magnetic field sensors can be applied to detect the magnetic tracer particle. We chose thin film sensors based on the planar Hall effect (PHE) due to their small size, high sensitivity, high signal-to-noise ratio and low cost. Our sensors have a size of only 2 mm x 2 mm and are capable of measuring magnetic fields as low as 10 nT at a sampling frequency of 1 Hz. A sensitivity of 20 V/T at a driving current of 1 mA was achieved by means of sensor bridging. Our PHE-sensors are almost as precise as currently used Fluxgate probes, but offer several advantages due to their reduced size. This includes being installed closer to the area to be measured, enabling finer grids of sensors and decreasing the detection volume, which increases the precision of the MPT as well as other tomographic methods.

A novel concept of a measurement technology for the localization and determination of the size of gas bubbles is presented, which is intended to contribute to a further understanding of the dynamics of efficiency-reducing gas bubbles in electrolyzers. A simplified proof-of-concept (POC) model is used to numerically simulate the electric current flow through materials with significant differences in electrical conductivity. Through an automated approach, an extensive data set of electric current density and conductivity distributions is generated, complemented with determined magnetic flux densities in the surroundings of the POC cell at virtual sensor positions. The generated data set serves as testing data for various reconstruction approaches. Based on the measurable magnetic flux density, solving Biot-Savart's law inversely is demonstrated and discussed with a model-based solution of an optimization problem, of which the gas bubble locations are derived.

**MHD effects on the alumina dissolution in aluminium electrolysis cells**

V. Bojarevics

University of Greenwich, UK

**Abstract.**

Numerical modelling has become a primary tool for design and optimization of commercial high amperage aluminium electrolysis cells. The design of industrial cells requires to account for a variety of their individual features: electric current and the associated magnetic field distribution, ferromagnetic parts effect, the velocity field in the two overlying fluid layers, and their interface deformation and wave motion, often referred to as the MHD instability. The normal electrolytic process is regularly disrupted due to the anode changes and the feeding of alumina ($Al_2O_3$) particulate material ensuring the continuity of the electrolytic aluminium production. The modelling technique of alumina dissolution from particles of various sizes is accounting for their inertia, drag in the turbulent flow, the electrolyte layer shape and the electromagnetic force at the location. The feed material initially forms rafts of frozen electrolyte + alumina, which gradually disperse and dissolve in the dependence of the local flow, turbulent diffusion, and the instantaneous concentration level below saturation in the location. The dispersed particles continue to travel with the flow to dissolve in the dependence of the local turbulence and the instantaneous concentration level until reaching a quasi-steady concentration distribution, while the concentration is continuously depleted due to the electrolytic metal production. The modelling is applied to illustrate optimization of the commercial cell performance, while avoiding regions of low concentration responsible for increased fluoride gas release due to the low voltage anode effect.

**Key words:** aluminium electrolysis cell, alumina dissolution, particle tracking, magneto hydrodynamics, turbulent mixing

# Multiphysical model experiments for crystal growth from melt

*K. Dadzis, A. Wintzer, I. Tsiapkinis, S. Foroushani*

Leibniz-Institut für Kristallzüchtung (IKZ), Berlin, Germany
kaspars.dadzis@ikz-berlin.de

The development and production of crystalline materials are an important part of the modern materials science. In particular, crystal growth processes from melt usually involve complex high-temperature vacuum furnaces and are governed by a large variety of physical phenomena, from heat and mass transfer to solid mechanics (see Fig. 1). Coupled with a large span of relevant spatial and time scales, the multiphysical, multi-scale growth process is a great challenge for numerical modeling. However, an even larger challenge is the development of the underlying physical models and their validation by experimental data [1] since crystal growth furnaces are hardly accessible for in-situ measurements. While model experiments under simplified conditions have been discussed in the literature for melt flow in particular (see [2] for a review), a coupled multi-physical analysis as sketched in Fig. 1 is still missing. We are addressing this gap in the NEMOCRYS project [3] and developing accessible crystal growth experiments [4] for model materials such as tin and cesium iodide with as much in-situ observation as possible. The experimental data are used to build a new generation of open-source crystal growth models with rigorously validated modeling assumptions and approaches [5]. We will summarize the current status of the project and present examples of model experiments, simulations, and further applications.

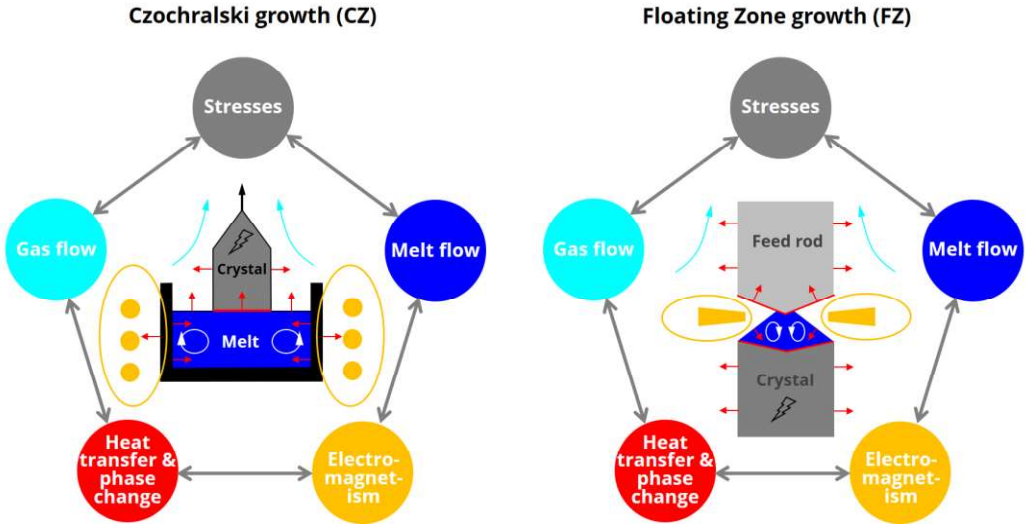


Fig. 1. Multi-physical phenomena in two common crystal growth processes from melt.

**Acknowledgement:** This work is funded by the European Research Council (ERC) under the European Union's Horizon 2020 research and innovation program (grant agreement No 851768).

**References**

[1] K. Dadzis, P. Bönisch, L. Sylla, and T. Richter, "Validation, verification, and benchmarking of crystal growth simulations," Journal of Crystal Growth, vol. 474, pp. 171–177, 2017, doi: 10.1016/j.jcrysgro.2016.12.091.
[2] K. Dadzis, O. Pätzold, and G. Gerbeth, "Model Experiments for Flow Phenomena in Crystal Growth," Crystal Research and Technology, vol. 55, no. 2, p. 1900096, 2020, doi: 10.1002/crat.201900096.
[3] Project homepage: https://nemocrys.github.io/
[4] K. Dadzis, Czochralski growth of tin crystals as a multi-physical model experiment, https://arxiv.org/abs/2305.06875
[5] A. Enders-Seidlitz, J. Pal, and K. Dadzis, "Development and validation of a thermal simulation for the Czochralski crystal growth process using model experiments," Journal of Crystal Growth, vol. 593, p. 126750, 2022, doi: 10.1016/j.jcrysgro.2022.126750.

# Innovative NbSi composites: investigation and development of an alloying process using cold crucible induction furnace

Egbert Baake[1*], Mattia Guglielmi[1], Alex Köppen[1], Elisa Holzmann[2], Sebastian Herbst[2]

1. Institute of Electrotechnology, Leibniz University of Hanover, Wilhelm-Busch-Str. 4, 30167 Hanover, Germany
2. Institute of Material Science, Leibniz University of Hanover, An der Universität 2, 30823 Hanover, Germany

*baake@etp.uni-hannover.de

**Abstract:** Refractory metals based on niobium are progressively gaining interest in the industrial world for the production of components used in high-temperature environments. With superior thermal and mechanical properties than nickel-based superalloys, NbSi-composites represent a promising alterative for the fabrication of aircraft components, and they open the way to a significant increase of the efficiency of their engines. The melting process of such refractories still faces though relevant technical limitations, related to their high melting point and chemical reactivity. Therefore, numerical simulations become fundamental for the detailed analysis and optimization of their melting process. With the help of multiphysical simulations and the particle tracking method, the addition of targeted metals within the NbSi base is also investigated.

**Keywords:** electromagnetic induction melting, cold crucible furnace, multiphysical simulation, particle tracking, alloying

## Introduction

The selection of appropriate material properties plays a key role in the production of components used in high-temperature environments. A significant example is represented by aircraft engines, where high-pressure blades are permanently exposed to enormous mechanical stresses and extreme temperatures, typically higher than 1000 °C. Currently, such high-performance components are mainly fabricated with nickel-based superalloys, which stand out mostly for their excellent creep behaviour and corrosion resistance. These alloys are though limited by operating temperatures of maximum 1150 °C. In order to achieve future improvements, especially in terms of engine efficiency, it is necessary to increase the permissible operating temperature of materials once again: the development of alternative alloys based on refractory metals is of particular interest. With a density of 6.6 to 7.2 g/cm$^3$, the so-called niobium-MASC systems (Metal And Silicide Composites) are characterized by high melting point, over 1750 °C, and reach the maximum operating temperature of 1300 °C. The phases of niobium (Nb) and silicon (Si) complement each other, providing good fracture toughness, high-temperature strength and oxidation resistance. The targeted addition of further elements – aluminium, titanium, chromium and hafnium – improves complementary properties such as creep resistance and fracture toughness. As a counterweight to these advantages, controlled production of such alloys faces major technical challenges: due to the high chemical reactivity of niobium melts, contamination of the cast by crucible materials can occur in conventional melting processes and the operating life of the crucible is compromised by extreme thermal loads.

For the cited reasons, semilevitation melting by electromagnetic induction in crucible furnace with cold walls (CCF) is proposed as innovative approach to process niobium melts. This enables largely contactless melting, increasing the quality of the melt and reducing the costs related to the materials of the crucible. The liquid workpiece is affected by strong electromagnetic stirring, that makes the CCF an excellent solution for mixing and alloying multi-component systems. The melt is strongly homogenized, with a significant improvement of the properties of the solidified cast. Melting by electromagnetic induction in CCF was intensively investigated by the authors for metals and alloys with a wide range of melting temperatures, but only in the last years it was applied to niobium-based materials [1]: a sample of pure niobium with the volume of 100 $cm^3$ was molten under the supplied power of 113 kW, at the frequency of 10 kHz. A composite made of niobium and silicon was successfully molten and alloyed with 47 kW and 10.55 kHz. The sample was produced in different volumes, up to 160 $cm^3$, under very stable and reproducible melting conditions [2]. This work aims to bring those investigations one step forward and summarizes the performed alloying process of the achieved NbSi matrix with “additional metals”, aluminium (Al), hafnium (Hf), chrome (Cr) and titanium (Ti). Properties of the materials impose challenging thermal conditions to the CCF, affect the alloying process and their homogenization with the matrix. Therefore, numerical models become fundamental to estimate the operational parameters of the melting process and calculate the distribution of the additional elements within the NbSi base. Their dispersion is analysed with the help of the Discrete Phase Model: elements are modelled as spherical particles and their motion inside the continuum is predicted with the particle tracking method.

**Numerical and mathematical model**

The melting process by electromagnetic induction takes place in a laboratory-scale crucible furnace with cold wall, surrounded by a copper inductor in symmetrical position to it (Fig. 1). The crucible has the volume of 282 $cm^3$, is made of copper and has 14 water-cooled palisades. The inductor consists of 6 turns and is cooled by water as well. The entire setup is hosted by a vacuum chamber, in which inert gas can be injected if necessary.

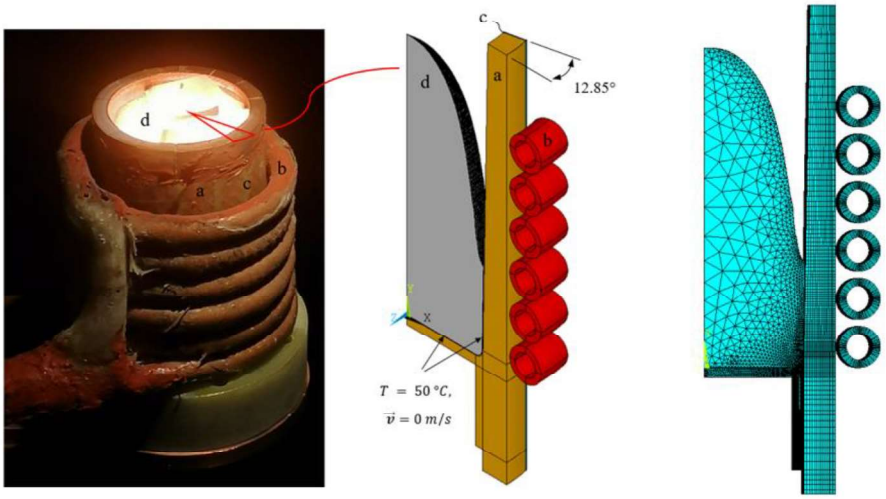


Figure 1. The experimental setup (left), its numerical model with half crucible palisade (centre) and the corresponding mesh (right). In the picture, with (a) it is indicated the palisade of the crucible, (b) the inductor, (c) the insulating layer and (d) the workpiece.

Electric power is generated by an EMA generator installed at the Institute of Electrotechnology, with the possibility to supply maximum active power of 300 kW and the frequency range 8-12 kHz.

The commercial software ANSYS® is used for the computational analysis of the melting process: the 3D numerical model is made of half palisade of the crucible, one insulating layer and the corresponding section of the inductor, and the simplification of the crucible geometry is possible due to the symmetry of the crucible. Assuming a stable and symmetrical deformation of the melt free surface, even the corresponding segment of the melt is included. Such a geometrical simplification significantly shortens computational time in comparison to the full 3D geometry, without any compromising decrement of the result quality. The melting process is simulated by multiphysical simulations, in which the package Mechanical APDL is coupled with ANSYS Fluent in the described way: *step 1)* the electromagnetic (EM) simulation calculates the Lorentz force and Joule heat distribution within the workpiece in harmonic and steady-state regime. The free surface of the workpiece is not assumed to be affected by any deformation during this phase, since the EM time constant, describing the variation of the EM forces, is significantly smaller than the mechanical time constant, which describes the geometrical variation of the free surface. *Step 2)* EM results are imported from ANSYS Mechanical APDL to ANSYS Fluent with the use of a *udf* function. *Step 3)* coupled fluid dynamic (FD) and thermal (TH) simulations are carried out in transient regime. Free surface dynamics of the liquid metal are calculated with the help of the Volume Of Fluid (VOF) method, as the distribution of the Lorentz forces and the Joule heat is cyclically computed on the base of the surface deformation of the melt. Typical Reynold number for liquid niobium and NbSi-based composites in the investigated CCF indicate a fully developed turbulent flow:

$$Re_{Nb} = \frac{r_o u \rho}{\mu} \approx 10^5. \quad (1)$$

The LES turbulence model is chosen for the fluid dynamic calculation. Thermal field within the workpiece is computed with the Energy and Solidification/Melting models, where the liquid fraction $\beta$ can be defined as

$$\beta = \frac{T - T_{solidus}}{T_{liquidus} - T_{solidus}} \quad \text{if} \quad T_{solidus} < T < T_{liquidus}, \quad (2)$$

or $\beta = 0$ and $\beta = 1$ if the temperature of the body is respectively lower and higher than the *solidus* temperature and the *liquidus* temperature. Constant temperature of T=50 °C is defined at the surface of contact between the wall of the crucible (side and bottom) and the workpiece. Thermal losses by radiation are modelled, while convection is neglected.

To predict the distribution of the additional metals (Al, Ti, Cr and Hf) within the NbSi base, the particle tracking method is chosen. Elements are modelled with the Discrete Phase Model (DPM) as spherical solid particles, moving inside the liquid NbSi (*continuum*) before the alloying process. Motion of particles is affected by the buoyancy force, the gravity force, the Stokes drag force and the EM force; no Saffmann's lift force is defined; interaction between particles is neglected. Let us assume the following parameters: the particle diameter of $d_p$=0.1 mm for each metallic element, the characteristic velocity of U≈1 m/s, the dynamic viscosity of the liquid phase of μ=0.0045 Pa·s and the characteristic length of L≈0.1 m; in this case, the dimensionless Stokes number

$$St = \frac{\rho_p d_p^2 U}{18\mu L} \tag{3}$$

is estimated to be $St_{Hf} \approx 0.16$ (for hafnium, with the highest density) and $St_{Al} \approx 0.0016$ (for aluminium, with the lowest density), with intermediate values for Cr and Ti. Particles are therefore fully affected by the liquid flow field.

The trajectory of the particles is predicted with the force balance equation:

$$\frac{d\overrightarrow{v_p}}{dt} = F_D\left(\vec{v} - \overrightarrow{v_p}\right) + \frac{\vec{g}(\rho_p - \rho)}{\rho_p} + \overrightarrow{F_{pEM}}, \tag{4}$$

where $\overrightarrow{v_p}$ is the particle velocity and $\vec{g}$ the acceleration of gravity. The drag force per unit particle mass $F_D\left(\vec{v} - \overrightarrow{v_p}\right)$ includes $\vec{v}$ the fluid phase velocity and defines

$$F_D = \frac{18\mu}{\rho_p d_p^2}\frac{C_D Re}{24}, \tag{5}$$

with $Re$ the relative Reynolds number of the particle

$$Re = \frac{\rho d_p |\overrightarrow{v_p} - \vec{v}|}{\mu}. \tag{6}$$

Leenov-Kolin forces are defined on spherical particles:

$$\overrightarrow{F_{pEM}} = -\frac{3}{2}\frac{\sigma - \sigma_p}{2\sigma + \sigma_p} V_p \overrightarrow{f_{EM}}, \tag{7}$$

where $\sigma$ is the electrical conductivity, $V_p$ the volume of the particle, and $\overrightarrow{f_{EM}} = 0.5Re\left(\vec{j} \times \vec{B}^*\right)$ is the average component of the Lorentz force generated by the action of the EM field.

**Melting and alloying of a NbSi-based composite**

Multiple samples of the alloy composed of niobium and silicon were already achieved by the authors with the supplied power of $P_{exp}$=47 kW and the working frequency of $f_{exp}$=10.55 kHz. Numerical simulations evidence very good agreement with the experimental results [2]. Samples have a volume between 65 and 160 cm$^3$ and are obtained from pellets of the single elements. The following investigation step will consider the sample volume of 130 cm$^3$, which shows the most stable FD and TH behaviour.

From the obtained NbSi base, this investigation steps forward and includes additional elements to the base. The alloying process is investigated computationally and experimentally: the numerical model considers a liquid phase (*continuum*) of NbSi, in which the motion of the additional metals is affected by different forces. Melting temperature of the NbSi base is corrected to 1960 °C. Additional elements are modelled as spherical, solid particles, with the same diameter of the powders used for the experimental investigation. A group of 10 particles for each material is injected within the liquid phase at the height of $Y_{inj}$=20 mm from the bottom of melt; this injection position is supposed to lead to a strong mixing of the elements, and to disperse them uniformly within the final cast. Numerical simulations are performed for 12 seconds and their final results are shown in Fig. 2: materials with lower mass density (Al, Ti and Cr) tend to distribute in the upper region of the melt volume, transported by the typical recirculation vortices of the flow field. Chromium occupies the highest region of the continuum for a significant residence time; this does not happen for aluminium, even if its mass density is

significantly lower (Tab. 1); in fact, stronger motion towards the top was expected. The distribution of hafnium is inhomogeneous and realistically affected by its high mass density; a smaller recirculation of its particles is visible in the central region of the melt.

Experimental results put in evidence interesting similarities with the numerical simulations but also some critical points of the alloying process: melting of the NbSi base with the additional elements is successfully achieved with the supplied power of 36 kW, measured inductor current of $I_{exp}$=1418 A rms and the frequency of $f_{exp}$=10.9 kHz; the workpiece melts

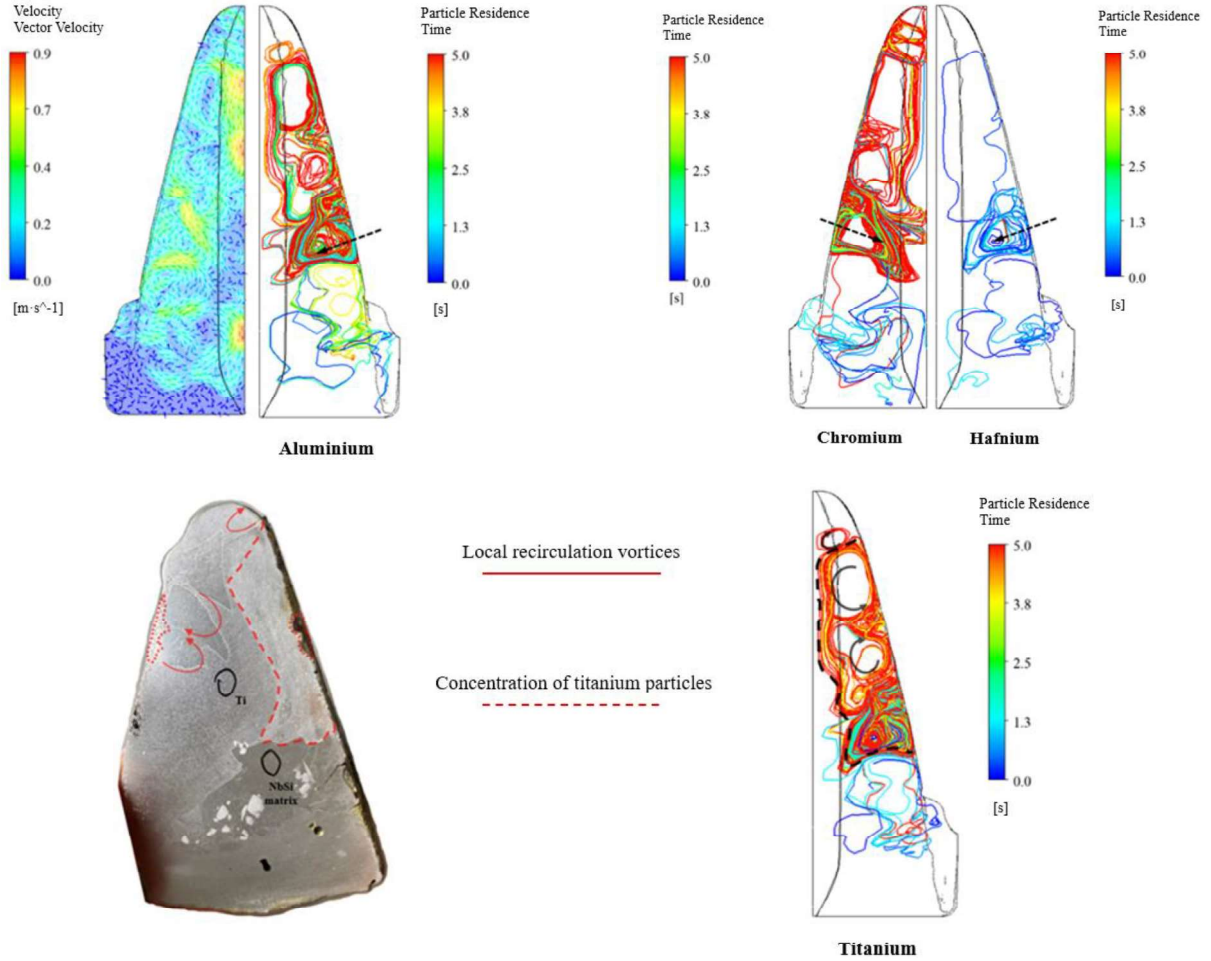


Figure 2. Numerical results of the particle motion of the additional metals within the liquid NbSi phase; particle tracing is used. The black dart identifies the starting injection position of the particles. The last picture on the right shows the solidified sample achieved in the experimental investigation: the lower region (dark grey) is mostly made of the alloy NbSi matrix plus Hf and 30% of Ti; the upper region (light grey) contains the remaining 70% of Ti. In the picture, typical flow patterns are indicated, and it can be noticed that significant similarities with the simulation are present in the distribution of Ti.

at the temperature of 1835 °C and the liquid melt maintains a stable meniscus. The chemical analysis evidences though an incomplete alloying of the base with the remaining materials: hafnium fully reacts with the NbSi base and mixes uniformly, while titanium partially reacts and shows recirculation patterns still visible in the upper region of the solidified cast. Such vortices are analogous to the ones calculated numerically, and denote very good agreement

between the experiment and the model. The simplification of the numerical model with half palisade could be responsible for the asymmetrical behaviour of the titanium flow patterns. Evaporation of aluminium and chrome is documented by the analysis: the remaining atomic percentage of Al inside the cast is 0.8%, while its initial value was 3%; the remaining atomic percentage of Cr is 0.3%, while its initial value was 4%. Such a massive evaporation is explained by the vacuum environment in which the melting process takes place: pressure of $10^{-2}$ mbar is used in this investigation step, and this dramatically decreases the boiling point of the targeted materials. The following experiments are carried out in inert gas environment, by filling the chamber with argon, and pressure is kept constant at the value of 300 mbar. In this case, chemical analysis proves that all the additional metals react, alloy and mix homogeneously with the base of Nb and Si, with no evaporation of any of them. The melting process remains extremely stable, and no significant change of the electrical parameters occurs for different volumes of the melt, as shown in Fig. 3.

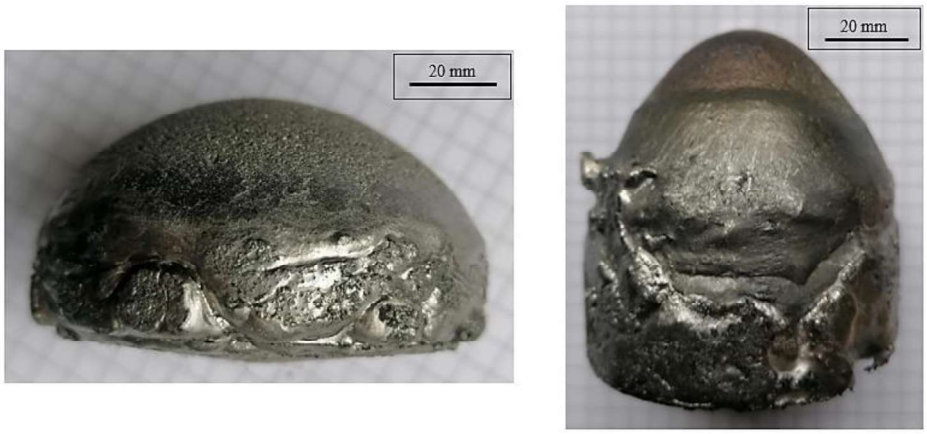


Figure 3. Experimental results with the injection of inert gas: solidified sample with the volume of 65 $cm^3$ (left) and 130 $cm^3$ (right). Free surface deformation is still visible as result of the rapid solidification of the cast.

**Conclusions**

The melting process in cold crucible furnace for composites based on niobium and silicon is successfully achieved, and the alloying process of the NbSi base with four additional elements is investigated and optimized. The mixing of the NbSi base with the additional elements cannot be achieved in vacuum conditions, due to the evaporation of Al and Cr, but such a problem is solved with the use of inert gas atmosphere and higher pressure. A homogenous NbSi-based matrix is obtained with relatively low electrical power and thermal stress for the cold crucible furnace. The distribution of additional elements before the complete alloying process can be simulated with the use of the particle tracking method.

**References**

[1] Guglielmi, M., Baake, E., Köppen, A., Holzmann, E., & Herbst, S. (2022). Induction melting in a cold crucible furnace applied to innovative high-melting temperature materials. Magnetohydrodynamics, Vol. 8 (4): 523-532.

[2] Guglielmi, M., Holzmann, E., Köppen, A., Baake, E., & Herbst, S. (2023). Investigation of an alloying process for NbSi-based composites in cold wall cruicble furnace. Proceedings of the HES-23 International Conference on Heating by Electromagnetic Sources, Padua, May 10-12.

**Modelling Contactless Ultrasonic Cavitation for Industrial Scaling**

Catherine E.H. Tonry*, Valdis Bojarevics, Georgi Djambazov, and Koulis Pericleous

Ultrasonic Treatment (UST) of liquid metals has shown great potential for both degassing of molten metals and grain refinement of cast alloys. Conventional UST methods use an immersed sonotrode to treat the melt. One of the main downsides with this approach, is that contact with the melt can introduce impurities and the sonotrode can also be dissolved. By use of a high frequency electromagnetic coil to induce ultrasound contact with the melt can be avoided, while having the additional benefit of adding heat and mixing. To ensure the resulting pressure waves reach the level required for cavitation it is necessary to tune the system for acoustic resonance. Extensive studies in aluminium have shown that this technique can produce grain refinement and enhance degassing. Recent modelling work has suggested that by using higher resonant modes of the system a larger crucible can be resonated. This leads to multiple treatment regions within the melt, combined with the strong stirring from the time average Lorentz force. This leads to the possibility of treating much larger volumes of metal melt, potentially enabling the scaling up of the process to industrial applications.

# RESULTS OF 3D SIMULATIONS OF ELECTROMAGNETIC INDUCTION PUMP USING ELECTRIC POTENTIAL FORMULATION

N. Jēkabsons*, L. Goldšteins, L. Buligins, K. Kravalis

Institute of Physics, University of Latvia,
3 Jelgavas street, LV-1002 Riga, Latvia
*Corresponding author's e-mail: Normunds.Jekabsons@lu.lv

***Key words**: electromagnetic, pump, potential, numerical, comparison.*

## Abstract

Due to contactless pumping and hermetic construction electromagnetic induction pumps (EMIP) are often used for transportation of liquid metals [1]. EMIP based on permanent magnets have proven to be an efficient and simple solution in many industrial and research applications [2].

Traditionally EMIP are modelled by solving induction equation for magnetic fields [1]. However, in many applications magnetic Reynolds number is small, thus induction-less, potential formulation for MHD problem is possible. This approach has several advantages:

1) A single scalar equation needs is solved instead of three vector field equations;
2) Any distribution of external, travelling magnetic field of permanent magnets can be applied;
3) Boundary condition of electric potential are well defined within liquid/channel domain, thus there is no need for far-field solutions.

In this paper we use potential formulation to describe a simple model of ideal EMIP based on well know formulas [1]. As a proof of concept, a simple numerical model block flow is used for estimation of integral characteristics such as pressure head and released total Joule heat. The full-scale 3D numerical model is developed for further studies of turbulent flow details. Both are validated with recent experimental results from 50 l/s liquid sodium EMIP in the Institute of Physics of University of Latvia. Conclusions about feasibility of approach are presented.

## References

[1] A. I. VOLDEK. Induction Magnetohydrodynamic Machines with Liquid Metals as a Working Medium (Energia Publ House, Leningrad, 1970) (in Russian).

[2] I. BUCENIEKS. Perspectives of using rotating permanent magnets for electromagnetic induction pump design. Magnetohydrodynamics, vol. 36 (2000), no. 2, pp. 151–156.

# Electromagnetic control of the direct strip casting process

Valters Dzelme[1], Andris Jakovičs[1], Egbert Baake[2]

[1]Institute of Numerical Modelling, University of Latvia
[2]Institute of Electrotechnology, Leibniz University Hannover

Direct strip casting (DSC) [1] is a novel continuous casting technology to produce metal strips with as-cast thickness below 20 mm. Liquid metal is poured onto an intensively-cooled moving belt, where it gradually solidifies forming a thin strip. A known issue in DSC is the backflow, where, upon impact on the belt, fraction of liquid metal flows opposite to the belt movement into the small gap between the belt and refractory. An inclined secondary refractory has been reported in [2] as a possible solution. Another problem is flow uniformity and free surface stability downstream. Electromagnetic brake and argon jets have been reported to stabilise the flow and surface oscillations.[1] We propose that the backflow can be efficiently limited using AC magnetic field. Combining this with DC or traveling field for flow stabilisation can provide a stable casting process and a uniform strip profile.

To understand the parameters and conditions under which AC magnetic field induces stable free surface deformation, we study a thin liquid Galinstan layer in a simple experimental setup shown in Fig. 1. Results show that smooth and stable deflection is achieved for relatively thin layers, while oscillatory edge patterns develop for thicker layers due to a parametric pinch-type instability.

To finally test the application of AC and DC field for realistic DSC conditions, we develop a numerical model in Elmer and OpenFOAM to simulate the belt casting process with electromagnetic control. Scheme of the model is shown in Fig. 2. Free surface dynamics at the backflow gap near the inductor exhibit similar characteristics to what was observed in the experimental setup. However, overall AC field prevents liquid metal from entering further into the gap. The addition of DC magnetic field helps stabilising the flow, resulting in stable process.

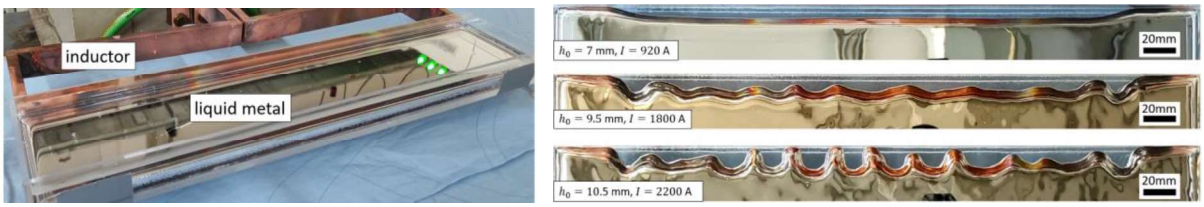


Fig. 1. Experimental setup (left) and example results with $f = 4$ kHz (right)

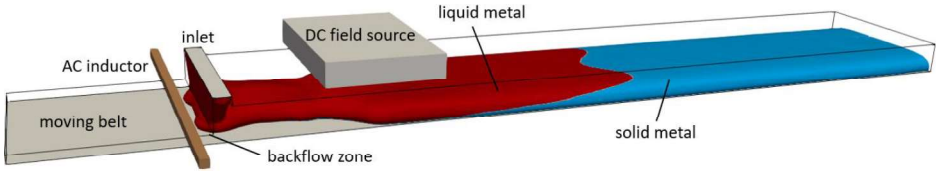


Fig. 2. Scheme of the DSC process with AC and DC magnetic field

[1] K. H. Spitzer, et al. Direct strip casting (DSC) – an option for the production of new steel grades. *Steel Research International*, Vol. 74 (2003), pp. 724–731.

[2] U. Niaz, M.M. Isac, and R.I.L. Guthrie. Numerical modeling of transport phenomena in the horizontal single belt casting (HSBC) process for the production of AA6111 aluminum alloy strip. Processes, Vol. 8 (2020), p. 529.

9th International Scientific Colloquium "Modelling for Materials Processing".
Riga, Latvia, September 18-19, 2023

# Advanced Electrode Melting for Highest-Purity Cast Parts

*Sergejs Spitans, Henrik Franz, Björn Sehring, Samuel Bogner*
ALD Vacuum Technologies GmbH, Otto-von-Guericke-Platz 1, 63457 Hanau, Germany

**Abstract**

Electrode Induction Melting Inert Gas Atomization (EIGA) is the state-of-the-art process for high-quality spherical powder production. In the EIGA process the lower end of the vertically hanged pre-alloyed electrode is continuously fed into the region of high-frequency electromagnetic (EM) field created by a conical coaxial induction coil located below. Induction melting takes place and a flow in a thin layer is formed at the conical tip of the electrode resulting in a metal down-stream on the axis. The application of electrode induction melting for investment casting could be exceptionally beneficial for achieving the highest cleanliness of the cast parts. However, the electrode induction melting for metallic powder production is currently a well-established technique only for relatively small melt rates (such as <2 kg/min). On top of that, the melt cannot be significantly superheated due to the small thickness of the liquid layer at the conical electrode tip and the fact that material instantly leaks out of the zone of EM heating as it turns liquid due to the gravity and pinching Lorentz forces. In the present work, we are using numerical modelling and experimental validation to demonstrate how the high-melt-rate and high-superheat electrode induction melting can be designed for investment casting applications.

**Introduction**

The Electrode Induction Melting Inert Gas Atomization (EIGA) process was developed and patented by ALD Vacuum Technologies [1] as a ceramic-free atomization process that is especially suited for production of high-purity, reactive and refractory metal powders (Fig. 1a). In the EIGA atomization process the pre-alloyed cylindrical electrode (< Ø150 mm and < 1 m length) is mounted on an electrode feeding device which continuously lowers the vertically hanged electrode into a conical induction coil. Then, energy is coupled into the electrode tip using a high-frequency electromagnetic (EM) field. As a result, a melt film is formed on the electrode surface and a molten metal stream or droplets fall from the electrode tip into the inert gas nozzle where a high-velocity gas stream atomizes the melt [2]. By this means, the generated micro-droplets solidify while traveling down in the atomization tower and form spherical shaped fine powders which are collected in a vacuum-tight powder container.

Our goal is to investigate if the advantage of crucible-free electrode induction melting can be combined with Investment Casting (Fig. 1b). In this case, a melt stream with sufficiently high superheat and a melt rate of 60-120 kg/min for typical Direct Solidification or Single Crystal process has to be created.

The main advantage of the EIGA-type electrode melting for Investment Casting is that it is crucible-free. There is no consumable part that has to be regularly replaced and might be a source for ceramic impurities found in castings. Therefore, the guarantee of an ultimate casting purity is a clear advantage. On top of that, the EIGA-type electrode melting is very easy to operate. If sufficient power is applied, the system finds the steady-state itself and runs in a self-sustained stable mode. Using an electrode as a feedstock material can save a lot of time - no need of charging and discharging the one-shot liner in the back-up crucible. Electrode melting can be stopped anytime and continued later on using the next mould. Apart from that, alloy manufacturer already casts and delivers material in form of cylindrical electrodes and foundries have to cut the ingot in order to fit it in the one-shot liner. Additional impurities caused by this step, approximately 2% of material loss and expenses for the ingot cutting could be saved.

On the other hand, electrode melting at a high melt rate requires high power generators that could be quite expensive. However, EIGA-type melting due to high efficiency still can offer an opportunity for the energy saving in the long-term.

Keeping this in mind, this work focuses on the feasibility study and reveals if it is possible to achieve a high melt rate and a high superheat melt stream required for Investment Casting applications. Currently well-established melt rates used for powder atomization are below 2 kg/min. Moreover, it is known that during EIGA-type electrode melting the melt instantly leaks out of the zone of EM heating (small residence time) via thin layer. The achieved superheat is low and this might be a fundamental issue for the casting applications even if higher melting rates are achievable.

Direct melt stream superheat measurement is barely possible, therefore, we have developed and verified a simulation tool that precisely describes EIGA-type electrode induction melting [3]. According to simulation results, a melt stream superheat reaches 40 C during Ø150 mm Ti64 electrode melting at a rate of 2 kg/min (Fig. 2). Insufficient superheat is indirectly confirmed by formation of flakes instead of powder in powder atomization experiments.

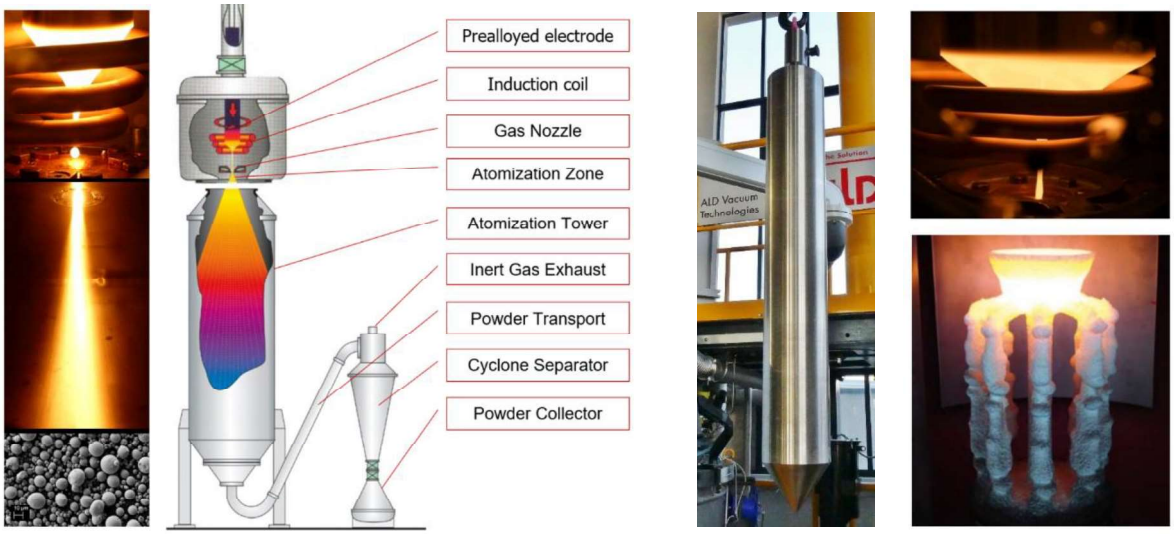


(a) (b)

**Fig. 1.** The EIGA process and a well-established atomization of Ø50 mm Ti64 electrode at a melt rate of 1 kg/min (a). The idea of EIGA-type Ø150 mm Ti64 electrode melting for investment casting application (b)

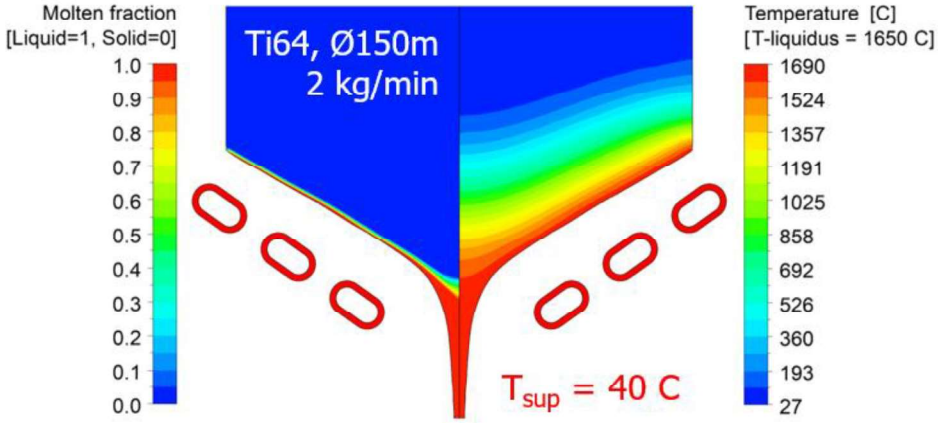


**Fig. 2.** Simulation results of the EIGA-type electrode steady-melting at 2 kg/min for powder atomization that reveal low melt stream superheat of 40 C. Contours of molten fraction are shown on the left (fully solid = blue, fully liquid = red) and temperature distribution on the right

**Results of numerical modelling**

***1) Melt rate***

An important parameter that is kept constant for further parameter study is the gap between the coil and electrode tip (controlled by inductance value in EM problem), because this distance determines the melting efficiency.

Simulation reveals that increase of the melt rate leads to a favourable increase of the volume-averaged melt stream superheat (Fig. 3). Note the large superheat of almost 250 C that can be achieved for Ti64 Ø150 mm electrode at a melt rate of 10 kg/min.

Let us take a look on the steady temperature profile in the electrode (Fig. 4). Somewhere far away above the melting front the electrode is cold, let's say at a room temperature. However, closer to the melting front the temperature rises and reaches the liquidus temperature at the melting front. Now, for simplicity of explanation, let us neglect thermal conductivity dependence on temperature and the latent heat. If the heat flux is flowing through the melting front, there must be a temperature gradient that drives it through the molten layer. Or the molten layer temperature at the free surface should be higher than liquidus temperature at the melting font. This is how the superheating still takes place in the molten layer.

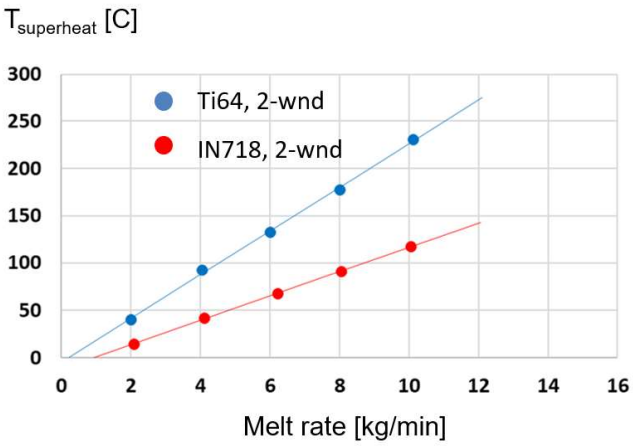


**Fig. 3.** Steady-state melt stream superheat depending on the electrode melt rate for Ø150mm Ti64 (blue) and IN718 (red) alloys

Now, if we double the feeding velocity (=double the melt rate), and accordingly increase the delivered power (increase the heat flux), the temperature rise in the solid electrode will get steeper (Fig. 4) that will lead to a larger superheat in the melt layer (Fig. 5).

Despite small superheat caused by the small melt rate in case of EIGA powder production, the superheat can be significantly increased by increase of the melt rate.

***2) Alloy***

Linear dependence of the superheat on the melt rate depends on the alloy thermophysical properties. For example, in case of IN718, we achieve less superheat at the same melt rate, if compared with Ti64 (Fig. 3).

If density is increased (with all other properties kept the same), the same melt rate requires less feeding velocity, and if material moves slower, the higher temperature penetrates deeper in the electrode. So, the temperature gradient is reduced inside the solid electrode and in the molten layer.

Further superheat decrease is achieved with higher thermal conductivity, lower liquidus temperature, lower latent heat, lower specific capacity of the solid fraction, etc. or larger electrode diameter (= slower feeding velocity if the melt rate is maintained constant).

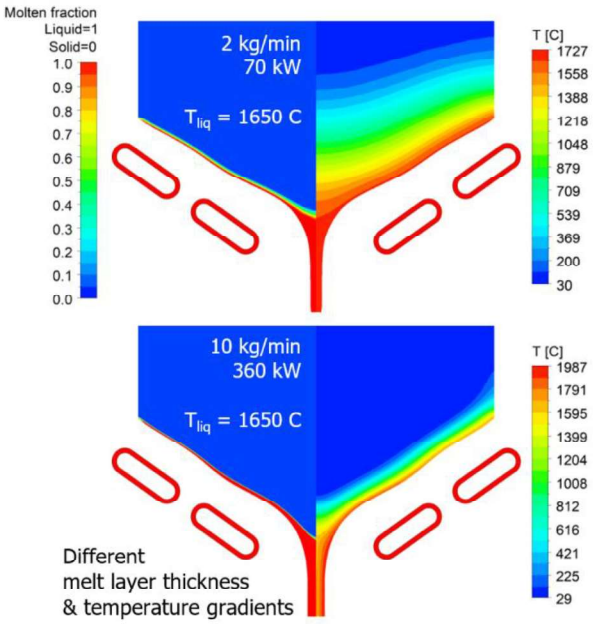


**Fig. 4.** Contours of molten fraction (on the left) and steady temperature distribution (on the right) in the Ø150mm Ti64 electrode being molten at two melt rates: 2 kg/min (upper figure) and 10 kg/min (lower figure)

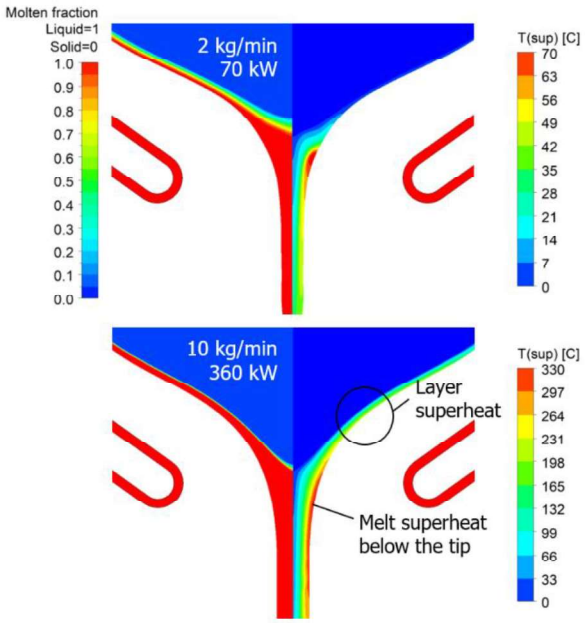


**Fig. 5.** Contours of molten fraction (on the left) and superheat temperature distribution (on the right) in the Ø150mm Ti64 electrode being molten at two melt rates: 2 kg/min (upper figure) and 10 kg/min (lower figure)

### *3) Inductor design*

Actually, it would be more convenient, if we could set the melt superheat and the melt rate separately.

In this case, design of inductor plays also an important role. Here is an example showing that a smaller number of inductor windings allows us to achieve higher superheat (Fig. 6). All the other parameters, including inductor generatrix and AC frequency are kept the same.

Note that despite the same melt rate, the total power required to maintain the same gap between the electrode and the 2-winding coil appears to be bigger than in case of 4-winding coil. This power difference converts directly in the melt superheating below the tip of the electrode (and has nothing to do with "layer superheat").

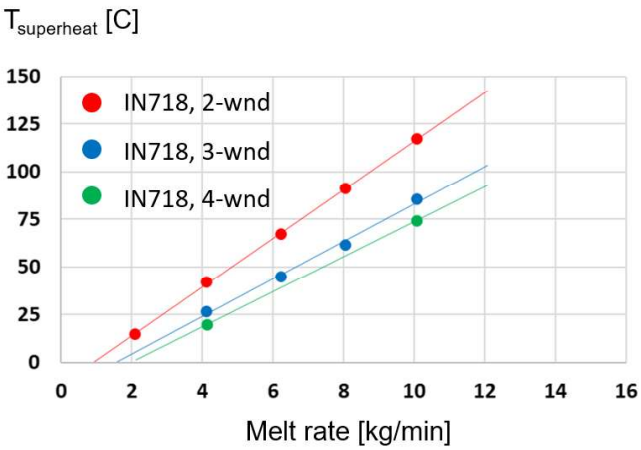


**Fig. 6.** Ø150mm IN718 electrode (10 kg/min) steady-state melt stream superheat depending on the number of inductor windings (2 - red, 3 - blue & 4 - green)

### *4) Total power level*

Another way how to control the superheat independently from the melt rate is to tune the level of the total power.

Let us think of the following experiment: you are steady-melting the electrode at a low total power level. This means that the net power that you induce in the electrode matches the melt rate (or the electrode feeding velocity). What would happen if we would instantly increase the total

power level? In this case we would instantly induce much more power in the electrode. However, keep in mind that we maintain electrode feeding velocity constant. So, you would instantly melt faster than you feed the electrode material and the gap between the coil and electrode would start to increase. If the gap increases, you are inducing less net power in the electrode. The gap will be increasing so far unless the net power in the electrode will match again the electrode velocity. This is an amazingly stable and easy to run system that drives itself into a steady regime.

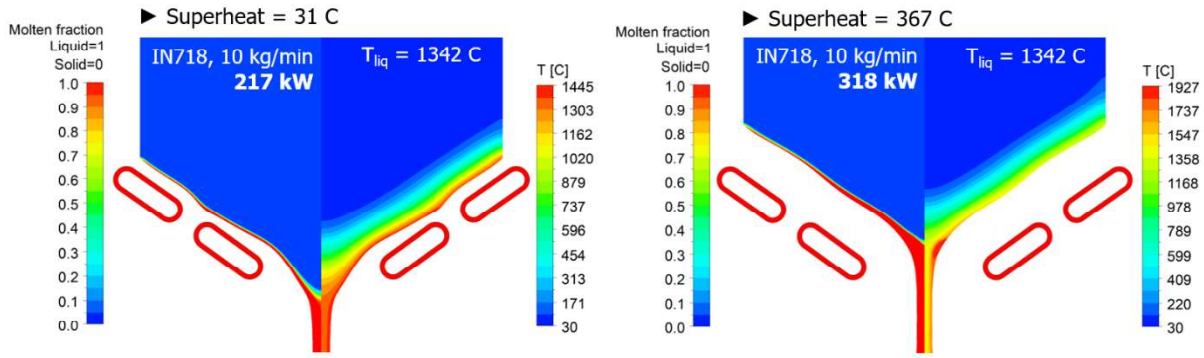


(a) (b)

**Fig. 7.** Contours of molten fraction (on the left) and steady temperature distribution (on the right) in the Ø150mm IN718 electrode being molten at 10 kg/min with two different total power levels: 217 kW (a) and 318 kW (b)

Now if you will melt two electrodes at the same melt rate and different power levels you will achieve smaller superheat in case of lower total power (Fig. 7a) and larger superheat in case of greater total power (Fig. 7b). In this case it has nothing to do with a "layer superheat". In this case you are superheating the stream below the tip of the electrode. Because of greater gap and higher power level the melt falls slightly longer through a stronger magnetic field and this results in a larger superheat.

So even as your melt rate is fixed, you are able to adjust the superheat by tuning the total power as a separate parameter – wide-range contact-free adjustment of the superheat is especially beneficial during large castings (Fig. 8).

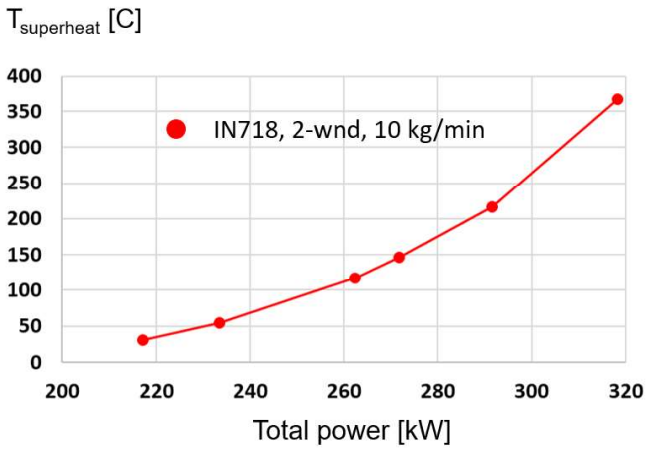


**Fig. 8.** Steady-state melt stream superheat depending on the total power for Ø150mm IN718 alloy electrode molten at 10 kg/min

Steady-state electrode melting is able to ensure a constant desired superheat, meanwhile, preheating of the electrode tip in combination with increased power at the start of the electrode melting can ensure higher superheat and higher melt rates in the beginning of the mould filling to avoid solidification in ceramic filter or in critical zone next to chill-plate.

**Qualitative validation of simulation results**

Up to now all the simulation results showed that it is possible to do the EIGA-type electrode melting at higher melt rate and higher superheat. And this brings us closer to satisfaction of requirements of investment casting.

In order to validate simulation results, we decided to carry out demonstrator experiment using a real EIGA powder atomization furnace. We have disassembled the nozzle and placed a copper

mould below the coil, and allowed the melt stream to solidify and form a Ø50 mm ingot (Fig. 9a). The surface quality of the ingot would act as a qualitative indicator of the melt superheat.

Note that due to small melt rates used for powder production the generator maximum power was only 100 kW.

► Test 1: the reference setting was 0.5 kg/min of Ti64 at a total power of 40 kW. Note the bad surface quality that indicated that the melt solidified before properly filling the mould (Fig. 9b).

► Test 2: we maintained the melt rate, but increased the total power up to 54 kW. Note the improvement of surface quality that is attributed 100% to a higher superheat (Fig. 9c).

► Test 3: we increased both AC current and melt rate. The surface quality is the best and this is because of two effects: 1) higher superheat due to higher power and higher melt rate and 2) increased thermal inertia due to higher melt rate (Fig. 9d).

To sum up, the experiment using the real EIGA furnace with limited generator power confirmed results of our simulations. Validation experiments with real castings remain to be done.

(a) (b) (c) (d)

**Fig. 9.** EIGA-type electrode melting and melt stream solidification in the copper mould for qualitative validation of simulation results (a). Solidified Ti64 ingot surface quality obtained with: 0.5 kg/min and 40 kW (b), 0.5 kg/min and 54 kW (c), 1.0 kg/min and 92 kW (d)

**Summary and conclusions**

► Melt rates up to 10 kg/min with adjustable superheat between 40 - 400 C were proven using validated numerical modelling. Total power needed to ensure 10 kg/min melt rate is 360 kW for Ti64 and 260 kW for IN718. Even higher melt rates are possible but require proportionally greater power.

► At this stage of the project "Advanced Electrode Melting for Highest-Purity Cast Parts" open points with DS/SX investment casting industry has to be discussed:

- The EIGA-type melt rate (= cast rate) is still a rather low compared to casting rates for DS/SX process of about 60 kg/min or higher.
- Adaptation of the casting system of the DS/SX shell mould cluster to the new melting/casting process.

► If the above-mentioned challenges can be overcome, the EIGA-type electrode melting offers attractive advantages over conventional vacuum induction melting with a back-up crucible and a one-shot liner for the DS/SX process, listed below:

- crucible-free (no wear/no consumables), contact-less melting
- ultimate casting purity
- easy to operate, reproducible, reliable
- electrode allows for higher productivity & flexibility
- higher melting efficiency resulting in a decrease energy consumption for melting

**References**

[1] M. Hohmann and N. Ludwig: G*erman patent DE 4102101 C2*, 1991
[2] X. Li and U. Fritsching: *J. Mater. Process. Technol.*, 2017, vol. 239, pp. 1-17
[3] S. Spitans, H. Franz and E. Baake: *Met. Mat. Trans. B*, 2020, 51(5), pp. 1918-1927

# Simulation of the Growth of Crystalline Silicon fibers for the 3rd Generation Gravitational Wave detectors

Lucas Vieira, Iason Tsiapkinis, Kaspars Dadzis and Robert Menzel

Leibniz-Institut für Kristallzüchtung (IKZ), Berlin, Germany

lucas.vieira@ikz-berlin.de

Third-generation gravitational wave detectors, like the future Einstein Telescope, will operate at cryogenic temperatures for improved sensitivity [1]. Due to the exceptional thermal and mechanical material properties of silicon (Si) in this temperature range, fibers of crystalline Si are a promising candidate for suspending the test mass of interferometers [2]. At the IKZ, a growth process for such crystalline Si fibers is being developed. Both the Float Zone and the Pedestal growth methods are investigated (Fig. 1). In this work, we present a numerical model in Comsol, validate the model with in-situ measurements, and perform a parameter study for process optimization. The numerical model accounts for inductive electromagnetic (EM) heating, heat transfer, fluid flow and phase interfaces for the two growth methods. Measurements of the molten zone shape and inductor current are utilized for validation, and good agreement between model and experiments is achieved. Simulation results reveal a significant influence of EM shear stress on fluid flow, which affects process stability. The model can thus help drive future inductor design and tune process parameters towards a more stable flow during fiber growth.

**Acknowledgement:** This work is carried out in frame of the research project third generation gravitational detector (3G-GWD) funded by the German federal ministry of education and research (BMBF) under grant number: 05A20BC1. I. T. and K. D. acknowledge funding by the European Research Council (ERC) under the European Union's Horizon 2020 research and innovation program (grant agreement No 851768).

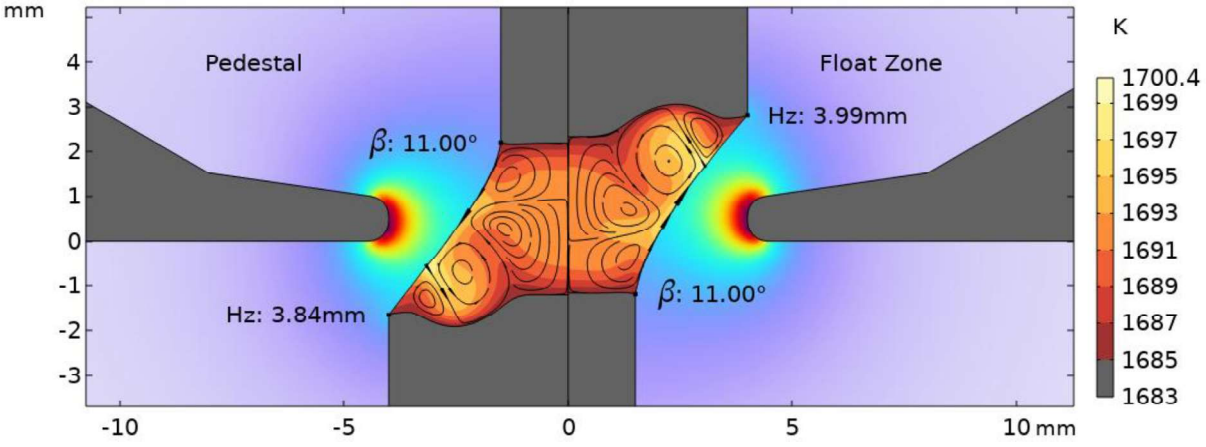


*Fig 1: Numerical model of two growth process in Comsol*

[1] – P R Saulson 1990 Phys. Rev. D 42 2437-45

[2] – A V Cumming et al 2014 Class. Quantum Grav. 31 025017

# New open-source software for simulation of thermal stresses and dislocations in crystals during the growth process

*A. Sabanskis[1], K. Dadzis[2], A. Wintzer[2], J. Virbulis[1]*

[1] Institute of Numerical Modelling, University of Latvia, Riga, Latvia
[2] Leibniz-Institut für Kristallzüchtung (IKZ), Berlin, Germany
andrejs.sabanskis@lu.lv

The Alexander-Haasen (AH) dislocation density model [1] is a well-known approach to calculate the relaxation of stresses by plastic deformation for classical semiconductors such as Si, Ge, and GaAs in particular, e.g., [2]. This model postulates expressions for dislocation velocity depending on the local temperature and stress as well as for local dislocation multiplication, both depending on several material parameters. While many AH models of varying complexity have been published in the literature, the underlying codes are usually not openly available. We have a developed a new open-source software MACPLAS [3] based on the deal.II finite element library [4] for the calculation of thermal stresses and dislocation densities according to the AH model in 2D (axisymmetric) and 3D including the time-dependence and changing crystal geometry during the growth (currently only in 2D), see Fig. 1. It has already been applied to analyze dislocation generation in Si during thermal treatment [5]. In this study, we introduce the MACPLAS code including its design. Its use is demonstrated for crystalline oxides, fluorides, and iodides as this class of materials is known to suffer from thermal stress and even crystal cracking while an analysis of stress relaxation phenomena in the literature has been rather scarce.

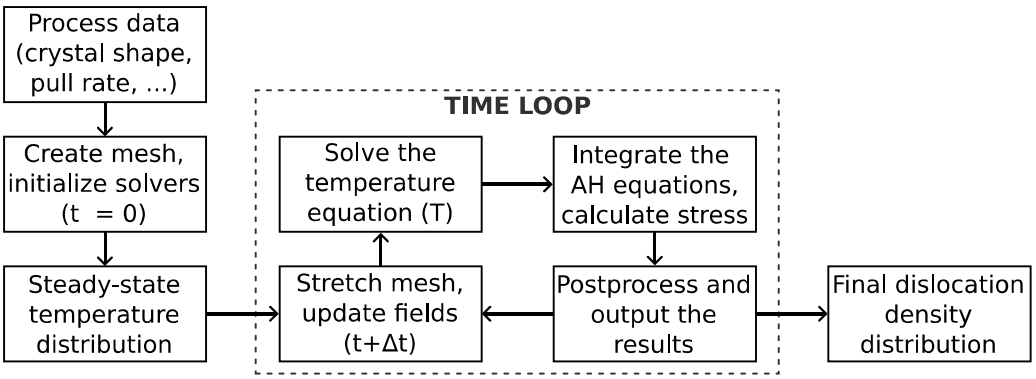


Fig. 1. Input and output parameters as well as calculation loops in the MACPLAS code.

**Acknowledgement:** A. S. acknowledges financial support from the PostDoc Latvia Project No. 1.1.1.2/VIAA/2/18/280. A. W. and K. D. acknowledge funding by the European Research Council (ERC) under the European Union's Horizon 2020 research and innovation program (grant agreement No 851768).

**References**

[1] Alexander H, Haasen P. Dislocations in nonmetals. Annu Rev Mater Sci 1972;2(1):291–312.
[2] Miyazaki N. Thermal stress and dislocations in bulk crystal growth. In *Handbook of Crystal Growth,* Vol. 2A (Elsevier, 2nd ed., 2015), pp. 1049–1092.
[3] MACPLAS: MAcroscopic Crystal PLAstcity Simulator. https://github.com/aSabanskis/MACPLAS
[4] Arndt D et al. The deal.II library, J. of Numer. Math. 2017;25(3):137–145.
[5] Sabanskis A, Dadzis K, Menzel R, Virbulis J. Application of the Alexander–Haasen model for thermally stimulated dislocation generation in FZ silicon crystals. Crystals 2022;12(2):174.

# Validation of high-frequency electromagnetic models for crystal growth applications

*I. Tsiapkinis, A. Wintzer, S. Foroushani, K. Dadzis*
Leibniz-Institut für Kristallzüchtung (IKZ), Max-Born-Str. 2, 12489 Berlin, Germany
iason.tsiapkinis@ikz-berlin.de

Induction heating is commonly used in many crystal growth processes with various inductor designs and frequency ranges. The inductor's shape, size, and positioning affect the magnetic field and, thereby, the heat transfer and flow driven by electromagnetic forces within the melt. Therefore, the inductor can have a significant impact on the growth process and hence the quality of the grown crystal. While numerical simulation of induction heating is an essential tool for process design and optimization [1], the validity of many existing models for crystal growth processes is questionable due to a lack of experimental data [2]. To address this gap, we will examine typical inductor designs for Floating Zone [3], Levitation Czochralski crystal growth [4], and skull melting process [5], as seen in Fig. 1. Two low-power generators with working frequencies of 50-800 kHz and 3 MHz will be used in the measurement setup. We will present measurements of various parameters, such as 3D magnetic field distribution (using self-made, calibrated induction coils), inductor current and voltage (using Rogowski and differential voltage probes, respectively), as well as temperatures of dummy loads. The measurement data will then be compared to 3D numerical models of electromagnetic induction and temperature using various skin layer approximations implemented in the open-source finite element solver Elmer [6].

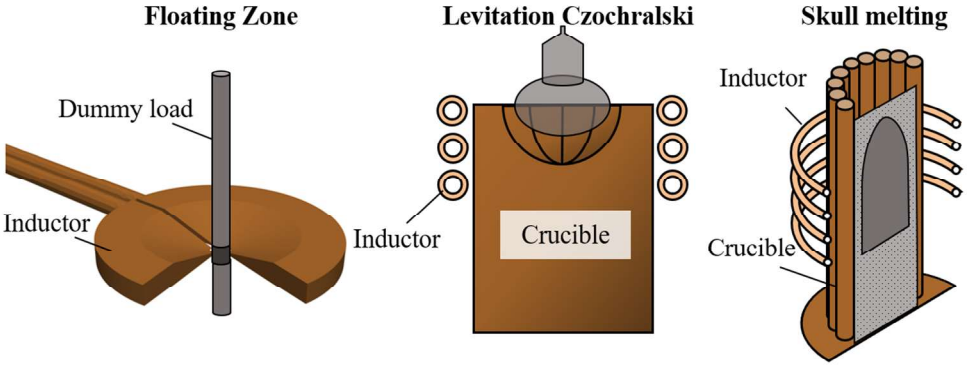


**Fig. 1**: Simplified sketches of Floating Zone, Levitation Czochralski and skull melting configurations.

**Acknowledgment:** The NEMOCRYS project has received funding from the European Research Council (ERC) under the European Union's Horizon 2020 research and innovation programme (grant agreement No 851768).

[1] S. Lupi et al., Induction and Direct Resistance Heating, *Springer International Publishing*, 2015. DOI: 10.1007/978-3-319-03479-9.
[2] A. Enders-Seidlitz et al. *J. Cryst. Growth*, 593 (2022) 126750. DOI: 10.1016/j.jcrysgro.2022.126750.
[3] A. Muiznieks et al. Handbook of Crystal Growth, 2nd Edition, *Elsevier*, DOI: 10.1016/B978-0-444-63303-3.00007-9
[4] R. Takke, W. Assmus, *J. Cryst. Growth*, 49 (1980) 97. DOI: 10.1016/0022-0248(80)90067-6.
[5] C. Gross et al., *Cryst. Research and Technology*, 34 (1999) 319. DOI: 10.1002/(SICI)1521-4079(199903)34:3<319::AID-CRAT319>3.0.
[6] P. Råback et al. CSC – IT Center for Science, *https://www.csc.fi/elmer*. 2022.

**Title**: Experimental and numerical investigation of LiBr crystal growth using the CZ method

**Authors**: K. Kalme, A. Sabanskis, J. Virbulis

**Institution**: University of Latvia, Faculty of Physics, Mathematics and Optometry, Institute of Numerical Modelling

**Abstract**: The scope of this research is to perform small-scale crystal growth experiments with Czochralski (CZ) method. The laboratory CZ growth furnace [1] is equipped with an optical camera for automatic crystal diameter measurements; the crystal pull rate and heater power are adjusted to grow a crystal of desired shape. Manual and PID (proportional–integral–derivative) process control of the (1) crystal diameter and (2) pull rate is considered to grow LiBr crystal with a typical diameter of 10 mm and length up to 50 mm. Besides experimental investigations, numerical simulations with previously developed mathematical model (program CZ-Trans) [1,2] are carried out and compared to the experimental results. Using the validated model, both sets of PID control parameters are optimized to reduce the crystal diameter oscillations. The optimized PID parameters are also tested experimentally.

**References**

[1] Bergfelds K, Pudzs M, Sabanskis A, Virbulis J. Experimental and numerical investigation of laboratory crystal growth furnace for the development of model-based control of CZ process. Journal of Crystal Growth 2019; 522:191–194.

[2] Sabanskis A, Bergfelds K, Muiznieks A, Schröck Th, Krauze A. Crystal shape 2D modeling for transient CZ silicon crystal growth. Journal of Crystal Growth 2013; 377:9–16.

# Simulation-Driven Process Development of AlN-Single Crystal Growth by the Physical Vapor Transport Method

Marc Hainke[1,2], Magdalena Lang[2], Shiva Krishna Tangedipelli[2], Christian Kranert[1], Jochen Friedrich[1*]

1. Fraunhofer Institute for Integrated Systems and Device Technology (IISB), Schottkystr. 10, 91058 Erlangen, Germany
2. Department of Industrial Engineering and Healthcare, Technical University Amberg-Weiden (OTH), Hetzenrichter Weg 15, 92637 Weiden, Germany

*marc.hainke@iisb.fraunhofer.de

**Abstract:** For commercial use of aluminum nitride grown by Physical Vapor Transport (PVT) the main challenge is currently the continuous increase of the diameter towards 4" substrates. Due to the extreme process conditions in AlN material production and the fact that the conditions inside the growth crucible are not directly experimentally accessible, numerical simulation plays a key role in process analysis and optimization. In the presented simulations both the multi-purpose tool Ansys, as well as the especially for crystal growth designed tool CrysMAS are applied. The simulations include RF-heating, the disciplines of heat and mass transfer as well as structural-mechanical analyses. Sensitivity analyses for the various model parameters are essential, especially since the material properties at the extremely high process temperatures are subject to uncertainties. Parameterized calculation models (including the CAD geometries) allow a systematic process analysis with the optional application of the Ansys optimization tools. As the growth rate of the AlN crystal is primarily dependent on the thermal conditions in the growth system, heat transfer calculations are exceptionally important. Exemplary studies on the influence of the powder raw material (like porosity and grain diameter) and the design of the crucible (geometry and material) on the crystal growth (growth rate and mechanical stress) are discussed.

**Keywords:** numerical simulation, crystal growth, process optimization, PVT, AlN

**Acknowledgments:** This work was supported by the Bavarian State Ministry for Science and the Arts (StMWK) under grant no. 15 49 TG 82. Boris Epelbaum und Andreas Lesnik from Fraunhofer IISB are acknowledged for providing the experimental data.

# Experimental and simulative studies on the electrothermal behaviour of carbon fibre resistive heating elements

Nico Sufis*, Jannis Schrade, Igor Niedzwiecki, Alexander Nikanorov, Egbert Baake

Institute of Electrotechnology, Wilhelm-Busch-Straße 4, 30167 Hannover, Germany
*sufis@etp.uni-hannover.de

**Abstract:** Industrial heat treatment plants are mainly heated by burning gas. Electrically heated carbon fibres, which produce no emissions during operation, represent an alternative heating technology. In this work, conductive heating with carbon fibres will be investigated. In particular, knowledge will be gained by evaluating experimental results, which will be reproduced in a simulation model. The aim is to simulate the temperature distribution of a real heating process. Temperature distributions are experimentally performed, recorded with a thermal imaging camera and subsequently evaluated. In conductive heating, the density of the heat source depends on the current flow and the geometry. Through them, the electromagnetic process is coupled with the temperature. The electrical conductivity is much higher in the fibre direction than in the cross-fibre direction. The reason for this is also the layer structure of a carbon fibre. This means that electrons can only move along the graphite layers. Accordingly, the electrical resistance in the fibre direction is very low and increases very strongly in the transverse direction, which results in a corresponding temperature pattern.

**Keywords:** carbon fibre, electrothermal behaviour, resistive heating, emissions savings.

## Introduction

Industrial heat treatment plants are mainly heated by burning gas. Electrically heated carbon fibres, which produce no emissions during operation, represent an alternative heating technology. In this work, conductive heating with carbon fibres will be investigated. In particular, knowledge will be gained by evaluating experimental results, which will be reproduced in a simulation model. The aim is to simulate the temperature distribution of a real heating process. Temperature distributions are experimentally performed, recorded with a thermal imaging camera and subsequently evaluated [1].

## Problem description

Carbon fibres are particularly suitable for electrical heating, as they have a low resistance that is much higher than that of copper. They therefore conduct electricity, but generate more heat for the same current than a copper conductor. In addition, carbon fibres are very malleable, and any shape or braid can be easily made and adapted to the application. When working with carbon fibres, one important issue must be taken into account. They have anisotropic material properties. This means that the properties in the fibre direction and in the transverse direction sometimes differ greatly from one another. This applies both to the mechanical properties, such as strength, and to the electrothermal properties, such as electrical and thermal conductivity.

Due to this layer structure, carbon fibres have very good electrical conductivity in the fibre direction. The same applies to thermal conductivity. This is why current flows preferentially in the fibre direction during conductive heating.

In simulation, the problem is to reproduce the anisotropic properties without having to simulate each individual fibre. This would extremely increase the simulation effort and duration. Therefore, a substitute geometry is to be generated.

**Experimental**

To examine the carbon fibres, they are supplied with direct current in the form of a braided sample. The carbon fibre sample studied is shown in Fig. 1.

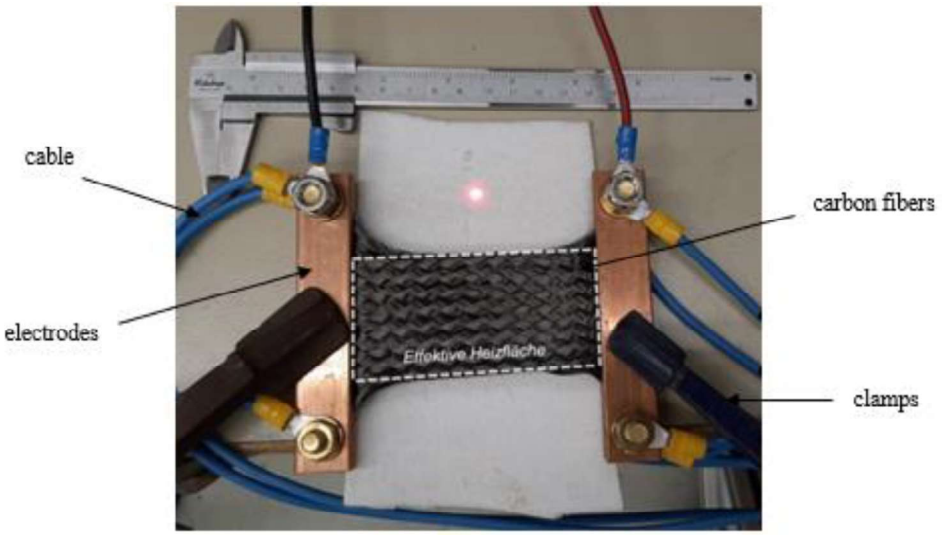


Figure 1. Experimentally studied carbon fibre sample.

The temperature distribution is recorded with the aid of a thermal imaging camera. Fig. 2 shows the thermal image at relatively low temperatures.

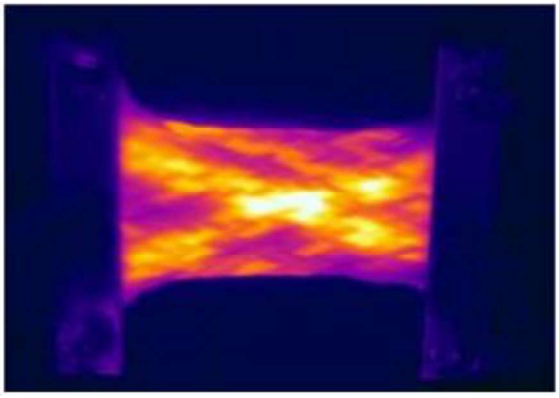

Figure 2. Thermal image at $T_{max}$ = 100 °C.

It is noticeable that the temperature distribution is not homogeneous, but inhomogeneous and asymmetrical. The highest temperatures occur in the centre of the specimen. Starting from the centre, the high temperature zones are concentrated along the fibre tapes. Especially at the upper and lower edges, the temperatures are lower. The thermal image at higher temperatures is shown in Fig. 3.

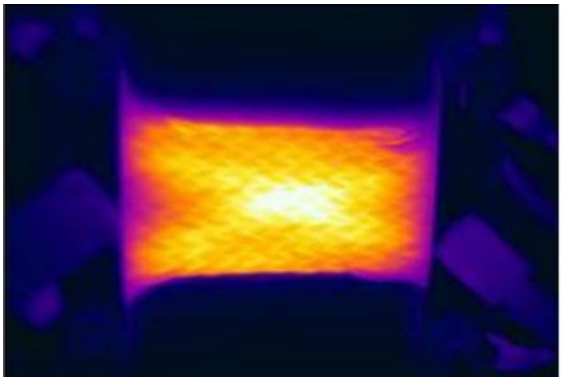

Figure 3. Thermal image at $T_{max}$ = 400 °C.

Also in this distribution, the highest temperatures occur in the centre of the sample. Furthermore, the high temperature zones are distributed X-shaped to the electrodes. In the interstices, the temperatures are lower.

The experimental investigations support the previously mentioned anisotropic behaviour of the carbon fibres. Since they exhibit high electrical and thermal conductivity in the fibre direction, the currents also flow in this direction. The heat thus generated is also distributed in the fibre direction due to the high thermal conductivity, which is why the pattern mentioned can be seen in the thermal images.

Furthermore, the resistance curve of the carbon fibres can also be determined on the basis of the measured values of current and voltage. This does not show the real values for an individual fibre, but it does show the general behaviour of the fibres at higher temperatures. The curve can be seen in Fig 4.

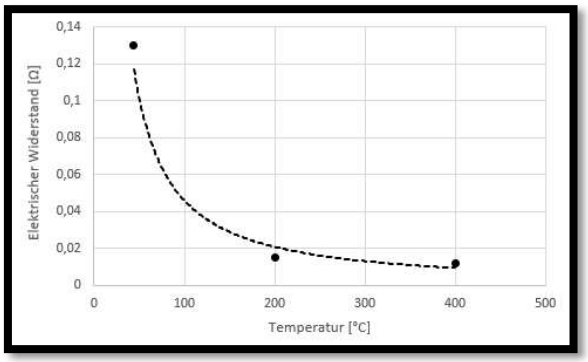


Figure 4. Temperature dependence of the electrical resistance.

It can be seen that the resistance decreases at high temperatures. Carbon fibres are therefore thermistors.

**Numerical model**

ANSYS® Mechanical APDL is used to simulate the temperature distribution. First, a cuboid geometry is created to represent the braided carbon fibre mat. The goal of the simulation is to use a surrogate geometry and not to simulate all fibres or tapes individually. In the end, the material properties must be adjusted so that the simulated temperature curves correspond as closely as possible to the real curves. Fig. 5 shows the simulated geometry:

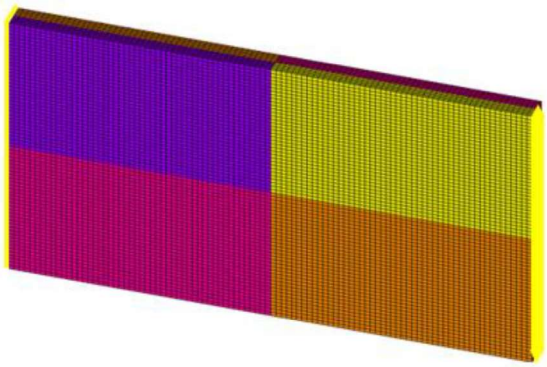

Figure 5. Mapped meshing of the carbon fibres. Current imprint on the yellow marked edge.

Due to the anisotropy of the carbon fibres, the material properties must be defined separately in the different coordinate directions. This applies above all to the electrical ρ and thermal conductivity λ. Other properties such as density, heat capacity or heat transfer coefficient are not affected by the anisotropy. Accordingly, the initial values of the anisotropic material properties for the following simulations are shown in Table 1:

Table 1: Anisotropic material properties of carbon fibres [1], [3].

| $\rho_x$ [Ωm] | $\rho_y$ [Ωm] | $\rho_z$ [Ωm] | $\lambda_x$ $[\frac{W}{m \cdot K}]$ | $\lambda_y$ $[\frac{W}{m \cdot K}]$ | $\lambda_z$ $[\frac{W}{m \cdot K}]$ |
|---|---|---|---|---|---|
| $8 \cdot 10^{-6}$ | $500 \cdot 10^{-3}$ | $500 \cdot 10^{-3}$ | 17,0 | 1,0 | 1,0 |

**Simulation results and discussion**

In order to be able to simulate the anisotropy of the carbon fibres as well as possible without having to simulate the individual fibres, several approaches are being tried out. In particular, the work with element coordinate systems yields good results. The element coordinate systems indicate the direction of the material properties. With the help of the “local” and "esys" commands it is possible to change the orientation of these coordinate systems in ANSYS® Mechanical APDL and thus align the material properties along the fibre directions.

One simulation approach is to divide the geometry into two layers. The element coordinate systems (ecs) of the upper layer (Volumes one, two, three and four) are rotated by +30° (ecs 1) around the z-axis and the element coordinate systems of the lower layer (Volumes five, six, seven and eight) are rotated by -30° (ecs 2). This is to emulate the different directions of the carbon fibre ribbons. In addition, a change is made to the basic material properties. The alignment of the element coordinate systems can be seen in Fig. 6.

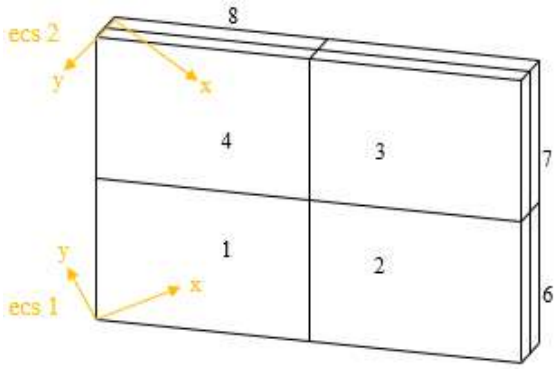


Figure 6. Alignment of the element coordinate systems.

To represent the interlacing of the carbon fibres, a very high thermal conductivity in the z-direction is assumed. This simulates a good heat exchange between the two layers. This value is not intended to be realistic, but only to serve as an aid for superimposing the temperatures. No change is made for the electrical resistances, since the fibres are insulated from each other and thus no current can flow between them. The adjusted properties can be found in Table 2:

Table 2: Anisotropic material properties for the coating approach.

| $\rho_x$ [Ωm] | $\rho_y$ [Ωm] | $\rho_z$ [Ωm] | $\lambda_x$ [$\frac{W}{m \cdot K}$] | $\lambda_y$ [$\frac{W}{m \cdot K}$] | $\lambda_z$ [$\frac{W}{m \cdot K}$] |
|---|---|---|---|---|---|
| $8 \cdot 10^{-6}$ | $500 \cdot 10^{-6}$ | $500 \cdot 10^{-3}$ | 17,0 | 1,0 | 300,0 |

The resulting simulated temperature distribution is shown in Fig. 7:

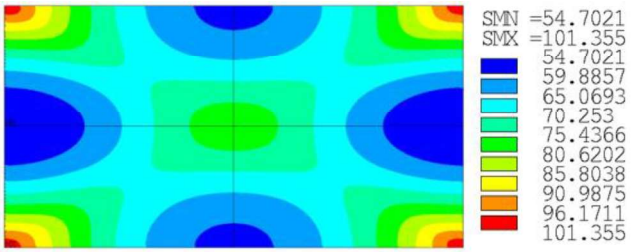


Figure 7. Thermal image after subdivision into two layers. The values have the unit °C.

Visually, some of the experimental observations are recovered. High temperatures occur in the centre of the sample. Even though the maximum temperatures occur in the corners, this is a good first approximation. Furthermore, the temperatures in the interstices are much lower at the respective edges. Based on this temperature distribution, the observed "X-shape" can also be seen, which extends from the centre to the electrodes.

Another approach to simulate the real results is to divide them into four quadrants of equal size. These are defined according to the geometry in Fig. 8. Subsequently, two different orientations of the element coordinate systems are used again. The volumes one, three, five and seven get an element coordinate system rotation of +30° (ecs 1) around the z-axis, the volumes two, four, six and eight by -30° (ecs 2).

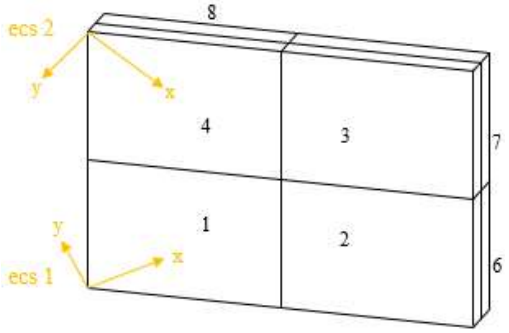


Figure 8: Assignment of quadrants and element coordinate systems.

No superposition of the temperatures of the upper and lower layers is needed in this case, so the thermal conductivity in the z-direction is again dimensioned as 1 W/(m·K). The material properties are shown in Table 3.

Table 3: Anisotropic material properties for the cuboid approach

| $\rho_x$ [Ωm] | $\rho_y$ [Ωm] | $\rho_z$ [Ωm] | $\lambda_x$ $[\frac{W}{m \cdot K}]$ | $\lambda_y$ $[\frac{W}{m \cdot K}]$ | $\lambda_z$ $[\frac{W}{m \cdot K}]$ |
|---|---|---|---|---|---|
| $8 \cdot 10^{-6}$ | $500 \cdot 10^{-6}$ | $500 \cdot 10^{-3}$ | 17,0 | 1,0 | 1,0 |

This approach yields the temperature distribution in Fig. 9.

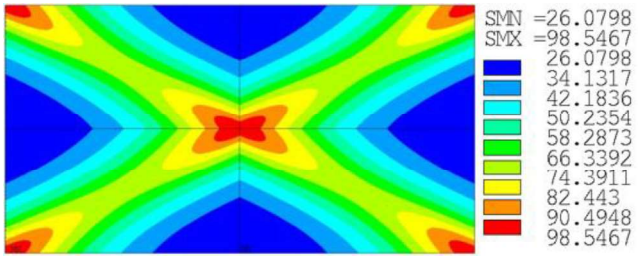


Figure 9. Thermal image according to the subdivision into quadrants.

The characteristic properties of the real temperature distribution can be recognized. The "X-shape" is formed with the highest temperatures in the centre. The low temperature areas are located in the intermediate spaces, which can be seen especially on the thermal image at low temperatures.

However, both simulation approaches do not take into account the asymmetry of the carbon fibre sample and thus the asymmetry of the temperature distribution. There are two ways to reproduce this. One is to divide the geometry into even more cuboids and then use several different element coordinate systems. The second way is to change the current imprint area. Just the experimental investigations have shown that there are different temperature distributions at the electrodes on both sides. This can also be reproduced by changing the current imprint area in the simulation.

**Conclusions**

In summary, some challenges arise due to the anisotropy of carbon fibres. The experimental investigations show that it is difficult to achieve a homogeneous temperature distribution. In simulation, the main problem is to describe the fibre directions with an equivalent geometry to and the material properties. With the two described approaches it is possible to generate the real temperature field, but there are still some deviations. The simulation model could be further improved by adjustments such as changing the current imprinting surface or additional element coordinate systems.

**References**

[1] Lengsfeld, H., Mainka, H. & Altstädt, V. (2019). Carbonfasern: Herstellung, Anwendung, Verarbeitung, Carl Hanser Verlag

[2] Constantinescu-Simon, L.: Handbuch elektrische Energietechnik: Grundlagen – Anwendungen, Vieweg + Teubner Verlag, 1996

[3] Flemming, M., Ziegmann, G. & Roth, S.: *Faserverbundbauweisen: Fasern und Matrices*, Springer Berlin Heidelberg, 1995

# Density-based topological optimization of 3D-printed casts for fracture treatment with *FreeFEM* software

Kristers Kokars[1], Armands Krauze[*1], Kārlis Muižnieks[1], Jānis Virbulis[1], Pauls Verners[2], Aleksandrs Gutcaits[3], Jānis Oliņš[4]

1. Institute of Numerical Modelling, Jelgavas str. 3, Riga LV-1004, Latvia
2. Institute for Mechanics of Materials, Jelgavas str. 3, Riga LV-1004, Latvia
3. Riga Technical University, HPC Center, P. Valdena str. 3, Riga LV-1048, Latvia
4. SIA CastPrint, Krišjāņa Barona str. 19, Riga LV-1011, Latvia

*Armands.Krauze@lu.lv

**Abstract:** Modern 3D printing technologies are used to produce plastic casts for bone fractures. To produce casts with optimum shapes, their topology must be optimized. In this article, a density-based topology optimization algorithm which uses a linear stress model is described. The main simulation results are discussed, and optimum simulation parameters are shown. The topology optimization algorithm was implemented in a cast production chain, which is used to generate 3D-printable cast geometries for an industrial cast producer. The results of mechanical tests of the plastic casts were used to validate the applied stress simulation model and have shown improved mechanical strength of optimized casts in comparison with original unoptimized casts.

**Keywords:** medical casts for bone fractures, 3D printing, topology optimization

## Introduction

3D printing is used to print plastic casts for medical treatment of bone fractures. Plastic casts have significant advantages over traditional plaster casts – they have complex geometries with holes to enhance skin ventilation and are made of lightweight, biodegradable material with anti-allergenic properties. The placement and shape of holes determines material costs, printing time, and mechanical durability. Optimization of the cast topology is therefore crucial for obtaining the most efficient cast shape.

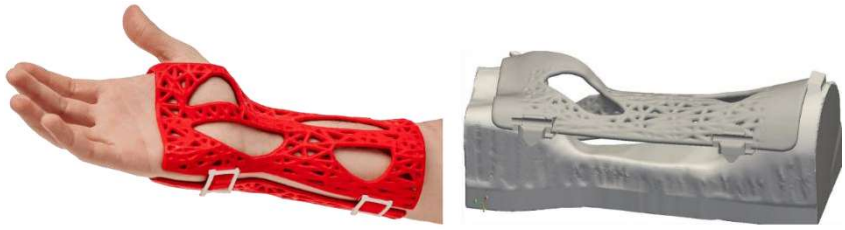

Figure 1. Examples of 3D printed casts. Left: a cast on a patient's arm (SIA CastPrint promotional materials). Right: A cast part placed on a lower test fixture for mechanical testing.

This paper presents a numerical implementation of a density-based topology optimization algorithm, also known as SIMP (solid isotropic material with penalization), [1,2]. The model was developed at the Institute of Numerical Modelling in cooperation with RTU HPC Center in the frame of a project to design an automated production chain for 3D-printed casts. It would allow a user to automatically create 3D-printable casts with improved quality and reduced price from scanned 3D surfaces of patients' arms. The project set limit to

calculation duration per cast: one hour. The chain would be implemented by SIA CastPrint, a leading commercial producer of 3D-printed casts in Latvia. The algorithm was implemented via scripts written in *python* and *FreeFEM*, [3], scripting languages.

In this article, a brief description of the optimization model is given, and the results of parametric simulation studies are shown and discussed. The results of mechanical testing of calculated cast shapes, done at the Institute for Mechanics of Materials, are also presented.

**Model for mechanical stresses**

A 3D-printed cast, Figure 1, consists of two separate parts connected with four connectors and fixed on the patient's arm. When used, the cast can interact with external objects (furniture, walls, sports equipment). Modeling such interactions requires a solution of dynamic contact problems between at least four objects, which could also involve non-linear deformations. To make simulations practical, the stress model was significantly simplified.

First, an equation (1) for linear steady-state stresses $\sigma^{ij}$ is solved:

$$\nabla\sigma^{ij} = 0 \tag{1}$$

where the gravity force is discarded due to its small importance. This equation is solved separately for each half of the cast. The interaction with the arm, the other cast's half, and external objects is modeled via simplified boundary conditions.

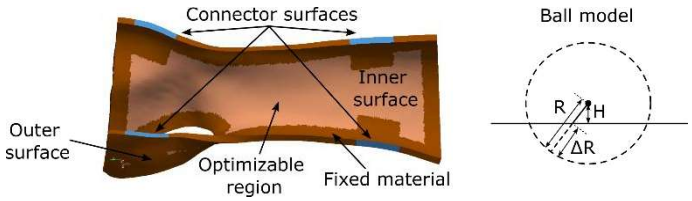


Figure 2. Left: numerical model of cast (one half). Right: model of solid ball on outer surface.

The interactions with external objects were simplified to an interaction with a small solid ball. The force created by the ball was modeled as a pressure distribution $p = A_{ball}\Delta R$ on the outside surface ($\Delta R$ is defined as shown in Figure 2). Physically, such a ball could correspond to hits by rounded furniture corners. Since such hits can happen everywhere on the outer surface, the stress distributions are calculated for several ball positions which are spread evenly on the outer surface, and their influence is averaged. Other objects such as planes and long cylinders were also considered, but they required full contact problem modeling, and so were discarded. The ball model has also the advantage that, by changing the number of positions, one can affect the size and distribution of holes.

The traction acting on the inner surface and connectors was modeled as a function of surface displacements $\vec{u}$. The force density applied on the inner surface was modeled as (2):

$$\vec{f} = -H(u_n)A_{skin}u_n\vec{n} \tag{2}$$

where $\vec{n}$ is normal, $u_n$ is the normal component of $\vec{u}$, $A_{skin}$ is a constant. $H(u_n)$ is the Heaviside step function, and it ensures that the force density is zero when the cast does not touch the skin. Similarly, the force density on connector surface is modeled as (3):

$$\vec{f} = -\Big(A_{soft} + H(u_n)\big(A_{hard} - A_{soft}\big)\Big)u_n\vec{n} - A_{soft}\vec{u}_\tau \tag{3}$$

where $A_{soft}$, $A_{hard}$ are constants, and $\vec{u}_\tau$ is the tangential $\vec{u}$ component. The tangential term ensures the numerical stability of the solution, and the normal component is asymmetric against the $u_n$ sign change.

This model was modified to simulate bending of casts in the mechanical testing facility, Figure 1. Zero force density is applied on the connectors, and on the inner surface it is (4):

$$\vec{f} = -H(u_n)\left(A_{skin}u_n\vec{n} + A_{skin,friction}\vec{u}_\tau\right)F_{groove,mask} \tag{4}$$

where $A_{skin,friction}$ is an artificial friction coefficient, introduced for numerical stability, and $F_{groove,mask}$ is a function with a value range $(0..1)$ which models the groove on the fixture. The pressure on the outer surface is generated by a cylinder the size of which corresponds to the upper fixture used in the experiments. The pressure is applied only on the surface parts filled with material.

**Density-based topology optimization algorithm**

The numerical model was based on a 2D topology optimization algorithm for a cantilever, found in [4]. This model was rewritten and expanded to a 3D cast optimization model. The model uses a fixed numerical simulation volume and introduces a scalar field $h$, which determines the material distribution in the cast ($h = 0$ means holes and $h = 1$ means filled areas). For example, the volume of the material in the cast is calculated as (5):

$$V = \iiint H(h,\beta)\,dv, \text{ where } H(t,\beta) = \frac{1/2(\tanh\beta/2 + \tanh\beta(t-1/2))}{\tanh\beta/2} \tag{5}$$

($H(t,\beta)$ is a smooth approximation of the Heaviside step function). The material properties (Lamè coefficients) are also defined as $h$ functions: $\lambda = \lambda_0\zeta\left(H(h,\beta)\right)$ and $\mu = \mu_0\zeta\left(H(h,\beta)\right)$, where $\lambda_0$ and $\mu_0$ are the material properties of the plastic, and $\zeta(t) = e_{rs} + (1-e_{rs})t^3$, where $e_{rs} = 0.001$ ensures that the hole has non-zero material properties. The optimal cast topology is obtained by iteratively modifying the field $h$ to minimize the functional (6):

$$J(h) = \iiint \sigma^{ij}\varepsilon_{ij}\,dv + e_{ll}\left(\frac{V - V_t}{V_0}\right)^2 \tag{6}$$

where the first term represents the total deformation energy. Minimizing it reduces the stresses in the cast and the risk of cast breaking. The second term is a penalty function that forces the solution to converge to a target material filling level $V_t/V_0$, where $V_0$ is the whole simulation volume.

The deviation $\delta h$ that minimizes $J$ is calculated in each iteration step as (7):

$$\delta h = -k\left(-\frac{\partial\sigma^{ij}}{\partial h}\varepsilon_{ij} + \frac{2e_{ll}(V - V_t)}{V_0^2}H'(h,\beta)\right)F_{opt} \tag{7}$$

where $k$ is an adjustable step size, and $F_{opt}$ is a special mask function that is used to ensure constant filling near the borders of the cast (10..20 mm in depth), Figure *2*. Before applying $\delta h$, it is smoothed by solving the equation: $\alpha^2 \Delta \delta h^* = \delta h^* - \delta h$.

Similar smoothing algorithm is applied to the $h$ field before calculation of material properties.

The applied model, strictly speaking, is valid only for constant surface forces. The surface forces on the inner surface and connectors depend indirectly on the field $h$, which is ignored in derivation of $\delta h$ expression.

**Numerical implementation of the model and simulation results**

The iterative topological optimization algorithm was implemented as a script for the finite element program *FreeFEM,* [3]. 1st order elements were used in the production script, and the equation system was solved on parallel computer processors, using RTU HPC Center resources.

Generation of a printable cast, Figure *3*, begins by meshing a scanned surface of a patient's arm with the *gmsh* program, [5], to obtain a surface mesh with the 1.5 mm cell size. The 3D mesh is obtained by extruding the surface mesh by 4 mm (the cast thickness). In the post-processing, *mmg* software [6] is used to cut holes, and sharp corners and edges are rounded. The post-processed 3D cast geometry can be printed after adding connectors.

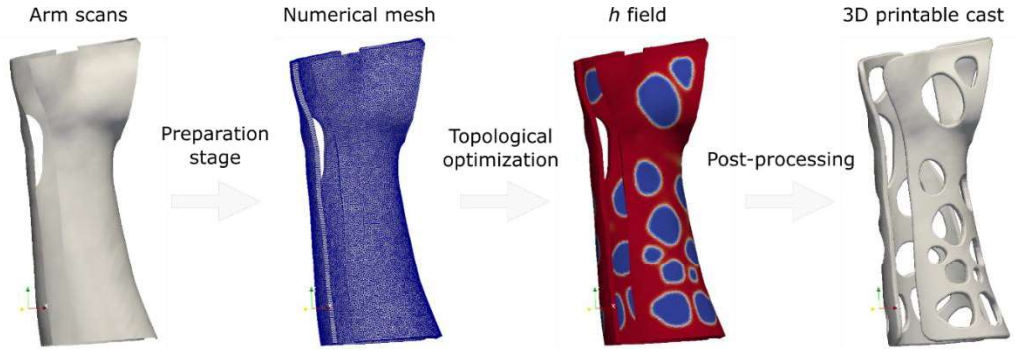


Figure 3. Outline of generation of 3D-printable casts from scanned patient arms.

Arm scans of five different persons, P1 to P5, were used in the simulations: four adults and a child (P3). Isotropic material properties of PLA plastics were used for the cast: Young's modulus $E = 2.9$ GPa, and Poisson's coefficient $\sigma = 0.36$. Two $A_{skin}$ values were used: 1 MPa/m (about the measured human skin elasticity, [7]) and 100 MPa/m (an estimated value for the lower fixture material in the experiments). $A_{hard} = 100$ GPa/m corresponded to ~30 mm thick PLA plate, $A_{soft} = 10$ GPa/m value was guessed; however, the solution was relatively insensitive to both $A_{hard}$ and $A_{soft}$. The ball radius was $R = 10$ mm, and its center elevation $H = 8.75$ mm. $A_{ball} = 3$ GPa/m value was picked arbitrarily to set stress scale.

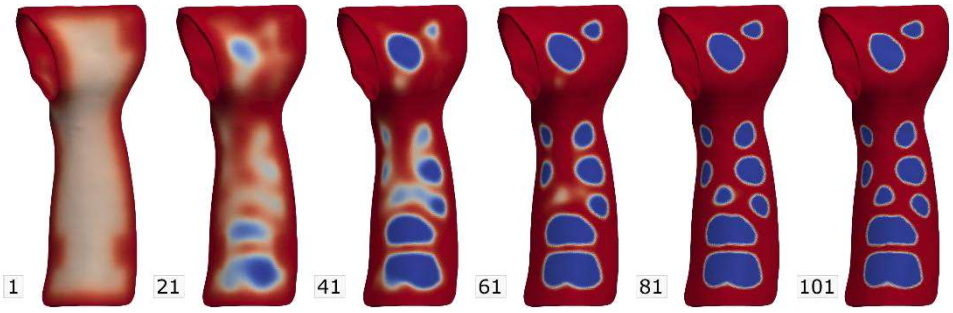


Figure 4. Convergence of field $h$ at different iterations. Topological optimization of P4. Target material filling level $V_t/V_0 = 0.75$, $e_{ll} = 1.5$ J, $A_{skin} = 1$ MPa/m.

A simulation with 2nd order elements for the largest cast, P1, lasted 5.1 h on 36 processors, which exceeded the 1 h limit set by the project. The same simulation with 1st order elements lasted only ~40 min. Therefore only 1st order elements and one-layer meshes fit the project requirements. An example of the field $h$ convergence in the 1st order element simulations, Figure *4*, shows that solutions converged in ~81 iterations.

The optimum material filling level for the casts was estimated to be ~0.70..0.75. With such fillings, the printing time of P1 is reduced by 1.4..1.7 h (comparing to 10.5 h required by unoptimized casts), and its mass is reduced by $20\% - 25\%$. The casts with lower filling levels (0.60) are mechanically weaker and have greater risk of the development of overhangs which 3D printers cannot print.

The simulations have shown that $e_{ll} = 1.5$ J guarantees reasonably small deviations (by few percent) of achieved filling levels from their target values for casts of different sizes, see Figure *5*. Larger $e_{ll}$ values could cause smeared $h$ field distributions.

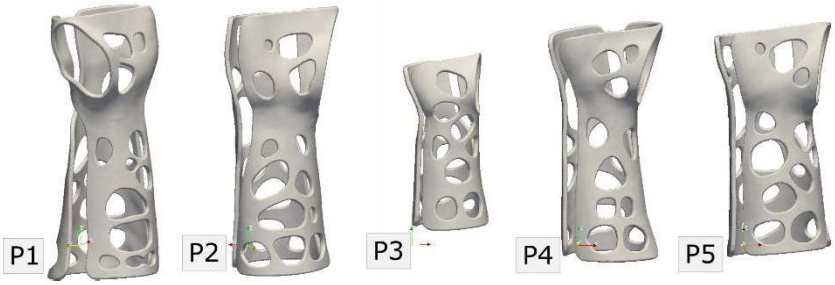


Figure 5. Optimized 3D-printable cast geometries for five test patients. Target material filling level $V_t/V_0 = 0.70$, $e_{ll} = 1.5$ J, $A_{skin} = 1$ MPa/m.

The hole size is affected by the smoothing scale $\alpha$. Its optimum value ($3 - 5$ mm) is determined by the thickness of the cast, and a smaller $\alpha$ can cause material layering.

Increasing the number of ball positions makes holes smaller and more numerous, but past an optimum position density $h$ field distributions become diffuse. Many positions also slow down the simulations. The optimum value for ball position density was estimated as $6.25 \cdot 10^{-4}$ m$^{-2}$ ($20 - 30$ positions per a fixator part for adults).

**Results of mechanical testing**

Samples were tested in ZwickRoell Z100 TEW material testing machine in a custom fixture that allowed bending of a cast perpendicularly to the fixture. The upper test support

was a 60 mm diameter cylinder. The lower test fixture was a copy of patient's arm with the middle section hollowed out to allow free movement of the sample during the bending test. Both fixtures were made of 3D-printed high-performance polyether-based thermoplastic polyurethane filament which smoothed the distribution of the applied force in a larger area.

In the first batch of experiments, unoptimized CastPrint casts were tested. The test results for the P4 cast show that the casts typically broke at specific spots at the palm base, Figure 6. The breaking spots correspond well to the calculated maxima of deformation energy density $\sigma^{ij}\varepsilon_{ij}$. Therefore, the linear stress model can still predict correctly critical stress concentrations against which the cast geometry should be optimized.

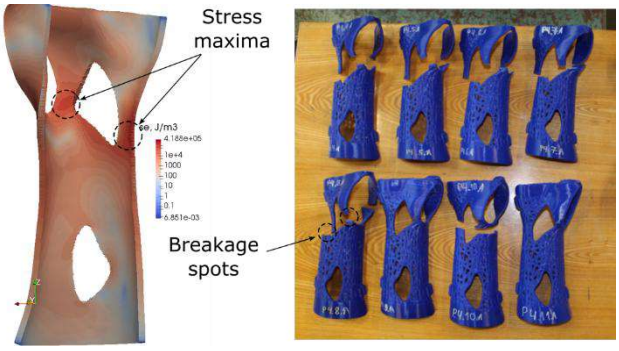


Figure 6. Left: simulated deformation energy density distribution in P4 casts in mechanical testing facility. Right: P4 casts broken in mechanical tests.

In the second test, a topologically optimized P3 cast, obtained with $A_{skin} = 100\ \mathrm{MPa/m}$, was printed and tested. The test showed that the average breakage force for the optimized cast (635 N) was about 1.5 times higher than for unoptimized casts (431 N). Thus, the topological optimization can potentially increase the mechanical strength of the casts.

**Conclusions**

A density-based topology optimization model was successfully developed for 3D-printed casts. Simulation results show significant reduction of printing times and used material for optimized casts. Mechanical tests have shown the optimized cast could have higher mechanical strength. The model needs further improvements: a more precise mathematical model and greater control over the size and shape of holes.

**Acknowledgements**

The work was financed by the project "Application of HPC Tools for the Optimization of 3D-printed Orthopedic Devices (H2020-JTI-EuroHPC-2019-2, Experiment 1109 – OrthoHPC)".

**References**

[1] O. Sigmund & K. Maute, (2013). "Topology optimization approaches", Structural and Multidisciplinary Optimization 48, 1031-1055.

[2] M. P. Bendsoe, (1989). "Optimal shape design as a material distribution problem", Structural optimization 1, 193-202.

[3] F. Hecht, "New development in FreeFem++", (2012). J. of Num. Mathematics 20, 251-265.

[4] E. Bonnetier & C. Dapogny, “Optimization of a cantilever beam with density-based topology optimization algorithm”, “An introduction to shape and topology optimization”, https://membres-lkj.imag.fr/Charles.Dapogny/coursoptim.html

[5] C. Geuzaine & J.-F. Remacle, (2009). “Gmsh: A 3-D finite element mesh generator with built-in pre- and post-processing facilities”, Intl. J. for Num. Methods in Engineering 79, 1309-1331.

[6] G. Balarac & al., (2022), “Tetrahedral remeshing in the context of large-scale numerical simulation and high performance computing”, MathematicS In Action, Vol. 11, 129-164.

[7] J. van Kuilenburg & al., (2012). “Contact modelling of human skin: What value to use for the modulus of elasticity?”, Proc IMechE Part J: J. Engineering Tribology, 227(4), 349–361.

# Inverse identification of SMC material properties – innovative implementation of flux concentrator losses in numerical design of inductive systems

I. Niedzwiecki*, A. Nikanorov, E. Baake, N. Sufis

Institute of Electrotechnology, Leibniz University Hannover
*niedzwiecki@etp.uni-hannover.de

**Abstract:** Magnetic flux concentrators (MFC) made from soft magnetic composites (SMC) can greatly improve the performance of inductive heating processes. SMCs are typically made from magnetic particles which are embedded in high performance polymer matrix under high pressure. Compared to concentrators out of ferrite, flux concentrators made from SMC can be used in stronger magnetic fields and high frequency applications. Although better regarding the electromagnetic performance, the implementation of SMC in a given process is limited by the significant internal losses at higher frequencies in combination with limited thermal conductivity and low temperature resistance. For these reasons an implementation of a comprehensive electrothermal analysis of SMC-MFC into the numerical design of inductive systems is necessary. Otherwise lack of simulation accuracy can lead to a possible overheating of the inductor or the MFC which respectively leads to a failure of the whole system. This work investigates the numerical inverse identification process of the anisotropic material properties of SMC flux concentrators with the goal of being able to fully describe the electrothermal behaviour.

**Keywords:** Magnetic Flux Concentrators, Soft Magnetic Composites, Inverse Parameter Identification, High Frequency Inductive Pipe Welding

## Introduction

Inductive high frequency welding is the most efficient process to continuously manufacture large volumes of steel pipe [1]. To enable the welding process, an impeder is used to guide the field within the pipe with the goal of forcing the induced current into the welding point. Usually, the impeder is made from ferrites. Although ferrites are well suited for the process, since they have good magnetic permeability and at the same time can be used at high frequencies, their disadvantage lies in a relatively low and temperature dependent saturation field density [2]. Especially, when welding pipes with thick walls and small diameters, critical field strength can occur locally, which can lead to a failure of the whole system. To improve the overall performance of impeders and the welding process itself, a hybrid approach is to be investigated where sections of a ferrite impeder, where a local saturation is expected, are replaced by a SMC with higher saturation field strength [3]. From the engineering point of view the implementation of SMC in each application is mostly limited by its low temperature resistance of around 200°C which is caused by the use of a polymer as matrix material for the composite. Therefore, for a successful numerical design of the welding process, an implementation of a comprehensive electrothermal simulation of the used SMC-MFC into the design process is mandatory. Due to the flat shape of the soft magnetic particles used in the manufacturing, the material properties of SMC, especially the thermal conductivity $\lambda$, and the hysteresis losses are highly anisotropic which in return lead to an anisotropic material behavior. To be able to fully simulate the electrothermal behavior of the SMC the anisotropic material properties are required to be identified first.

**Method of investigation**

All material parameters were identified using the inverse identification method. In the presented paper this method consists of three steps. First step is the development of an experimental setup which, in a controlled manner, reduce the dependence of the resulting thermal losses of an SMC-MFC solely to a dependance on the used press direction in regard to the inductor current direction. The second step consists of developing a digital twin based on a 3D-FEM-simulation. The third step consists of fitting the numerical output to the experimental data through the variation of the material parameters which are to be identified.

**Experimental setup**

The experimental setup used as a base for the inverse parameter identification process consists of a single winding, water cooled, copper inductor, a high frequency generator with an output frequency range of 50-200 kHz, a maximum output power of 100 kW and a serial capacitor bank suited for high frequency applications. On the bottom part of the inductor SMC-MFC, which have to be investigated, are placed and fixed with thermal paste for optimal cooling (Figure 1). All MFCs used in the experiment were made from FLUXTROL50, a state-of-the-art industry grade SMC made by FLUXTROL INC. All MFCs are fabricated to the same size, out of the same sample of FLUXTROL50 material. The only difference in the fabrication is the orientation of the press direction of the SMC regarding to the inductor current direction. In the configuration shown in Figure 1, the left MFC is fabricated from SMC with the press direction orientated orthogonal in regard to the inductor current direction, the middle and the right MFC is fabricated from SMC with the press direction orientated parallel to the inductor current direction. Since the MFCs are placed on the same inductor it can be assumed that all MFC are subjected to the same electromagnetic conditions and the difference in the resulting thermal losses is solely caused by the press-direction-dependent material properties.

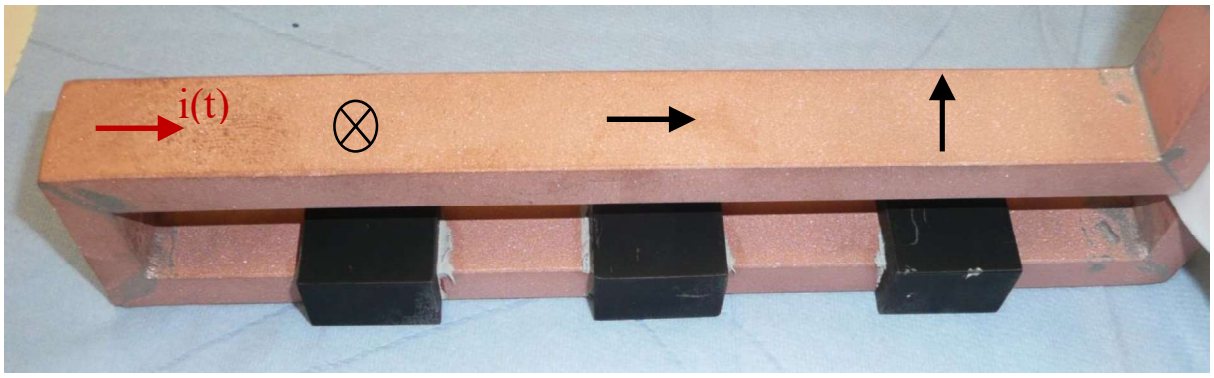


Figure 1. Experimental setup used for the identification of anisotropic material properties of SMC-MFC.

**Experimental results**

The experimental data used in the identification process was derived from 60 s heating process with a constant inductor current of 674 A and a constant frequency of 97 kHz. The heating process was captured and measured with thermal imaging. No internal measurements were conducted since any invasive method would change the electromagnetic behavior of the MFC. Figure 2 shows the resulting steady state temperature distribution as a line measurement

in the middle of the MFCs. As expected, the internal heating of each MFC is showing an anisotropic behavior in regard to the press direction of the SMC. MFC with orthogonal orientated press directions of SMC (left) experience approximately 35 % less internal heating in comparison to MFC with parallel orientated press directions (middle, right). In addition, no significant difference in internal heating can be established which is dependent on an additional rotation of the parallel orientation (middle, right).

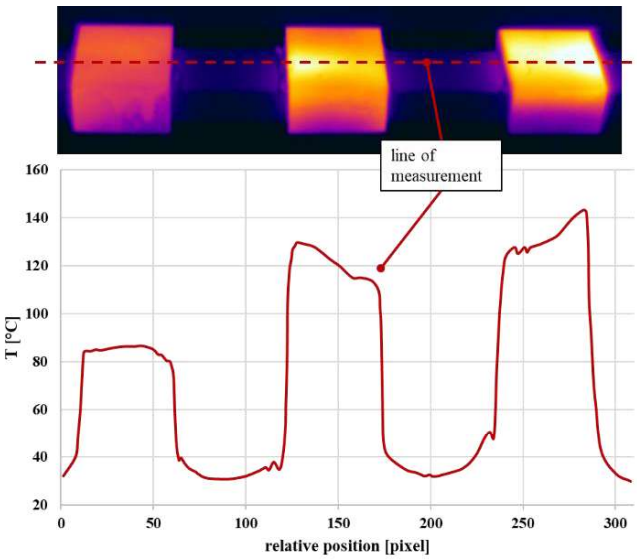


Figure 2. Steady state temperature distribution.

**Simulation model**

The numerical simulation was performed with the help of the commercial software ANSYS®. Figure 3 shows the symmetry extension of the simulation geometry since due to the geometrical symmetry of the setup, the simulation of only a quarter of the shown geometry is sufficient without any loss of simulation quality and at the same time significantly reducing the calculation time. As a point of investigation, the middle point on the surface of the main component of the MFC was chosen as explained by the following arguments. First, the surface temperature is measured directly by thermal imaging. Second, the position of identification is farthest away from neighboring MFC and from its own edges. This way the chance of cross influence from neighboring MFC and the influence from edge effects is reduced. Last, the distance between the position of the identification point and the water-cooled inductor is at its minimum and in return the temperature gradient at its maximum. Therefore, it can be assumed that the main component of the heat flux has only one directional component, which in return can reduce the complexity of the identification process.

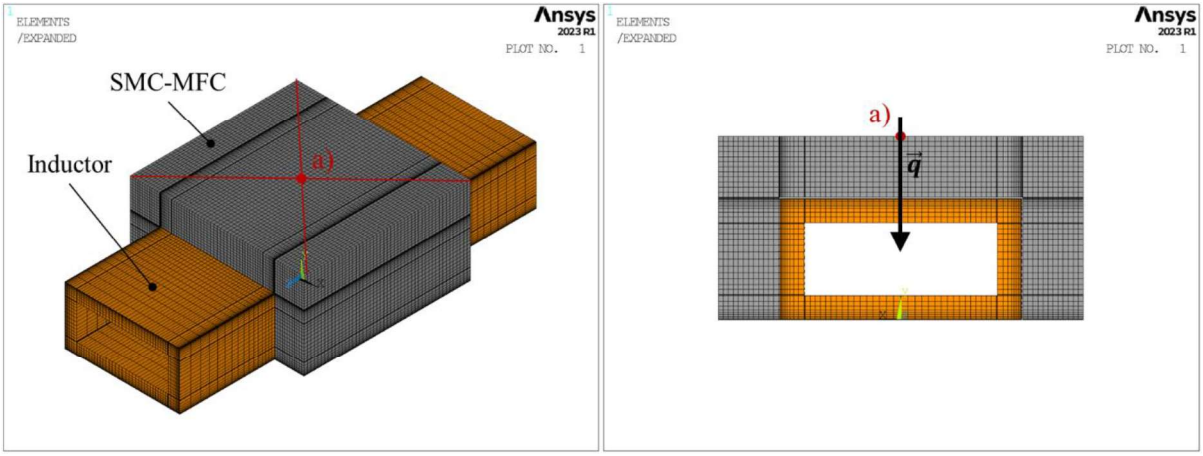


Figure 3. Symmetry expansion of the simulation geometry, a): point of identification.

The simulation is carried out by coupling the electromagnetic (EM) and thermal (TH) fields. In the first step a harmonic EM simulation is conducted to calculate the local distribution of magnetic flux density (B [T]) inside the MFC. For this calculation the curve of the relative magnetic permeability μr as a function of magnetic field strength (H [A/m]) is approximated by a combination of provided data from the manufacturer for H < 40 kA/m and a curve approximation based on a proportionality to the well-known carbon steel data for higher field strengths (Figure 4). The temperature dependance of μr is not documented by the manufacturer and is therefore not considered during this investigation. To improve the quality of the simulated B-distribution, five consecutive harmonic calculation steps were performed with each time updating the distribution of μr(H) based on the output of the previous steps at the start of each simulation. In the second step of the simulation the time dependent temperature distribution is calculated by solving multiple transient thermal calculations. The basis of the transient thermal calculation is a distribution of heat sources inside the MFC which in return is caused by the internal losses. Since the soft magnetic particles used in the manufacturing of the SMC have a size in the order of μm and in addition are electrically insulated from each other through the polymer matrix, no eddy currents are formed under such conditions. Therefore, only hysteresis losses are considered while calculating the distribution of heat sources. For an approximation of volumetric losses of an MFC based on the frequency f and integrated magnetic flux density B, the manufacturer provides a formula as shown in eq. (1). The distribution of hysteresis heat sources inside the MFC used as input for the transient TH simulation is calculated element wise using eq. (1).

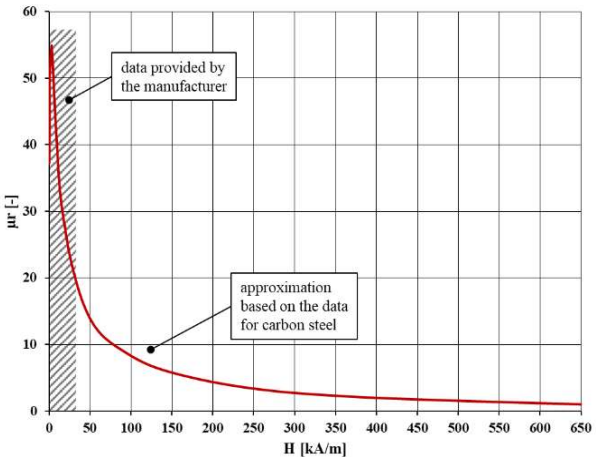

Figure 4. μr as a function of the magnetic field strength.

$$P_{Loss} = 2.73 \cdot f^{1.125} \cdot B^{2.3} \quad (1)$$

**Parameter identification**

For the identification process the simulation model was coupled with a genetic optimization algorithm with the goal to approximate the measured time dependent temperature curve in the identification point with the simulated results through the variation of identification parameters shown in Table 1. The object function in the optimization is the Root Mean Squared Error between the measured and calculated temperature.

Table 1. Identification parameters.

| Parameter | Unit | Description |
|---|---|---|
| $\mathbf{CFP_{Loss}}$ | [-] | Correction factor for the calculation of the internal losses. |
| $\mathbf{CF\mu_r(H)}$ | [-] | Correction factor for the magnetic field strength dependent $\mu_r$. |
| $\boldsymbol{\lambda}$ | [W/mK] | Thermal conductivity. |

The results of the optimization process in Figure 5 concludes, that the time dependent heating in the identification point of the MFC with orthogonal, as well as parallel oriented press direction of the SMC is very well approximated with the identified parameter set. To evaluate the quality of the identified parameter set, Table 1 shows a direct comparison between the identified parameters and their respective values which are provided by the manufacturer. The compared values are very close to each other except the added correction factor for the loss calculation which was expected since the used approach to calculate the losses element wise differs from the integral method of calculation for which eq. 1 was provided.

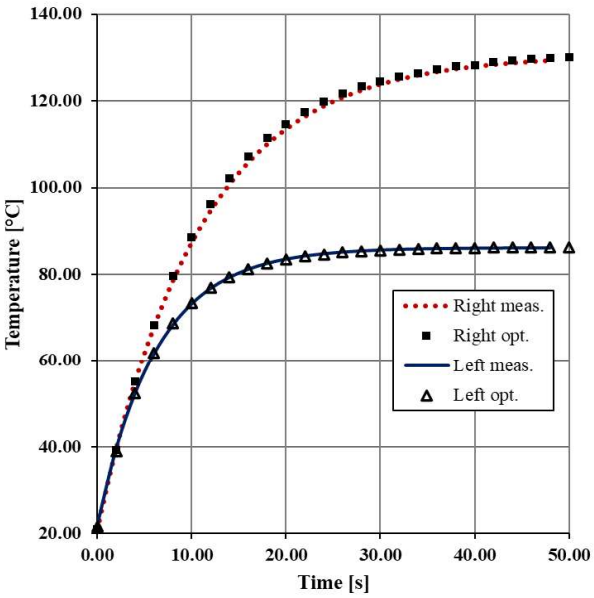


Figure 5. Optimized simulation results in comparison to the measured values.

Table 2. Comparison of the identified parameters with the provided manufacturer data.

| | | **Orthogonal press direction** | | **Parallel press direction** | |
|---|---|---|---|---|---|
| **Parameter** | **Unit** | **Identified** | **Data sheet** | **Identified** | **Data sheet** |
| $\mathbf{CFP_{Loss}}$ | [-] | 0.405 | - | 0.233 | - |
| $\mathbf{CF\mu_r(H)}$ | [-] | 0.6 | 0.6 | 1 | 1 |
| $\boldsymbol{\lambda}$ | [W/mK] | 7 | 8.4 | 3.4 | 3.6 |

**Conclusions and future work**

In this article the first approach to describe the anisotropic material properties for MFC made from SMC was made by using an inverse identification method. It has been shown that the inverse identification is not only sufficient to build a numerical twin of an anisotropic process through the variation of optimization parameters, but also the material parameters themselves which were identified this way are comparable to measured data provided by the manufacturer. In the future the results from the identification shown in this article are to be used as starting points for an optimization of a simulation model which takes all anisotropic properties of the SMC into account at the same time. This way it should be possible to fully describe the anisotropic electrothermal behavior of an SMC-MFC inside an impeder during the inductive pipe welding process.

**References**

[1] Stahlrohrproduktion in Deutschland bis 2017 | Statista.” https://de.statista.com/statistik/daten/studie/485355/umfrage/stahlrohrproduktion-in-deutschland/ (Access: 27.07.2023)
[2] EPCOS, “EPCOS Product Profile 2018 - Impeder Cores - For High Frequency Welding.” p. 20, 2018.
[2] Muyskens, S. M., Eddir, T. I., & Goldstein, R. C. (2020). Improving induction tube welding system performance using soft magnetic composites. COMPEL-The international journal for computation and mathematics in electrical and electronic engineering, 39(1), 185-191.

# Porous material for gas thermal compression in space conditions. Thermal design aspects.

Igors Ušakovs

Allatherm SIA, Pulka 3, Riga LV-1007, Latvia
Igors.Usakovs@allatherm.com

**Abstract:** It is almost impossible to name a field of human activity where porous materials are not used. Filters, membranes, thermal insulators, fuel cells, catalysts, wicks of heat transfer devices, sorbents, textiles, and other examples of porous materials explain such an increased interest in studying of their properties, designing new materials, and developing technologies for their manufacture. The recent need for in-orbit spacecraft refuelling has led to the development of gas thermal compression technology based on the use of porous material as both a fuel retention mechanism and thermal interface. The present paper reveals the thermal aspects of porous material design for a device intended for pumping xenon in zero-gravity conditions, fuel for ion thrusters, – Xenon Refuelling Compressor.

**Keywords:** porous media, metal fibres, nonwoven porous materials, metal felt, gas thermal compression, thermal conductivity of porous materials

## Introduction

The gas thermal compression principle is easiest to understand by considering the operational cycle of a gas thermal compressor (TC). The compressor function is to increase the pressure of fluid (for the sake of generalization, I will further use the term "fluid" rather than "gas".) taken from Servicer (S) tank to a pressure exceeding the one in Client (C) tank, allowing fluid transfer into the C tank.

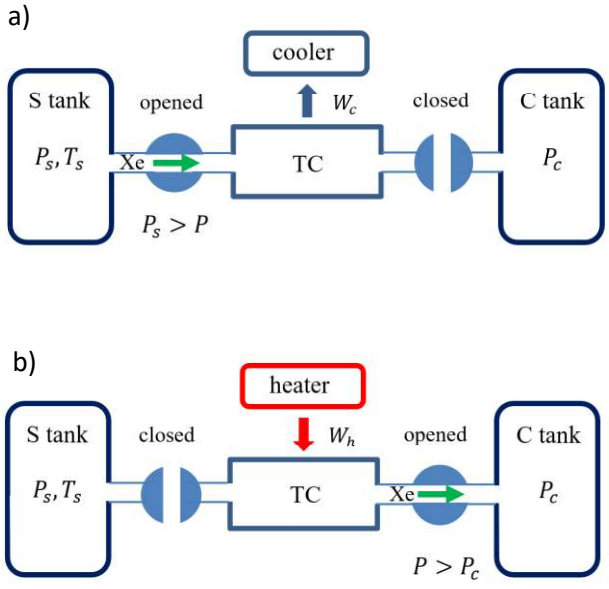


Figure 1. Thermal Compressor operation. a) charging stage, b) discharging stage.

Therefore, the compressor is switched on at the moment when the pressure $P_s$ in the S tank becomes lower than the pressure $P_c$ in the C tank and the fluid can no longer flow from S to C naturally, due to pressure head. TC operational cycles consist of alternating cooling (charging) and heating (discharging) stages. At the cooling stage thermal compressor (TC) is hydraulically connected to the S tank and disconnected from the C tank (Figure 1, a). Pressure in the compressor decreases below $P_s$ with temperature decrease and fluid fills the compressor and condenses. The compressor is charging. At the following heating stage TC is disconnected from the S tank and connected to the C tank. Pressure inside the compressor increases with temperature rise, becomes higher then $P_c$ and fluid transfers into the C tank (Figure 1, b). The compressor is discharging. At the next step the compressor disconnects from the heater and connects to the cooler again and returns to the initial state for transferring the next amount of fluid. It means that the compressor operates in repeated cycles transferring portions of fluid from the low-pressure tank to the high-pressure tank. Simplified, single cycle consists of two isobars and two isochores.

**General requirements for porous materials intended for thermal compressors.**

As is clear from the above description, the compressor is essentially a heat exchanger (HX). Therefore, when designing a compressor, it is necessary to apply to it the requirements characteristic of a good heat exchanger, considering the features of its operation in space. Firstly, its internal structure must ensure the efficient heat exchange between the cooling/heating system and fluid. For that, a developed heat exchange surface should be created inside of the compressor. Secondly, considering that the compressor operation is planned in zero-gravity conditions, there must be some arrangement inside the compressor, which will provide the fluid retention mechanism. A porous body (PB), for example, made of high thermal conductive material, can work in the capacity of such arrangement. On the one hand pores have a large surface area available for heat transfer and on the other hand they can hold fluid by capillary forces. In this case, the material must be well wetted by the fluid. The above leaves no alternative but to use a highly thermally conductive metal, such as copper, to produce the porous structure. The PB can be made of metal powder or metal fibres by sintering in vacuum. The leading parameter of porous materials is porosity $\varphi$, which is the fraction of pore volume $V_p$ to the total volume $V$ of the PB.

$$\varphi = \frac{V_p}{V} = \frac{V - V_m}{V} = 1 - \frac{m}{\rho_m \cdot V} \quad (1)$$

Where $V_m, m, \rho_m$ – volume, mass and density of the pure material used to PB fabrication. In space, the mass and dimensions of the devices used are of great importance, so these parameters must always be optimized in the design. For a compressor, this means that the proportion of retained fluid per unit mass must be maximized. This means that the porosity of the PB must be high. With powders it is difficult to obtain porosity greater than 60%, which is not the case with metal fibres. Fibres allow to obtain structures with porosity >90%. In this case, as will be shown below, thermal conductivity and structural strength become the limiting factors. It was experimentally obtained that the optimal value of porosity is ~80%. Several models of the compressor were manufactured with this structure inside [1]. The choice of thermal compression technology for pumping fuel is also due to the extreme requirements for molecular and particulate contamination. The compressor in this case is a passive device that cannot introduce contamination only if its structural elements react chemically with the fuel or if some

particle of the structure breaks off. The probability of particulate contamination for powder sintered material is significantly higher than for material made of metal felt. Also, the sintering of powder can form useless closed pores that are not accessible to filling of fluid, which is not possible for metal fibres. All these considerations do suggest that the PB should be made of metal felt.

**Thermal parameters optimization.**

The parameters that determine the thermal characteristics of a porous material are heat capacity, density and thermal conductivity. There is not much we can do with the first two, since they are determined by the chosen material and porosity, while the thermal conductivity is highly dependent on the PB structure. Density:

$$\rho = \rho_m \cdot (1 - \varphi) \tag{2}$$

Specific heat capacity:

$$c = c_m \tag{3}$$

The production of a porous structure consists of three steps: selection of the material with the required parameters, moulding, and sintering. Each of the steps leaves its own mark on the final properties of the material. To obtain a material with the desired properties it would be good to simulate these properties in one way or another. But many conclusions can be drawn without complex modelling using qualitative analysis based on general physical considerations. Firstly, the problem is immediately simplified by its formulation. We need to design a material so that it has maximum thermal conductivity at a given porosity. It is known that the initial material should be copper fibres. Regardless of the structure, porous materials have the property that the upper limit of apparent thermal conductivity $\lambda_{max}$ is determined by their porosity $\varphi$ and the thermal conductivities of the material $\lambda_m$ and the fluid filling the pores $\lambda_p$. (In reality, heat inside a PB can be transferred not only by heat conduction, but also by convection and radiation inside the pores. But if the pores are small enough and there are no large temperature gradients inside the PB, as in the case of our interest, these types of heat transfer can be neglected.) The apparent thermal conductivity will reach its maximum value if the conductances of each phase simply adds up. Using Fourier's law this can be written mathematically as follows:

$$\lambda_{max} \cdot \frac{\Delta T}{L_0^2} \cdot L_0 \cdot S = \lambda_m \cdot \frac{\Delta T}{L_0^2} \cdot L_0 \cdot S_m + \lambda_p \cdot \frac{\Delta T}{L_0^2} \cdot L_0 \cdot (S - S_m) \tag{4}$$

Here, a piece of material with cross section $S$ perpendicular to the heat flux and length $L_0$ is taken for the sample. Thus, the volume of the piece is $V = L_0 \cdot S$ and $S_m$ is total cross-sections of solid substance (copper). Taking into account that for copper the condition $\lambda_m \gg \lambda_p$ is fulfilled and the second summand in (4) can be neglected, the expression (4) can be rewritten through volumes taking into account (1) in the form:

$$\lambda_{max} \cdot \frac{\Delta T}{L_0^2} \cdot V \approx \lambda_m \cdot \frac{\Delta T}{L_0^2} \cdot (1 - \varphi) \cdot V \tag{5}$$

(Here on purpose both sides are not reduced by $\frac{\Delta T}{L_0^2} \cdot V$, because in this form we will need expression (5) for further reasoning.) Thus, the maximum thermal conductivity that can be obtained from the fibre is determined only by the porosity:

$$\lambda_{max} \approx \lambda_m \cdot (1 - \varphi) \tag{6}$$

Indeed, as can be seen from (1), the mass of the used fibres is determined only by the porosity. Consequently, the structure with maximum thermal conductivity should only contain fibres oriented along the heat flow. Each fibre oriented transversely does not transfer heat but occupies useful volume. The pore space is formed by the gaps between the fibres, and they also serve as capillaries holding the condensed fluid. An ideal structure in this sense is shown in Figure *3* (b). Over the last 150 years of study of porous materials, dozens of expressions for calculating frame thermal conductivity have been derived ([2], [3]). Most of the expressions have a narrow field of applicability and represent thermal conductivity as a function of porosity and thermal conductivity of pure material. In fact, the expression for thermal conductivity must also contain microstructural parameters such as fiber thickness $d$ (diameter) and individual fibre length $l$. For example, in [4], a correlation of porosity and thermal conductivity on the fibre's aspect ratio was established, from which it follows that longer and thinner fibres are desirable. The influence of fibre length can be qualitatively explained by considering the skeleton of a porous structure sintered from randomly oriented fibres, which is the case for most metal-fibre materials. Heat is transferred through both the fibres body and the contact spots between them (see Figure *3*, a). The contact thermal resistance $R$ of the contact spots is difficult to predict although there are various attempts of modelling them. It is determined by the sintering parameters. The shorter the fibres, the more contact points in the heat path, the worse the thermal conductivity. The influence of contact resistances is well described in paper [5]. It contains a rather extensive experimental and analytical study of porous copper and steel fibre materials of different porosity developed at the Fraunhofer Institute, including numerical modelling of the porous structure geometry based on micro-computed tomography (ICT) images of real material. The heat transfer was then modelled by Lattice Monte Carlo [6] and Finite Element methods. The thermal conductivity was also calculated using several analytical relationships. The experimental results showed a significant discrepancy with the models for porosity below 60%, which was explained by not considering the contact resistances between the fibres, the number of which logically increases with decreasing porosity. Summarizing the above, we can conclude that in order to form a good structure, it is desirable to use a material with long, or better even continuous, fibres, such as the one shown in Figure 2.

Figure 2. Copper yarn with continuous $20\mu$ thick filament.

The second important parameter is the fibre diameter $d$. As mentioned above, it is necessary to create a developed heat exchange surface inside the compressor. It is not difficult to show that

the heat exchange surface per unit volume $S_h$ depends on the fibre diameter and porosity as follows:

$$S_h = \frac{4}{d}(1-\varphi) \quad (7)$$

The same relationship determines the length of the wetted perimeter, which is the guiding factor for the capillary properties of the material. As can be seen from (7) the above-mentioned material properties improve with decreasing fibre diameter. Thus, it is better to select a continuous fibre with the smallest possible diameter to fabricate the structure. We managed to find fibre with a thickness of 20 microns. The experience of its use shows that this size is optimal, because with a thinner fibre there may be difficulties related to felting and the subsequent moulding of the structure for sintering, as well as with the strength of the PB.

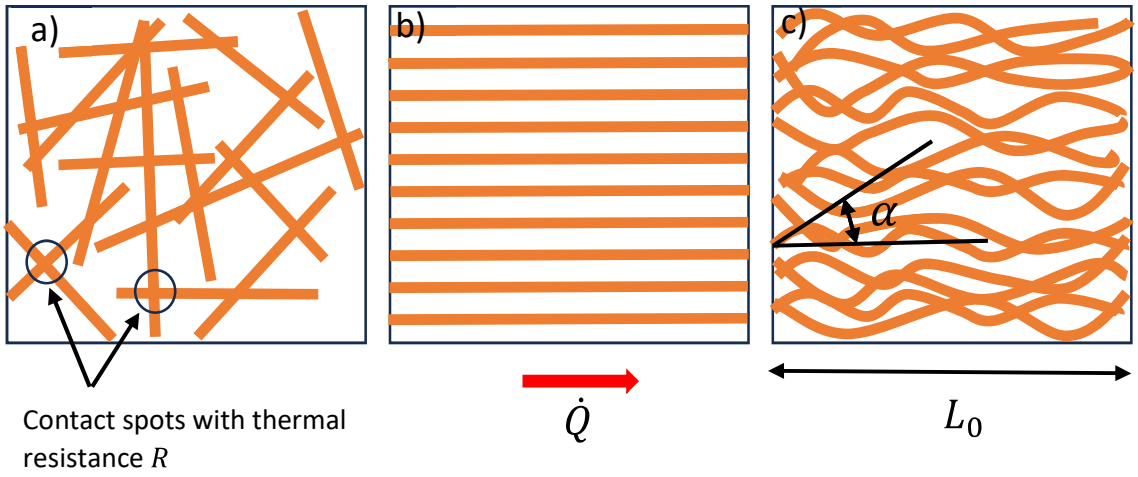


Figure 3. Three patterns of fibrous porous structures. a) Randomly oriented fibres; b) porous structure with maximum thermal conductivity; c) Real structure with oriented felt direction.

Obviously, it is impossible to produce a PB corresponding to the ideal structure shown in Figure *3* (b), consisting only of fibres directed in parallel of the heat flow. Some number of transverse fibres forming the structural skeleton must be present. By applying the technique of directional felting, it is possible to obtain a structure like the one shown in Figure *3* (c), where the individual fibres are intertwined to form a spatial skeleton but retaining in general a given direction. The deviation of the fibres from the heat flow direction can be characterized by some angle α randomly distributed in some range $[0, \alpha_{max}]$, where $\alpha_{max} \leq {}^{\pi}/_{2}$ and can be controlled by the width of single strand. The thermal conductivity of the obtained structure will be less than the maximum (6) due to two reasons. Firstly, as the fibre length $L$ increases, the path passed by the heat through the PB increases, which can be written as:

$$L = \frac{L_0}{cos\,(\alpha)} \quad (8)$$

Secondly, since the mass of fibres per unit volume for a given porosity is fixed, the number of fibres per unit volume will decrease with fibre elongation. Both factors will be automatically taken into account if $L$ from (8) is substituted into the right-hand side of expression (5) instead of $L_0$. Reducing both sides by $\frac{\Delta T}{L_0^2} \cdot V$, we obtain an expression for thermal conductivity depending on the $\alpha$ angle:

$$\lambda = \lambda_m \cdot (1-\varphi) \cdot cos^2(\alpha) = \lambda_{max} \cdot cos^2(\alpha) \quad (9)$$

To obtain the final expression for the thermal conductivity of the material, it is necessary to average the expression (9) over the $\alpha$ angle in the range of its variation:

$$\bar{\lambda} = \frac{\lambda_{max}}{\alpha_{max}} \cdot \int_0^{\alpha_{max}} cos^2(\alpha)\, d\alpha = \frac{\lambda_{max}}{2 \cdot \alpha_{max}} \left[\alpha_{max} + \frac{1}{2} sin\,(2 \cdot \alpha_{max})\right] \quad (10)$$

In the worst case, assuming $\alpha_{max} = {}^{\pi}/_{2}$ we obtain the minimum value of thermal conductivity:

$$\bar{\lambda}_{min} = \frac{1}{2}\,\lambda_{max} \quad (11)$$

**Conclusions**

The above rather simple analysis provides a practical guide to the development of a fabrication technique for the porous structure best suited for a TC. It is interesting to see the obtained results in numbers. Assuming the thermal conductivity of copper to be $394\ W/m \cdot K$ for the thermal conductivity of a PB at a porosity of 80%, we get a value (eq. 6 and 11) lying in the range: $39.4 \leq \bar{\lambda} \leq 78.8$. This is a very encouraging result, considering that for randomly oriented fibres the thermal conductivity is well described by the given in paper [7] relation:

$$\lambda = \frac{\lambda_m \cdot (1-\varphi)}{1+11 \cdot \varphi^2} = \frac{\lambda_{max}}{1+11 \cdot \varphi^2} \quad (12)$$

Which gives value the thermal conductivity of just $9.8\ W/m \cdot K$ for the same porosity. In the previous stage of compressor development, we obtained exactly such results because we used structures with random fibre orientation. We are currently developing a new moulding technology in line with the proposed approach. The parameters of the new material are planned to be tested experimentally in order to validate the applied methodology.

**References**

[1] Ušakovs I., Mishkinis D., Rohrbeck M., Tijsterman R., Bodendieck F., Aziz S. (2022). 2nd International Conference on Flight Vehicles, Aerothermodynamics and Re-entry Missions & Engineering (FAR), 19 - 23 June 2022. Heilbronn, Germany.
[2] Collishaw P. G., Evans J. R. G., (1994) An assessment of expressions for the apparent thermal conductivity of cellular materials, Journal of materials science, 29 (1994) 486-498.
[3] Mantle W. J., Chang W. S., (1991) Effective Thermal Conductivity of Sintered Metal Fibres, J. Thermophysics, VOL. 5, NO. 4, OCT.-DEC. 1991.
[4] Semena M. G., Zaripov, V. K., (1977) Influence of the Diameter and Length on Material Heat Transfer of Metal-Fibre Wicks of Heat Pipes, Teploenergetika, Vol. 24, No. 4, 1977, pp. 82-84.
[5] Veyhl C. Fiedler T., Andersen O., Meinert J., Bernthaler T., Belova I.V., Murch G.E., (2012) On the thermal conductivity of sintered metallic fibre structures, International Journal of Heat and Mass Transfer 55 (2012) 2440–2448
[6] Belova I.V., Graeme E. Murch G.E., Fiedler T., Öchsner A., (2008), The Lattice Monte Carlo Method for Solving Phenomenological Mass and Thermal Diffusion Problems, Defect and Diffusion Forum Vol. 279 (2008) pp 13-22
[7] Koh J. C. Y., Fortini A, (1973) Prediction of thermal conductivity and electrical resistivity of porous metallic materials, int. J. Heat Mass Transfer. Vol. 16, pp. 2013-1022.

**Analysis of energy efficiency of heat exchangers with variable section based on the modeling of the heat and mass transfer processes**

Sakipova S.E., Nussupbekov B.R., Shaimerdenova K.M., Ospanova D.A., Edris A.

E.A. Buketov University, Karaganda, Kazakhstan, sesaule@mail.ru

One of the main priorities in the modern thermal power engineering development is the problem of energy saving due to the economical use of fuel and energy reserves. Increasing energy consumption with a simultaneous increase in energy prices and widespread environmental degradation necessitates the development and implementation of energy efficient technologies to save fuel, materials and labor costs. The object of research are tubular heat exchangers with variable cross section are widely used in steam generators of nuclear power plants, gas turbine and transport plants. Heat is transferred through the processes of heating, cooling, boiling, condensation, evaporation, etc. So, study of heat and mass transfer of inhomogeneous liquid flows into channels of variable cross section the regularities are importance.

Using method of group consideration of arguments, an analysis of experimental data on the influence of inhomogeneity on the heat transfer of the coolant that is flowing through channels with variable cross section was carried out. The regression analysis allowed to reveal some patterns of heat transfer of a non-uniform flow in diffusers. A semi-empirical formula for calculating heat transfer is obtained, in which takes into account the separate influence of three parameters and their covariance. The principles of implementing technologies aimed at intensifying heat transfer, reducing hydraulic and heat losses in heat exchangers are formulated.

# Directional Solidification of Silicon: Experimental Results

Michele Forzan, Mattia Guglielmi

University of Padova, Department of Industrial Engineering, Via Gradenigo 6a, Padova, Italy

**Abstract:** In this paper, we present some experimental results of casting, by directional solidification, multi crystal (mc) silicon ingots in a vacuum melting furnace that makes use induction heating systems, installed at the Laboratory for the Electroheat at University of Padua (Italy). The design of the electromagnetic system was carried out by resorting to numerical modeling and the same numerical models have been used to design the thermal process necessary to carry out the melting and directional solidification of the ingot. Numerical models were applied to simulate the electromagnetic and thermal behavior of the apparatus and also the directional crystallization process, by optimizing the speed of the solidification front, and the effect of electrodynamic forces that create a mixing effect in the molten bath. Three different processes, that last about 60 hours each, have been carried out in laboratory for Electroheat in Padova, to melt and crystallize about 120 kg of recycled silicon. Some experimental results are presented in this paper.

**Keywords:** Directional solidification, Numerical models, Electromagnetic Stirring

## Introduction

Some years ago, an innovative technology that makes use of Induction Heating has been proposed in DSS furnaces (Directional Solidification System) for the production of multi crystal silicon, mcSi, used in photovoltaic (PV) industry. Some industrial scale i-DSS furnaces (induction DSS) have been realized and tested in industrial environment. The i-DSS furnace installed in LEP was capable to cast about 120 kg of silicon in a G2,5 (400x400 mm) silica crucible. In this paper we present for the first time some results obtained from the three casting experiments carried out at the laboratory of electro heat at University of Padua.

The i-DSS furnace features three independent inductors: a top pancake inductor, a side multi-turns inductor and a bottom pancake inductor that also acts as heat sinker. The side inductor heats the isostatic graphite plates providing mechanical support to the crucible. The side inductor works at relatively low frequency, about 2 kHz, and the isostatic graphite has a relative shielding effect. The intensity of the induction field outside the molten silicon is, in working conditions, about 10 mT.

The top and bottom inductors heat by induction the top susceptor and the bottom DS-block. The side inductor heats the graphite walls around the crucible. The bottom inductor has been properly designed in order to be used as an efficient cooler. The water cooled copper surface of the bottom inductor can exchange heat efficiently by radiation with the bottom graphite susceptor. The thermal flux can be controlled by moving the bottom inductor up or downward in order to vary the thermal coupling and/or by changing the cooling water flow rate in order to reduce or increase the copper temperature. By switching on and off the inductor's power supply, it is possible to obtain a further tuning of the thermal flux and optimize the velocity of the solidification front. This fine tuning is almost impossible in a traditional resistor furnace.

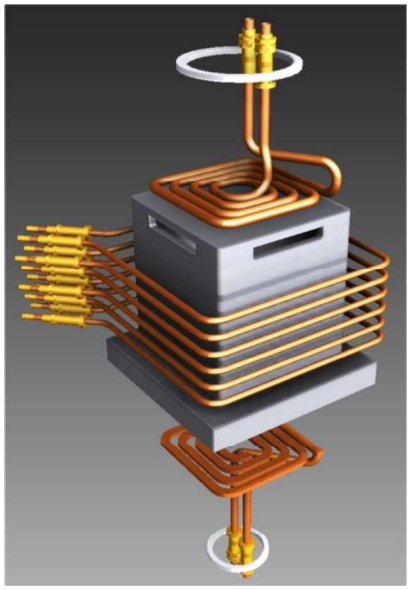

Figure 1. 3D model of the induction heating system and hot zone of the iDSS furnace

**Numerical model**

Numerical modelling, mostly based on FEM, has been intensively applied both to design the furnace and to predict the process parameters.

The different positions of each heating source guarantee an accurate control of the temperature field inside the hot zone during all the process phases. In order to maximize the energy efficiency of the process, the thickness of the lateral insulating graphite, that are placed between the susceptors made of isostatic graphite and the lateral inductor, has been chosen in order to guarantee an appropriate balance between thermal losses and inductor efficiency. The thickness of graphite felts has an obvious impact on the insulation, but an increasing thickness has also a negative impact on the inductor efficiency. Due to significant distance between the bottom and top inductors from the melt, the AMF generated by these two inductors is negligible in the silicon.

On the contrary, the electromagnetic field generated by the lateral inductor is not negligible inside the molten silicon. The side inductor works at a relative low frequency enabling a significant intensity of the magnetic field on the boundaries of the molten silicon. In Fig. 2 the colour map shows the distribution of induction field intensity, while in Fig. 3 arrows show the electrodynamic forces that arise in the liquid silicon. The intensity of the induction field reaches about 11 mT (rms value) when the side inductor is series fed with about 1300 A.

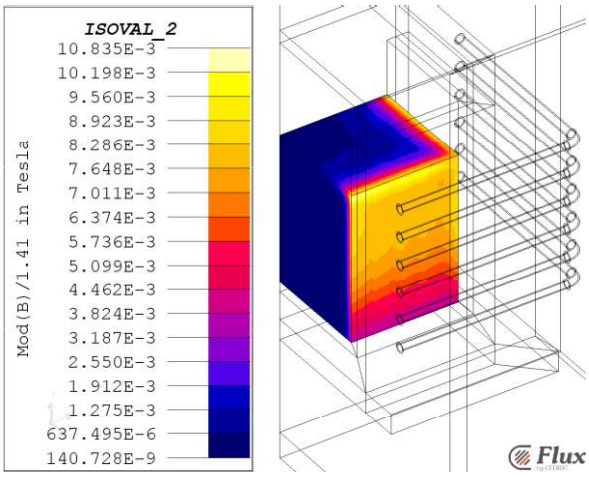


Figure 2. Magnetic induction intensity [T] on the molten silicon.

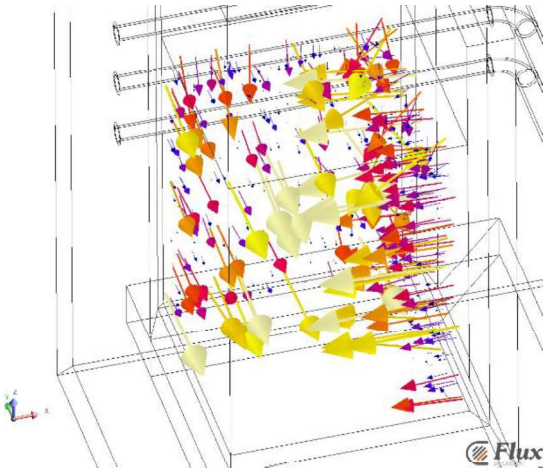


Figure 3. Averaged component of the Lorentz forces on the silicon.

The process steps for producing multi-crystalline silicon ingots for photovoltaic applications using a directional solidification furnace are the following and are schematically represented in Figure 4 and Figure 5:

- Heating,
- Melting,
- Thermal gradient creation in the melt,
- Directional solidification,
- Annealing,
- Controlled cooling,
- Free cooling.

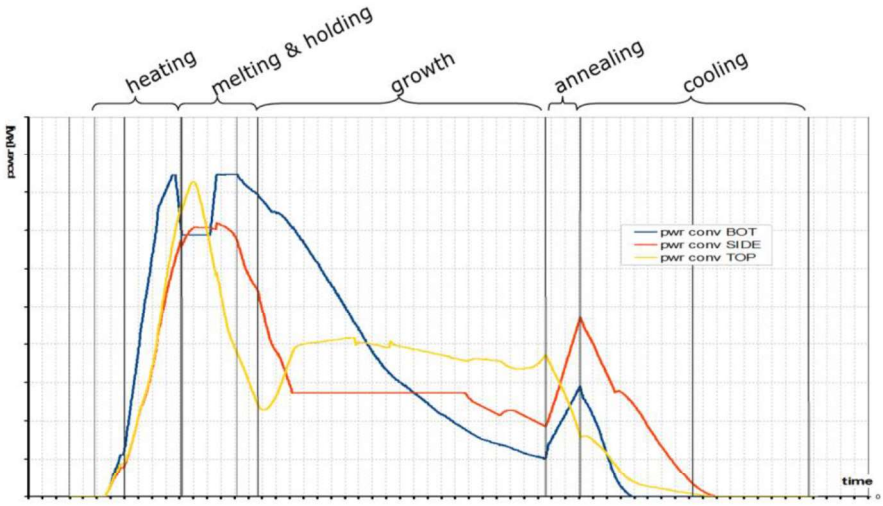


Figure 4. Process power during a multi-crystalline casting process using a 3 heaters induction-heating DS furnace.

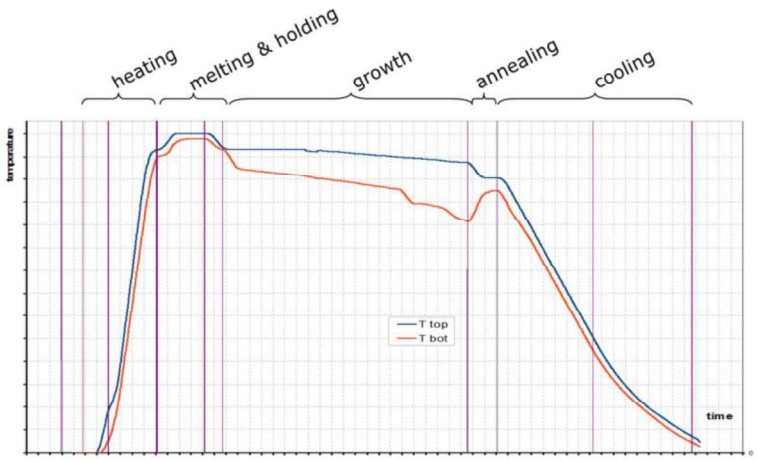


Figure 5. Process temperature during a directional solidification casting process

Numerical simulations have been carried out also to predict the effect of Lorenz's forces in the bath and the position of the solidification front during the growth step. In order to compute the distribution of velocity field at the end of melting and during the solidification process, simplified 2D axisymmetric models have been considered. COMSOL simulation code was used to analyze the fluid dynamics, applying the RANS approach and specifically k-ε formulation. The distribution of the electrodynamic forces has been computed with the same FEM software.

Numerical results obtained with this extremely simplified approach showed that two main vortexes arise in the molten bath, the upper and bigger one is separated from the smaller bottom one. Since it is expected that Silicon Carbides precipitates can pollute the melt mainly from the upper surface, the computed stirring paths suggest that these inclusions should be confined in the upper part of the melt.

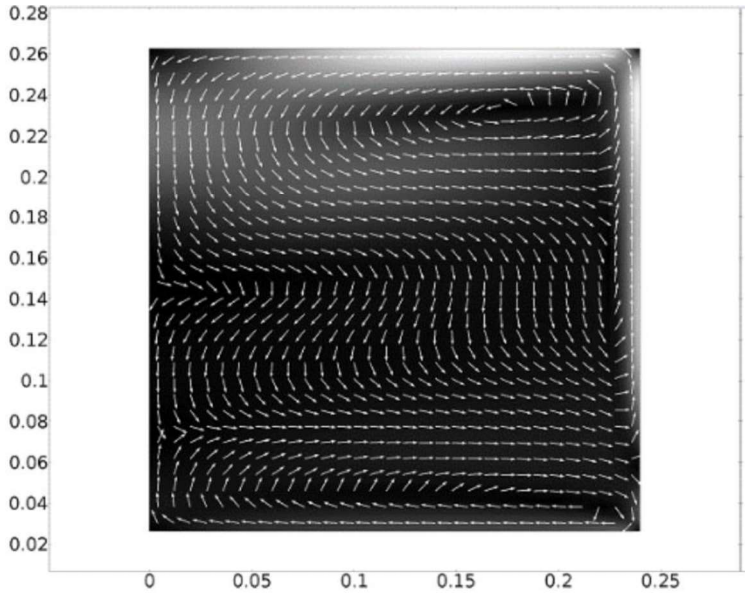


Figure 6. Computed velocity distribution of the molten silicon before the solidification in a simplified axisymmetric model.

**Experimental**

The profiles of temperature measured on the top and bottom susceptors are presented in Fig. 7. They were successfully forecasted by means of simulations results, thus allowed to find a correct crystallization recipe with only 2 experimental tests.

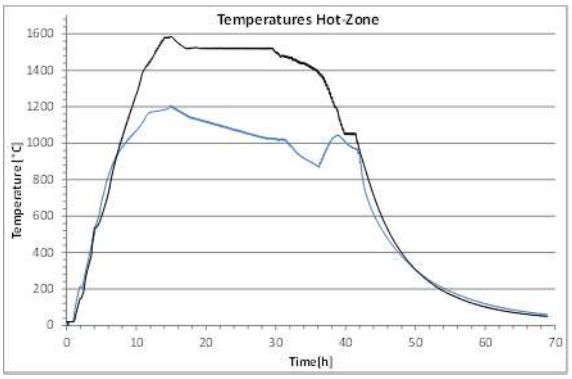


Figure 7. The process recipe: measured temperatures on the top and bottom graphite susceptors.

Figure 8. The ingot casted and solidified at LEP. The upper layer of the ingot is mostly silicon carbide.

Fig. 8 shows the silicon ingot produced applying the process. Notably, a huge amount of SiC is distributed on the top surface of the ingot. On the top of the silicon ingot and in the cold part of the vacuum chamber there is also a significant quantity of silicon nitride. Metallurgical and chemical analysis of powders deposed on the ingot top (Cambridge Stereoscan 440 SEM and probe EDS Philips PV9800) demonstrated the significant presence of Silicon Carbides.

Figure 9. Photo of a cross section and of a side of a brick cut from the ingot.

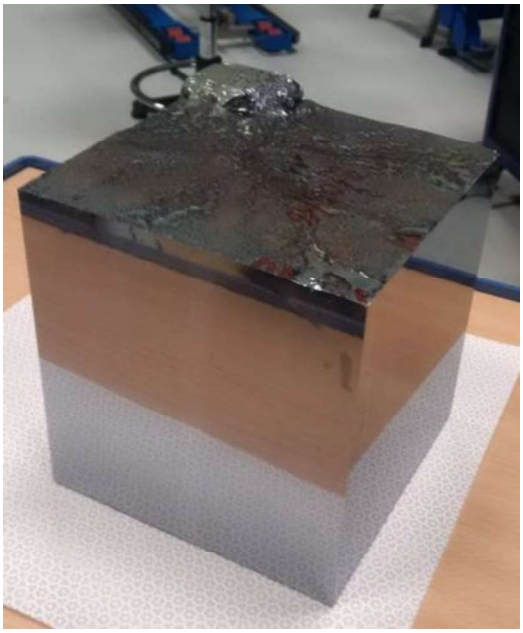

Figure 10. The brick has been grinded with Arnold surface grinding machine
Precision: +- 0.05 mm Roughness: < 0.1µm

Infrared inspections of some bricks were carried out the Fraunhofer Center for Silicon Photovoltaics CSP, Halle Germany. The brick was fine-grinded to permit the IR inspection (Fig. 10) and some IR images (Intego NIR-Inspection system with a resolution of 100µm made with the aim of detecting Si3N4/SiC inclusion structures are shown in Fig.11. They clearly show that SiC inclusions occur only in the upper part of the ingot, giving somehow a validation of the simple numerical fluid dynamic models developed.

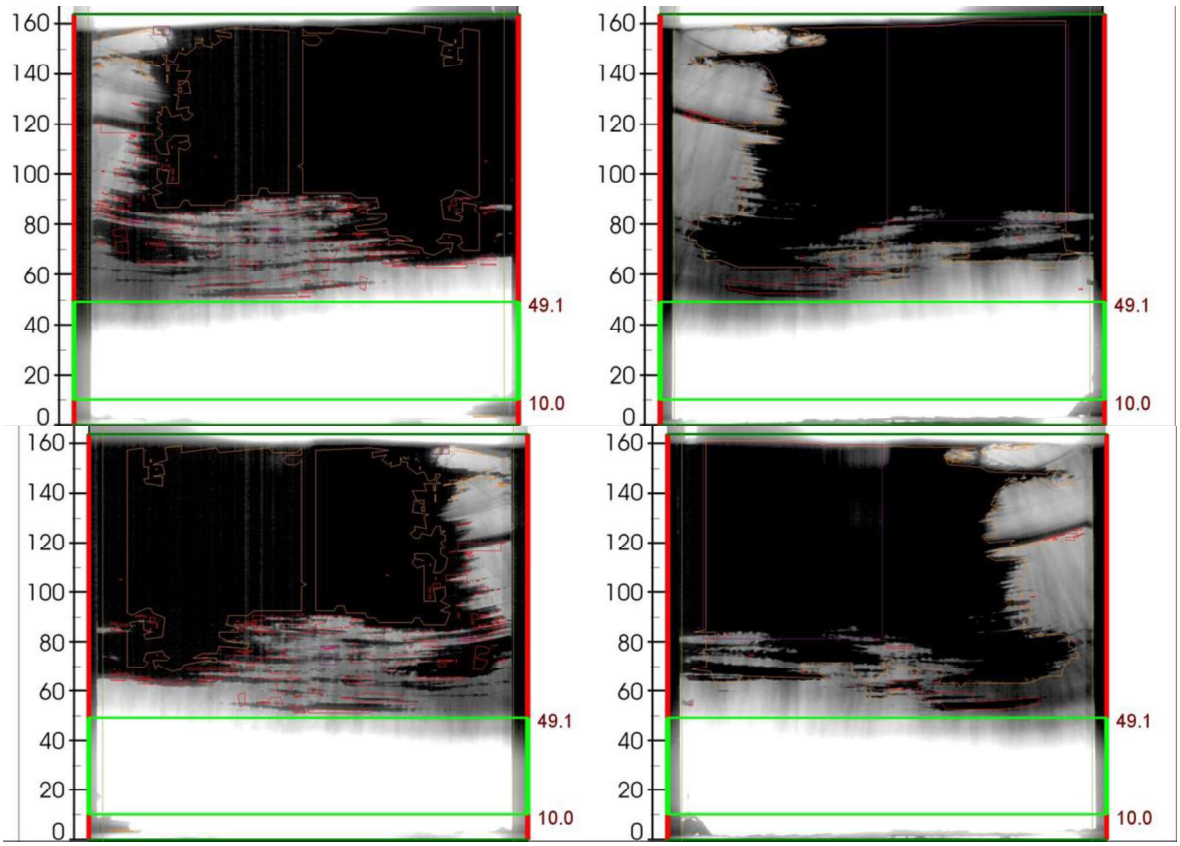


Figure 11. IR measurement results. The darker regions contain SiC inclusions.

**Conclusions**

In this article we present some experimental results of casting multi crystal (mc) silicon ingots that confirmed that numerical models allow for a precise design of the electromagnetic device and also for an accurate prediction of the system behavior. This way the experiments were successfully carried out by resorting to a very limited number of tests.

**References**

[1] F. Dughiero et al. (2011). Multi-crystalline silicon ingots growth with an innovative induction heating directional solidification furnace. Photovoltaic Specialists Conference (PVSC), 2011 37th IEEE, 002151-002156.

[2] Djambazov, G., Pericleous, K., Bojarevics, V., Forzan, M., & Dughiero, F. (2016). Modeling the Electromagnetic Processing of Recycled Silicon Dust. REWAS 2016: Towards Materials Resource Sustainability, 17.

# Numerical study of the Bridgman directional solidification process of photovoltaic silicon ingot using the power control technique

Brahim Hiba[1*], Abdallah Nouri[1], Lakhdar Hachani[1] and Kader Zaidat[2]

1. Laboratoire Physique de Matériaux, Université Amar Telidji de Laghouat, BP 37 G Boulevard des martyrs, Laghouat 03000, Algérie.
2. SIMAP-EPM PHELMA, University of Grenoble Alpes, BP 75, 38402 Saint-Martin-d'Hères Cedex, France.

*b.hiba@ens-lagh.dz

**Abstract:** This work is related to the improvement of silicon photovoltaic solar cells using an Electro-Magnetic Stirring (EMS) in a prior processing step by controlling the hydrodynamics of the silicon bath during the ingot solidification. A vertical Bridgman directional solidification furnace called VB2 using a controlled power-down technique under forced convection generated by a Travelling Magnetic Field (TMF), was numerically investigated; i.e. a full 3D numerical model of the VB2 furnace was developed using Comsol Multiphysics$^{TM}$ software. Enthalpy formulation based on fixed-grid techniques is used for the phase-change phenomena; accounting for magnetohydrodynamic (MHD) forced convection created by Lorentz force generated by a specific cylindrical Bitter coil. The model provides the temperature distribution of the entire furnace as well as specific details regarding the solidification process (i.e. solidification fraction and solid-liquid interface shape), flow patterns and liquid velocities. The numerical results show good consistency with experimental measurements and analysis, on the one hand, and can be considered as useful orientation to improve the solidification process, on the author hand. It is shown that the TMF acting in the melt creates moderately turbulent flow, which has a significant impact on solid-liquid interface in terms of morphology and symmetry during silicon solidification, and consequently on the tight control of the crystallization process that can affect silicon crystal morphology and impurity distributions.

**Keywords:** Electromagnetic stirring, polycrystalline photovoltaic silicon, solid-liquid interface, travelling magnetic field, vertical Bridgman directional solidification.

## Introduction

Polycrystalline silicon is one of the most widely used materials for production of photovoltaic solar cells. In order to ensure a high efficiency of final cells, a silicon feedstock of high purity must be used. For cost reduction, it is possible to start from acceptable metallurgical solar-grade silicon feedstock with appropriate directional solidification process for ingots production [1]. However, the raw material used for photovoltaic polycrystalline silicon ingot production, with actual directional solidification process, contains impurities distribution that have a major impact on the final ingot; therefore, on the performance of the solar cells where it can reduce its efficiency [2-3]. To enhance the quality of the final ingot, i.e. the impurities distribution and crystal structure, it's necessary to control the factors that affect it during the solidification process as the growth rate, the temperature gradient, the cooling rate and the hydrodynamic motion of the silicon melt. Mainly, controlling the configuration of the hydrodynamic motion of the melt and the thermal configuration of the furnace should be leading to a better control of the solid–liquid interface shape and therefore the segregation process of impurities and crystal structure during the directional solidification process [4].

The use of the EMS to control the hydrodynamic motion in the case of the conductive charge within the liquid phase has become an interesting technic. However, the configuration of the MHD flow pattern is strongly depending on the design of the electromagnetic inductor which is the source of the creation, distribution and action of the Lorentz forces in the silicon bath. In the case of the cylindrical system with symmetry axis (i.e. the TMF apparatus used in VB2 furnace), the choice of 2D models to simulate hydrodynamic motion driven by the TMF during the solidification process which is obviously based on an axisymmetric approach, does not always predict the real case of the existing MHD flow configuration. Based on this, Mircea et al. [1, 5, 8] numerically examined the effect of two configurations of TMF (Upward and Downward) on the solid-liquid interface in a vertical Bridgman directional solidification experiment (VB2 furnace) using a 2D axisymmetric model. As results, it was shown that there are two possible regular shapes of the solid-liquid interface, seen from the solid: convex and concave, depending on the direction of the TMF stirring upward or downward, respectively. However, our recent 3D numerical investigation (Hiba et *al.* [7]), focused on the analysis of the MHD flow configuration and instability under identical experimental conditions of VB2 furnace, confirmed that the real topology of the MHD flow is not always axisymmetric but only, can be assimilated to a quasi-symmetric with respect to a specific meridian plane. In fact, this paper is part of an extensive continuity of our previous work, which the primary objective will be focused on a 3D numerical study on the real TMF apparatus (Bitter coil Fig. 1 & Fig.3) supposed to be more predictive, in order to examine the effect of TMF stirring on the flow configuration as well as the stability and the shape of the solid-liquid interface during the solidification of silicon under power down technique.

## 1. Experimental process

The VB2 device is a cylindrical resistive furnace where a benchmark of vertical Bridgman solidification experiment can be conducted in order to create cylindrical polycrystalline silicon ingots of 2 inches in diameter. It was performed at the SIMaP/EPM Laboratory in Grenoble, France.

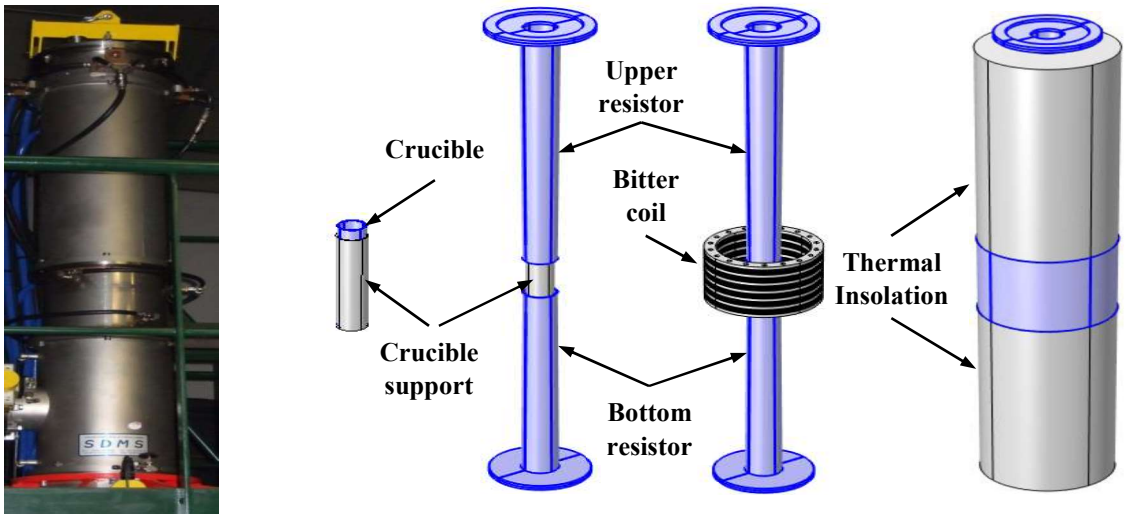


**Figure 1.** Main components of VB2 furnace (SIMaP/EPM Laboratory, Grenoble, France).

As shown in Fig. 1, the VB2 furnace is composed by three principal parts: two graphite resistors (top and bottom), surrounding by thermal insulation in graphite foam and in between an adiabatic zone to improve the control of the radial and vertical thermal gradients within

the silicon melt. The two resistors are in form of electrical heaters in graphite; they can generate a controlled thermal heat flux as well as an applied temperature gradient $\Delta T$ and cooling rate Cr, through the electrical power down technique. In the central adiabatic region solar metallurgical grade silicon is placed in a cylindrical fused silica crucible with 2.5 cm in diameter, which is partially filled (12 cm high) and carried by graphite support surrounding by multilayer foam insulation. In addition, an electromagnetic Bitter coil generating an external travelling magnetic field (TMF) is used to control the magnetohydrodynamic (MHD) flow of the silicon melt bulk during the solidification process without contaminating it. The Bitter coil apparatus has a height of $H_{IN}$ = 18 cm and internal and external diameters of 20 and 25 cm, respectively. The TMF is characterized by the wavelength $\lambda$ and the pole pitch $\tau$, where $\lambda = 2\tau$ =168 mm, so that the wave number is $k = 2\pi/\lambda = 37.4\ m^{-1}$. The coils of the Bitter coil consist of six blocks of discs, each having a stack of ten separate copper discs with Kapton electrical insulation. The TMF system is powered by the three-phase currents shifted by $2\pi/3$ at network frequency $f_0$ = 50 Hz. A power down technic is used for the resistive graphite resistors (top and bottom) with an applied thermal gradient to ensure a vertical direction solidification process of silicon melt.

## 2. Numerical model

The full 3D multidisciplinary developed model, dealing with the entire VB2 furnace, is governed by the non-linear coupling set of equations; including electromagnetism, fluid mechanics, and heat transfer with phase change phenomena (see Table 1). The electromagnetic part solving the set of Maxwell's equations in harmonic mode for the different coils composing the Bitter coil was based on the A-V potential formulation, in order to calculate the TMF generated and subsequently the Lorentz force induced in the silicon liquid charge. A realizable k-ε turbulent model was adopted to treat the fluid flow under electromagnetic stirring. However; in VB2 furnace (i.e. in the adiabatic zone) the buoyancy forces were neglected due to the absence of thermal gradients in the radial direction and the positive vertical gradient in z direction i.e. (The bottom zone is cold and the upper zone is hot). The reader is referred to Hiba et al. [6-7] for further details concerning the turbulent model developed to resolve the set of magnetohydrodynamic equations, fundamentally based on low frequency and low magnetic induction, and on an averaged expression of the Lorentz forced. The energy part concerning the heat transfer in the whole furnace, took into account all the existing energy exchange mechanisms: conduction, convection and radiation. It is important to mention that the heat source resulting from the Joule effect was included as a source term in the part of the heat transfer in solid dealing with the two graphite resistors, and it was neglected in the silicon melt (i.e. electromagnetic heat induction) due to the used low network frequency (50 Hz), which is much more converted into dynamic effect (i.e. electromagnetic stirring). For silicon phase change modelling, an enthalpy formulation based on a fixed-grid approach is adopted to predict the solidification process in terms of solid-liquid interface location, morphology and its advancement in the ingot. The liquid was assumed to be incompressible with a constant density and viscosity. The no-slip flow boundary condition was applied for the melt. The thermodynamic/physical properties used in the current simulations are listed in Table 2.

**Table 1.** Set of PDE governing the three main parts of the developed numerical model.

| | |
|---|---|
| Electromagnetic part: | $$\overrightarrow{J_s} = \boldsymbol{\sigma}\left(-\frac{\mathbf{1}}{\boldsymbol{\sigma\mu}}\boldsymbol{\nabla^2}\overrightarrow{\boldsymbol{A}}\right) - \boldsymbol{\sigma}\left(-\frac{\boldsymbol{\partial}\overrightarrow{\boldsymbol{A}}}{\boldsymbol{\partial t}} - \overrightarrow{\boldsymbol{\nabla}}.\emptyset + \overrightarrow{\boldsymbol{u}} \times \overrightarrow{\boldsymbol{\nabla}} \times \overrightarrow{\boldsymbol{A}}\right)$$ $$\overrightarrow{\boldsymbol{F_L}} = \overrightarrow{\boldsymbol{J_i}} \times \overrightarrow{\boldsymbol{B}};\ \overrightarrow{\boldsymbol{J_i}} = \boldsymbol{\sigma}\left(-\frac{\boldsymbol{\partial}\overrightarrow{\boldsymbol{A}}}{\boldsymbol{\partial t}} - \overrightarrow{\boldsymbol{\nabla}}\emptyset + \overrightarrow{\boldsymbol{u}} \times \overrightarrow{\boldsymbol{\nabla}} \times \overrightarrow{\boldsymbol{A}}\right);\ \overrightarrow{\boldsymbol{B}} = \overrightarrow{\boldsymbol{\nabla}} \times \overrightarrow{\boldsymbol{A}}$$ $\overrightarrow{J_S}$**:** current source intensity; $\vec{A}$: vector potential of the magnetic field; *Φ:* electrical potential with ($\nabla^2\emptyset = 0$); $\overrightarrow{J_i}$: induced current density; $\vec{u}$: velocity of the melt and $\vec{B}$: the magnetic field. |
| Fluid mechanics part: | $$\boldsymbol{\rho_0}\left[\frac{\boldsymbol{\partial}(\boldsymbol{f_l V_l})}{\boldsymbol{\partial t}} + (\boldsymbol{f_l V_l}.\boldsymbol{grad})\boldsymbol{V_l}\right] - \boldsymbol{\nabla}.(\boldsymbol{\mu_l}.\boldsymbol{\nabla}.\boldsymbol{f_l V_l}) + \boldsymbol{S(T)V_l} = -\boldsymbol{f_l grad(p)} + \boldsymbol{f_l \rho_0 g} + \boldsymbol{f_l F_{LTZ}}$$ $$\boldsymbol{S(T)} = \boldsymbol{A_{mush}}\frac{\boldsymbol{f_l^3}}{(\mathbf{1}-\boldsymbol{f_l})^2};\qquad \boldsymbol{\nabla}.(\boldsymbol{f_l V_l}) = \mathbf{0}$$ $A_m = 10^6$ kg.m$^{-3}$.s$^{-1}$ is mushy zone constant; $f_l$: liquid fraction; |
| Global heat transfer with phase change part: | ▪ Heat transfer in the liquid with phase change: $$\frac{\boldsymbol{\partial}(\boldsymbol{\rho Cp T})}{\boldsymbol{\partial t}} + \frac{\boldsymbol{\partial}(\boldsymbol{\rho f_l L})}{\boldsymbol{\partial t}} = -\boldsymbol{\nabla}(\boldsymbol{\rho u h}) + \boldsymbol{\nabla}(\boldsymbol{\lambda \nabla T}) + \boldsymbol{S_T}$$ $$\boldsymbol{h} = \begin{cases} \boldsymbol{C_{p\,s}\,T}, & \boldsymbol{T \le T_m} \\ \boldsymbol{C_{p\,l}\,T + H_f}, & \boldsymbol{T > T_m} \end{cases}$$ $$\boldsymbol{Cp(T)} = \boldsymbol{Cp_s} + \boldsymbol{f_l(T)}.(\boldsymbol{Cp_l} - \boldsymbol{Cp_s}) + \boldsymbol{D(T)}.\boldsymbol{L}$$ With $\boldsymbol{D(T)} = \frac{e^{-\left(\frac{T-T_m}{\Delta T/4}\right)^2}}{\sqrt{\pi}\Delta T/4}$ and $$\boldsymbol{f_l}\begin{cases} \mathbf{1}\ \boldsymbol{for}\ \boldsymbol{T > T_m} + {}^{\Delta T}/_{2} \\ \frac{T-(T_m-{}^{\Delta T}/_{2})}{\Delta T} \qquad \boldsymbol{for}\ \boldsymbol{T_m} + {}^{\Delta T}/_{2} \ge \boldsymbol{T} \ge \boldsymbol{T_m} - {}^{\Delta T}/_{2} \\ \mathbf{0}\ \boldsymbol{for}\ \boldsymbol{T < T_m} - {}^{\Delta T}/_{2} \end{cases}$$ $T_m$: melting temperature of silicon; *ΔT:* half-width of temperature transition; $h_f = f_l.L$, $L$ is the latent heat, $C_P$ the specific heat coefficient; *D (T):* Gaussian distribution function;<br>▪ Heat transfer in the solid: $$\frac{\boldsymbol{\partial}(\boldsymbol{\rho CpT})}{\boldsymbol{\partial t}} = \boldsymbol{\nabla}(\boldsymbol{\lambda \nabla T}) + \boldsymbol{Q_{elec}}$$ $$\boldsymbol{Q_{elec}} = \frac{\boldsymbol{J^2}}{\mathbf{2}\boldsymbol{\sigma_{elec}}};\quad \boldsymbol{Q_{rad}} = \boldsymbol{FA\sigma\epsilon}\left(\boldsymbol{T_1^4} - \boldsymbol{T_2^4}\right)$$ *F:* radiation configuration factor; σ = 5.67×10$^{-8}$ J/(s·m$^2$·K$^4$) is the Stefan-Boltzmann constant, *A:* the surface area of the object; *e*: the emissivity of the object; *J*: electric current; $\sigma_{elec}$: electric conductivity. |

The phase change domain consists of a silicon charge in cylindrical form of 12 cm in height and 5 cm in diameter. Different results are obtained, however, in this work the focus will be at first on the temperature field, for validation purposes of the thermal boundary conditions used in the experimental process, then a numerical investigation about the topology of magnetohydrodynamic filed resulting as well as its effect on the shape, instability and the advance of the solidification front (i.e. solid-liquid interface), will be presented.

**Table 2:** Thermo-physical properties of pure silicon

| ***Property*** | ***Symbol*** | ***Si solid*** | ***Si liquid*** | ***Unit*** |
|---|---|---|---|---|
| *Density* | $\rho$ | *2310* | *2560* | $Kg/m^3$ |
| *Specific heat,* | $C_p$ | *1032* | *1032* | $J\,kg^{-1}\,K^{-1}$ |
| *Latent heat* | $L$ | --- | *1400000* | *J/kg* |
| *thermal conductivity* | $k$ | *19* | *56.5* | $Wm^{-1}K^{-1}$ |
| *Dynamic viscosity* | $\mu$ | --- | $7.5\times10^{-4}$ | *Pa s* |
| *Electrical conductivity* | $\sigma$ | --- | $1.5385\times10^{6}$ | *S/m* |

## 3. Results and discussions

In the present work, we deal with solidification of silicon with a specific system cooling controlled by power down technique. More details about the experiment and related results can be found in [1, 8].

### 3.1.Treatment of experimental boundary conditions

It should be underlined that in the experiment temperature boundary conditions prior the solidification as well as cooling process during solidification are programmed and controlled via electrical resistor heaters in graphite. Moreover, due to the high melting temperature of the silicon, the experimental installation cannot provide the precise information needed for the boundary conditions (i.e. exact temperature profiles on the crucible and the silicon melt) for such full model, the entire furnace geometry was reproduced in the numerical model not only the solidification region. Fig. 2-a depicts a close-up view on the central region of the VB2 furnace, where the two graphite heaters and the insulating layers are highlighted. The approach for the numerical model validation was a direct comparison with experimental measurements.

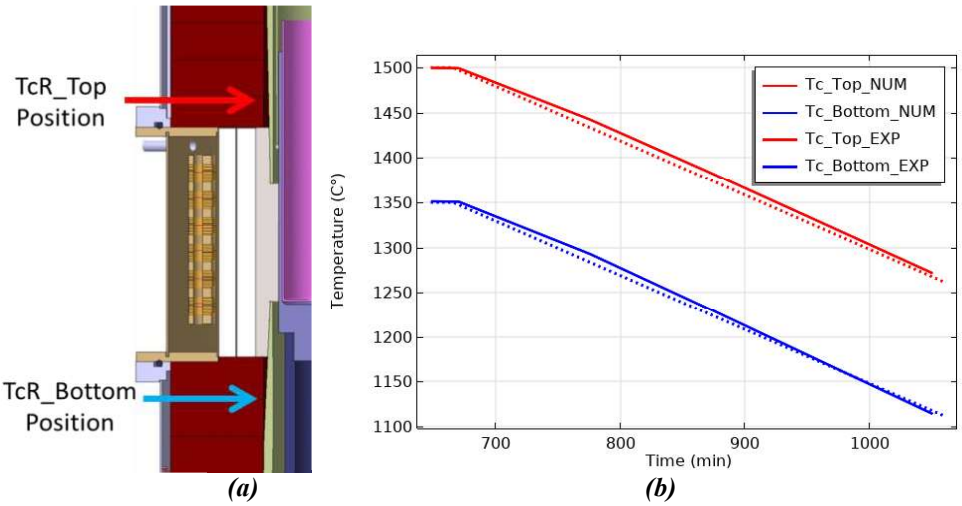


**Figure 2.** (a) Close-up view on the central part of the VB2 furnace with highlighted thermocouples positions, heaters and insulating layers; (b) Numerical and experimental results of temperatures of the two thermocouples TcR_Top and TcR_Bottom during solidification for a cooling rate of $10^{-2}$ K/s [1].

Using thermocouples attached to the graphite foam support at different heights, namely the temperatures of the two resistors (TcR_Top and TcR_Bottom), were measured. The measured temperatures and the simulated temperatures are compared in Fig. 2-b. The comparison is performed for a power supply of 155A and 145A in the resistors upper and down, respectively. In order to have a cooling rate of $10^{-2}$ K/s carefully controlled, a power down in current intensity of CI_bottom = $7\times10^{-4}$A/s for the bottom resistor and CI_Top = $45\times10^{-4}$A/s for upper resistor, was applied. The temperature difference between experimental and simulated values, at the thermocouples mentioned above, is more or less lower to 2.5K during the solidification stage, while the temperature distribution is almost similar. With this acceptable difference between experimental and simulated temperatures presented in Fig. 2-b, the numerical model is considered to be a close representation of the experimental furnace. Similarly for validation purposes, a full-scale Bitter coil (Fig. 3-a) was built to perform the electromagnetic calculation using Comsol Multiphysics$^{TM}$ software. Firstly, the radial component Br of the simulated travelling magnetic field along the central axis (R = 0 mm) without the crucible and silicon charge was numerically calculated and compared with experimental measurements, of which they are carried for three different values of the same three-phase power supply 400, 600 and 800 A.

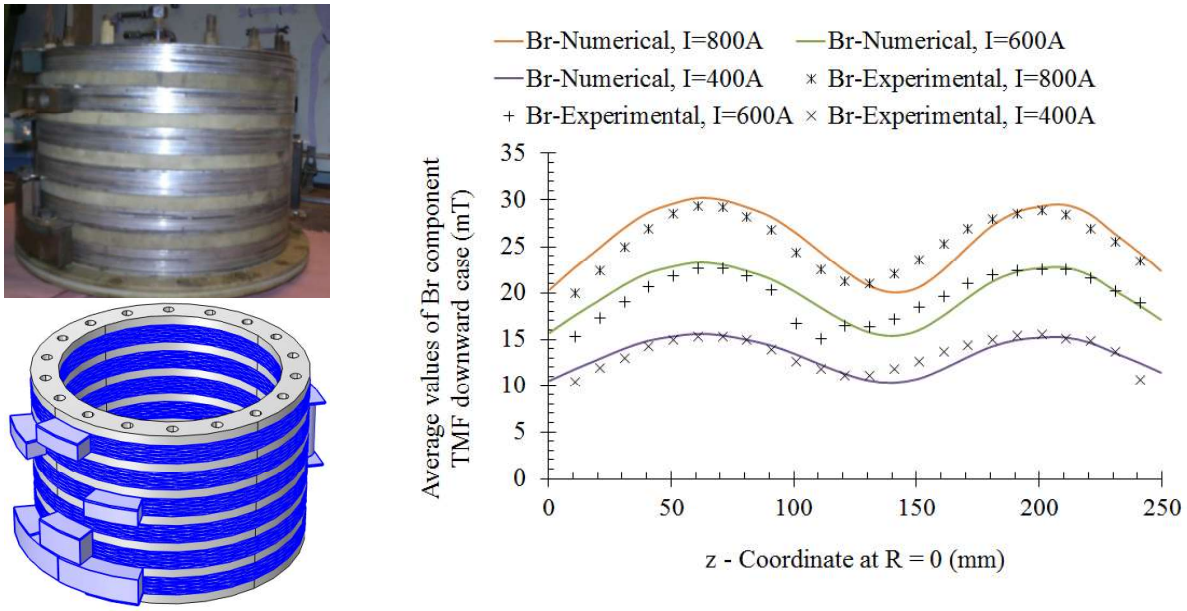


**Figure 3.** (a) Picture & schematic view of the Bitter coil; (b) Comparison of the measured and calculated values of the radial component Br in the absence of the silicon sample along the central axis (R = 0 mm) for downward TMF case for the same three-phase power supply: $I$ = 400, 600 and 800A and frequency $f_0$ = 50Hz.

The comparison for the downward TMF case is shown in Fig. 3-b. The superposition of the curves clearly shows the right consistency between the numerical results and those of the experimental measurements. Then the time-averaged $\langle \vec{F}_{LTZ} \rangle$ was calculated by solving Maxwell's equations, and the extracted value was implemented into the CFD calculation. It was then weighted by the corresponding liquid phase volume fraction ($f_l$), and used as a source term in the momentum conservation equations. Fig.4 presents the evolution of the Lorentz force magnitude averaged in time at different positions distributed on the azimuth plan at the level of the magnetic skin (δ = 1 mm). Demonstrative of numerical calculation of four positions in the azimuthal direction, namely P1, P2, P3 and P4, is shown in Fig. 4. The

results clearly illustrate that in both cases (TMF downward and upward); the vertical distribution of the Lorentz force is not identical from one position to another. However, there is some relative resemblance in the distribution of the Lorentz force between P2 and P4 for both cases. This behaviour may explain the presence of two loops almost symmetry in the plan YZ and consequently a concave or convex solidification front, depending on the direction of rotation of the silicon melt related to the applied TMF direction. Moreover, the significant difference in the Lorentz force intensity distribution between P1 and P3, explains the appearance of only one dominate vortex in XZ plan and therefore the inclined curved shape of the solidification front, which will be the subject of the next section.

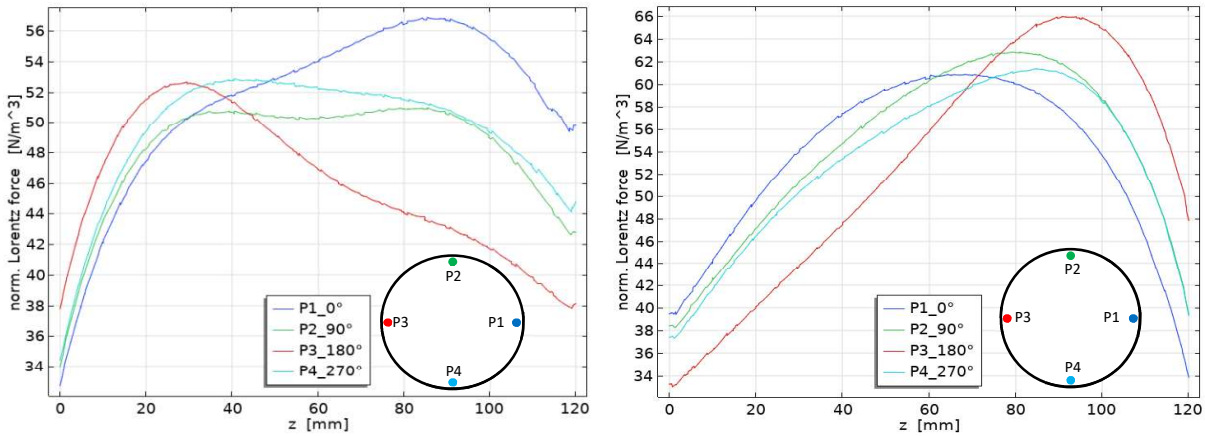


**Figure 4.** Vertical evolution of the Lorentz force density averaged in time $<F_{LTZ}>$ in the magnetic skin for current $I_1 = I_2 = I_3 = 200A$, (a) TMF Downward and (b) TMF Upward.

### 3.2.Effect of the TMF stirring on the solidification process

To illustrate the TMF induced flow and its effect on the solidification front of silicon; the solidification sequence was analyzed for 3D global geometry of the crucible and the meridian vertical plans (XZ and YZ). Two cases of TMF stirring are examined: downward and upward. Schematic views of the liquid flow pattern and solidification process are shown for the case of downward stirring in Fig. 5 and similarly for the case of upward stirring in Fig. 6, after one hour of the solidification beginning (t = 3600 s). As expected, the Reynolds number estimated for maximum velocities $Re= (U_{max}H^2/v.D)$, where the silicon melt velocity $U_{max}$ is equal to 3.4 cm/s for the case of downward and 2.9 cm/s for the case of upward, clearly indicated that the flow is likely turbulent. As preliminary results, the MHD flow generated by the Bitter coil significantly changes the usually expected axisymmetric torus-type MHD flow topology and results in a distinct 3D flow configuration. Indeed, Fig. 5-b and Fig. 6-b show that in the YZ plan the MHD flow configuration presents the possibility of two loops almost symmetry with opposite direction rotation. However, in the XZ plan (Fig. 5-c and Fig. 6-c); both cases illustrate the appearance of one principal predominant vortex in the crucible adjacent by a secondary small one. For more details about the configuration of the resulting MHD flow the reader can refer to our previous paper (Hiba et *al.* [7]).

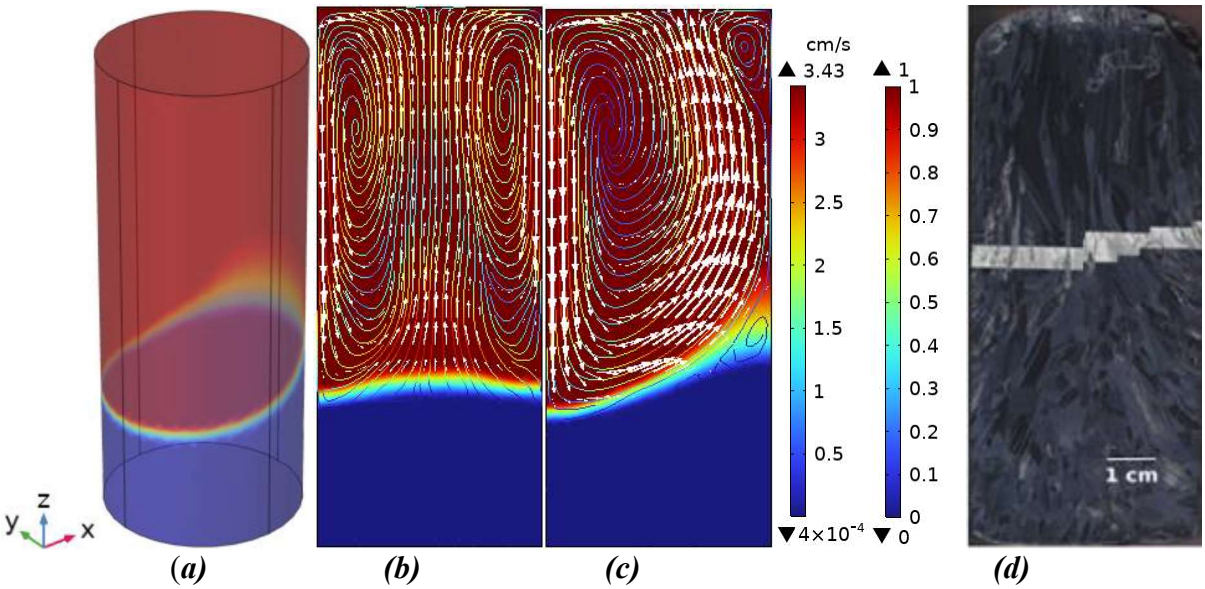


**Figure 5.** Schematic views of the MHD liquid flow pattern at a chosen instant (t = 1h): (a) 3D view; (b) YZ plan; (c) XZ plan and (d) the picture of the solidification front of the corresponding experiment ingot slice [8] with downward TMF stirring.

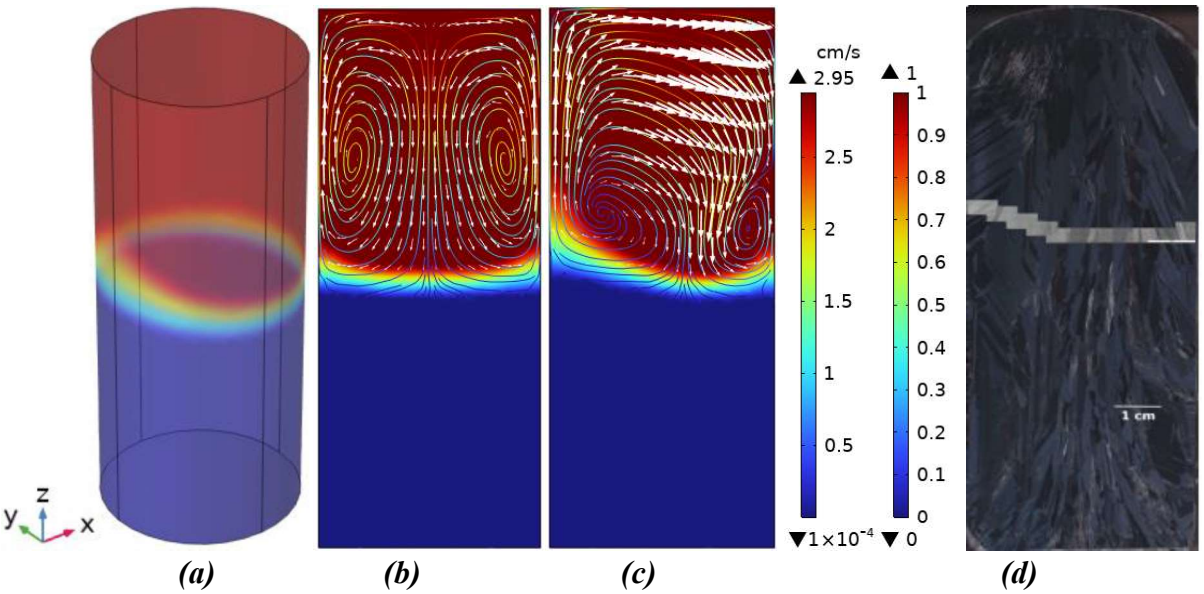


**Figure 6.** Schematic views of the MHD liquid flow pattern at a chosen instant (t = 1h): (a) 3D view; (b) YZ plan; (c) XZ plan and (d) the picture of the solidification front of the corresponding experiment ingot slice [8] with upward TMF stirring.

Fig. 5 and 6, also shows a comparison between the simulated solidification front and their corresponding experiments with the same configuration of TMF stirring. Satisfactory agreements between the measurements and simulation results are obtained. The solidification front marked on the silicon ingot slices presented in Fig. 5-d and 6-d, was performed by the Peltier electric solid-liquid front detection technique (M. Cablea et *al.* [5]). It is clear that the flow pattern in silicon melt significantly affects the shape of the solid-liquid interface and its advancement. Indeed, the solidification front after one hour of cooling presents a remarkable advance in case of upward stirring compared to the case of downward one. A concave and convex shape of the solid-liquid interface obtained by numerical simulation, as shown in Fig.

5-b and 6-b in YZ plan. However, the numerical results corresponding to the XZ plan presented in Fig. 5-c and 6-c, illustrate that the solid-liquid interface corresponds to a shape of curvature leaning on one side according to the MHD flow configuration. This form of curvature leaning on one side characterized the interface of solidification front in XZ plans are in good consistence with their corresponding experimental silicon ingot slices (Fig. 5-d and 6-d), for both cases of TMF stirring (i.e. TMF downward and TMF upward).

We can highlight some findings about the effect of the two different TMF stirring modes applied to the solidification process, particularly concerning the shape and the advancement of solidification front:

- The quasi-concave or convex shape located in the YZ plan for all modes of TMF stirring (downward and upward) is the direct consequence of the direction of rotation of the convective loop created by the electromagnetic stirring within the liquid phase;
- The relative dominance of the vortex located in the XZ plan is responsible for the curvature leaning on one side of the solidification front;
- The relative delay in the advancement of the solidification front for the downward TMF case compared to the upward one can be attributed also to the electromagnetic stirring that exerts two main effects. First, the Lorentz force in the case of downward TMF imposes consequently a downward movement on the hot currents which will homogenize the pool and lower the temperature gradients, thus creating unfavourable conditions for the advancement of the solidification front. Second, the hot flow transported by convection impinging the solid-liquid interface, under certain conditions can enhance the re-melting of this latter, which in turn may cause to the front delayed progress.

## Conclusions

Full 3D numerical multidisciplinary model of the vertical Bridgman 2 inches (VB2) furnace was numerically investigated and consolidated with experimental validations. The used model has shown its effectiveness in predicting the behaviour of the magnetohydrodynamic (MHD) flow, thermal field configuration, phase change phenomenon and solid-liquid interface shape and progression. Two configurations of travelling magnetic field (TMF) have been examined: downward and upward. Each TMF mode provides a specific configuration of electromagnetic forces lead to a particular hydrodynamic configuration in silicon melt. The simulated 3D model illustrated clearly that the MHD convection has a significant effect on the solid-liquid interface in terms of shape and symmetry. It was found that the geometric form of the solidification front does not exhibit a perfect concave or convex shape. In the light of this preliminary numerical investigation, we can conclude that the irregular shape of the solidification front according to the azimuthal direction is an indicative factor that could call into question of the control of the solidification process. We believe that the designed Bitter coil and the current electromagnetic parameters used in the VB2 furnace can certainly create an adequate MHD flow within the melt but remains ineffective to ensure carefully a controlled shape of the solid-liquid interface during the directional solidification process. For this purpose, it seems that the TMF apparatus needs a set of adjustments in terms of design and size, a particular electrical phase distribution and a different specific power supply for each phase, which will be a motivate perspective and an interesting subject of the next future study.

## References

[1] M. Cablea, (2015). Numerical and experimental studies of magnetic field effects on solidification of metallurgical silicon for photovoltaic applications. Ph.D. thesis, Grenoble University, France.

[2] T. Yoshikawa, K. Morita. (2009). Refining of silicon during its solidification from a Si-Al melt. Journal of Crystal Growth, Vol. (311), p776-779.

[3] N. Dropka, I. Buchovska, U. Degenhardt, Frank M. Kiessling, B. (2020). Influence of impurities from SiC and TiC crucible cover on directionally solidified silicon. Journal of Crystal Growth, Vol. (542), 125692.

[4] K. Zaïdat, N. Mangelinck-Noël, R. Moreau. (2007). Control of melt convection by a travelling magnetic field during the directional solidification of Al-Ni alloys, C. R. Mecanique, Vol. 335 (7-8), pp. 330–335.

[5] M. Cablea, K. Zaidat, A. Gagnoud, Ab. Nouri and Y. Delannoy. (2014). Directional solidification of silicon under the influence of travelling magnetic field. J. Crystal Growth, vol. 401, pp883.

[6] B. Hiba, Ab. Nouri, L. Hachani and K. Zaidat. (2022). 3D numerical simulation with experimental validation of a traveling magnetic field stirring generated by a Bitter coil for silicon directional solidification process, 2022 IOP Conf. Ser.: Mater. Sci. Eng. 1223 012001.

[7] B. Hiba, Ab. Nouri, L. Hachani and K. Zaidat. (2022). Analysis of the symmetry of 3D silicon melts flow generated by a Bitter travelling magnetic field in a cylindrical crucible, Magnetohydrodynamics, vol. 58, pp397-408.

[8] M. Cablea, K. Zaidat, A. Gagnoud, Ab. Nouri, G. Chichignoud and Y. Delannoy.( 2015). Multi-crystalline silicon solidification under controlled forced convection. J. Crystal Growth, vol. 417, pp44.

# Pulsed Electromagnetic Field Effects on Dendritic Solidification in a Thin Cell

Natalia Shevchenko[1]*, Qingwei Bai[1,2], Andrew Kao[3], Sven Eckert[1]

1. Helmholtz-Zentrum Dresden-Rossendorf, Germany
2. TU Dresden, Germany
3. Centre for Numerical Modelling and Process Analysis, University of Greenwich, UK

*n.shevchenko@hzdr.de

**Abstract:** This study aims to investigate how pulsed electromagnetic fields (PEMF) can affect grain refinement and microstructure during the solidification of a model Ga-In alloy. The magnetic system used generates field intensities of 8 - 11 mT and frequencies in the domain between 10 and 300 Hz, a duty cycle of 50%. We record the dendritic structures at the end of solidification experiments after switching OFF the electromagnetic field via X-ray radiographic imaging. Preliminary lab-scale results show that the solidification under frequencies above 100 Hz leads to dendrite fragmentation and solute redistribution in the mushy zone. No evidence of a CET is observed despite numerous fragmentation events. The fragments that detached from the dendritic network were unable to grow as equiaxed dendrites in the liquid as they became trapped within the dendritic network.

**Keywords:** Solidification; X-ray radiography; Dendrite fragmentation; Ga - In alloys; Pulsed electromagnetic fields

## Introduction

Fine crystalline grain sizes significantly enhance the mechanical properties of industrial alloys, making it essential to understand the mechanisms involved in grain refinement. In the last two decades, many studies demonstrate that applying electromagnetic methods during solidification can lead to the formation of homogeneous, fine-grained, globular structures (see e.g. [1-2]). Electromagnetic grain refinement methods are based on using externally applied fields to exert a force on the liquid, either directly by stirring [2] or indirectly by using an electromagnetic field [3]. The moving fluid interacts with the dendrite network, resulting in break up into fragments and/or destabilization of growth conditions, resulting in dendrite fragmentation [4]. For instance, the use of rotating magnetic fields during the solidification of Pb-Sn alloys refines both columnar and equiaxed grains [2].

Electromagnetic vibrations are also effective in refining the microstructure of bulk materials without the need for inoculants [5]. The optimal frequency range for structural refinement of metallic materials falls between 150 Hz and 500 Hz [5], suggesting the presence of additional mechanisms at higher frequencies.

However, despite existing theoretical and experimental studies, a comprehensive understanding of the involved mechanisms remains incomplete. Liotti et al. [4] suggested an underlying mechanism for fragmentation under a PEMF based on the induced movement of solute-rich inter-dendritic liquid, which breaks local solid–liquid interfacial equilibrium and destabilizes the solid phase. Nonetheless, this mechanism may not apply to high-frequency processes.

To address these research gaps, a joint theoretical and experimental programme (HZDR, University of Greenwich and Technical University Dresden) using synchrotron radiation was designed to understand how the application of a pulsed electromagnetic field (PEMF) could

control fine-grain structure formation. We focus on model experiments on laboratory scale, which simplifies the problems and generates more information about physical mechanisms. In an X-ray lab-scale and synchrotron experiments, the model alloy system Ga-In is used that has similar characteristics to industrial alloys, but is liquid at room temperature and so easier to handle. The first step of our research program is to develop and to test the setup of the model solidification experiment for studying the effect of a pulsed electromagnetic field on dendrite fragmentation and grain refinement. This paper concerns the X-ray radiography study of solidification of the Ga-In alloy under PEMF at different frequency ranges.

**Experimental**

Solidification experiments were performed at Helmholtz-Zentrum Dresden-Rossendorf (HZDR). The solidification cell (Fig. 1a) was already employed in previous radiographic investigations carried out by means of a microfocus X-ray tube and was described in detail elsewhere [6]. The nominal composition of the Ga - 25 wt%In alloy was prepared from 99.99% Ga and 99.99% In. The alloy was melted and filled into a Hele-Shaw cell with a liquid metal volume of $30 \times 30 \times 0.15$ mm$^3$. Synchronised power of both Peltier elements allows the cooling rate and the thermal gradient to be controlled. The temperature gradient was 2 K/mm, the cooling rate was 0.02 K/s. The solidification cell was positioned near the edge of the electromagnetic coil as shown in Fig. 1b. The geometric center of the solidification unit coincided with the axis of the coil. This arrangement can produce magnetic fields perpendicular to the sample surface. The distance between the cell and the coil cover was 30 mm as illustrated in Figure 1b.

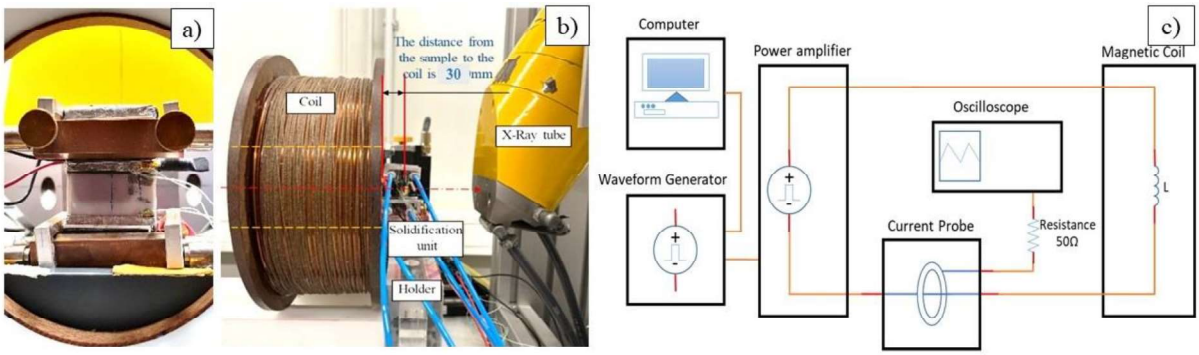


Figure 1. (a) a solidification cell, (b) the experimental setup and (c) a scheme of the pulse electromagnetic field system.

The main parameters of the coil are: 314 windings with Ø 3.5 mm copper wire surrounded by insulation, DC resistance of 0.31 Ω, inductance of 17.1 mH (at a frequency of 100 Hz), the outer coil diameter of Ø 230 mm (Ø 275 mm), a coil length of 87 mm (103 mm), the value in parentheses indicates the coil sizes with the insulation cover. The diameter of the hole at the center of the coil is Ø 90mm. Figure 1c displays a scheme of the pulsed electromagnetic field system. To generate the input current for the coil, the waveform generator (Agilent 33220A) controlled the power amplifier (HERO®POWER PA2024). The magnetic flux density was measured with the Hall Effect Gaussmeter (Lake Shore®460). The current was measured by a current probe (Tektronix® TCPA300 amplifier and TCP303 probes) and the data was transmitted to an oscilloscope (Tektronix® TDS210).

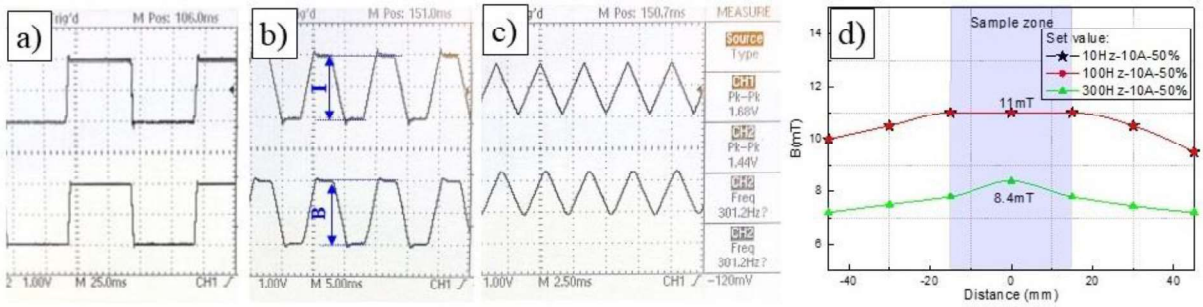


Figure 2. Waveforms of current (channel 1) and magnetic flux density (channel 2) (a) 10Hz-10A-50%；(b) 100Hz-10A-50%；(c） 300Hz-10A-50%; (d) magnetic field distributions along a central lateral line of the solidification cell.

Fig. 2(a-c) shows the current and magnetic flux density waveforms measured under the set parameters. The input current adjustments are all in square waveform. The peak current setting and the peak magnetic flux density are indicated by I and B, respectively, see Fig. 2b. The actual waveform changes after passing through the coil due to the inductance effect, and the higher the frequency, the more significant the waveform changes. A good square waveform is maintained at 10 Hz, while at 300 Hz it becomes almost a triangular waveform. The waveform of flux density is similar to that of the input current.

Fig. 2d shows the magnetic flux density distribution along a central lateral line of the solidification cell. The magnetic flux density at 10 Hz-10 A-50% and 100 Hz-10 A-50% shows a similar value and distribution. The magnetic field is non-uniform in the sample size zone at 300 Hz, while at 10 Hz and 100 Hz it can be considered as a uniform magnetic field in the lateral direction. Since the sample is thin enough, it can also be viewed as a uniform magnetic field in the axial direction.

**Numerical study scheme**

The numerical study comprises the two phases. A macroscale model of the pulsed magnetic field is currently being developed by using COMSOL. The geometry of the solidification experiment and the parameters of an electromagnetic coil are included to predict the spatial and temporal force distribution within the thin sample along with characteristic macroscale fluid flow fields. The model coil and sample configuration and the first simulation results are shown in Figure 3. The pulsed magnetic flux density waveform displayed by the oscilloscope and the simulation results agree well. The magnetic flux density distribution along a coil axis at DC and 100 Hz-10 A-50% is compared and the model is considered credible. The eddy currents and Lorentz forces caused have their maximum at the edge of the sample.

These force distributions will then be implement them into numerical code Thermo Electric Solidification Algorithm (TESA). This parallelized microstructure solidification code that includes the effects of convection to predict how microstructure evolution is altered. TESA has been validated and applied to various similar systems, including a study of channel formation in Ga-25 wt%In alloy [7] and Thermoelectric Magnetohydrodynamic effects [8].

A systematic parametric study of key dependent variables, a pulse frequency, a pulse length, solidification variables (i.e. thermal gradients, cooling rates etc.) will be conducted to identify those that have the most significant effect on the microstructure.

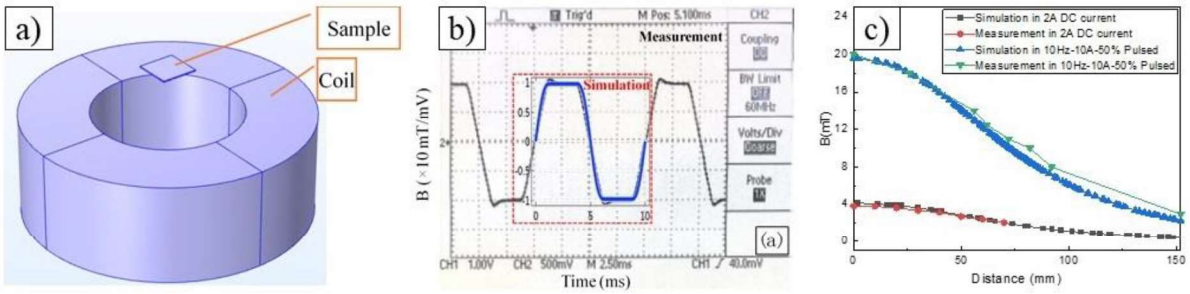


Figure 3. (a) The model coil and the sample; (b)-(c) experimental and simulation results of magnetic flux density distribution: (b) pulsed magnetic flux density waveform, (c) distribution along a coil axis.

**Results and discussion**

The Ga–25wt%In alloy was solidified directionally in vertical direction from the bottom of the solidification cell. In this experimental endeavor, we performed several solidification cycles under identical thermal boundary conditions with and without PEMF. Ga-25wt%In is a hypereutectic alloy. This means that during solidification, the growing dendrites are formed of the primary In phase, and Ga solute is rejected into the interdendritic and bulk liquids. Figure 4a shows the dendritic structures at the end of solidification experiments in the presence of natural convection (without PEMF). The dark dendrites correspond to the primary In crystals which grow from the bottom of the cell. Plume-like flow pattern above the mushy zone can be observed. The plume flow pattern was considered in more detail in the works [6].

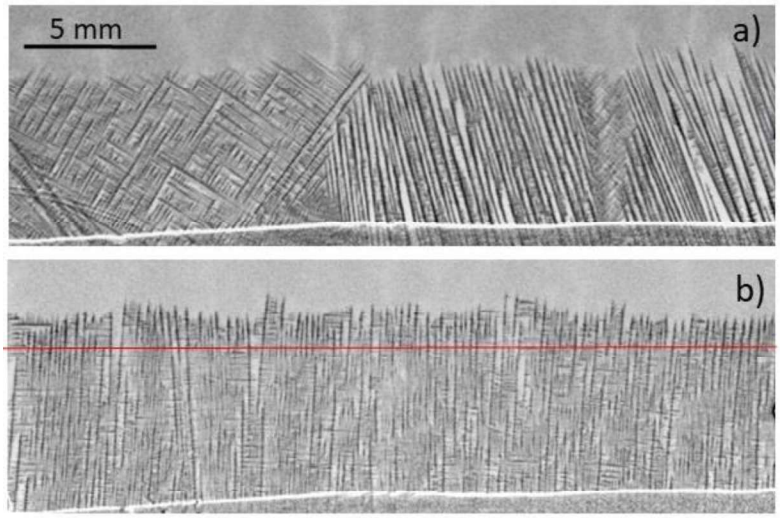


Figure 4. The dendritic structures at the end of solidification experiments (T = 0°C): (a) without PEMF and (b) under PEMF at a frequency of 300 Hz: In the cases of PEMF the images recorded after 360 sec of switching off of the PEMF. A red line indicates the time when the PEMF was switched off. The microstructure below the red line was formed under PEMF; the microstructure above the red line was captured after PEMF switching off.

The lab-source based in situ experiments with the PEMF have been impossible, due to the interaction of the electromagnetic field with an electron beam of the lab X-ray source. It is only possible to record the dendritic structures at the end of solidification experiments after switching OFF the electromagnetic field (Fig. 4b). The structure of the dendrites grown under PEMF becomes finer and more irregular. There is a tendency to reduce the distance between the primary branches and their diameter. Some areas of the dendritic structure appear blurred

and unclear due to insufficient spatial resolution of X-ray images. After turning off the magnetic field, the dendritic layer becomes dense and more contrasting, indicating an increase in solid fraction.

Image processing was performed using ImageJ to make the changes in the dendritic morphology more visible. The processed image was calculated using the absolute difference operator by ImageJ: (processed_image =|image(time@step) – reference_image|) where a reference image is fully liquid state. After data processing white color patterns are dendrites and dark grey areas are liquid phase (Figure 5).

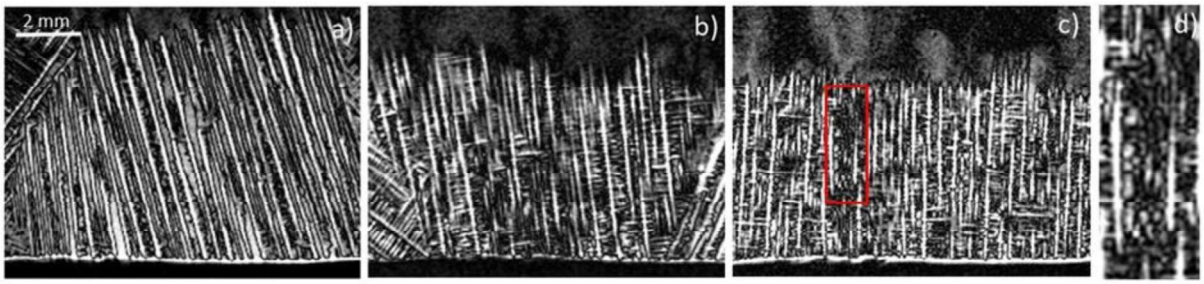


Figure 5. (a) Dendrite structure of selected FOI (Field Of Interest) after image processing of samples: (a) without PEMF and (b) – (c) under pulsed EMF at different frequencies: b) 100 Hz, c) 300 Hz; (d) close-up of the red rectangle area in (c). After data processing: white colour – dendrites; dark grey – liquid phase.

Despite low resolution of images, the data processing shows that the blurred areas in original radiographs contain small fragments of dendrites (Fig 5d). A tendency of increasing number and areas of such fragmented zones can be observed due to increasing of frequency of the PEMF from 100 to 300 Hz.

Probably there is difference in fragmentation process between 100 Hz and 300 Hz treated samples. In the case of 100 Hz PEMF the detachment of dendrite secondary arms in local zones could be observed (Fig. 5b). Besides fragmentation of secondary arms, the primary dendrites are shorter and not perfectly aligned in the grain after solidification under PEMF at 300 Hz (Fig. 5c). Analysis of dendrite length distributions in the reference sample (without PEMF) and in the 300 Hz PEMF solidified sample showed that, the number of dendrites with a length less than 1 mm doubled after PEMF solidification. The phenomenon could be explained by the following two reasons: (i) the growth of dendrites is blocked by secondary arms of neighbor dendrites; (ii) fragmentation of primary dendrite arm occurs.

One possible interpretation of the high fragmentation rates under PEMF involves an increased accumulation of solute ahead of the growing dendrite front and in the inter-dendritic regions due to damping the movement of the plume. PEMF interacts on the rising plumes resulting in eddy current. According to Lenz's law, eddy currents flow inside the conductor along such paths and directions that their effect is as strong as possible to resist the cause that causes them. Consequently, plumes, which act as good conductors, experience a braking force due to the interaction of eddy currents with the magnetic field. Damping of the movement of the plumes leads to the progressive build-up of solute in the inter-dendritic regions and in the boundary layer. Although the underlying mechanism cannot be established from these laboratory experiments, the experiment was designed so that it can easily be migrated to a source where the electromagnetic field does not interfere, such as an X-ray synchrotron. Our previous synchrotron radiography experiments under the similar conditions with the same alloy have already shown [8] that solute redistribution effects can be captured and are primarily

responsible for fragmentation in experiments. The results obtained here with a pulsed magnetic field are consistent with microstructure observations in the literature [4] and with in situ imaging, further details of the mechanism will become clear.

For a more comprehensive understanding of the interplay between melt flow, dendritic growth, and PEMF effects, further in situ experiments and numerical studies of the flow field, solute distribution, and temperature are necessary.

**Conclusions**

A setup of the model solidification experiment for studying the effect of a pulsed electromagnetic field on dendrite fragmentation and grain refinement based on X-ray imaging has been developed. This setup makes it possible to study the effect of a PEMF over a wide frequency range from 10 to 300 Hz and with different pulse shapes. The application of a 100 Hz and 300 Hz pulsed electromagnetic field to an array of indium dendrites in the Ga-In alloy led to fragmentation and grain refinement. The lab-source based experiment will be adapted to the in situ synchrotron experiment at Diamond. In situ synchrotron experiments allow us to resolve the complex dynamics of grain refinement and simultaneously show how local conditions as well as large-scale flow fields may alter them. The model with the same setup as the experiment will be validated by direct comparison with qualitative and quantitative analysis of the collected in situ data. The validated model will in turn be applied to predict flow, which is critical for understanding the grain multiplication control mechanisms.

**Acknowledgments**

Dr. Q. Bai was funded by the German Academic Exchange Service (DAAD).

**References**

[1] Eckert, S., Nikrityuk, P. A., Willers, B., Räbiger, D., Shevchenko, N., Neumann-Heyme, H., Travnikov, V., Odenbach, S., Voigt, A., Eckert, K. (2013). Electromagnetic melt flow control during solidification of metallic alloys. Eur. Phys. J. Spec. Top. 220, 123-138.

[2] Willers, B., Eckert, S., Michel, U., Haase, I., Zouhar, G. (2005). The columnar-to-equiaxed transition in Pb-Sn alloys affected by electromagnetically driven convection. Mater. Sci. Eng. A 402, 55–65.

[3] Davidson, P. A., (1999). Magnetohydrodynamics in materials processing. Ann. Rev. Fluid. Mech., 31, 273-300.

[4] Liotti, E., Lui, A., Vincent, R., Kumar, S., Guo, Z., Connolley, T., Dolbnya, I.P., Hart, M., Arnberg, L., Mathiesen, R.H., Grant P.S. (2014). A synchrotron X-ray radiography study of dendrite fragmentation induced by a pulsed electromagnetic field in an Al–15Cu alloy. Acta Materialia, 70, 228-239

[5] Mizutani, Y., Tamura, T., Miwa, K. (2007). Effect of Electromagnetic Vibration Frequency and Temperature Gradient on Grain Refinement of Pure Aluminium Transactions. Materials, Vol. 48, No. 3, 538-543

[6] Shevchenko, N., Roshchupkina, O., Sokolova, O., Eckert, S. (2015). The effect of natural and forced melt convection on dendritic solidification in Ga–In alloys. Journal of Crystal Growth, 417, 1-8

[7] Kao A., Shevchenko N., Alexandrakis M., Krastins I., Eckert S., Pericleous K. (2019). Thermal dependence of large-scale freckle defect formation. Phil. Trans. R. Soc. A., 377, 20180206

[8] Fan, X., Shevchenko, N., Tonry, C., Clark, S. J., Atwood, R.C., Eckert, S., Pericleous, K., Lee, P. D., Kao, A. (2023). Controlling solute channel formation using magnetic fields. Acta Materialia, 256, 119107

**Title: Incorporating Interdependent Structural Mechanical Mechanisms into Modelling Three-Dimensional Microstructure Solidification**

Authors: Dr. Peter Soar, Dr. Andrew Kao & Prof. Koulis Pericleous

Abstract: The solidification of dendritic microstructures is a complex process that can be significantly altered by interaction with underlying structural mechanical phenomena. Experimental results have demonstrated that dendrites can bend or twist significantly, which can act as a key factor in the formation of defects in cast parts such as stray grains and slivers. Despite the importance of these mechanical effects, they are often neglected when modelling the microstructure solidification process, with existing attempts generally being limited to twodimensional models which ignore a wide variety of complex deformation behaviours required to accurately capture the formation of many solidification defects. To allow accurate simulation of problems such as these a three-dimensional Finite Volume Structural Mechanics Solver has been developed which uses displacements to alter the preferential growth orientation of the dendrites. This novel approach intimately couples structural mechanics to microstructure solidification within a larger modelling framework also capable of simulating fluid flow and electromagnetism, allowing for a more accurate simulation of the complex interplay between different physical processes when modelling solidification phenomena. Example simulations have been conducted to investigate these fundamental mechanisms that can lead to the formation of casting defects, which were then compared to observed experimental results.

# 300 mm Silicon Mono Czochralski Crystals: Parameters and Conditions for Crystal Growth

Frank Zobel, Peter Dold,

*Fraunhofer Center for Silicon Photovoltaics CSP, Otto Eißfeldt-Str. 12, 06120 Halle,*
*Frank.zobel@csp.fraunhofer.de*

Keywords: Silicon, Solar, Czochralski, Crystal Growth

Growing 300mm silicon mono ingots for solar applications poses several challenges. Due to economic reasons, a magnet is not available at the crystal puller, yet fast crystallization is required without compromising the yield. The process window for growth conditions and control parameters is narrow and requires precise examination.

Several 300mm experiments were conducted at the Fraunhofer CSP, and the results will be presented, showcasing the current state of process development. The findings reveal a significant correlation between stable growth conditions, process parameters, shoulder growth, control parameters and the process yield.

A scientific and methodological approach can be used to optimize these parameters, which can be further addressed through 3D Multiphysics simulations.

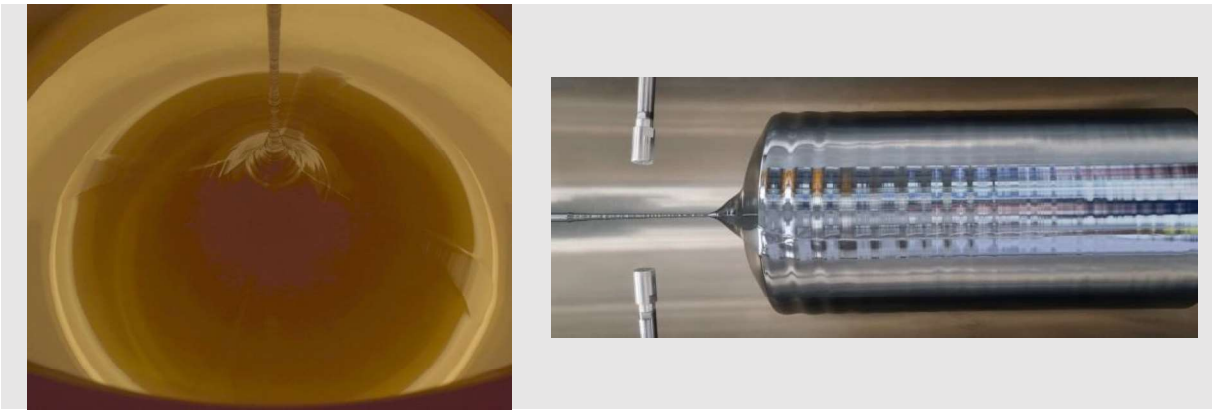

*Figure 1: Growth of a 300 mm Crystal at the Fraunhofer CSP. Shoulder growth (left) and 300 mm crystal (right)*

# Surface deformations of liquid metal flow in porous media in external uniform magnetic field

**D. Berenis*, I. Grants, L. Buligins**

Institute of Physics, University of Latvia, Miera iela 32, LV-2169, Salaspils, Latvia

***Corresponding author e-mail:** didzis.berenis@lu.lv

**Topic**: EM shaping

## ABSTRACT

Direct numerical simulation of liquid metal flow in external uniform magnetic field was performed for the cases of three and six cells, which are assumed to be part of a porous material. Free-surface deformations were studied in terms of external magnetic field direction and strength, as well as, in terms of pressure drop, which was applied perpendicular to the direction of gravitation. Numerical results showed that magnetic field in the direction of pressure drop is the most effective to decrease the height difference between the inlet and outlet. In contrast, magnetic field direction perpendicular to pressure drop and gravitation produced the largest height difference.

**Keywords**: liquid metals, free-surface, MHD, plasma facing components, fusion reactors

## INTRODUCTION

Due to the very harsh conditions that the plasma facing components (PFCs) must endure in magnetic fusion reactors, a proposition has been made to introduce liquid metal (LM) free-surface layer [1]. The LM layer could potentially be introduced and supported by utilizing porous materials [2]. Additionally, magnetic fields via the Lorentz force could stabilize and shape the LM surface [3]. An important part of using LMs for the PFCs is to maintain a LM layer, which would mitigate the damage to the solid components of the walls [1]. On the other hand, high LM velocities should be maintained to decrease the LM exposure time and thus, limit the plasma contamination [1]. At the same time, surface instabilities should be minimized to avoid splashing of LM droplets in the plasma [4]. Numerical studies of LM PFCs often use porous media modelling techniques to study the global characteristics of PFCs [2,4]. Instead, in this study we have performed direct numerical simulation to investigate the LM free-surface flow around individual cells in external magnetic field. The current study on the scale of porous cells advances the general knowledge of the system and could be beneficial for deciding, which direction of the magnetic field relative to the LM velocity and gravitation direction is preferable to maintain the desirable LM free-surface conditions.

## FORMULATION AND METHODS

CFD calculations were performed with OpenFOAM software (https://openfoam.org/ ). A structured mesh, where each cell consisted of 40 thousand volume elements, was prepared (Fig.1). Boundary conditions (BCs) of inlet, outlet and top boundaries where set to inlet-outlet. Bottom and side boundaries where set to slip and pore walls to no-slip BCs.

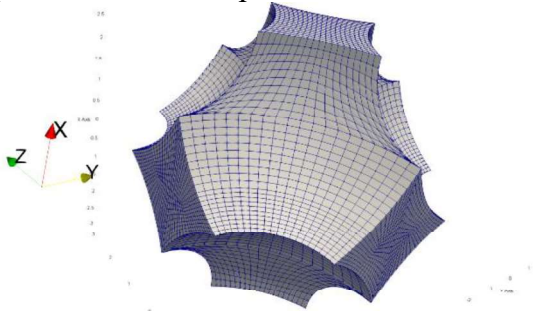


**Figure 1.** Mesh for one cell of a porous material used for OpenFOAM calculations.

The system parameters are shown in Table 1. Electromagnetics modelling was performed with ElmerFEM software, (http://www.elmerfem.org/ ) together with EOF-Library [5], which works as communication between OpenFOAM and ElmerFEM. By default, in EOF-Library the electromagnetics are set to be updated whenever the maximum relative velocity change in a volume element exceeds 50%. However, for this setup it was found to produce non-physical results, so the parameter was decreased to 5%. Surface tension was set to zero to decrease the computational difficulty of the study. Physically this represents a system where Weber number >> 1 and this requirement was sufficiently fulfilled in the model setup.

| **Parameter** | **Symbol** | **Value** |
|---|---|---|
| Liquid phase viscosity | $\nu_{liqm}$ | $3.35 \times 10^{-7}$ m$^2$/s |
| Liquid phase density | $\rho_{liqm}$ | 6400 kg/m$^3$ |
| Gaseous phase viscosity | $\nu_{air}$ | $1.51 \times 10^{-5}$ m$^2$/s |
| Gaseous phase density | $\rho_{air}$ | 1.420 kg/m$^3$ |
| Surface tension | $\gamma$ | 0 N/m |
| Electrical conductivity of the liquid | $\sigma$ | $3.27 \times 10^{6}$ S/m |
| Free fall acceleration | $\boldsymbol{g}$ | $(-9.81, 0, 0)$ m/s$^2$ |
| Characteristic length | $L$ | $8.66 \times 10^{-5}$ m |
| Cell side length | - | $5.4 \times 10^{-4}$ m |

Table 1. Geometrical and material parameters.

For the result presentation, the length, velocity, pressure, and flow rate were scaled according to $L$, $L^2/\nu_{liqm}$, $\rho_{liqm}{\nu_{liqm}}^2/L^2$, and $L^4/\nu_{liqm}$, respectively. The Reynolds number (Re) was defined as the maximum dimensionless velocity in the liquid phase. A set of external magnetic fields B = [0, 1, 2, 3, 4] T were used in the parametric calculation, corresponding to Hartmann numbers Ha = [0, 3.38, 6.76, 10.15, 13.53], respectively. Dimensionless pressure, P, was set at the inlet in the range P = [13:535].

## RESULTS

Initially a steady-state calculation was performed for single-phase setup without the external magnetic field (Fig.2a, Fig.3a). Next, steady-state single-phase calculation was performed with the external magnetic field in x-direction, y- direction, and z- direction (Fig.2b-d, Fig.3b-d).

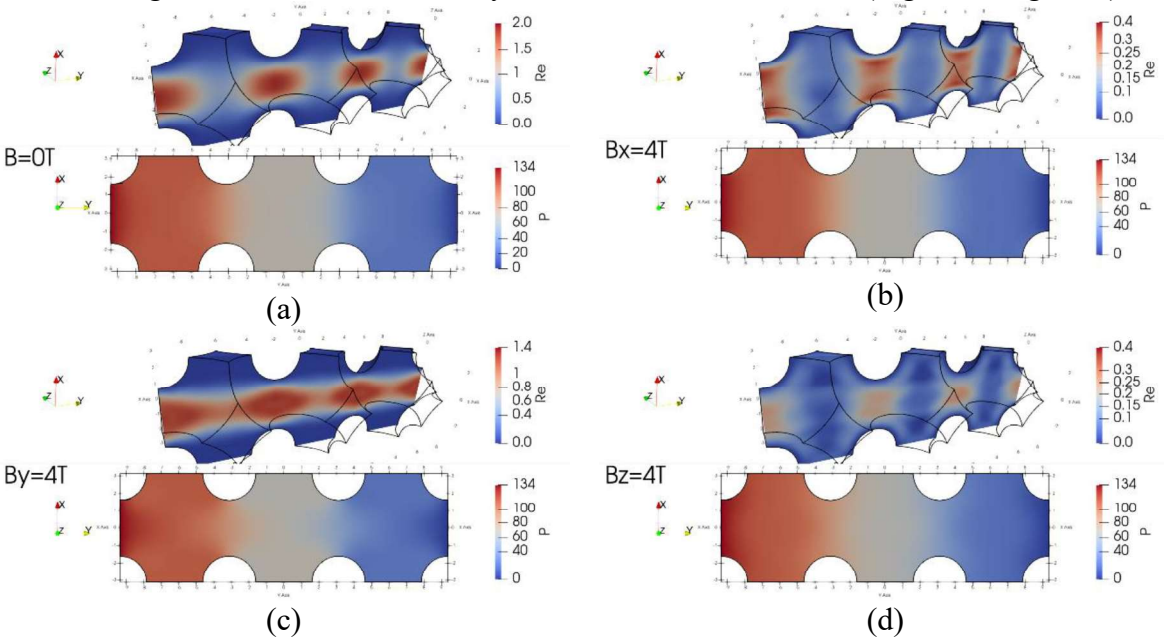

**Figure 2.** Dimensionless velocity and pressure distribution for one-phase steady-state simulation with inlet-outlet pressure drop P=134.

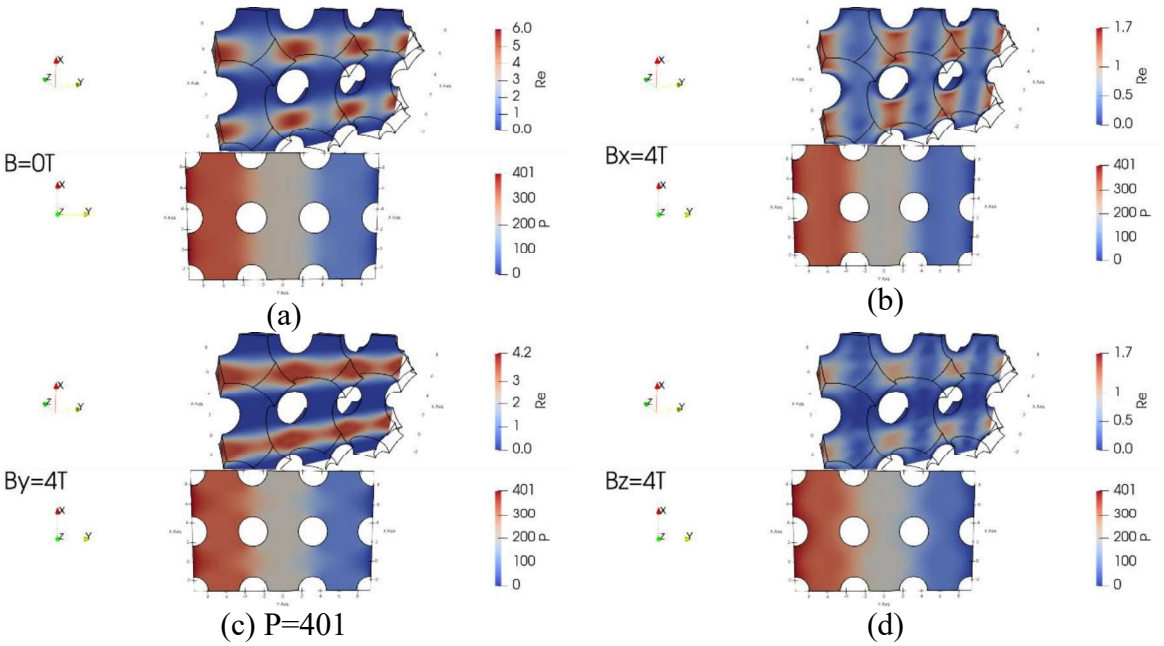


**Figure 3.** Dimensionless velocity and pressure distribution for one-phase steady-state simulation with inlet-outlet pressure drop P=401.

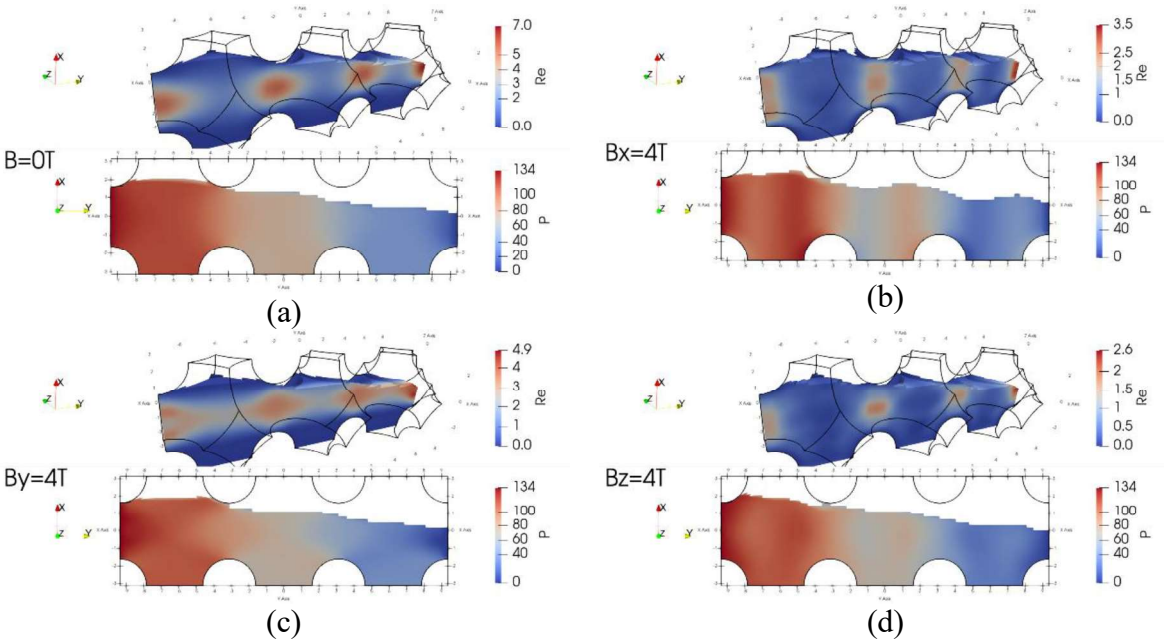


**Figure 4.** Dimensionless velocity and pressure distribution for two-phase transient simulation with inlet-outlet pressure drop P=134.

In the two-phase transient simulation with one row (three cell) geometry (Fig.4) a set of pressures P = [13,67,134] were used for parametric calculation. For the two row (six cell) geometry (Fig.5-7) a set of dimensionless pressures P = [200,267,334,401,468,535] were used. Comparing two-phase with one-phase simulation results, it can be seen that the effect of introducing magnetic field is similar in terms of velocity distribution in the liquid phase. However, in the two-phase simulation the maximum velocity is increased due to the height difference between inlet and outlet.

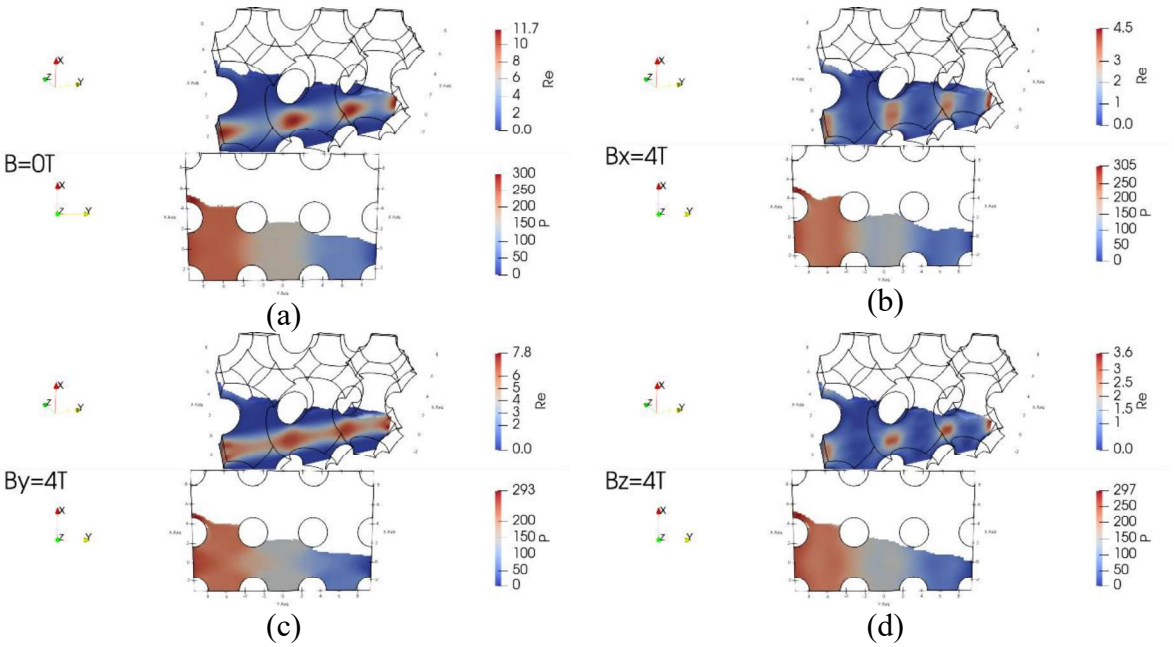


**Figure 5.** Dimensionless velocity and pressure distribution for two-phase transient simulation with inlet-outlet pressure drop P=267.

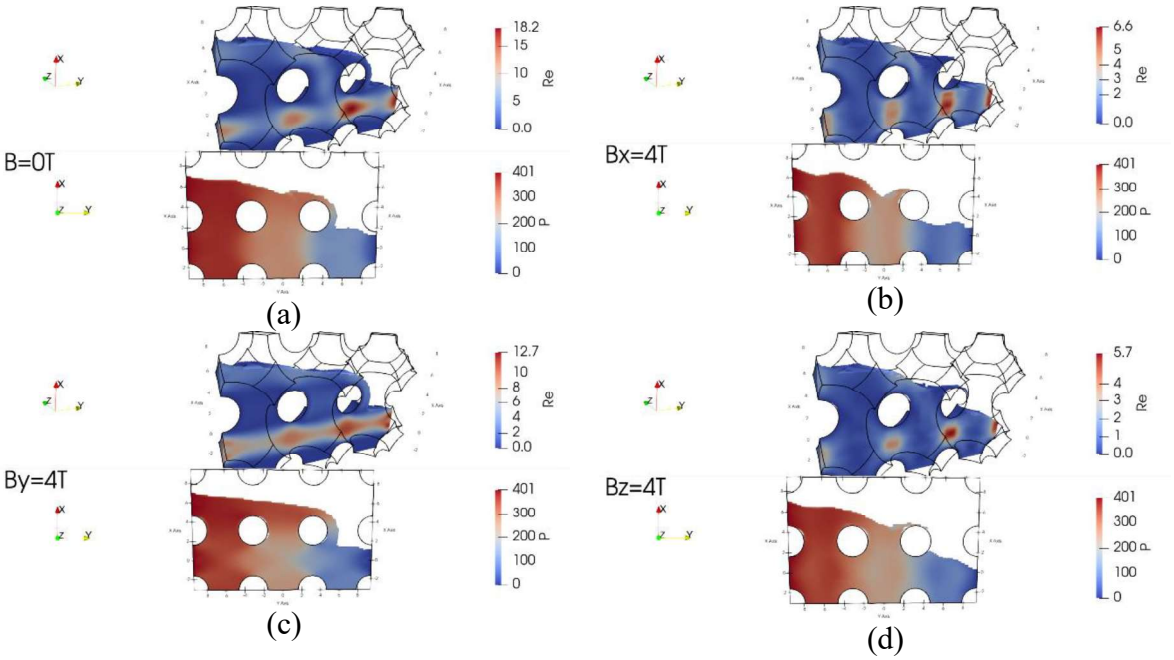


**Figure 6.** Dimensionless velocity and pressure distribution for two-phase transient simulation with inlet-outlet pressure drop P=401.

Applying magnetic field in the direction of the main flow (Fig.4c, Fig.5c, Fig.6c, Fig.7c) results in a surface profile, which is similar to the case without external magnetic field (Fig.4a, Fig.5a, Fig.6a, Fig.7a). On the other hand, applying magnetic field perpendicular to the main flow direction (Fig.4b,d, Fig.5b,d, Fig.6b,d, Fig.7b,d) results in a different surface deformations, where more of the solid walls are uncovered.

In Fig. 8 we have compared flowrate vs. pressure drop curves between one-phase steady-state simulations (Fig. 8a) and two-phase transient simulations (Fig. 8b). Here, flowrate is calculated to the equivalent for two-row geometry. In steady-state simulations the magnetic field in the flow direction (y-direction) affects flowrate the least. External magnetic fields in the perpendicular direction to the flow (x-direction and z-direction) affect the flow by the same amount.

In two-phase transient simulations (Fig. 8b) there seems to be a different tendency for the smallest pressures. This could be due to the different geometries that were used for smaller pressures (one row with three cells) and for larger pressures (two rows with 6 cells). Gravity in this setup is in the negative x-direction, so magnetic field perpendicular to the gravitation (in the z-direction) has more braking effect on the flow than magnetic field in the direction of gravitation (x-direction).

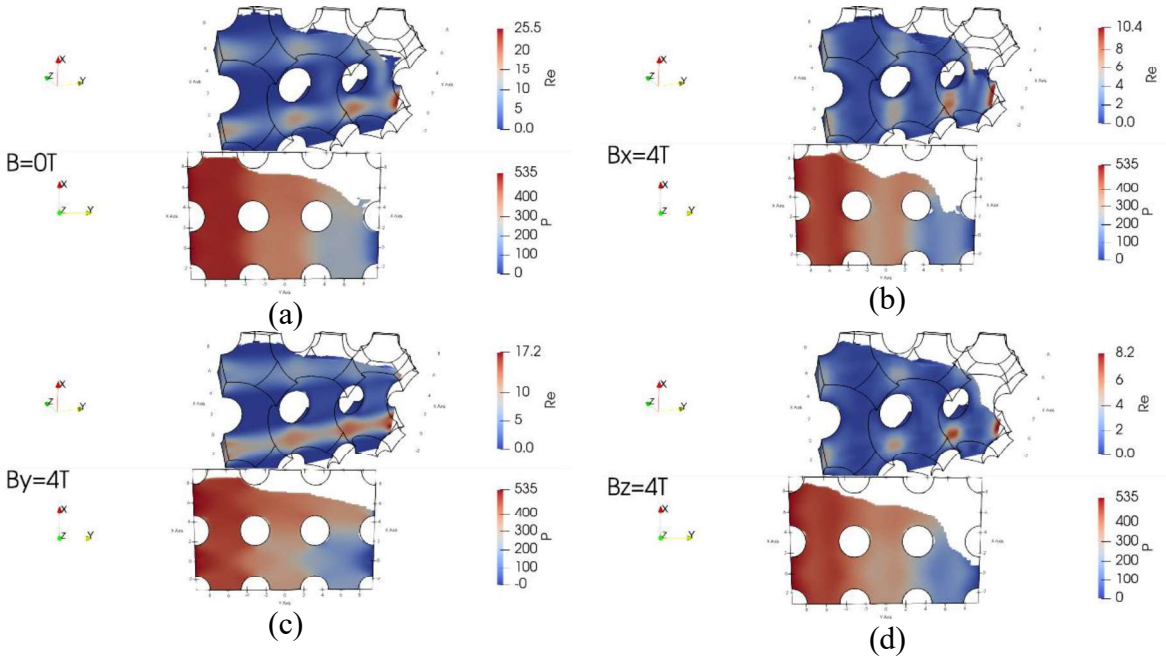


**Figure 7.** Dimensionless velocity and pressure distribution for two-phase transient simulation with inlet-outlet pressure drop P=535.

In Fig. 9 a height difference between inlet and outlet is calculated. Due to the discontinuous inlet and outlet, in practice the inlet height was calculated as the maximum liquid metal height in the domain but the outlet height was liquid metal height at the outlet. In the case that surface level near outlet was in-between the first and second row, the height was calculated at the closest cell connection between the rows.

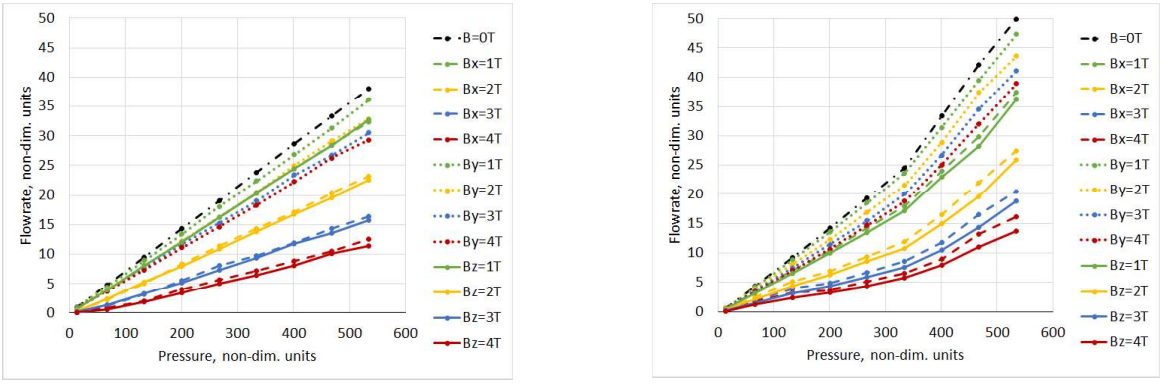


**Figure 8.** Flowrate dependency on the inlet pressure in (a) one-phase steady-state simulations; (b) two-phase transient simulations.

There seems to be a jump between P=134 and P=200 but this is likely due to the change from one-row to two-row geometry. It is difficult to see a clear dependency on the external magnetic field. The differences at larger pressures could be simply due to difficulty of precisely calculating the height at the outlet because of some air pockets which might have disappeared if the simulation was continued for a longer time. Additionally, flow near the inlet starts to creep towards the top boundary, which could lead to incorrectly calculated inlet height. Nonetheless, there are few general tendencies for the

choice of the direction of the external magnetic field. Magnetic field in z-direction results in the largest height difference. In contrast, magnetic field in the y-direction affects the inlet to outlet height difference the least or even slightly decreases in comparison to simulation without external magnetic field.

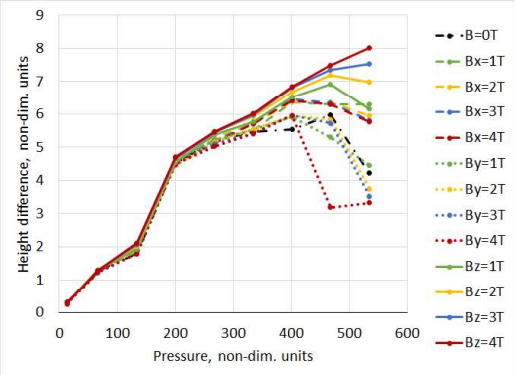


**Figure 9.** Height difference dependency on the inlet pressure in two-phase transient simulations.

In the setup of this study the pressure drop was only applied perpendicular to the gravitation direction. An additional study would be necessary to investigate surface deformations in external magnetic field for other relevant angles between gravitation and applied pressure drop.

## CONCLUSIONS

- It is possible to perform two-phase direct numerical simulation of liquid flow in a few cells of a porous media placed in uniform external magnetic field.
- Qualitatively the direction and strength of the magnetic field affects the liquid flow similarly as in a single-phase simulation.
- In the two-phase simulation, the magnetic field direction perpendicular to the applied pressure drop and gravitation direction has the strongest braking of the flow. Consequently, larger surface of the solid wall is uncovered compared to case without magnetic field. In contrast, magnetic field parallel to the applied pressure drop has the least braking affect.
- The numerical results show that the magnetic field parallel to the applied pressure appears to slightly decrease the height difference between inlet and outlet, whereas the perpendicular magnetic field directions increase the height difference. However, these results were not convincing and should be validated.

**References**

[1] C. E. Kessel et al, *Critical Exploration of Liquid Metal Plasma-Facing Components in a Fusion Nuclear Science Facility*, Fusion Science and Technology, 75:8, 886-917, **2019**, DOI: 10.1080/15361055.2019.1610685

[2] A. Khodak, R. Maingi, *Modeling of liquid lithium flow in porous plasma facing material*, Nuclear Materials and Energy, Volume 26, 100935, **2021**, DOI: 1016/j.nme.2021.100935

[3] M.G. Hvasta et al, *Demonstrating electromagnetic control of free-surface, liquid-metal flows relevant to fusion reactors,* Nucl. Fusion 58, 016022, **2018**, DOI: 10.1088/1741-4326/aa9344

[4] J. Rudolph, G. Miloshevsky, *Analysis and Modeling of Lithium Flows in Porous Materials,* Plasma Phys. Rep. 44, 685–691, **2018**, DOI: 10.1134/S1063780X1807005X

[5] J. Vencels et al, *EOF-Library: Open-source Elmer FEM and OpenFOAM coupler for electromagnetics and fluid dynamics,* SoftwareX, Volume 9, 68 – 72, **2019**, DOI: 10.1016/j.softx.2019.01.007

9th International Scientific Colloquium "Modelling for Materials Processing".
Riga, Latvia, September 18-19, 2023

# Continuous Casting Simulation With MAGMASOFT®

Evgenii Shvydkii*, Jakob Fainberg, Erik Hepp, Sebastian Koldorf

MAGMA Gießereitechnologie GmbH, Kackertstr. 16-18, 52072 Aachen, Germany
*e.shvydkii@magmasoft.de

**Abstract:** Continuous casting is used in the making of the majority of the steel produced worldwide. It is a complex process with a harsh environment. Thus, numerical models can provide new insights into understanding some aspects of the process and potentially improve casting quality. This includes the entire process, from the tundish and the flow into the mold to the solidifying strand which is withdrawn through various cooling zones. The steel continuous casting process is simulated in the commercial simulation program MAGMASOFT®. Validation of the computational model is done by comparing velocity profiles with measured ones in a laboratory-scale experiment. Case studies simulating the superheat transport, segregation and air gap formation phenomena are covered.

**Keywords:** Continuous casting, numerical simulation, solidification, electromagnetic stirring.

## Introduction

Continuous casting is a standard process in the production of steel. During this process, a liquid steel is poured into a water-cooled mold and solidified metal is continuously withdrawn. It includes coupled fluid dynamic, heat transfer and solidification phenomena. Moreover, to control the flow into the mold and liquid core, external magnetic fields are used. Besides its multi-physical nature, a wide range of length and time scales makes modeling of this process even more challenging [1]. This paper shows several cases simulating different phenomena during continuous casting of steel. More specifically, issues such as fluid flow in the mold, electromagnetic stirring and superheat transport, macrosegregation and the thermomechanical deformation of the solidifying shell are briefly covered. All of the simulations are done in the commercially available software MAGMASOFT®.

## Numerical Model

The numerical model is based on the finite volume method. The temperature and velocity field in the withdrawn strand including solidification are calculated. The L-VEL turbulence model is used in the simulation. Thermophysical parameters depend on temperature and solid fraction. Heat transfer coefficients are set to simulate primary heat extraction in the mold and secondary cooling. Electromagnetic field and Lorentz forces are calculated once due to the low magnetic Reynolds number and act as a body force in the momentum equation. A more detailed description of the numerical model can be found in reference [2].

## Validation

Fluid mechanics plays a crucial role in steel continuous casting. This includes a turbulent flow driven by inertia, thermosolutal buoyancy or electromagnetic forces. Reynolds numbers in industrial-scale casters achieve ~$10^5$ in the submerged entry nozzle (SEN) and ~$10^4$ in the mold. To validate the fluid-dynamic part of the model, we refer to the mini-LIMMCAST experiment [3, 4]. This experiment uses a GaInSn alloy as a liquid medium and ultrasound

Doppler velocimetry as a measurement method. The liquid metal circulates through a SEN and a slab-shaped mold with two outlets, imitating a continuous casting process.

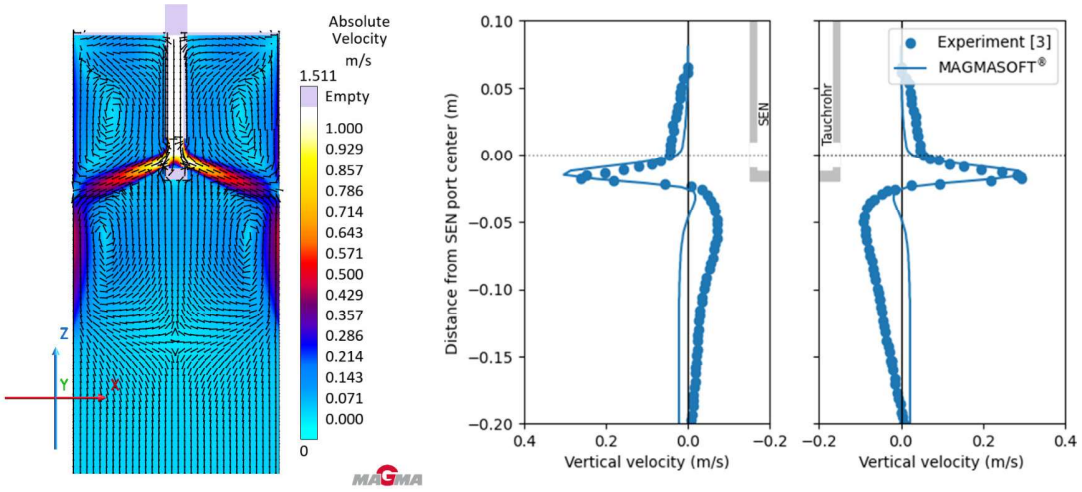


(a) (b)

Figure 1. Calculated velocity field in the mold (a) and vertical velocity profiles at x=±20 mm from the SEN axis (b)

In Figure 1(a), the simulated velocity field is shown. Flow coming out of the two SEN ports with a velocity above 1 m/s slows down towards the mold side walls and forms 4 vortices. In the lower half of the mold, velocity is directed downwards corresponding to the withdrawal direction. To compare this computational result, two vertical velocity profiles are shown with the measured ones in Figure 1b. The data was taken at x = ± 20 mm from the SEN axis. The upper eddies produce a downward velocity above the SEN port center. Just below the SEN ports, a velocity of about 0.2 m/s is shown, which agrees with the experiment. Below it, a difference between the simulated and measured values is observed. In the experiment, the fluid flow is directed upwards, whereas in the simulation, it is directed in the withdrawal direction. This discrepancy can be explained by the design of the experimental set-up that consists of two horizontal outlets, while in our simulation, the strand is withdrawn downwards.

**Case Studies**

*1. Superheat Transport.*

Superheat temperature in continuous casting is defined as the difference between liquidus and casting temperatures, indicating an energy contained in the melt heated to above liquidus temperature. Controlling this parameter can affect macrostructure formation phenomena such as columnar to equiaxed transition (CET) or centerline segregation [5]. To control and optimize this superheat dissipation in the mold, electromagnetic stirring (EMS) is used. It generates a primary rotating swirling flow and two secondary toroidal flows into the liquid core of the strand. This fluid flow affects the heat transfer in two ways. Firstly, it increases the superheat dissipation in the mold by preventing its penetration down along the strand. And secondly, it enhances the transport of undercooled liquid from the lower liquid core volume up to the EMS level. In this way, the stirrer acts not as a dendrite breaker but more as a cooler [6].

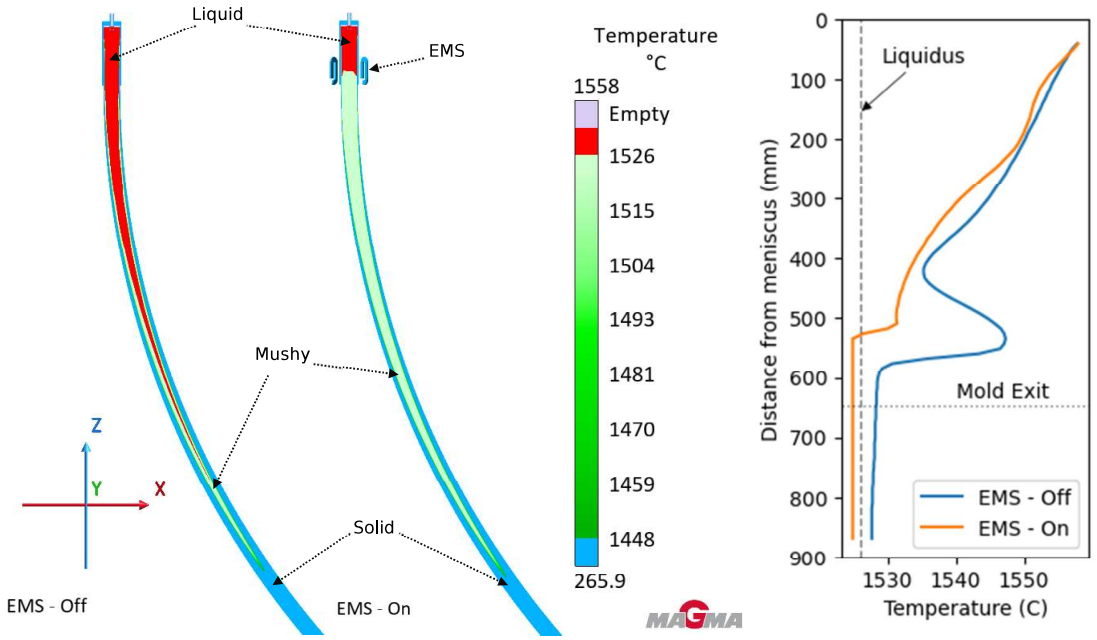


Figure 2. (a) – Temperature field results for cases with and without EMS. The superheated zone is red, the mushy zone is green and the solid phase is blue. (b) –Temperature profiles along the strand centreline

As a reference case, a billet continuous casting with mold electromagnetic stirring from reference [5] is chosen. Figure 2 (a) shows results of the simulated temperature distribution on the strand middle plane. The color bar is subdivided into three ranges indicating both the liquid and solid phases and the mushy zone. For the case "EMS – Off", melt with the temperature above the liquidus temperature penetrates down into the strand, forming a long narrow mushy-zone layer. In the case with EMS, however, a stable mushy zone is formed already at the EMS level. The graph in Fig. 2 (b) shows that the centerline temperature drops under the liquidus line before the mold exit. Therefore, more liquid core volume is undercooled. Such conditions are desirable for stable equiaxed grain development in the middle of the strand. Only after the superheat is dissipated and the liquid cools to a temperature between the liquidus and solidus regions, small equiaxed crystals can appear in and coexist with the liquid phase. The result illustrates and confirms findings shown in the review paper [6].

*2. Segregation Formation.*

Segregation is a casting defect defined as a non-uniform distribution of alloy components in the semi-finished casting product. Numerical modeling can help to predict this defect and to define optimal casting or EMS parameters to avoid it.

As a reference case for segregation formation modeling, we refer to reference [7] where stainless steel continuous casting with EMS is simulated. A slab-shaped casting with a cross section of 200×1258 mm is withdrawn with a casting speed of 1.2 m/min. The electromagnetic stirrer consists of two traveling magnetic field inductors placed at the mold wide faces just below the meniscus. The temperature-dependent thermophysical properties of the casting alloy are calculated using the JMatPro tool [8].

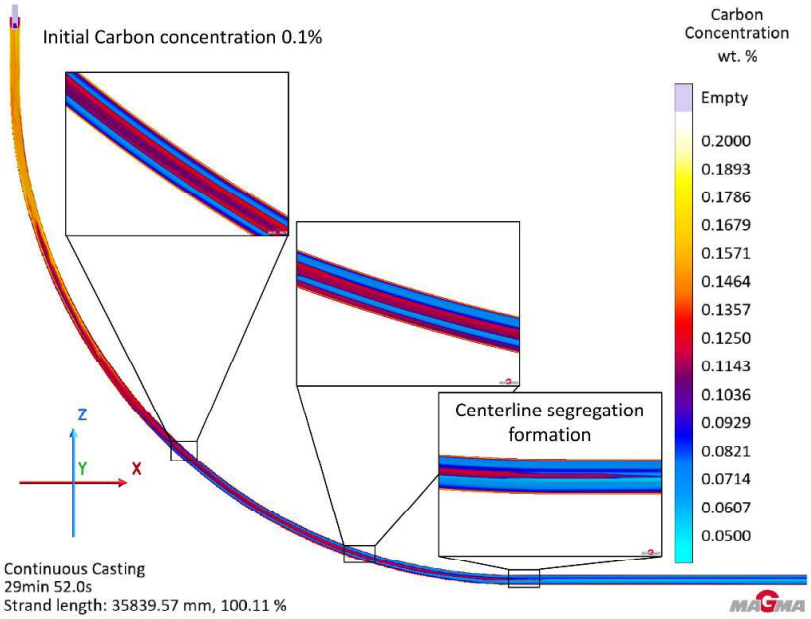


Figure 3. Carbon concentration in the slab-shaped strand

Figure 3 shows the carbon concentration distribution in the strand midsection. The initial concentration is 0.1%. In the zoom views, a segregation formation mechanism is shown. The solidified metal rejects carbon into the liquid phase in the strand center and has a concentration of less than 0.1%. This solute-rich liquid keeps getting narrower along the withdrawn strand. At the end of the strand bow (where it is horizontal), centerline segregation formation is shown.

*3. Thermomechanical Coupling.*

In modeling of different thermal processes, an interfacial heat transfer plays an important role. This especially applies in solidification applications where the cooling conditions are governed by the heat transfer coefficient (Htc) between cast material and water-cooled mold. Due to intensive cooling, a thermal distortion of the strand occurs, leading to non-uniform contact and even air gap formation between the strand and mold surfaces. Precise definition of the local Htc in the mold is important to get an accurate calculated heat removal and solidification conditions. To obtain this 3D heat transfer coefficient, thermomechanical modeling was applied. In this approach, a temperature field was taken as the driving force to calculate the thermal distortion of the solidified strand and the contact gap in the mold is obtained. The local heat transfer coefficient, *Htc*, was assumed to be related to the gap by:

$$Htc = \frac{1}{\frac{1}{h_0} + \frac{1}{h_{air} + h_{rad}}} \quad (1)$$

where $h_0$ – initial heat transfer coefficient, $h_{air} = \frac{\lambda_{air}}{\delta_{gap} + r_c}$, $\lambda_{air}$ – thermal conductivity of air, $\delta_{gap}$ – air gap between strand and mold, $r_c$ – surface roughness and $h_{rad}$ – radiation heat transfer coefficient.

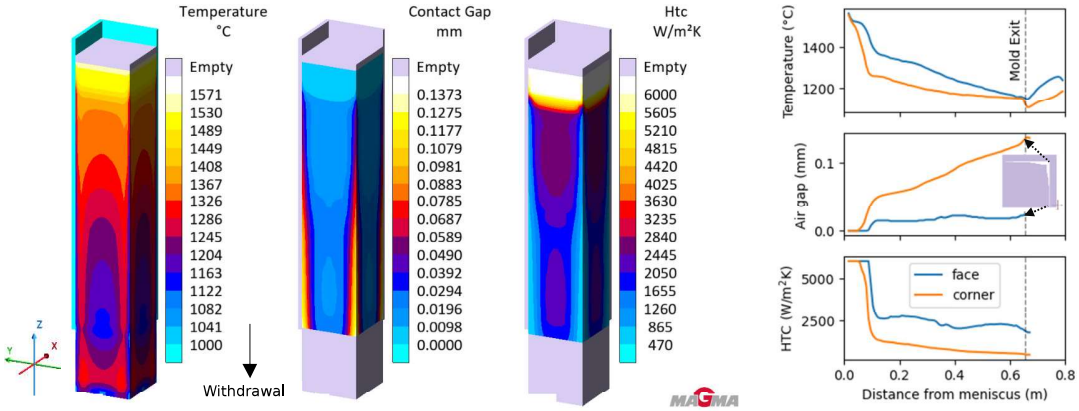


Figure 4. Temperature, contact gap and heat transfer coefficient in the strand-mold interface

To test thermomechanical coupling, a laboratory-scale case from [9] was taken. The same material properties, boundary conditions and casting parameters were applied, only the geometry of the strand was modified from round to a square-shaped billet. Figure 4 shows results of this test case simulation. The initial temperature of the withdrawn billet decreases from 1570 to ~1150°C due to the heat extraction in the mold. This cooling leads to mechanical deformation of the solidified shell, and gap between the billet and mold occurs. This contact gap is more pronounced in the corners of the mold, reaching 0.13 mm. According to equation (1), the heat transfer coefficient between the casting and mold surface is recalculated, taking into account the air gap. The Htc is reduced from the initial 6000 W/m$^2$K to 2500 at the billet faces and to 500 at the corners of the billet.

**Conclusions**

In this paper, the simulation of multiphysical phenomena in the steel continuous casting process is shown. Specifically, liquid metal flow (including EMS), heat transfer, solidification and thermomechanical deformation are considered. Validation of the fluid dynamics was done by comparing calculated with experimentally measured velocities. It is shown how, by means of EMS, it is possible to control the superheat distribution, thereby creating the desired condition for equiaxed crystal growth. The simulation results of the segregation formation for industrial-scale continuous casting are demonstrated. Calculated gap formation between casting and mold can help to predict an accurate heat transfer between casting and mold. The presented results mirror the summary of current developments in MAGMASOFT® for continuous casting applications.

**References**

[1] Thomas, B. G. (2018). Review on Modeling and Simulation of Continuous Casting. steel research int., 89, 1700312. https://doi.org/10.1002/srin.201700312

[2] Fainberg, J., Hepp, E., and Shvydkii, E. (2023). How electromagnetic stirring influences fluid flow in continuous casting of steel. IOP Conference Series: Materials Science and Engineering, 1281, 012030. https://doi.org/10.1088/1757-899x/1281/1/012030

[3] Timmel, K. (2014). Experimentelle Untersuchung zur Strömungsbeeinflussung mittels elektromagnetischer Bremsen beim kontinuierlichen Strangguss von Stahl. PhD-Thesis, TU Bergakademie Freiberg.

[4] Timmel, K., Kratzsch, C., Asad, A., Schurmann, D., Schwarze, R., & Eckert, S. (2017). Experimental and Numerical Modeling of Fluid Flow Processes in Continuous Casting: Results from the LIMMCAST-Project. IOP Conference Series: Materials Science and Engineering, 228, 012019. https://doi.org/10.1088/1757-899x/228/1/012019

[5] Zhang, Z., Wu, M., Zhang, H., Ludwig, A. and Kharicha, A. (2022). The Role of Mold Electromagnetic Stirring in the Dissipation of Superheat during the Continuous Casting of Billets. steel research int., 93, 2200065. https://doi.org/10.1002/srin.202200065

[6] Kunstreich, S. (2003), Electromagnetic stirring for continuous casting - Part 2. Rev. Met. Paris, 100 (11), 1043-1061.

[7] Kihara, K., Okada, N., Saito, S., & Kawashima, K. (2022). Numerical Simulation of Macrosegregation in a Continuous Casting Mold with Electromagnetic Stirring. ISIJ International, 62 (9), 1862–1873). https://doi.org/10.2355/isijinternational.isijint-2022-120

[8] https://www.sentesoftware.co.uk/jmatpro

[9] Kelly, J. E., Michalek, K. P., O'Connor, T. G., Thomas, B. G., & Dantzig, J. A. (1988). Initial development of thermal and stress fields in continuously cast steel billets. In Metallurgical Transactions A., 19 (10), 2589–2602. https://doi.org/10.1007/bf02645486

**Influence of External Magnetic Field on 3D Electro Vortex Flow Inside Conducting Liquids**

Mohamad Al-Nasser, Hadi Barati, Ebrahim Karimi-Sibaki, Menghuai Wu, Christian Redl, Anton Ishmurzin, Nikolaus Voller, Gernot Hackl, Abdellah Kharicha

A numerical study is presented to investigate the 3D flow structures inside conduction Liquids when current flows. The current interacts with the magnetic field to induce the electro-vortex flow (EVF) in the liquid. The flow structure and the strength of the flow are dictated by the current value and the presence of an external magnetic field. The results presented reveal a typical electro-vortex structure for low currents. Higher currents induce more mixing inside the domain and swirl flow can be observed without any presence of an external magnetic field. The axial external magnetic field induces new flow structures like rope tornado, Tornado, and Cyclone. The presence of a horizontal magnetic field deflects the flow. The flow is dictated mainly by two parameters the current applied and the value and orientation of the external magnetic field.

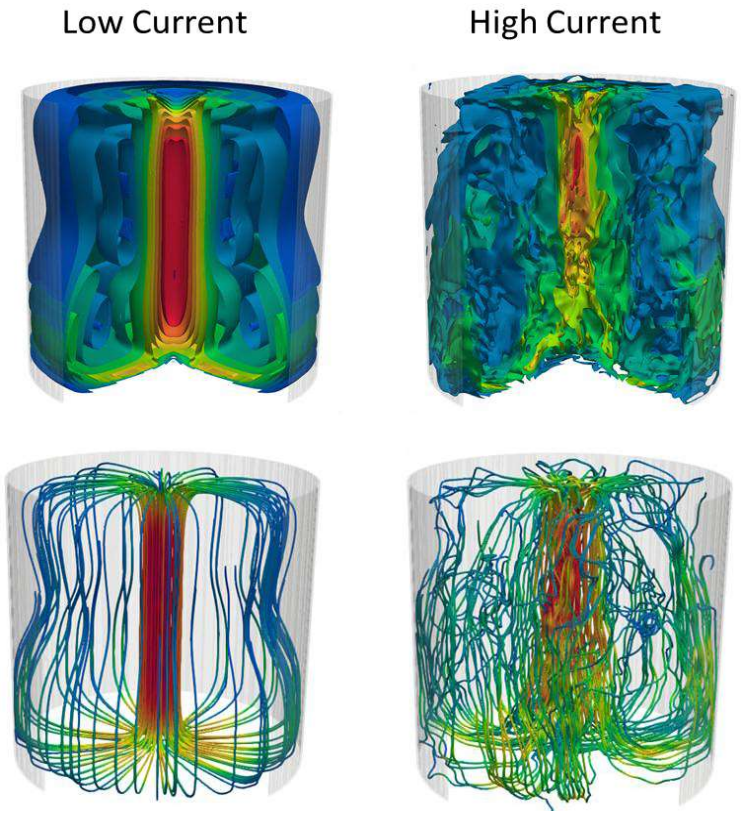


*Figure 1: Electro Vortex Flow inside liquid metal. The top shows the iso-surface for velocity distribution while the bottom shows the flow streamlines.*

# Modeling of magnetohydrodynamics in liquid metals with a free surface using OpenFOAM

Valentina Giovacchini[1*], Simone Mingozzi[2]
1. Renaissance Fusion, 22 rue J. P. Timbaud, 38600 Fontaine, France
2. Eindhoven University of Technology, De Zaale, Eindhoven 5612AZ, The Netherlands
*valentina.govacchini@renfusion.eu

**Abstract:** In this work, we develop the Magnetohydrodynamic (MHD) multiphase solver *interMhdFoam*, that self-consistently model MHD effects envisioned for free surface liquid metal flow applications in nuclear fusion reactors. A flowing liquid metal layer on the internal walls of the reactor offers critical advantages for plasma-facing applications, including heat flux handling and plasma confinement, and tritium breeding control [1]. However, the control and stabilization of this flow are challenging and require a proper numerical model. The solver has been developed by extending *interFoam*, a Volume of Fluid (VOF) solver for two immiscible and incompressible fluids, provided within the OpenFOAM library. The induction-less approximation holds in DC for low magnetic Reynolds number $Re_m$ and allows us to implement and solve the Poisson equation for the electric potential. The continuity of current can be obtained by using a conservative formula for the Lorentz force [2] [3]. Preliminary numerical results show the feasibility of the solver to describe and model the physics involved in liquid metal magnetohydrodynamics with a free surface. In particular, the solver will be used to model and assist in designing the in-house experiment at Renaissance Fusion, where the suspension and stabilization of a flowing free-surface liquid metal layer against gravity are attempted using centrifugal and Lorentz forces.

**Keywords:** liquid metals, nuclear fusion, two-phase MHD flows

## Introduction

The application of flowing liquid metals as coolants in magnetic confinement fusion reactors has greatly influenced the study of MHD phenomena in liquid metals over the past decades. The effects of magnetic field on heat transfer and hydrodynamic drag have been investigated through numerical models in various geometries relevant to first wall, divertor and blanket applications [4] [5] [6].

One promising design for future commercial fusion reactors proposes the use of liquid metals directly as plasma-facing material, to simultaneously remove heat flux and attenuate neutrons, providing a continuously regenerated surface and eliminating the maintenance issues of solid first walls [1] [7]. Taking advantage of the strong plasma-confining magnetic field, it might be possible to actively suspend thick layers of liquid metal by applying a careful balance of centrifugal and Lorentz forces through the injection of electrical currents [8] [9]. Renaissance Fusion is designing and operating proof-of-concept experiments to validate the use of liquid metals systems. To assist the design of the in-house experiment, a numerical tool capable of handling two-phase flows and MHD phenomena is needed, which has been developed in the framework of the open-source library OpenFOAM-v2212 [10].

The new solver, *interMhdFoam*, is written as an extension of the existing *interFoam*, a two-phase VOF-based solver, by including the effects of the Lorentz force conservatively [3] and based on the assumption of low magnetic Reynolds, which is reasonable on a laboratory scale. The validation of this numerical tool for modeling self-consistently MHD phenomena in two-phase flows in the presence of injected currents is crucial and it is the main objective of the present work.

There are several benchmarks and validations for single-phase MHD flows in literature [2] [11] [12], while validation studies focusing on multi-phase MHD phenomena are considerably fewer, especially when concerned with current injections. In [13], a two-dimensional multi-phase MHD flow in presence of an imposed magnetic field and electric potential was studied, and an analytical expression for the elevation of the liquid/air interface was obtained. In [14] the deformation of the free surface of liquid metal in electrically induced vortical flows was studied experimentally and numerically.

The main goal of the present study is to obtain and validate the results of our newly developed solver for multi-phase MHD flows with current injections. After the description of the mathematical model and the implemented numerical algorithm, we present the numerical results. We analyze the shallow 2D multi-phase cavity [13] and the electrically induced vortex [14], and compare the obtained numerical results with the available reference data, i.e., analytical solutions, experimental and numerical data.

**Governing equations for multi-phase MHD flows**

We consider a system composed of two incompressible, Newtonian, isothermal and immiscible fluids. One, or both fluids, can be modeled as electrically conductive. The system is affected by an imposed external magnetic field through the Lorentz force. The conservation of mass and momentum can be used to describe the MHD flow and can be formulated as

$$\nabla \cdot \boldsymbol{u} = 0, \tag{1}$$

$$\frac{\partial(\rho \boldsymbol{u})}{\partial t} + \nabla \cdot (\rho \boldsymbol{u}\boldsymbol{u}) = -\nabla p + \nabla \cdot [\mu(\nabla \boldsymbol{u} + \nabla \boldsymbol{u}^T)] + \nabla \cdot \tau^R + \rho \boldsymbol{g} + \boldsymbol{f_\gamma} + \boldsymbol{J} \times \boldsymbol{B}, \tag{2}$$

where $\boldsymbol{u}$ represents the velocity shared by the two fluids throughout the flow domain, $p$ the pressure, $\boldsymbol{J}$ is the current density, $\boldsymbol{B}$ is the imposed magnetic field, $\tau^R$ is the Reynolds stress tensor, $\boldsymbol{f_\gamma}$ is the surface-tension force. In Equations (1)-(2), $\rho$ and $\mu$ are the density and dynamic viscosity of the mixture, while $\boldsymbol{g}$ is the gravitational acceleration. In the momentum equation (2), the MHD interactions are accounted for through the Lorentz term $\boldsymbol{J} \times \boldsymbol{B}$. For low magnetic Reynolds numbers, i.e. $Re_m = UL/\eta \ll 1$ ($\eta$ is the magnetic diffusivity, $U$ and $L$ are proper velocity and length scales), the Ohm's law can be written as

$$\boldsymbol{J} = \sigma(-\nabla \phi + \boldsymbol{u} \times \boldsymbol{B}), \tag{3}$$

where $\sigma$ is the electric conductivity of the mixture and $\phi$ is the electric potential such that the electric field can be expressed as $\boldsymbol{E} = -\nabla \phi$. By imposing the divergence-free current density condition in the Ohm's law, the Poisson equation for the electric potential is obtained

$$\nabla \cdot (\sigma \nabla \phi) = \nabla \cdot (\sigma \boldsymbol{u} \times \boldsymbol{B}) . \tag{4}$$

In the momentum equation (2), in addition to the Lorentz force, the surface-tension force $\boldsymbol{f_\gamma}$ is included to consider the interaction between the two fluids. It is evaluated using the continuum surface force model $\boldsymbol{f_\gamma} = \gamma \kappa \nabla \alpha$, where $\gamma$ is the surface tension, $\kappa$ is the mean curvature of the free surface, and $\alpha$ is the volume fraction described by the following transport equation

$$\frac{\partial \alpha}{\partial t} + \nabla \cdot (\alpha \boldsymbol{u}) + \nabla \cdot \left(\boldsymbol{u_r} \alpha(1-\alpha)\right) = 0, \tag{5}$$

where $\boldsymbol{u_r}$ is the artificial compression velocity used for the interface sharpening [15]. The physical properties of the mixture are calculated as weighted averages based on the distribution of the volume fraction

$$\rho = \alpha \rho_l + (1-\alpha)\rho_g, \qquad \mu = \alpha \mu_l + (1-\alpha)\mu_g, \qquad \sigma = \alpha \sigma_l + (1-\alpha)\sigma_g, \tag{6}$$

where we have indicated with subscripts $l$ and $g$ the properties of the pure gas and liquid.

Self-induced magnetic field

When there is an injection of current in the system, even in absence of an imposed magnetic field, a Lorentz force can be generated by the interaction between the current density and the

self-induced magnetic field. In this case, we need to solve an additional equation to determine the self-induced magnetic field. We can introduce the magnetic vector potential $\boldsymbol{A}$ such that

$$\boldsymbol{B} = \nabla \times \boldsymbol{A}. \quad (7)$$

By substituting this definition into Ampere's law, we obtain $\nabla \times \nabla \times \boldsymbol{A} = \mu \boldsymbol{J}$ that can be reformulated as

$$\nabla(\nabla \cdot \boldsymbol{A}) - \nabla^2 \boldsymbol{A} = \mu \boldsymbol{J}, \quad (8)$$

where $\boldsymbol{J}$ is computed using the Ohm's law (3).

Numerical algorithm

The numerical procedure implemented in the solver *interMhdFoam* is based on *interFoam* [15] and PIMPLE algorithm, that have been modified to include the MHD effects. To handle the Lorentz force in equation (2) in a conservative manner, we have implemented the Four Steps Projection Method (FSPM) proposed by Ni et al. [3]. For each outer correction iteration of the PIMPLE loop, the algorithm consists in the following steps:

1. Compute the volume fraction α and update mixture properties.
2. Calculate the magnetic flux at cell faces $\psi = \sigma_f (\boldsymbol{u} \times \boldsymbol{B})_f \cdot \boldsymbol{S}_f$
3. Solve equation (4) and find the electric potential $\phi$ at the cell centres. If necessary, compute the magnetic vector potential solving (8).
4. Calculate the cell face normal component of current density $J_n$ using the surface-normal gradient of the electric potential $J_n = -\sigma_f \nabla_n \phi |\boldsymbol{S}_f| + \psi$.
5. Calculate the fully conservative form of the Lorentz [3], $\boldsymbol{J} \times \boldsymbol{B} = (-\sum_f \boldsymbol{J}_n \cdot (\boldsymbol{B} \times \boldsymbol{C})_f - \boldsymbol{C} \times \sum_f \boldsymbol{J}_n \cdot \boldsymbol{B}_f)/\Omega_C$, where $\boldsymbol{C}$ and $\Omega_C$ are the cell centre and volume.
6. Assemble the velocity matrix and momentum predictor step.
7. Assemble the pressure matrix and momentum corrector steps.

These steps are repeated until the convergence is reached for each time step.

**Results and discussion**

Multi-phase MHD shallow cavity flow

The first example of MHD multi-phase test case is a shallow cavity subjected to combined effects of an imposed non-uniform magnetic field and electric potential difference. We consider a two-dimensional cavity with characteristic length $L$ and partially filled with an electrically conductive liquid. A schematic of the geometry can be found in the reference paper [13]. The liquid layer height is indicated with $d$ and we introduce the ratio $A = d/L$. The upper part of the cavity is filled with a non-conductive fluid, air in our case. The external magnetic field is perpendicular to the cavity and presents the linear distribution $\boldsymbol{B} = -b_0 (1 + \alpha_b x/L) \hat{\boldsymbol{z}}$.

The left wall of the system is kept at a fixed electrical potential $-\Delta\phi/2$, the right wall at $\Delta\phi/2$, and the bottom wall is electrically insulated ($\nabla\phi \cdot \boldsymbol{n} = 0$). In equilibrium, electric currents flow from the right to the left wall. Due to its interaction with the external magnetic field, a downward Lorentz force is originated on the conducting liquid. The force is stronger at the right side than at the left side, causing a circulating flow inside the fluid that deforms the interface. The analytical solution of the interface deformation is reported in [13] as a function of Bond and Capillary numbers, and it has been derived for $Re = O(A)$, $Ha = 1$, $Bo = O(A^2)$ and $Ca = O(A^4)$. In the present work, we keep constant $Re = A$ and $Ha = 1$, and the aspect ratio of the domain $A = d/L = 0.1$, while we change $Bo$ and $Ca$.

In Figure 1, we show the non-dimensional vertical elevation $\Delta h/d$ of the free surface as a function of $Bo$ and $Ca$ numbers, comparing analytical and numerical computations. In the left, $B$ is kept constant and we can observe that the vertical elevation increases with an increase in

$Ca$. In the right, by increasing $Bo$ and keeping constant $Ca$, we assist to a decrease in the vertical elevation.

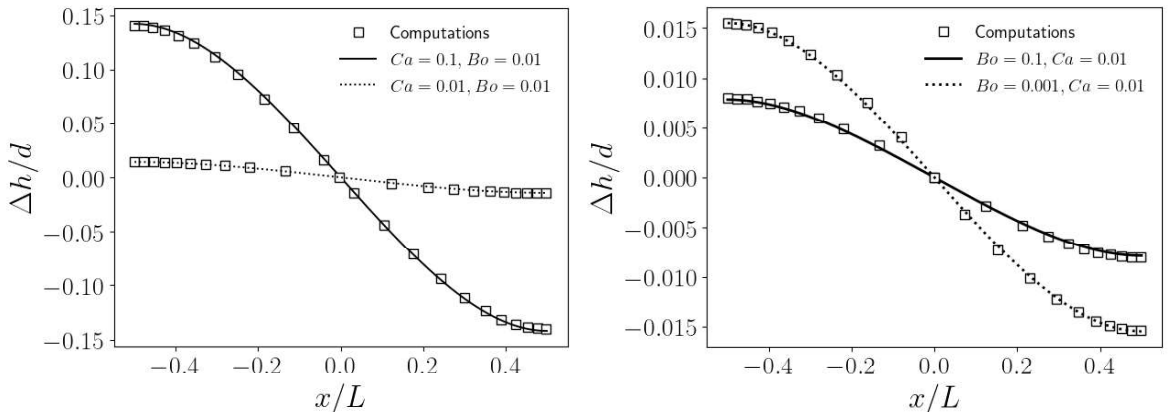


*Figure 1* Free surface elevation for various $Ca$ and $Bo$. Comparison between the analytical solution *[13]* (lines) and OpenFOAM results (square markers).

A quantitative analysis of the accuracy of the numerical solution is reported in Table 1, where the normalized $L^2$-distance between the numerically calculated elevation and the analytical solution is reported. The results are normalized by the $L^2$-norm of the analytical elevation $\Delta h_{an}$. This distance is a measure for the deviation of the numerical results from the analytical solution and it represents the cumulative error, which is at most equal to 3%.

| Case | 1 | 2 | 3 | 4 |
|---|---|---|---|---|
| $Ca$ | 0.1 | 0.01 | 0.01 | 0.01 |
| $Bo$ | 0.01 | 0.1 | 0.01 | 0.001 |
| error | 0.01329 | 0.02798 | 0.03037 | 0.01897 |

*Table 1* Normalized $L^2$-distance between the surface elevation profile obtained with the numerical simulations and the analytical solutions, for different $Ca$ and $Bo$ numbers.

Electrically induced vortex

The second example of MHD multi-phase test case is an electrically induced vortical flow system. The investigated geometry and the physical properties can be consulted in the reference paper [14]. It consists of a cylindrical container, with an insulating bottom surface, a small bottom electrode at the centre of the cylinder and conducting side walls. The imposed electric potential difference induces an electric current flowing radially through the liquid metal layer. The electric current interacts with the self-induced magnetic field causing an upward jet and a free surface deformation above the small electrode.

The experiments were run in AC, but according to [14], the difference between Lorentz forces in DC and AC cases were negligible, if DC computations were run by applying the effective (RMS) current used in the experiments. We confirmed this aspect with separate computations using COMSOL Multiphysics®. Thus, in the present study, a DC electric potential is applied.

The free surface deformation height measured during the experiments was reported for several values of injected currents for an initial liquid height of 15mm and 22mm. According to experimental results from the original study [14], a linear relation could be observed between the elevation of the free surface at the centre of the system and the RMS of the injected current. Numerical computations of a 2D axisymmetric and 3D model confirmed this trend [14].

For our simulations, we consider a 2D axisymmetric model of the cylinder, including both liquid and gas phases, discretized with a uniform mesh with characteristic size of 0.25mm. In

[14], numerical computations were performed evaluating the electromagnetic fields at the initial time with the undeformed free surface using the software Elmer FEM. The resulting Lorentz force distribution was interpolated and imported in OpenFOAM to solve the two-phase problem with *interFoam*. Instead, in our approach, we modify the implementation of *interFoam* to update electric current, magnetic field, and Lorentz force self-consistently with the free surface deformation, at every time step. We used a $k-\omega$ SST turbulence model, as in [14].

Our numerical results are shown in Figure 2, compared to experimental and numerical data from [14]. Overall, there is an excellent agreement with the numerical data and the linear behaviour can be observed. The discrepancies between the two solutions are considered to be predominantly due to our different self-consistent approach for the iterative solution of the electromagnetic fields.

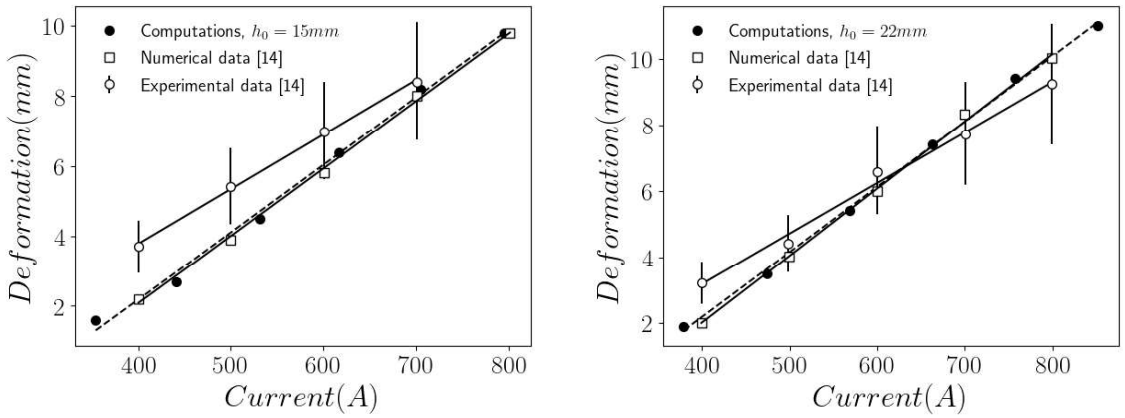


Figure 2 Free surface maximum elevation versus injected currents, for $h_0 = 15mm$ (left) and $h_0 = 22mm$ (right). Comparison between the in-house numerical computations with experimental data with error bars and numerical data from [14].

## Conclusions

We presented a newly developed solver for multi-phase MHD flows, obtained by implementing the set of MHD transport equations in the opensource code OpenFOAM-v2212. The solver was developed with the goal of modeling and describing the interaction phenomena between Lorentz force, inertia, viscous force, gravity in thick liquid metal layers for fusion reactor applications. For this reason, a VOF-based multi-phase model has been preferred among other modeling strategies. We are particularly interested in validating the new code for two-phase MHD applications with electrodes and current injections. For this reason, two configurations were tested. The first one is a shallow cavity, and the numerical results were compared with the analytical solution of the free surface elevation due to current injection in a nonuniform magnetic field. The numerical computations are in good agreement with the theoretical solution, with a cumulative error below 3% for all cases tested. The second configuration is an electrically induced vortex, in which the Lorentz force is generated by the interaction of an injected current and the self-induced magnetic field. The numerical results have been compared with experimental and numerical data. Again, the results are in excellent agreement with reference data. Next steps for the validation involve configurations in which the initial inertia of the fluid is not negligible.

## References

[1] R. Nygren and F. Tabarés, "Liquid surfaces for fusion plasma facing components—A critical review. Part I: Physics and PSI," *Nuclear Materials and Energy,* pp. 6--21, 2016.

[2] C. Mistrangelo and L. Bühler, "Development of a numerical tool to simulate magnetohydrodynamic interactions of liquid metals with strong applied magnetic fields," *Fusion Science and Technology,* 2011.

[3] M.-J. Ni, R. Munipalli, N. Morley, P. Huang and M. Abdou, "A current density conservative scheme for incompressible MHD flows at a low magnetic Reynolds number. Part I: On a rectangular collocated grid system," *Journal of Computational Physics,* pp. 174--204, 2007.

[4] N. B. Morley, S. Smolentsev, L. Barleon, I. R. Kirillov and M. Takahashi, "Liquid magnetohydrodynamics — recent progress and future directions for fusion," *Fusion Engineering and Design,* 2000.

[5] S. Smolentsev, T. Rhodes, Y. Jiang, P. Huang and C. Kessel, "Status and progress of liquid metal thermofluids modeling for the US fusion nuclear science facility," *Fusion Science and Technology,* pp. 745-760, 2021.

[6] L. Bühler, C. Mistrangelo, J. Konys, R. Bhattacharyay, Q. Huang, D. Obukhov, S. Smolentsev and M. Utili, "Facilities, testing program and modeling needs for studying liquid metal magnetohydrodynamic flows in fusion blankets," *Fusion Engineering and Design,* pp. 55-64, 2015.

[7] F. L. Tabarés, "Present status of liquid metal research for a fusion reactor," *Plasma Physics and Controlled Fusion,* 2016.

[8] M. A. Abdou, A. Ying, N. Morley, Gulec K., S. Smolentsev, M. Kotschenreuther, S. Malang, S. Zinkle, T. Rognlien, P. Fogarty, B. Nelson, R. Nygren, K. McCarthy, M. Z. Youssef, N. Ghoniem, C. Wong, M. Sawan, H. Khater and T. Uchimoto, "On the exploration of innovative concepts for fusion chamber technology," *Fusion Engineering and Design,* pp. 181-247, 2001.

[9] N. B. Morley, S. Smolentsev, R. Munipalli, M.-J. Ni, D. Gao and M. Abdou, "Progress on the modeling of liquid metal, free surface, MHD flows for fusion liquid walls," *Fusion Engineering and Design,* pp. 3-34, 2004.

[10] H. G. Weller, G. Tabor, H. Jasak and C. Fureby, "A Tensorial Approach to Computational Continuum Mechanics Using Object Orientated Techniques," *Computers in Physics ,* pp. 620-631, 1998.

[11] S. Smolentsev, S. Badia, R. Bhattacharyay, L. Bühler, L. Chen, Q. Huang, H.-G. Jin, D. Krasnov, D.-W. Lee, E. M. De Les Valls and others, "An approach to verification and validation of MHD codes for fusion applications," *Fusion Engineering and Design,* pp. 65-72, 2015.

[12] A. Blishchik, M. van der Lans and S. Kenjeres, "An extensive numerical benchmark of the various magnetohydrodynamic flows," *International Journal of Heat and Fluid Flow,* 2021.

[13] B. W. Righolt, S. Kenjereš, R. Kalter, M. J. Tummers and C. R. Kleijn, "Analytical solutions of one-way coupled magnetohydrodynamic," *Applied Mathematical Modelling,* 2016.

[14] V. Dzelme, A. Jakovics and E. Baake, "Liquid metal free surface deformation in electrically induced vortical flow," *Magnetohydrodynamics,* pp. 67-74, 2020.

[15] S. S. Deshpande, L. Anumolu and M. F. Trujillo, "Evaluating the performance of the two-phase flow solver interFoam," *Computational science & discovery,* 2012.

# Simulation of melt flow in steel continuous casting considering transient clogging of submerged entry nozzle

Barati H[1,2*], Wu M[2], Kharicha A[2,3], Ludiwg A[2]

[1]K1-MET, Franz-Josef Street 18, 8700 Leoben, Austria
*Email: hadi.barati@k1-met.com

[2]Chair for Modeling and Simulation of Metall. Processes, Dept. Metall., Montanuniversitaet Leoben, Franz-Josef Street 18, 8700 Leoben, Austria

[3]Christian-Doppler Laboratory for Metallurgical Applications of Magnetohydrodynamics, Dept. Metall., Montanuniversitaet Leoben, Franz-Josef Street 18, 8700 Leoben, Austria

**ABSTRACT**

Clogging of the submerged entry nozzle (SEN) in continuous casting of steel occurs due to the solid material build-up on the inner wall of the SEN. Different mechanisms have been proposed for clogging but attachment of solid non-metallic inclusions (NMIs) is supposed to be the dominant mechanism. Considering this mechanism, the main steps of clogging are (a) transport of NMIs by turbulent fluid flow towards the SEN wall; (b) interactions between the fluid and the wall, and adhesion of the NMI on the wall; (c) formation and growth of the clog by the continuous NMI deposition on the clog front and the flow-clog interactions; (d) detachment/fragmentation of a part of clog due to the flow drag force, as shown in Figure 1.

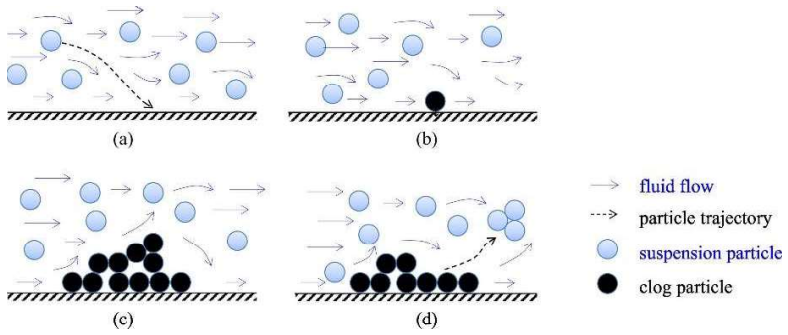


Figure 1. Schematic of main steps of clogging.

In this paper, an Eulerian-Lagrangian model was used to calculate the flow field (Eulerian) and track solid particles (Lagrangian). The growing clog was treated as a porous medium. Clogging resulted in an asymmetric flow pattern and consequently an asymmetric temperature distribution in the mold region. The simulation results showed also a dynamic flow direction on the meniscus. Using this numerical model, the effects of clogging on the different parts during the casting process can be predicted.

**Influence of the rotational component of a submerged entry nozzle jet on the free surface oscillations under the applied DC magnetic field**

Alexander Vakhrushev[1], Abdellah Kharicha[1], Ebrahim Karimi-Sibaki[1], Menghuai Wu[2], Andreas Ludwig[2], Gerald Nitzl[3], Yong Tang[3], Gernot Hackl[3], and Josef Watzinger[4]

[1]Christian Doppler Laboratory for Metallurgical Applications of Magnetohydrodynamics, Montanuniversität Leoben, Leoben, Austria

[2]Chair of Simulation and Modelling of Metallurgical Processes, Department of Metallurgy, Montanuniversität Leoben, Leoben, Austria

[3]RHI Magnesita GmbH, Austria

[4]Primetals Technologies, Austria

**Abstract**

Magnetohydrodynamics (MHD ) technique is effectively applied in a wide range of liquid metal flows. The generated Lorenz force, which occurs due to the application of the DC magnetic field, acts in the liquid bulk as well as it highly interacts with the jet-type flows. It was shown previously, that the MHD force action can be both braking and accelerating based on the closure of the induced electric current lines and on the conductivity of the domain boundaries [1]. The liquid melt flow inside a continuous casting (CC) mold cavity represents a combination of a highly turbulent flow of the feeding jets coming from the submerged entry nozzle (SEN) ports, recirculation motion in the melt bulk and free surface waving due to the sub-meniscus flow. When the DC magnetic field is applied in the CC mold in a form of the electromagnetic braking (EMBr), the flattening of the SEN feeding jets occur along the magnetic field direction, and the reverse zones are formed from either side of the flat-jet [2]. With the growing strength of the EMBr, that results in the opposite vortex formation in the meniscus region of the mold cavity [3]. The complex MHD flow structure strongly affects the free surface motion [4]. Moreover, the anisotropic turbulence is transformed into a quasi-2D coherent MHD vortex structures under the magnetic field. Thereby, an inlet flow type has a significant contribution to the formation of the free-surface waves, their collapsing and consequent entrapment of the gas bubbles or droplets of the covering protective layer. In this work a comparative study is presented, revealing the influence of the intensifying stream-wise rotational component of the feeding turbulent jets on the meniscus oscillations and free surface instability.

**References**

1. Vakhrushev, A.; Kharicha, A.; Liu, Z.; Wu, M.; Ludwig, A.; Nitzl, G.; Tang, Y.; Hackl, G.; Watzinger, J. Electric Current Distribution During Electromagnetic Braking in Continuous Casting. *Metall. Mater. Trans. B* **2020**, *51*, 2811–2828, doi:10.1007/s11663-020-01952-3.
2. Kharicha, A.; Vakhrushev, A.; Karimi-Sibaki, E.; Wu, M.; Ludwig, A. Reverse Flows and Flattening of a Submerged Jet under the Action of a Transverse Magnetic Field. *Phys. Rev. Fluids* **2021**, *6*, 123701, doi:10.1103/PhysRevFluids.6.123701.
3. Vakhrushev, A.; Kharicha, A.; Karimi-Sibaki, E.; Wu, M.; Ludwig, A.; Nitzl, G.; Tang, Y.; Hackl, G.; Watzinger, J.; Eckert, S. Generation of Reverse Meniscus Flow by Applying an Electromagnetic Brake. *Metall. Mater. Trans. B* **2021**, *52*, 3193–3207, doi:10.1007/s11663-021-02247-x.
4. Vakhrushev, A.; Karimi-Sibaki, E.; Bohacek, J.; Wu, M.; Ludwig, A.; Tang, Y.; Hackl, G.; Nitzl, G.; Watzinger, J.; Kharicha, A. Impact of Submerged Entry Nozzle (SEN) Immersion Depth on Meniscus Flow in Continuous Casting Mold under Electromagnetic Brake (EMBr). *Metals* **2023**, *13*, 444, doi:10.3390/met13030444.

## Thermoelectric Magnetohydrodynamic Control in Alloy Solidification

**Andrew Kao**[a], Xianqiang Fan[b,c], Natalia Shevchenko[d], Catherine Tonry[a], Peter Soar[a], Ivars Krastins[a,e], Sven Eckert[d], Koulis Pericleous[a], Peter D. Lee[b,c]

[a] Computational Science and Engineering Group, University of Greenwich, UK
[b] UCL Mechanical Engineering, University College London, UK
[c] Research Complex at Harwell, Harwell Campus, Didcot, UK
[d] Helmholtz-Zentrum Dresden-Rossendorf, Institute of Fluid Dynamics, Dresden, Germany
[e] Insitute of Physics, University of Latvia, Latvia

Magnetic fields have been shown to have a significant effect during solidification in a wide range of conditions from the slow growth of traditional casting to the more rapid growth of Additive Manufacturing. An underlying phenomenon is Thermoelectric Magnetohydrodynamics (TEMHD), which, due to inherent thermal gradients, generate thermoelectric currents and ultimately a Lorentz force through interaction with the magnetic field. In casting this leads to inter-dendritic convective solute transport. This can be used to control freckle defect formation, as demonstrated in a GaIn experiment, where the magnetic field can be used to reposition the freckle channel, introduce preferential growth of secondary arms, govern plume migration and lead to complex grain boundary interactions. These mechanisms, observed via X-ray synchrotron experiments, were predicted by TESA (ThermoElectric Solidification Algorithm), a parallel Cellular Automata Lattice Boltzmann based numerical model.

In laser AM, melt pools are subject to large thermal gradients and consequently form relatively large thermoelectric currents. The system behaviour is highly dependent on the orientation and strength of the magnetic field, with competition between Marangoni flow and TEMHD resulting in control of the depth, width and potential deflections of the melt pool. This leads to significant changes in the microstructure including modification to the melt pool boundary layer and epitaxial growth. The numerical predictions also compare favourably to X-ray synchrotron experiments.

## Mass transport and solutal convection in a sodium-zinc molten salt battery with liquid electrolyte: comparison of modelling and experiments

Martins Sarma*, Carolina Duczek, William Nash, Norbert Weber, Tom Weier

*Institute of Fluid Dynamics, HZDR, Dresden, Germany*
*m.sarma@hzdr.de

Within the Horizon 2020 project SOLSTICE, a molten salt battery has been developed. The battery employs sodium and zinc as anode and cathode respectively and operates at around 600 °C with a completely liquid interior. The primary advantage of this design is its low materials' cost. However, multiple challenges must be overcome if it is to become commercially viable. These include corrosion of metallic components by the molten salt electrolyte, and self-discharge promoted by transport of cathode materials ($Zn^{2+}$ ions) to the anode. Efforts to suppress the latter especially benefit from modelling, as the rate of self-discharge is primarily determined by mass transport processes in the electrolyte. Such models require experimental validation, thus, a small-scale experimental cell has been constructed for this purpose. It has been designed specifically for operation during analysis by radiographic methods (neutron beam and X-ray imaging). The distribution of the active materials can be observed at different stages of the charging-discharging cycle. This presentation will provide an overview of current modelling activities at HZDR related to the sodium-zinc battery, together with first (preliminary) experimental results and the most recent progress towards designing a "transparent" cell.

# Role of thermoelectromagnetic effect in metal additive manufacturing

Imants Kaldre*, Valdemārs Felcis[2]

University of Latvia, Jelgavas street 3, Riga LV-1004, Latvia
*Imants.kaldre@lu.lv

**Abstract:** Metal additive manufacturing (AM) is a rapidly rising new technology. During AM process a small quantity of metal is melted and then solidified. During melting phase, a small melt pool is formed, where various physical phenomena take place, which affects the heat and mass transfer in the melt pool and subsequently the solidified morphology and microstructure. Solid and liquid phases have different Seebeck coefficients, thus when subjected to high thermal gradient, thermoelectric currents may appear at the interface. This small-scale current circulation allows us to control heat and mass transfer by applying external magnetic fields.

In this work we present an experimental scale model to quantify the role of thermoelectromagnetic effect in a melt pool during additive manufacturing. We used a copper hemispherical cavity filled with GaInSn and an immersed cobalt electrode. Heat flux is applied through the cobalt electrode and thermoelectric currents are generated at the interface between electrode and the liquid metal. In this work we measure the liquid metal motion created by different orientation of static magnetic field up to 0.2 T. This result is compared with numerical model and analytical estimations. Experimental and numerical results demonstrate that thermoelectromagnetic effect can be significant during additive manufacturing process.

Additive manufacturing, Thermoelectric effect, Magnetohydrodynamics

## Introduction

Metal additive manufacturing using electric arc is one of the most popular wire-fed additive manufacturing methods. During this process a small melt pool of liquid metal is created. Heat and mass transfer in this melt pool is responsible for the microstructure formation and properties of the solidified material [1]. There are not many ways we can influence the physical processes of the solidification of melt pool material, but one of the perspective ways is application of external magnetic fields which can significantly affect the melt pool flow and consequently affect the solidified structure and properties [2].

Particularly interesting is thermoelectromagnetic effect and to understand how it can affect real additive manufacturing process. Thermoelectric current is forming between electrode and the liquid metal if the interface is subjected to temperature gradient [3]. Cobalt is chosen as electrode material, because of its high Seebeck coefficient. It is known that thermoelectric effect combined with external magnetic field can drive liquid phase convection. Thermoelectromagnetic convection (TEMC) can be the dominant flow in certain cases, because this convection can be generated at a very small length scale comparable to viscous boundary layer. This phenomenon is observed during the dendritic solidification of metallic alloys, where a large local thermal gradient is present [4-6]. Depending on the magnetic field direction, convection pattern differs. It is shown that in axial magnetic field with primary

dendrite arms, fluid rotates around the dendrite arm. If magnetic field is transverse, then crucible scale convection is forming perpendicularly to the direction of magnetic field [7].

It is difficult to investigate this process directly because of the small scale, rapid process, and high temperature, thus we have developed a large-scale model where we can look at the different physical phenomena taking place in the liquid metal pool and later use the results for better understanding of AM processes [8]. Similar laboratory experiment is developed to investigate electrovortex flow in liquid metal under combined AC magnetic fields [9].

## Experimental

The experimental setup used in this work consists of hemispherical copper cavity (R=30mm) filled with liquid GaInSn alloy, cobalt electrode (r=5 mm) is immersed in the gallium pool (Fig. 1a). External magnetic field is created by permanent magnet system which is placed around the central part of the experiment (B=0.1 T). Heat flux is created by 200 W electric heater around the top of the cobalt electrode. The outer part of the copper part is kept at room temperature. In this situation heat flux through the cobalt electrode creates thermal gradient along the electrode interface with GaInSn and thermoelectric current circulates at the interface. Experimental setup is shown in Fig. 1b.

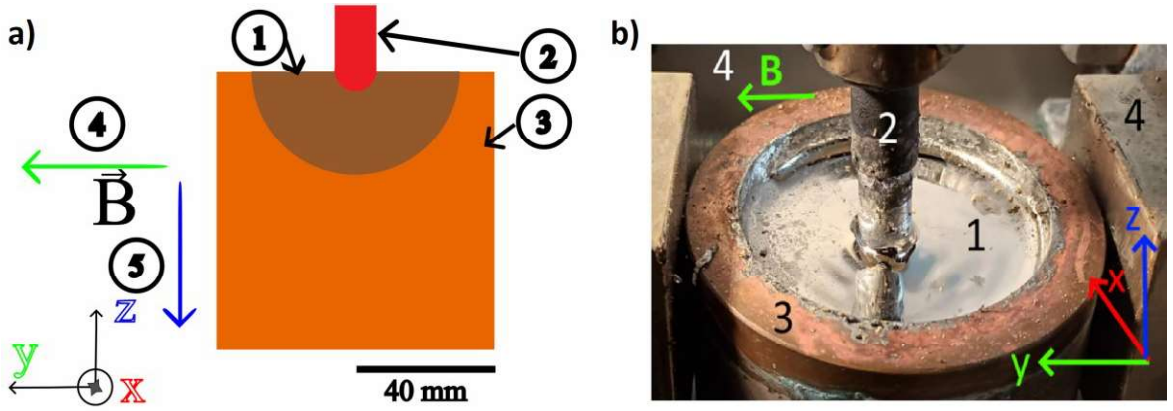


Figure 1. a) Scheme of the experimental setup, b) Experimental setup photo; 1 – Liquid GaInSn, 2 – Cobalt electrode, 3 – Copper hemisphere, 4– Transverse magnetic field, 5-Axial magnetic field

## Analytical description

Experimental setup is designed to maximize the thermoelectromagnetic effect and to ensure the opportunity to conduct direct experimental measurements of the liquid GaInSn convection created by thermoelectric current and magnetic field. Various physical phenomena appear in this experiment. For analytical description of the process, we use stationary, incompressible fluid model. Heat is transferred by conduction in solid parts, while in the liquid phase convective heat transfer is also considered according to Eq.1. Where $\rho$ is density, $c$ is thermal capacity, $q$ is volumetric heat source, $k$ is thermal conductivity, $S$ is Seebeck coefficient, $\mu$ is dynamic viscosity, $\gamma$ is surface tension, $L$ is characteristic length scale.

$$\rho c\boldsymbol{u} \cdot \nabla T + \nabla \cdot (-k\nabla T) = q \qquad \text{(Eq.1)}$$

Current flow is described by the Ohms law Eq.2.

$$\boldsymbol{j} = \sigma(\boldsymbol{E} + \boldsymbol{u} \times \boldsymbol{B} - S\nabla T) \quad \text{(Eq.2)}$$

Fluid flow is governed by stationary Navier-Stokes equation, which balances all volume forces acting on the fluid element (Eq.3).

$$\rho \boldsymbol{u} \cdot \nabla \boldsymbol{u} = -\nabla p + \mu \nabla^2 \boldsymbol{u} + \boldsymbol{j} \times \boldsymbol{B} + \boldsymbol{f} \quad \text{(Eq.3)}$$

Marangoni force appears on the free surface of the liquid GaInSn when subjected to a temperature gradient. Marangoni stress on the surface can be expressed as $f = \frac{\partial \gamma}{\partial r}$ $[\frac{\mathrm{N}}{m^2}]$.

Boyancy force appears due to temperature variation along the electrode, causing the liquid metal to rise near the electrode. Dimensionless numbers characterizing the ratios between various effects are calculated to understand the significance of the various effects and which to take into account in the numerical model and interpretation. Material properties used in calculations and numerical models are summarized in table 1.

*Table 1. Properties of the model materials*

| Property/material | Symbol (unit) | GaInSn | Cobalt | Copper |
|---|---|---|---|---|
| Density (at 20 ºC) | $\rho_0$ (kg/m$^3$) | 6360 | 8900 | 8940 |
| Thermal conductivity | $k$ (W/m·K) | 16 | 100 | 398 |
| Heat capacity | $c$ (J/kg·K) | 371 | 450 | 386 |
| Electric conductivity | $\sigma$ (MS/m) | 3.3 | 16 | 58 |
| Seebeck coefficient | $S$ (μV/K) | -0.4 | -25 | 2 |
| Dynamic viscosity | $\mu$ (Pa·s) | 0.03 | | |
| Volumetric thermal expansion | $\beta$ (1/m$^3$) | $1.22 \cdot 10^{-4}$ | | |
| Surface tension | $\gamma$ (N/m) | $0.58 - 1.09 \cdot 10^{-5} \cdot$ T[K] | | |

Ratio between viscous and inertial forces is characterized by Reynolds number *Re*. Ratio between conductive and convective heat transfer is the Peclet number *Pe*. Grasshoff number *Gr* characterizes the ratio between buoyancy and viscous force. Marangoni number *Ma* shows the ratio between Marangoni force and viscous force. Velocity induced magnetic field is characterized by Stuart number *N*.

$$Re = \frac{\rho u L}{\mu}, \qquad Pe_L = \frac{L \rho c u}{k}, \qquad Gr = \frac{L^3 \rho^2 \beta \Delta T g}{\mu^2}, \qquad Ma = \frac{\partial \gamma}{\partial r} \frac{L \rho c \Delta T}{\mu k}, \qquad N = \frac{B^2 L \sigma}{\rho u}$$

Calculation of the dimensionless numbers gives *Re*=150, *Pe*=100, *Gr*=2700, *Ma*=30, *N*=2. Substituting Eq.2 in Eq.3 we can balance thermoelectric term and inertial flow term, velocity order of magnitude can be estimated.

$$u = \sqrt{\frac{L \sigma B S \nabla T}{\rho}} \quad \text{(Eq.4)}$$

This calculation gives us the characteristic TEMC velocity of $u$=34 cm/s

We use optical observation of the free surface to determine the velocity field on the liquid metal pool surface. Tracer particles on the surface are tracked and velocity of the liquid metal is measured. Measured velocity magnitude is up to 10 cm/s. Liquid metal free surface oxidation is one of the problems limiting our ability to observe flow pattern in liquid metal from the surface. Weak HCl acid solution is used to dissolve this oxide film for improved observations.

**Numerical model**

Various physical phenomena are calculated using Comsol 6.0 software. Numerically calculated temperature and temperature gradient is shown in Fig. 2a. Calculated thermoelectric current distribution is shown in Fig. 2b. Calculated buoyancy velocity is shown in Fig.2c and Marangoni velocity in Fig. 2d. Thermoelectromagnetic convection velocity with axial and transverse magnetic fields are shown in Fig. 2e and Fig. 2f respectively. Results show that localized velocities are up to 20 cm/s. Results are in good agreement with estimation of TEMC velocity and flow morphology predicted before and also with results published in previous works. Flow velocity due to Buoyancy (Fig. 2c) and Marangoni (Fig. 2d) effects are much smaller than thermoelectromagnetic flow. For TEMC flow calculation transient 3D model is developed, while for Marangoni and buoyancy convection axially symmetric model gives sufficiently accurate results.

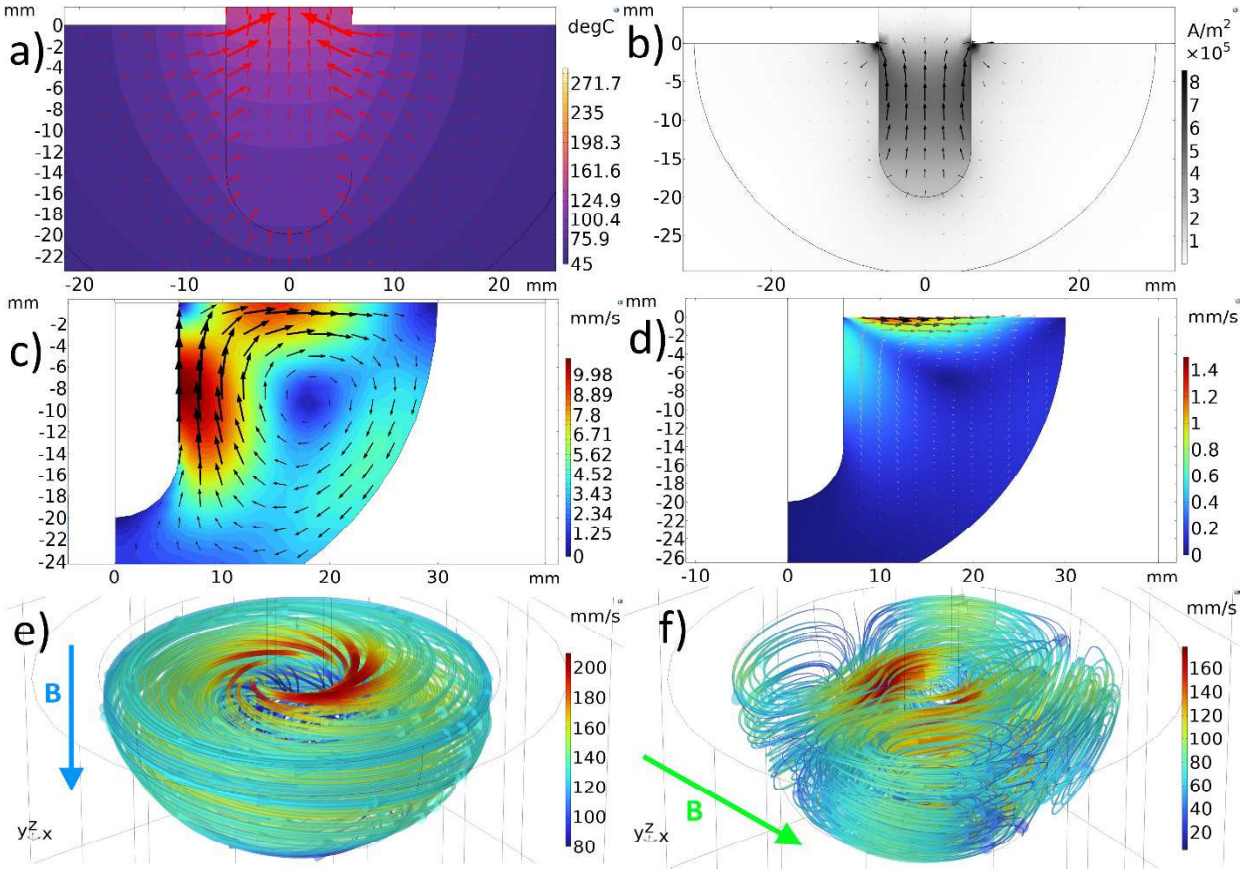


Figure 2. Numerical simulation results: a) Temperature distribution; b) Thermoelectric current distribution; c) Buoyancy velocity; d) Marangoni velocity; e) TEMC velocity with axial magnetic field $B$=0.1 T; f) TEMC velocity with transverse magnetic field $B$=0.1 T

## Conclusions

In this article it was demonstrated that thermoelectromagnetic force can cause significant liquid phase flow. In realistic additive manufacturing situation, a large thermal gradient is present, thus TEMC can be the source of significant molten metal flow. One of the methods to influence the liquid metal flow in the melt pool during additive manufacturing is using a magnetic field and consequently also influencing the solidified structure of the metal. The agreement between observed and numerically calculated results and analytical prediction of the behavior of melt pool under external DC magnetic field is good.

## References

[1] Liu, Cm., Gao, Hb., Li, Ly. et al. (2021). A review on metal additive manufacturing: modeling and application of numerical simulation for heat and mass transfer and microstructure evolution. China Foundry. Vol. 18, 317–334.

[2] Kao, A., Gan, T., Tonry, C., Krastins, I., Pericleous, K. (2020). Thermoelectric magnetohydrodynamic control of melt pool dynamics and microstructure evolution in additive manufacturing. Phil. Trans. R. Soc. A. Vol. 378: 20190249.

[3] Shercliff, J. (1979). Thermoelectric magnetohydrodynamics. Journal of Fluid Mechanics. Vol. 91(2), 231-251.

[4] Kaldre, I., Fautrelle, Y., Etay, J., Bojarevics, A., Buligins, L. (2013). Thermoelectric current and magnetic field interaction influence on the structure of directionally solidified Sn10 wt.%Pb alloy. Journal of Alloys and Compounds, Vol. 571, pp. 50-55.

[5] Xi, L., Gagnoud, A., Ren, Z., Fautrelle, Y., Moreau, R. (2009). Investigation of thermoelectric magnetic convection and its effect on solidification structure during directional solidification under a low axial magnetic field. Acta Materialia. Vol. 57(7), pp. 2180-2197.

[6] Kaldre, I., Fautrelle, Y., Etay, J., Bojarevics, A., Buligins, L. (2010). Investigation of liquid phase motion generated by the thermoelectric current and magnetic field interaction. Magnetohydrodynamics. Vol. 46(4), pp. 371-380.

[7] Kaldre, I., Bojarevics, A., Fautrelle, Y., Etay, J., Buligins, L. (2012). Current and magnetic field interaction influence on liquid phase convection. Magnetohydrodynamics. Vol. 48(2), pp. 399-406.

[8] Kaldre, I., Wang, C., Baranovskis, R. (2019). Experimental investigation of weld pool flow under external dc magnetic field. Magnetohydrodynamics. Vol. 55(4), pp. 469-474.

[9] Vinogradov, D.A., Teplyakov, I.O., Ivochkin, Yu. P., Kharicha, A. (2018). On the applicability of the electrodynamic approximation in the simulation of the electrovortex flow in the presence of an external magnetic field. IOP Conf. Series: Journal of Physics: Conf. Series 1128. 012112.

# Modelling azimuthal velocity of liquid metal in a 2D centrifugal separator driven by a travelling magnetic field

L. Terlizzi*, R. Strazdiņš, L. Goldšteins
Institute of Physics, Jelgavas street 3, Riga LV-1004, Latvia
*lor.terlizzi@gmail.com

**Abstract:** In this study we investigate the EM force and fluid velocity that is developed in a 2D liquid metal centrifugal system driven by a travelling magnetic field. Pressure, azimuthal velocity and torque of a simple analytical model are compared with numerical model results using COMSOL Multiphysics software. An acceptable qualitative agreement between analytical and numerical results is achieved.

**Keywords:** centrifugal, electromagnetic, separator, velocity, numerical.

## Introduction

Purification of liquid metal from small, unwanted solid particles that are by-products of industrial processes is a common problem in metallurgy. In practice purification is achieved using various filtration methods such as sedimentation, mechanical filters, etc.
Another used method is centrifugation that uses rotation of the fluid and inertial forces to separate particles with a density different from that of the fluid itself. Rotation of the liquid metal can be achieved by using a travelling magnetic field, thus inducing a separation of particles. Such a magnetic field can be created by externally rotating magnets, making the system completely contactless – no moving parts are in contact with the liquid metal at any time, thus also improving overall safety, especially for alkali metals.
In this study the developed EM force density in a 2D centrifugal system is investigated numerically and then compared to existing analytical descriptions. The analysis of forces in the system is arguably the first step in its development, as this allows calculating the operational azimuthal velocity of the fluid, which is necessary to find the centrifugal force that the polluting particles will be subjected to.

## System definition and analytical description

Consider a cylindrical liquid metal chamber below which lies a disk with a permanent magnet system. The liquid metal chamber is completely sealed, and the external disk rotates while the chamber remains stationary. Rotation of the disk produces a traveling magnetic field within the chamber. It must be noted that the magnets lie below the outer rim of the chamber visible in Fig. 1, which shows the 2D simplification used to represent the described system. Thus, the external magnetic field in the outer rim area is defined in a complex form of a travelling wave using polar coordinates:

$$\boldsymbol{B_e}(\varphi, t) = B_0 \cdot e^{i(m\varphi - \omega t)} \cdot \boldsymbol{e_z} \quad (1)$$

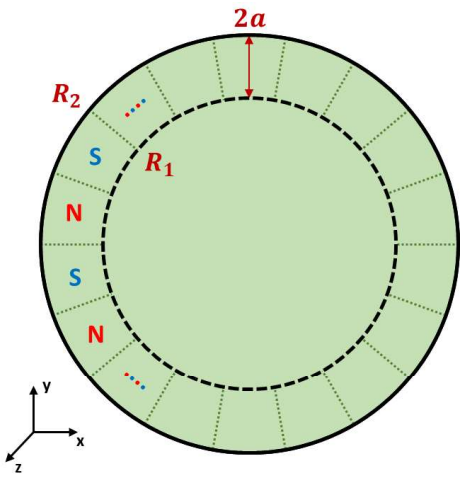


Figure 1. Top view schematic of the centrifugal system. Magnets are placed below the outer rim in periodically opposite polarities. $R_2$ is the external radius of the chamber, while $R_1$ is the radius at which external magnet placement begins.

Here $B_0$ is a constant characteristic magnetic field strength, $m$ is the wave number of N-S pole pairs in the system, and $\omega$ is the angular frequency of the wave, defined as:

$$\omega = 2\pi \cdot n \cdot m \quad (2)$$

Where $n$ is the rotational frequency of the external disk, or in other words the rpm of the motor.

In case of no radial flowrate, it is possible to obtain an expression for the radially averaged azimuthal velocity in the outer rim area [1]:

$$v_\varphi = \frac{v_B N_\lambda}{2} \cdot \left( \sqrt{1 + \frac{4}{N_\lambda}} - 1 \right) \quad (3)$$

Where $N_\lambda$ is known as the interaction parameter, which is defined as:

$$N_\lambda = \frac{\sigma B_0^2 k_v D_h}{\lambda \rho v_B} \quad (4)$$

Where $\sigma$ and $\rho$ are liquid metal conductivity and density, respectively. $v_B$ is the mean tangential speed of the magnet disk, $D_h$ is the hydraulic diameter, and $\lambda$ is a semi-empirical coefficient used to account for turbulent friction.

The factor $k_v$ is the Voldek coefficient [2], which is used to account for the transversal end effect. This coefficient is a nonlinear function of the $Rm_s$ and system geometry:

$$k_v = Re\left[\frac{\alpha^2}{\gamma^2}\left(1 - \frac{tanh(\gamma a)}{\gamma a}\right)\right] \quad (5)$$

$$\gamma = \alpha\sqrt{1 - iRm_s} \quad (6)$$

Where $\alpha$ is the linear wave number and $\tau$ is half the wavelength:

$$\alpha = \frac{2\pi}{2\tau} \quad (7)$$

$$\tau = \frac{2\pi R}{2m} \quad (8)$$

The slip magnetic Reynolds number is defined as:

$$Rm_s = \frac{\mu_0 \sigma (v_B - v_\varphi)}{\alpha} \quad (9)$$

The azimuthal velocity can in turn be used to estimate the pressure developed over the radial direction [1]:

$$\Delta p = \frac{\rho}{2} \cdot \frac{R_2^2 - R_1^2}{R^2} \cdot v_\varphi^2 \quad (10)$$

Where $R$ is the mean radius between $R_1$ and $R_2$. It should be noted that the analytical expressions presented here are based on a few important assumptions. First, the height of the chamber is relatively small compared to the radius. Furthermore, the magnetic field strength is considered constant over the height, and so effects over the height are neglected.

Next, it is assumed that the fluid rotates as a solid body with constant angular velocity, hence the azimuthal velocity is proportional to the radius. Curvature of the system is also neglected so that:

$$R_2 - R_1 = \Delta R \ll R \quad (11)$$

From here, the radially averaged azimuthal EM force density on the system can be found [1]:

$$f_\varphi = \frac{\sigma B_0^2 k_v}{2}\left(v_B - v_\varphi\right) \quad (12)$$

An estimate for the total system torque can be obtained by integrating the torque density $R \cdot \mathrm{f}_\varphi \cdot \boldsymbol{e_z}$ over the active part of the chamber:

$$M = \int_0^b dz \int_0^{2\pi} d\varphi \int_{R_1}^{R_2} R \cdot R \cdot f_\varphi dr = 2\pi b \cdot R^2 f_\varphi (R_2 - R_1) \quad (13)$$

Where $b$ is the height of the chamber. In order to use Eq. 3 and Eq. 10 to find the average azimuthal velocity and pressure over the radial profile, an iterative approach is used with an initial guess of $v_\varphi \approx \omega_B R/2$. Then Voldek's coefficient $k_v$, the friction factor $\lambda$ and the interaction parameter $N_\lambda$ are calculated to find a new $v_\varphi$ according to Eq. 3. This cycle is repeated until $v_\varphi$ has converged.

**Numerical COMSOL model**

The numerical model is based on the same geometry as that of Fig. 1 and solved using COMSOL Multiphysics commercial software. Coupled 2D Navier-Stokes and induction equations are solved with respect to induced magnetic field amplitude using a time harmonic approach. In this model, the magnetic fields are defined as follows:

$$B_e = B_{e0}(x, y) \cdot e^{-i\omega t} \quad (14)$$

$$B_i = B_{i0}(x, y) \cdot e^{-i\omega t} \quad (15)$$

Here, no inherent assumption is made on the spatial distribution of the induced magnetic field, but the external magnetic field is known from Eq. 1. $B_{i0}$ is found from the following convection-diffusion equation:

$$i\omega(B_{e0} + B_{i0}) - v_x \frac{\partial B_{e0}}{\partial x} - v_y \frac{\partial B_{e0}}{\partial y} = -\frac{1}{\mu_0 \sigma} \Delta B_{i0} + v_x \frac{\partial B_{i0}}{\partial x} + v_y \frac{\partial B_{i0}}{\partial y} \quad (16)$$

This is done by the *cdeq* module. Force density is then found from the following expressions:

$$\boldsymbol{j} = \left(\frac{1}{\mu_0} \cdot \frac{\partial B_i}{\partial y}\right)\boldsymbol{e_x} - \left(\frac{1}{\mu_0} \cdot \frac{\partial B_i}{\partial x}\right)\boldsymbol{e_y} \quad (17)$$

$$\boldsymbol{f_{em}} = \left(Re[B] \cdot Re[j_y]\right)\boldsymbol{e_x} - \left(Re[B] \cdot Re[j_x]\right)\boldsymbol{e_y} \quad (18)$$

From the EM force of Eq. 18 an azimuthal semi-empirical friction force is added. This is given by the following equation [1]:

$$\boldsymbol{f_{loss}} = -\frac{\lambda}{D_h} \cdot \frac{\rho_m |\boldsymbol{v}|}{2}\left(v_x \boldsymbol{e_x} + v_y \boldsymbol{e_y}\right) \quad (19)$$

The friction factor $\lambda$ of Eq. 19 is updated in real time based on the current average azimuthal velocity of the simulation. The obtained volume force is then applied to the liquid metal to cause motion of the fluid. This is done by the *spf* module, which solves the following momentum equations:

$$\rho(\boldsymbol{v} \cdot \boldsymbol{\nabla})\boldsymbol{v} = -\boldsymbol{\nabla} p + \boldsymbol{f_{em}} + \boldsymbol{f_{loss}} \quad (20)$$

$$\boldsymbol{\nabla v} = 0 \quad (21)$$

Liquid sodium at 140 degrees Celsius was used as a reference metal. The main material properties used in the simulation are visible in table 1. The MUMPS solver was used to solve the fully coupled problem, with constant Newton method with a 0.2 damping factor. A triangular mesh with around 20000 elements was used, as visible in Fig. 2, which also depicts the respective boundary conditions used on the walls of the chamber. The mesh elements had an average area of 3.34 $mm^2$ per element.

Table 1. Main system parameters.

| | | | |
|---|---|---|---|
| σ, [S/m] | $9 \cdot 10^6$ | μ, [Pa · s] | $5.94 \cdot 10^{-4}$ |
| ρ, [kg/m$^3$] | 920 | $B_0$, [T] | 0.20 |

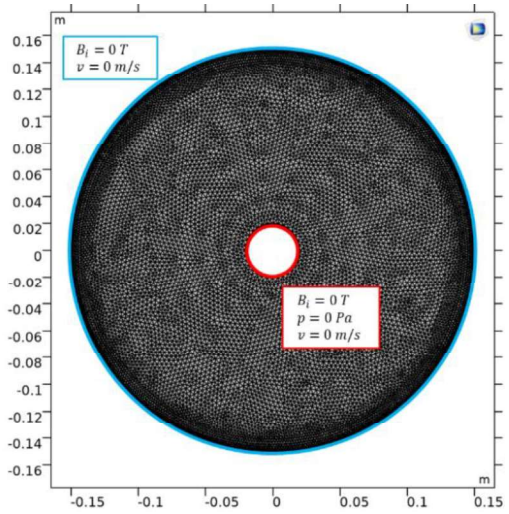


Figure 2. Triangular COMSOL mesh used in the simulation. The text boxes show the respective boundary conditions.

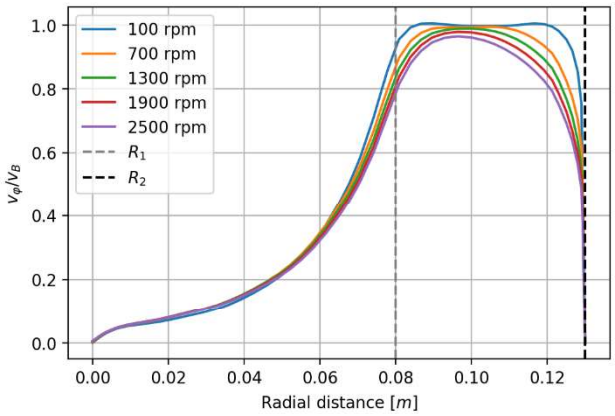


Figure 3. Relative velocity profiles over the radial direction. The curves are the ratio between the tangential velocity of the fluid at a certain radial distance and the tangential velocity of the magnet disk at that same radial distance.

## Results

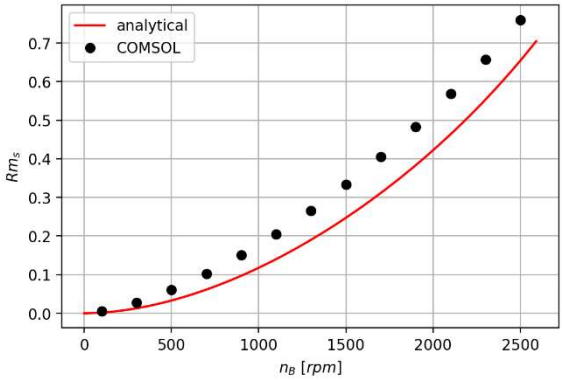


Figure 4. Slip magnetic Reynolds number ($Rm_s$) as function of disk rpm ($n_B$).

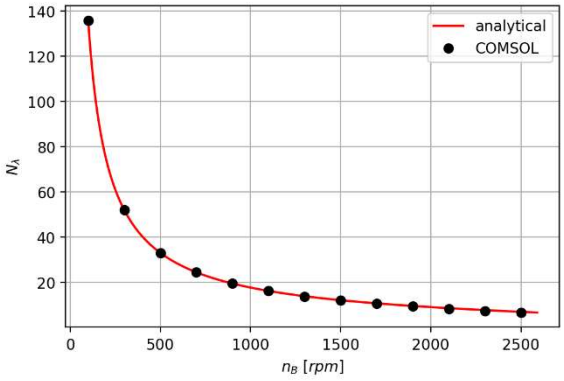


Figure 5. The interaction parameter ($N_\lambda$) as a function of disk rpm ($n_B$).

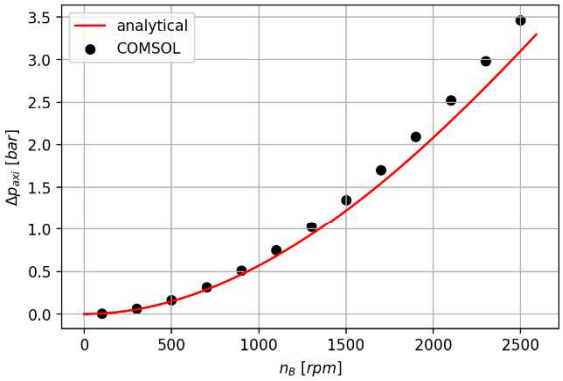


Figure 6. System developed pressure.

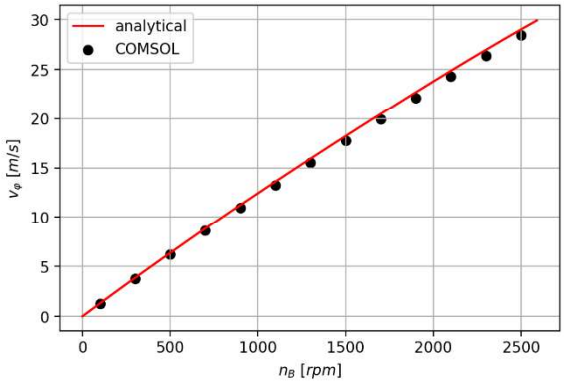


Figure 7. Average system azimuthal velocity.

Fig. 4 and Fig. 5 show the behavior of the main dimensionless system parameters with respect to changing disk speed. Fig. 4 shows that, as the rpm increases, the slip of the system does so too, along with the $Rm_s$. The interaction parameter of Fig. 5 is analytically calculated based on Eq. 4. Numerically it is calculated according to the same formula, but $\lambda$ and $Rm_s$ are updated live during the simulation based on the current average azimuthal speed. Unlike the $Rm_s$, the interaction parameter decreases with increasing disk rpm. Fig. 6 and Fig. 7 depict system pressure and azimuthal velocity, respectively. The pressure of Fig. 6 is the pressure of the liquid at the very outer circumference of the chamber. The figure shows a comparison between data points obtained through COMSOL and Eq. 10. Fig. 7 shows the average system azimuthal velocity. This is the average azimuthal velocity component over the active radial profile. A comparison is shown between data points obtained through COMSOL and the method outlined in Eq. 3.

A comparison of the total system torque is also visible in Fig. 8. This is obtained by integrating the torque density over the entire volume of the chamber. A comparison is shown between data points obtained through COMSOL and the analytical approach of Eq. 13.

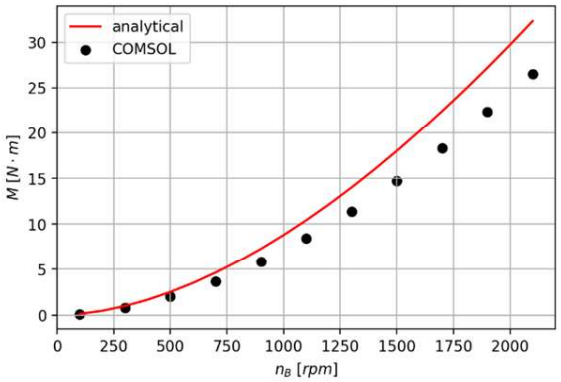


Figure 8. System torque.

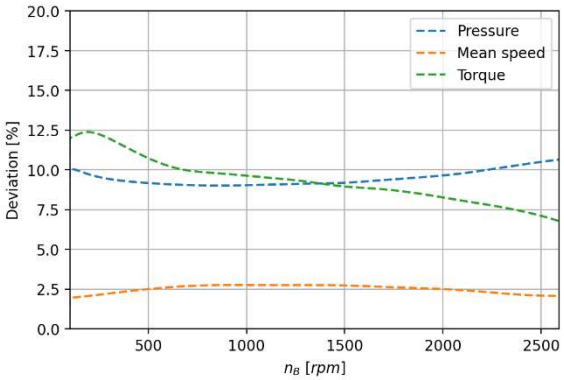


Figure 9. Relative deviations from the numerical model.

The presented figures show an acceptable agreement between the two methods. Fig. 3 specifically shows that the solid body approximation becomes less valid as the rpm of the system increases. A more apt indicator for the validity of the solid body assumption is the interaction parameter $N_\lambda$. It has been shown [1] and analyzed [3] that for large $N_\lambda$: $v_\varphi \approx v_B$ but for low $N_\lambda$: $v_\varphi \approx v_B\sqrt{N_\lambda}$. It is shown in Fig. 5 that the higher this parameter, the more the relative velocity profile of the fluid resembles that of solid body rotation, which in the absolute case is a horizontal line. It should be noted that, in Fig. 3, the system area before $R_1$ is an inactive area where currents do not meaningfully interact with the magnetic field, and hence its contribution to pressure is minimal. Fig. 9 shows the relative deviations of the analytical model from the numerical model for the pressure, mean speed and torque of Fig. 6, Fig. 7, Fig. 8. For the most part, the relative deviation tends to stay below 10% for all 3 indicators.

**Conclusions**

From the presented study it can be concluded that an acceptable agreement between numerical and analytical models was achieved. Fig. 3 in combination with Fig. 5 shows the validity of the solid fluid body rotation assumption for the calculation of average azimuthal velocity with Eq. 3. As the magnet disk rpm increases, the interaction parameter $N_\lambda$ decreases. This is correlated with a change of the relative velocity profile, where the profile becomes less of a horizontal line, which is the solid body case, and begins to curve more and more.

The most important benefit of the presented numerical model is that it can be used to find realistic operational azimuthal velocities of the fluid. In the case of the centrifugal filter, this azimuthal velocity can be used to find the radial velocity at which a particle in the filter will tend to move. That is done by writing out the equilibrium equation for the forces acting on the particle and solving for the radial velocity.

**References**

[1] Goldsteins, L., Bucenieks, I., Buligins, L. (2014). A simplified model of the centrifugal electromagnetic induction pump (CEMIP) with rotating permanent magnets. Magnetohydrodynamics, 50(2), 165-178.

[2] Voldek, A. I. (1974). Induction magnetohydrodynamic machines with a liquid metal working body. (Energia Publ House, Leningrad) (in Russ.)

[3] Goldšteins, L. (2022). Numerical study of a centrifugal electromagnetic induction pump with zero flowrate. Magnetohydrodynamics, 58(1-2), 167-176.

**Magnetic field distribution in disc-type electromagnetic pump with permanent magnets**

*A. Brēķis[1, 2*], A. Šiško[1], I. Bucenieks[1]*

*[1] Institute of Physics University of Latvia, 32 Miera street, Salaspils, Latvia*
*[2] Faculty of Electrical and Environmental Engineering, Riga Technical University, 12/1 Azenes street, Riga, Latvia*

*Corresponding author's e-mail: arturs.brekis@lu.lv

***Key words***: 1) Induction type electromagnetic pumps; 2) disc-type configuration; 3) permanent magnet as main magnetic flux source; 4) magnetic field distribution numerical modelling and experimental mapping.

## Abstract

For this study, disc-shaped medium-power liquid sodium (Na) electromagnetic pumps on permanent magnets were fabricated. The paper presents an analytical formulation of a disc-type induction pump's magnetic field calculation problem. Before the liquid metal experiments in the Na circuit, the distribution of the primary magnetic field due to permanent magnets was experimentally measured. In order to compare this with a theoretical simulation, a numerical 3D model of the magnetic field was constructed. Finally, the p-Q curves of the pump have been experimentally obtained on a new sodium circuit built at the Alkali Metals Laboratory of the Latvian University Institute of Physics (LUFI) and compared with the calculation of the p-Q curves through numerical simulation of the magnetic field.

# Simulation of autothermal reforming of methane in a packed-bed reactor

V. Dzelme, V. Geža, A. Jakovičs
Institute of Numerical Modeling, University of Latvia

Autothermal reforming (ATR) is a process of methane reforming where energy for endothermic reactions is supplied by exothermic oxidations reactions.[1] The main feed components are methane (or natural gas), steam and oxygen (or air). The heat balance and product composition can be controlled by the ratio of carbon/oxygen/steam.[2]

ATR is typically performed over various catalysts, such as small porous pellets with Ni or Pt content.[2][3] Reaction kinetics depend on specific active element, effective surface area, support material etc., and are normally determined experimentally.

In this work, we develop a numerical model of ATR in Ansys CFX using reaction kinetics from literature [4]. The model considers the catalyst bed as a porous medium, with the effective hydraulic and thermal parameters determined from particle-resolved simulations with a small number of catalyst pellets. We study the influence of feed composition, temperature and pressure on product gas composition.

[1] J.R. Rostrup-Nielsen. Production of synthesis gas. *Catalysis Today*, Vol. 18, 1993. https://doi.org/10.1016/0920-5861(93)80059-A
[2] S. Ayabe, H. Omoto, T. Utaka, R. Kikuchi, K. Sasaki, Y. Teraoka, K. Eguchi. Catalytic autothermal reforming of methane and propane over supported metal catalysts. *Applied Catalysis A: General*, Vol. 241, 2003. https://doi.org/10.1016/S0926-860X(02)00471-4
[3] L. Chen, Z. Qi, S. Zhang, J. Su, G.A. Somorjai. Catalytic hydrogen production from methane: a review on recent progress and prospect. *Catalysts*, Vol. 10. 2020. https://doi.org/10.3390/catal10080858
[4] M.H. Halabi, M.H.J.M. de Croon, J. van der Schaaf, P.D. Cobden, J.C. Schouten. Modeling and analysis of autothermal reforming of methane to hydrogen in a fixed bed reformer. *Chemical Engineering Journal*, Vol. 137, 2008. https://doi.org/10.1016/j.cej.2007.05.019

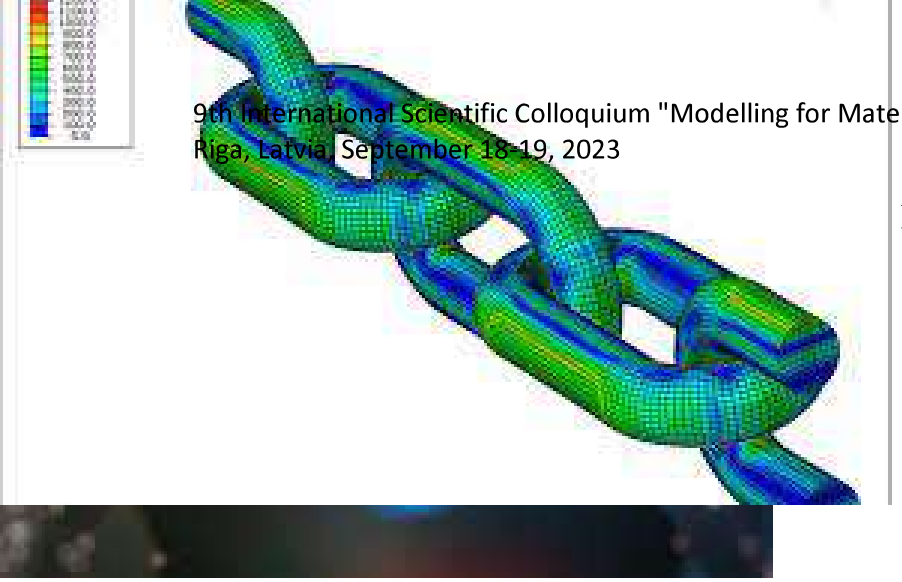

9th International Scientific Colloquium "Modelling for Materials Processing".
Riga, Latvia, September 18-19, 2023

# Finite element method calculations coupled with circuit simulator

Vadims Geza[1], Kirill Bolotin[1*]

1. University of Latvia, Jelgavas street 3, Riga LV-1004, Latvia

*kirill.bolotin@lu.lv

Abstract: Modeling of electromagnetic systems using the finite element method (FEM) usually involves a number of simplifications, such as changes in geometry, the absence of some elements and boundary conditions. It should be noted separately that current or voltage sources may also be subject to simplification, while real conditions may be more complex and have a significant impact on the result. SPICE (Simulation Program with Integrated Circuit Emphasis) is a powerful open-source simulator used for designing and analyzing various electrical circuits. Its application in combination with FEM-based models allows for a more detailed description of the investigated electromagnetic system. Publication discusses the advantages and disadvantages of popular software packages based on SPICE, as well as some limitations and issues associated with the numerical methods used in them. The final part includes an example of investigating an induction crucible furnace and its power supply system.

**Keywords:** Finite element method, electromagnetic, SPICE, numerical simulation, modeling

## Introduction

Finite element simulations of electromagnetic systems are usually a simplification of real system. Simplifications involve changes in geometry (neglecting irrelevant geometrical objects like screws, holes), neglecting physical phenomena that has low order of impact. Boundary conditions prescribed at the border of finite element model is also a simplification. In electromagnetic systems those are magnetic field behavior at outer boundary and prescribed source. Usually fixed current or fixed voltage is used as source condition in numerical simulations.

However, real conditions are more complicated, as those can involve power conditioners, impedance matching and other electronic components. Also, power source can be power controlled (output is fixed power instead of fixed voltage/current). Furthermore, AC power source output frequency can depend on load impedance. General purpose finite element method packages have limited features for including these electronics-related effects in the model. E.g. two popular electromagnetic simulation open-source packages (Getdp [1] and Elmer [2]) both have possibility to include simple circuits in the model, but they are limited to simple circuits with only R, L, and C components. Creation of more complex circuits is limited in these software packages. For instance, it is not possible to include MOS device using data manufacturers data directly. On the other hand, simulation of electric circuits is much easier in programs that are specially designed for this purpose.

SPICE (Simulation Program with Integrated Circuit Emphasis) is an open source general purpose electronic circuit simulator. It is a program used in the design of both integrated circuits and printed circuit boards to check the integrity of the circuit and to analyze its behavior. It's combines various analysis modes (DC Analysis, AC Small-Signal Analysis, Transient Analysis, Pole-Zero Analysis, Small-Signal Distortion Analysis, Sensitivity Analysis, Noise Analysis and others) and an extensive library of device models (liner and non-liner elements, semiconductor, logic and others) [3]. As an input, SPICE allows to use both a netlist with a description of the circuit, and enter information through a graphical command interface, the analysis results are also formed as a separate text file, and can be displayed in a graphical representation.

Thus, SPICE is a powerful simulator that allows to design and analyze various circuits, but it also has limitations, for example, the researcher himself must monitor the admissibility of using certain components, since the simulator cannot simulate their failure due to an incorrect mode of operation, other than that, it should be understood that SPICE idealizes the circuit. To understand how this happens, need to say a few words about the methods of its work. Simulator is based on the calculation of the formed sparse system of differential equations, based on the modernized method of nodal potentials, therefore, the methods for solving this system of equations play an important role, since they can affect not only the mathematical part, but also the physical representation of the processes it describes. Another difficulty is related to the modeling of magnetic circuits that describe the magnetic circuits of both electronic components and in electrical installations.

SPICE has three approaches to this problem: linear and non-linear inductance modeling, and magnetic coupling modeling. In the first and second cases, we are talking about the analysis of electronic components, for which many different parameters of resistance, capacitance and inductance are considered. The third case considers an ideal transformer consisting of several linear inductors. All three methods have limitations and do not allow modeling and analyzing real components and installations, the magnetic core of which can have a complex and branched shape, and the windings can have a non-standard connection scheme. In [4] the author partially circumvents this limitation by using a modernized method of magnetic coupling, using the elements of an electric circuit to represent a magnetic circuit, this method has the right to life, but the magnetic circuit is again idealized in it, so again its shape is not taken into account, which can significantly affect the final result.

Other possibility to tackle this problem is, again, coupling with FEM models where precise magnetization curve is taken into account.

**NgSpice2FEM**

Finite element models allow calculating local field values and also global variables like inductance, resistance, power loss, etc. for complicated geometries, but cannot tackle complex electrical circuits. To tackle this problem, small library (500 lines of code) is written to allow coupling of NgSpice with fem package. Library is available in git https://gitlab. com/vadims.geza/ngspice2fem In this case FEM package is a controller, which calls circuit calculation at needed point. Fig. 1 shows schematic of NgSpice2Fem workflow:

1. FEM program needs certain values for calculation (e.g. current, voltage, frequency),

and calls NgSpice2Fem dynamic library. Input required from FEM program is

(a) Values from FEM calculation (e.g. inductance, resistance)

(b) Spice netlist to execute (usually in .cir format)

(c) Which values should be returned

2. NgSpice2Fem calls NgSpice

3. NgSpice performs netlist calculation

4. NgSpice2Fem gathers all the data and performs required operations, (averaging, ff t, etc)

5. NgSpice2Fem sends requested data back to FEM program

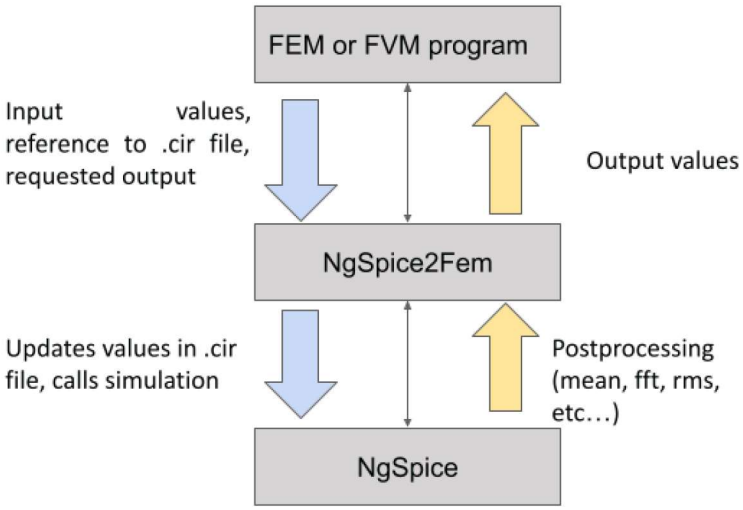


*Figure 1. Schematic of NgSpice2Fem workflow.*

In this work flow NgSpice can be called multiple times during an iterative process. NgSpice calculations are run in the time domain, therefore NgSpice2Fem performs required operations to obtain results that are applicable for the FEM model. For this purpose, external libraries are utilized - Armadillo [5] and BLAS [6].

**Example of work**

First usage example a crucible filled with aluminum which is molten by means of Joule heating. Here EM stirring is not taken into account, and only electromagnetic and thermal problems are solved. System consists of a crucible with height 570mm and diameter 316mm filled with aluminum, and an inductor connected to the power circuit (Figure 2). Although this is simple scheme of Royer oscillator, it is capable to of showing the principle of coupling and possibilities that circuit coupling offers. The figure for showing the circuit is created in LTSpice which is free to download, but it lacks described API to allow coupling. For this reason, circuit after creation is exported to spice netlist. Sometimes it requires small editing, as NgSpice has slight differences. Also NgSpice lacks library of components, but those can be downloaded from manufacturers website and included in the model.

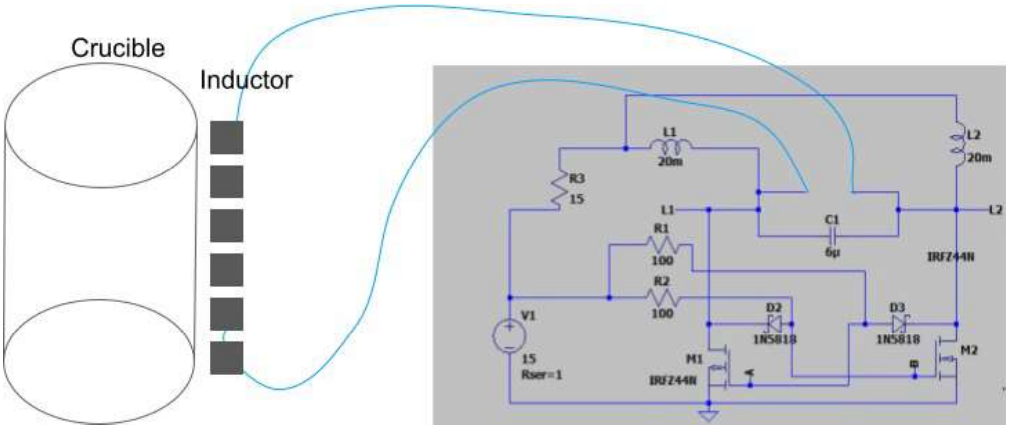


*Figure 2. FEM model of aluminum melting crucible connected to spice-circuit*

In the described system it is expected that inductance of load changes when aluminum goes over melting temperature. It happens due to increase in aluminum resistivity which leads to increased inductance. Inductance changes are related to variation of skin-depth and magnetic flux area. This, however, leads to changes in operating frequency.

In Figure 3 process parameters are shown (Frequency, Voltage, Load Inductance). At the initial stage, frequency is 7550 and it immediately starts to decrease and drops to around 6 kHz at the end of process. Changes in maximal temperature reached in aluminum are shown in Fig. 4 Resulting changes in temperature due to inclusion of frequency variation are approx. 50 degrees. A conclusion can be drawn that taking into account frequency variation can really change the results but these changes are of low impact.

On the other hand, in industrial usage it might still be important to use this circuit coupling, as it allows testing equipment with real process parameters instead of just specifying voltage or current at the load.

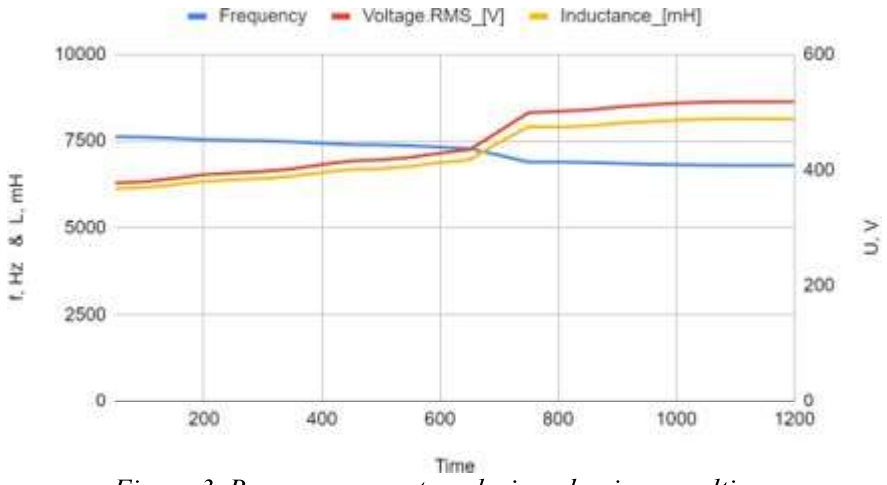


*Figure 3. Process parameters during aluminum melting*

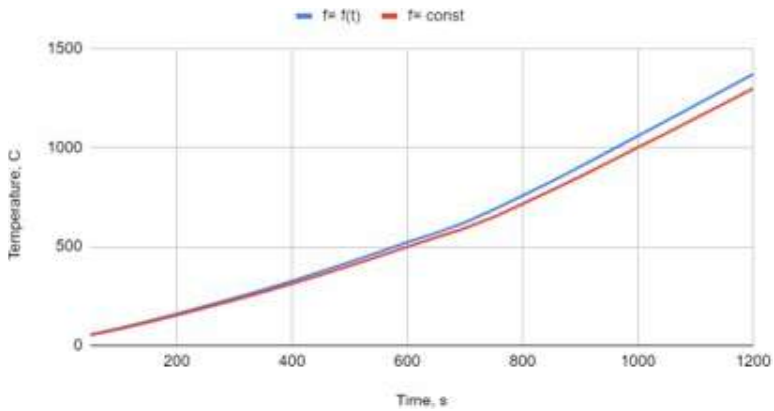


Figure 4. Maximal temperature reached in aluminum during heating with fixed and varying frequencies

**Conclusions**

There are other possible applications where circuit coupled FEM approach can be used.

1. PID controlled simulations. E.g. this would allow specifying expected temperature, and controller would set regulate power to achieve and hold expected temperature. Manually performing these operations is very time-consuming. Although creating cir- cuit of PID controller is more complicated than using equations that represent it, this approach would still be interesting for those who are interested in electronics part of PID. Coupling of PID with FEM is also already known idea - such approach is already shown in [7] where the finite element model in the feedback control loop in the Matlab-Simulink was used.

2. Induction MHD pumps. Such pumps usually have many windings and what is also observed, that phase shift imbalance can lead to reduced efficiency. These problems are investigated in electrical motors [8]. Similar approach can be used for MHD pumps and circuit coupling would help investigating such problems.

3. MHD generators. To accurately simulate electrical machines it is useful to connect FEM simulation with frequency converter, transformer, network and other components. Such approach is realized in [9]. MHD generators simulation would benefit from including electrical circuit as it would allow obtaining more industry-relevant parameters.

NgSpice2Fem is a self made library which simplifies calling of Spice circuit simulator an obtaining data required for FEM calculation. The API is still tested with only few applications and software packages. However, it can be freely modified if necessary as it is open source.

**References**

[1] P. Dular and C. Geuzaine . GetDP reference manual: the documentation for GetDP, a general environment for the treatment of discrete problems. http://getdp.info.

[2] I. Kondov and G. Sutmann . Multiscale Modelling Methods for Applications in Materials Science (2013).

[3] T. Quarles . Spice3 version 3f3 user's manual, 1993.

[4] V. Volodin (2008). Modeling of complex electromagnetic component of the spice simulator lt-spice/swcad iii. Komponenty i tekhnologii, vol. 4, pp. 175–182.

[5] C. Sanderson and R. Curtin (2016). Armadillo: a template-based c++ library for linear algebra. Journal of Open Source Software, vol. 1, no. 2, p. 26.

[6] R. van de Geijn and K. Goto (2011). BLAS (Basic Linear Algebra Subprograms), Boston, MA, pp. 157–164.

[7] D. Marcsa (2015). Control of a fi nite element based dynamic system. PRZEGLD ELEKTROTECH-NICZNY , vol. 1, pp. 157–160.

[8] A. Adekitan and A. Ogunjuyigbe (2019). The impact of supply phase shift on the three phase induction motor operation. Engineering Review, vol. 39, pp. 270–282.

[9] S. Kanerva, S. Seman, and A. Arkkio (2005). Inductance model for coupling finite element analysis with circuit simulation. Magnetics, IEEE Transactions on, vol. 41, pp. 1620 – 1623.

**Optical imaging of MHD bubble flow in a Hele-Shaw liquid metal cell**

A. Jegorovs, M. Birjukovs, A. Jakovics
University of Latvia

Bubble flow in liquid metal controlled by magnetic field (MF) is a topic of interest in both metallurgy (e.g., melt mixing or purification) and physics in general. Understanding bubble path oscillation and inter-bubble interaction mechanisms in MF is vital for scientific and engineering advancement – however, general mechanisms are still widely debated [1]. Relatively precise measurements of bubble flow in downscaled systems can be done using X-ray or neutron radiography [2]. To some extent, bubble flow can be studied optically if metal is confined between closely spaced transparent plates (a Hele-Shaw cell), resulting in quasi-2D flow. The major benefits of this method are its much lower cost and complexity. Hele-Shaw bubble flow in MF is also of interest for studying collective dynamics, which are intensified by geometric confinement. Previous optical imaging attempts were limited to 1 mm cell thickness [3]. In this paper, we explore the use of an optical method to analyse characteristics of bubble flow subjected to different configurations of applied stationary MF. The experimental setup consists of an acrylic Hele-Shaw cell with internal dimensions of 160 x 100 x 3 mm3, argon gas supply and mass flow controller, a stationary camera (350fps, 2MP, grayscale), and illumination. To prevent the formation of oxides, a low concentration of hydrochloric acid (HCl) is used. Homogeneous backlight and side illumination enable the capture of bubbles that contact one or both walls via light transmittance through the bubble or via light reflection of the bubble's interface. The developed data processing pipeline includes bubble position extraction from images using contour recognition and subsequent contour analysis as a time-series. Preliminary results indicate that observed physical interactions are in-line with observations from radiography cases. Major challenges are oxide formation on acrylic vessel walls and data extraction of bubble position based solely on the bubble's interface reflections. Nonetheless, developed method provides cheap and reproducible method for studying bubble flow collective dynamics. Data processing code is in active development and is available on GitHub.

[1] Keplinger, O., Shevchenko, N., & Eckert, S. (2019). Experimental investigation of bubble breakup in bubble chains rising in a liquid metal. In International Journal of Multiphase Flow (Vol. 116, pp. 39–50). Elsevier BV. https://doi.org/10.1016/j.ijmultiphaseflow.2019.03.027
[2] Birjukovs, M., Trtik, P., Kaestner, A., Hovind, J., Klevs, M., Gawryluk, D. J., Thomsen, K., & Jakovics, A. (2021). Resolving Gas Bubbles Ascending in Liquid Metal from Low-SNR Neutron Radiography Images. In Applied Sciences (Vol. 11, Issue 20, p. 9710). MDPI AG. https://doi.org/10.3390/app11209710
[3] Klaasen, B., Verhaeghe, F., Blanpain, B., & Fransaer, J. (2014). A study of gas bubbles in liquid mercury in a vertical Hele-Shaw cell. In Experiments in Fluids (Vol. 55, Issue 1). Springer Science and Business Media LLC. https://doi.org/10.1007/s00348-013-1652-x

# Numerical analysis of condensation risk in different multilayer building structures

B. Jirgensone, A. Jakovičs

Institute of Numerical Modelling, University of Latvia

In this mainly numerical study we compare thermal comfort conditions in different structures with cooling conditions in capillary heating systems and will it affect mold risk in the constructions. Numerical models were created in WuFi and Comsol. Both programs model one-dimensional and use the finite volume method. Each structure was adapted to the walls, ceilings and floors in the experiment. The properties of the construction materials have been searched from the available resources and compared as much as possible to the existing materials. In order to have as similar boundary conditions as possible in both programs, calculations will be performed initially without moisture and heat radiation transfer, if the results converge, moisture and heat radiation will be applied.

There is a constant heat flux boundary condition in each construction in the whole air layer to create a similar layer as heat capillary system. For cooling capillary heat flux interval is $q = -20$ to $-90\ W/m^2$. The heat flux was changed to see at what point there will be mold risk in construction.

Numerical modeling results show that there is no risk of mold when the capillary system is used as a cooling system in exactly these used structural models at certain capillary system capacities. More attention should be paid to the air layer, where the cooling capillary system and the largest temperature difference in the entire structure are located. Experimental measurements will be used to validate and adjust both numerical models.

**Title: The calibration of turbulence model for melt flow in floating zone growth of silicon crystals**

Authors: K. Surovovs, S. Stroževs, M. Surovovs, J. Virbulis

Institution: Institute of Numerical Modelling, Faculty of Physics and Mathematics, University of Latvia

Keywords: silicon, crystal growth, floating zone

Multiple numerical models exist for the melt flow during the floating zone growth of silicon. They consider several aspects in detail, for example, dopant transport in gas [1] or non-symmetrical 3D shape of the crystallization interface [2]. However, there are at least two ways how these models can be improved, which are targeted in the present work.

Firstly, due to the limited experimental data, the range of applicability of the melt flow model is not known. The verification of these models was performed using only one crystal growth experiment for each model. It is therefore useful to compare the results of the model with the series of latest available experiments, performed in the Institute for Crystal Growth, Berlin.

Secondly, the previously developed models use a laminar approximation of the melt flow. However, Reynolds numbers for liquid silicon motion in the floating zone system are in the range of 2000-4000, depending on what is considered as a characteristic geometrical size of the system.

The present work is devoted to the numerical modelling of phase boundaries, turbulent melt flow and dopant transport in the floating zone system with crystal diameter of 102 mm. The model verification is performed by comparison with the photographs of experimental process and with the measured electrical resistivity distribution in the grown crystals. The coefficients of the large eddy simulation (LES) turbulence model are calibrated based on the performed parameter studies.

[1] A. Sabanskis, K. Surovovs, J. Virbulis, "3D modeling of doping from the atmosphere in floating zone silicon crystal growth", *Journal of Crystal Growth.*, vol. 457, p. 65-71, 2017.

[2] X. Han, X. Liu, S. Nakano, H. Harada, Y. Miyamura, K. Kakimoto, "3D numerical analysis of the asymmetric three-phase line of floating zone for silicon crystal growth", *Crystals*, vol. 10, p. 121, 2020.

# A well coupled multi-scale model of additive manufacturing based on phase field method, cellular automata method and lattice Boltzmann method

**Ling Shi[a], Jiang Wang[a,*], Songzhe Xu[a,*], Jingjing Li[a], Chaoyue Chen[a], Tao Hu[a], Hari Sundar[b], Zhongming Ren[a]**

[a]State Key Laboratory of Advanced Special Steels, School of Materials Science and Engineering, Shanghai University, Shanghai, China

[b]School of Computing, University of Utah, Salt Lake

## Abstract

A multi-scale model of additive manufacturing process is established based on phase field, automata cellular method and lattice Boltzmann method. For macro-scale, the VISCA method (modified automata cellular method) and shan-chen model (lattice Boltzmann method for multi-phase flow) are deeply coupled to reproduce the grain growth, powder melting, molten pool flow. The solidification structure and pore defects of multi-layer additive manufacturing process can be simulated by macro scale model. The crystal orientation distribution and pore defects were experimental observed by EBSD and SEM for the validation of macro-scale model. For meso-scale, a tiny domain around macro molten pool boundary is modeled by phase field method. Based on the crystal orientation, temperature gradient and solidification velocity witch solved by macro-scale model, the dendritic growth and laves phase formation is simulated by phase field model. The solidification microstructure and laves phase distribution were experimental observed by SEM for the validation of meso-scale model.

*Keywords:* Additive manufacturing; Cellular Automata method; Lattice Boltzmann method; Phase field method; Solidification microstructure; Solidification defects

∗Corresponding author

Email addresses: songzhex@shu.edu.cn (Songzhe Xu), jiangwang@i.shu.edu.cn (Jiang

# Modelling Liquid Metal Free-Surface Capillary Flow for Nuclear Fusion Applications

S.Mingozzi[a,b], M. Iafrati[c]

[a]*Eindhoven University of Technology, De Zaale, Eindhoven 5612AZ, The Netherlands*
[b]*Renaissance Fusion,22 Rue Jean Pierre Timbaud, 38600 Fontaine, France*
[c]*ENEA, C.R. Frascati, Via E. Fermi 45,00044 Frascati, Roma, Italy*

**Abstract**

In this work we developed a numerical model to investigate liquid metal capillary flows for fusion reactor applications. Liquid Metal (LM) boundaries for the reactor walls offer critical advantages in terms of Plasma-Facing (PF) Components, including heat flux handling, plasma confinement, extended component lifetimes [1]. The most mature LM technology is based on the use of Capillary Porous Systems (CPS) for delivering and retaining the metal [2, 3]. However, issues concerning replenishment and stabilization of the free LM surface still prevent the deployment of LM systems [4, 5]. The development of clear metrics and modelling tools are necessary to address these issues.

Here, we focused on capillary rise as a benchmark. We developed a numerical model to investigate how different CPS internal geometries affect the capillary performance in terms of capillary pressure and rising velocity of liquid metal.

The COMSOL Multi-physics model built resolves the time-dependent multi-phase flow of two immiscible and incompressible fluids: liquid tin in a gaseous molecular hydrogen atmosphere. Inside the CPS domain, the liquid front is tracked with the Level-Set method [6]. The CPS is modelled by the spatial repetition of an elementary cell.

Preliminary studies have shown that different CPS geometries exhibit different capillary performance. This suggests the possibility of using this tool to discriminate between different CPS designs. Preliminary results hint that increasing the wetted perimeter increases the capillary pressure, thus the replenishment speed and possibly free surface stabilization. Future work will aim to provide quantitative numerical and experimental insights to help optimize CPS design and improve LM-based systems for fusion applications.

*Keywords:* Nuclear Fusion, Liquid Metals, Capillary Porous Systems, Free-Surface, Interface-resolved modelling, CFD, Plasma-Facing Components

## References

[1] A. De Castro, C. Moynihan, S. Stemmley, M. Szott, D. N. Ruzic, Lithium, a path to make fusion energy affordable, Physics of Plasmas 28 (2021).

[2] R. E. Nygren, F. L. Tabarés, Liquid surfaces for fusion plasma facing components—A critical review. Part I: Physics and PSI, Nuclear Materials and Energy 9 (2016) 6–21.

[3] S. Roccella, G. Dose, R. de Luca, M. Iafrati, A. Mancini, G. Mazzitelli, CPS Based Liquid Metal Divertor Target for EU-DEMO, J Fusion Energ 39 (2020) 462–468.

[4] G. Zuo, et al., Results from an improved flowing liquid lithium limiter with increased flow uniformity in high power plasmas in EAST 59 (2018) 016009. Number: 1 Publisher: IOP Publishing.

[5] T. W. Morgan, A. Vertkov, K. Bystrov, I. Lyublinski, J. W. Genuit, G. Mazzitelli, Power handling of a liquid-metal based CPS structure under high steady-state heat and particle fluxes, Nuclear Materials and Energy 12 (2017) 210–215.

[6] COMSOL, Comsol 6.1 cfd userguide, https://doc.comsol.com/6.1/docserver/#!/com.comsol.help.cfd/cfd_ug_math_levelset_phasefield.14.37.html, 2023.

*Corresponding author
*Email address:* simone.mingozzi@renfusion.eu (S.Mingozzi)

# Numerical modelling of feed rod melting dynamics during floating zone silicon crystal growth

Maksims Surovovs[1]* and Janis Virbulis[1].
*lead presenter: maksims.surovovs@lu.lv
1 Institute of Numerical Modelling, University of Latvia, 3 Jelgavas street, LV-1002, Riga, Latvia

Present work showcases stationary and time-dependent numerical modelling of inhomogeneous melting front structures in the floating-zone single silicon crystal growth. In such systems, the open melting front of polycrystalline feed rod is covered with thin fluid film that ensures a continuous flow of molten silicon into the melt. This flow is influenced by fine (~3 mm) island and ring structures that are present due to non-uniform melting of the polycrystalline material. The size of these structures is dependent on the process parameters and can increase, slowing or interrupting the steady flow in the fluid film. In extreme cases, these structures can reach the inductor coil surface, leading to system failure.

The aim of the present study is to address the shortcomings of the previous attempts of open melting front modelling. Plate et al. [1] modelled the melting of the polycrystalline feed rod using a 3D model, but neglected the presence of inhomogeneous structures. Bergfelds et al. [2] used a local model to describe the development of ring-like structures, however, melt flow was not included in the coupled simulations, leading to reduced precision of the obtained structure shape.

The developed program uses open-source software OpenFOAM and couples electromagnetic field, heat transfer, and melt flow simulations in a thin fluid layer on the open melting front. Three phase environment is considered, and precise shapes of phase boundaries can be determined applying moving meshes. Initial simulations were quasi-stationary and focused on determining the shape of the melting front structures and the resulting fluid film thickness. Then, the time-dependent change of these criteria was considered, including the breaking of the film and forming of solid islands. To achieve this, melt flow simulations were performed using volume of fluid method.

Parameter studies were performed and the influence of different process parameters, such as crystal pulling rate and inductor coil frequency, on the shape and size of the inhomogeneous melting front structures at different positions on the melting front was evaluated. Simulations show that the size of these structures increases in outer parts of the feed rod, as well as in regions with large interface slopes. Time-dependent simulations were employed to determine if and how the continuous flow can be re-established in such cases with large melting front structures.

[1] M. Plāte, K. Dadzis, A. Krauze, R. Menzel, J. Virbulis, *Journal of Crystal Growth*, **2019**, 521, 46-49.

[2] K. Bergfelds, J. Virbulis, A. Krauze, *Magnetohydrodynamics*, **2015**, 51(2), 397-406.

# Numerical study of heating and melting of metal in industrial direct current electrical arc furnace

S. Pavlovs[1*], A. Jakovics[1], A. Chudnovsky[2]

1. University of Latvia, Jelgavas street 3, Riga, Latvia
2. JSC LATVO, Ganibu Dambis street 53, Riga, Latvia
*e-mail: sergejs.pavlovs@lu.lv

**Abstract:** The article is devoted to the study of the heating and melting processes for industrial direct current electrical arc furnace (DC EAF). Numerical modelling was performed using the enthalpy and porosity approach at equal values of the solidus and liquidus temperatures of the metal, when mushy zone is represented with linear distribution of mass fraction. Heat flux, supplied through arc spot, is estimated using heat balance equation taking into account metal heating and melting, *Joule* heat, radiation at metal mirror and convective heat transfer at metal vessel, covered with firebrick. Electrical parameters of arc between top electrode and melt mirror are estimated using heat flux value. Computed distributions of metal liquid/solid mass fraction make it possible to estimate duration of heating and melting.

**Keywords:** electrovortex flow (EVF), Large Eddy Simulation (LES), enthalpy and porosity approach, fine metal, mushy zone.

## Introduction

Previous studies of the authors are related to the numerical and experimental study of the EVF and the temperature field in a liquid metal, placed in a vessel with DC power supply through a system of bifilar electrodes [1]. The developed and experimentally verified numerical approach [1] was applied to calculate the turbulent EVF of the melt, the homogenization process of melt temperature and alloying additive concentration [2] in the industrial DC EAF.

The further development of numerical approach [3], which is associated with the simulation of heating and melting of metal, was approved for mini DC EAF (with a capacity of 4.6 kg of molten steel). Mini furnace was developed, manufactured and installed at *LATVO JSC* (Riga, Latvia). The melt temperature measurements using probe with thermocouples sensor and with infra-red camera as well as melt speed estimations using snap-shots of particle moving at melt mirror were performed [3].

The current paper deals with the simulation of heating and melting in industrial scale DC EAF with a capacity of 3.6 tons of molten steel. The prototype is DC EAF, which is installed at *LATVO* plant (detailed references can be found in [2]).

The schematic of DC EAF is shown in Fig. 1a [2]. The geometric parameters of electrodes and supplied DC, the geometric parameters of melt and vessel as well as physical parameters of melt, electrodes and vessel are collected in Tables 1, 2.

## Numerical modelling of heating and melting processes

An enthalpy and porosity approach is used for modelling of heating and melting processes [4].

In order to track melt interface the liquid fraction $\xi_l$ in every cell volume of mesh in metal domain is computed at each iteration taking into account an enthalpy balance. The liquid fraction indicates the fraction of the cell volume that is in liquid form. For so-called “mushy region” the value of liquid fraction $\xi_l$ is $0 < \xi_l < 1$. The relationship between liquid fraction $\xi_l$ and solid fraction $\xi_s$ is as follows

$$\xi_l = 1 - \xi_s \quad (1)$$

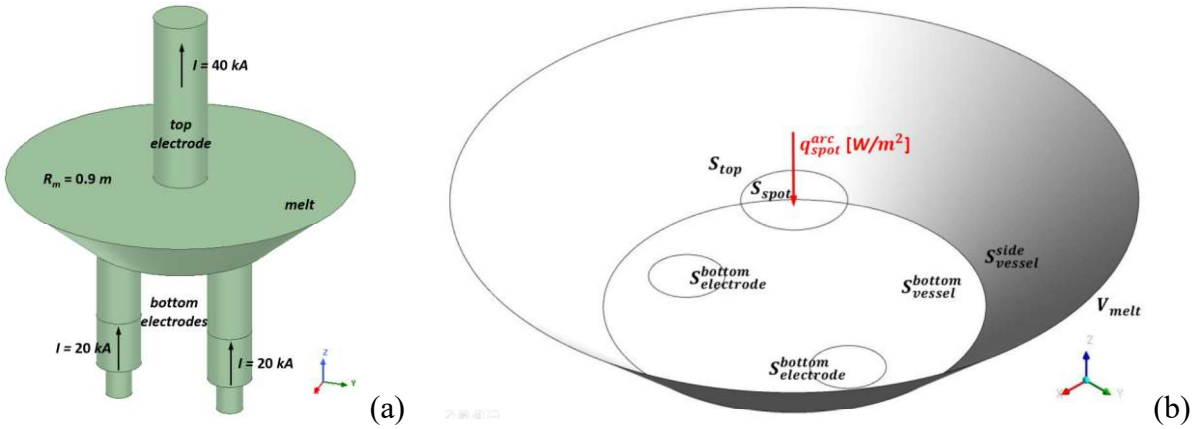


Figure 1. Models of industrial scale DC EAF for computations of: (a) electromagnetic field; (b) solid/liquid metal temperature and melt EVF – with *Ansys Maxwell* and *Fluent* packages

The mushy region with partially melt material is considered as a pseudo-porous medium. The value of porosity $\Pi$ increases from $\Pi_s = 0$ for solid phase to $\Pi_l = 1$ for liquid phase as the material is melting: $\Pi_s = 0 < \Pi < 1 = \Pi_l$. The relationship between porosity and solid or liquid fraction is the following: $\Pi = 1 - \xi_s = \xi_l$.

Sequent, the velocity increases from $\boldsymbol{V} = \boldsymbol{V}_s = 0$ for solid material in a cell, when porosity is $\Pi_s = 0$, to the velocity value in fully liquid cell $\boldsymbol{V} = \boldsymbol{V}_l$

$$\boldsymbol{V} = \begin{cases} \boldsymbol{V_l} & \text{for liquid phase} \\ (1-\xi_s)\boldsymbol{V}_l = \xi_l \boldsymbol{V}_l & \text{for the mushy region} \\ \boldsymbol{V}_s = 0 & \text{for solid phase} \end{cases} \quad (2)$$

The enthalpy $H$ of the material is defined as the sum of the sensible enthalpy $h$ and the latent heat $\Delta H$

$$H = h + \Delta H \qquad h = h_{ref} + \int_{T_{ref}}^{T} c_p dT \quad (3)$$

where $h_{ref}$ is reference enthalpy, $T_{ref}$ is reference temperature, $c_p$ is specific heat at constant pressure.

The latent heat $\Delta H$ is considered as function of temperature $T$ in the following form

$$\Delta H(T) = \begin{cases} \Delta H = h_{melting} & \text{for } T \geq T_{liquidus} \\ [1-\xi_s(T)]h_{melting} = \xi_l(T) h_{melting} & \text{for } T_{liquidus} > T \geq T_{solidus} \\ 0 & \text{for } T < T_{solidus} \end{cases} \quad (4)$$

where $h_{melting}$ is the latent heat of the material.

In order to identify the latent heat evolution in the mushy region, the relationship of the local solid fraction and the temperature is chosen in linear form

$$\xi_s(T) = \begin{cases} 0 & \text{for } T \geq T_{liquidus} \\ \dfrac{T_{liquidus} - T}{2T_{liquidus}} & \text{for } T_{liquidus} > T \geq T_{solidus} \\ 1 & \text{for } T < T_{solidus} \end{cases} \quad (5)$$

Mushy zone is represented with linear distribution of mass fraction.

This relationship (5) can be applicable for pure materials (e.g. fine metals), where phase changes occur at a distinct temperature, t.i. in the case of equal liquidus and solidus temperature values $T_{solidus} = T_{liquidus}$ of metal.

When the phase change occur over temperature range (e.g. alloys), it is necessary to apply more complicated equilibrium diagrams of phase change.

Table 1. Geometric parameters of the melt, the electrodes and parameters of supplied DC

| **Melt vessel (a truncated cone)** | |
|---|---|
| Top (melt mirror) radius | $r_m^{top} = 0.9\ m$ |
| Bottom radius | $r_m^{bottom} = 0.5\ m$ |
| Height | $H_m = 0.335\ m$ |
| **Top electrode** | |
| Radius of the arc spot at the melt mirror | $r_{el}^{top} = 0.14\ m$ |
| **Bottom electrodes** | |
| Radius of electrode without blades | $r_{el}^{bottom} = 0.115\ m$ |
| Distance between the axes of electrodes | $L_{el-el}^{bottom} = 0.6\ m$ |
| Offset of the electrode axes from the symmetry plane | $L_{shift}^{bottom} = 0.1\ m$ |
| **Direct current (DC)** | |
| Top electrode | $I_{el}^{top} = 40\ kA$ |
| Each of two bottom electrodes | $I_{el}^{bottom} = 20\ kA$ |

Table 2. Physical parameters of the electrodes, the melt, and firebrick vessel

| **Iron (Fe) melt** | |
|---|---|
| Electrical conductivity | $\sigma_m = 1.1 \cdot 10^6\ S/m$ |
| Density | $\rho_m = 6.8 \cdot 10^3\ kg/m^3$ |
| Viscosity | $\eta_m = 1.2 \cdot 10^{-3}\ kg/(m \cdot s)$ |
| Thermal expansion coefficient | $\beta \sim 9.9 \cdot 10^{-6}\ K^{-1}$ |
| Specific heat capacity | $c_m = 775\ J/(kg \cdot K)$ |
| Thermal conductivity | $\lambda_m = 33\ W/(m \cdot K)$ |
| Emissivity | $\varepsilon_m = 0.5$ |
| Melting point | $T_{melting} = 1538.85℃$ |
| Latent heat of melting | $h_{melting} = 2.471 \cdot 10^5\ J/kg$ |
| Boiling point | $T_{boiling} = 2860.85℃$ |
| Latent heat of vaporization | $h_{vapor} = 6.088 \cdot 10^6\ J/kg$ |
| **Furnace cover** | |
| Emissivity | $\varepsilon_{cover} = 0.3$ |
| Temperature | $T_{cover} = 873\ K$ |
| **Firebrick vessel** | |
| Density | $\rho_f = 1.8 \cdot 10^3\ kg/m^3$ |
| Specific heat capacity | $c_f = 1250\ J/(kg \cdot K)$ |
| Thermal conductivity | $\lambda_f = 0.5\ W/(m \cdot K)$ |
| Thickness | $d_f = 0.25\ m$ |
| Convective heat transfer coefficient | $\alpha_{conv} = 10\ W/(m^2 \cdot K)$ |
| **Graphite (C) top electrode** | |
| Electrical conductivity | $\sigma_e^{top} = 7 \cdot 10^4\ S/m$ |
| **Steel bottom electrodes** | |
| Electrical conductivity | $\sigma_e^{bottom} \sim 1.1 \cdot 10^6\ S/m$ |
| Thermal conductivity | $\lambda_e = 33\ W/(m \cdot K)$ |

**Governing equations**

Governing equations – energy (6), momentum (7) and continuity (8) – for melting problems solution can be written as follows:

$$\frac{\partial(\rho H)}{\partial t} + \nabla(\rho H \boldsymbol{V}) = \nabla(\lambda \nabla T) + \frac{|\boldsymbol{J}|^2}{\sigma} - \frac{\partial\left(\rho \overline{V'_\iota h'}\right)}{\partial x_i} \quad (6)$$

$$\frac{\partial(\rho \boldsymbol{V})}{\partial t} + \frac{\partial\left(\rho V_i V_j\right)}{\partial x_j} = -\nabla p + \eta \Delta \boldsymbol{V} + \rho \boldsymbol{g}(1 - \beta \Delta T) + \boldsymbol{J} \times \boldsymbol{B} + \boldsymbol{f}_{mush} - \frac{\partial\left(\rho \overline{V'_\iota V'_J}\right)}{\partial x_j} \quad (7)$$

$$\frac{\partial \rho}{\partial t} + \nabla(\rho \boldsymbol{V}) = 0 \quad (8)$$

Buoyancy, or the *Archimedes* force, is modelled with the *Boussinesq* approximation.

Physical fields and parameters in equations (6)–(8) are the following: $\boldsymbol{V}, p$ are the velocity and pressure fields in the melt; $\boldsymbol{J}$ and $\boldsymbol{B}$ are electrical current density and its self-magnetic field; $T$ is temperature; $\boldsymbol{g}$ is gravitational acceleration; $\eta, \rho, \beta, c, \lambda, \sigma$ are dynamic viscosity, density, coefficient of thermal expansion, specific heat capacity, thermal conductivity, electrical conductivity.

The momentum sink in the mushy zone due to the reduced porosity in equation (7) is derived as follow:

$$\boldsymbol{f}_{mush} = -\frac{(1 - \xi_l)^2}{\xi_l^3 + \epsilon} \cdot \boldsymbol{V} \cdot A_{mush} \quad (9)$$

where $\epsilon = 0.001$ is a small number in order to prevent division by zero and $A_{mush}$ is the mushy zone constant with dimension $[kg/(m^3 \cdot s)]$.

The vector of turbulent enthalpy flux $\rho \overline{V'_\iota h'}$ and tensor of turbulent (*Reynolds*) stresses $\rho \overline{V'_\iota V'_J}$ are modelled with LES approach. Note, that sink, which is similar to equation (7) with the same constant, is added to all equations, which describe transport of turbulence.

The numerical approach is realized in *Ansys Fluent* commercial software package.

**Boundary conditions**

The scheme of industrial DC EAF for numerical modelling of the melt EVF and for the heating and melting processes is shown in Fig. 1b.

The boundary conditions for melt flow are the following:

• no-slip conditions at surfaces of the vessel ($S_{vessel}^{side}; S_{vessel}^{bottom}$) and the bottom electrodes ($S_{electrode}^{bottom}$) as well as at liquid/solid boundaries in case of partly molten metal.

• free slip conditions at the melt mirror ($S_{top}; S_{spot}$).

The boundary conditions for temperature are the following:

• heat flux $q_{spot}^{arc}$ is supplied through the spot of arc ($S_{spot}$);

• heat radiation from the top surface of the metal ($S_{top}$;) accept for the arc spot zone;

• convective heat transfer at the vessel ($S_{vessel}^{side}; S_{vessel}^{bottom}$) taking into account thermal resistance of firebrick with thickness $d_f$ (Table 2);

• heat transfer through bottom electrodes ($S_{electrode}^{bottom}$) from the melt to cross-sections of electrodes, which are not covered with firebrick.

**Heat flux supplied through the spot of the arc**

Heat flux $q_{spot}^{arc}$, which is supplied through the spot of the arc ($S_{spot}$) at the melt mirror, is estimated with heat balance equation (10) in case when whole volume of liquid metal is at temperature $T_{melting}$. The right part of equation (10) contains the following terms:

• heat radiation from the top surface of the metal; the furnace has a cover with emissivity $\varepsilon_{cover}$ and temperature $T_{cover}$;

• convective heat transfer with coefficient $\alpha_{conv}$ at metal vessel covered with firebrick ($S_{vessel}= S_{vessel}^{side} + S_{vessel}^{bottom}$);

• heat transfer through bottom electrodes ($S_{electrode}^{bottom}$); temperature of electrodes, which are not covered with firebrick, is cooling temperature $T_{cooling}$;

• metal heating from chosen initial temperature $T_{initial}$ till melting temperature $T_{melting}$ and then metal melting;

• *Joule* heat source.

$$q_{spot}^{arc}S_{spot} = \frac{\sigma_{SB}\left(T_{melting}^4 - T_{cover}^4\right)S_{top}}{1/\varepsilon_m + 1/\varepsilon_{cover} - 1} + \frac{\alpha_{conv}\lambda_f}{\lambda_f + \alpha_{conv}d_f}\left(T_{melting} - T_a\right)S_{vessel} + \frac{2\lambda_e}{d_f}\left(T_{melting} - T_{cooling}\right)S_{electrode}^{bottom} + \frac{c_m\rho_m V_{melt}\left(T_{melting} - T_{initial}\right)}{\Delta t} + \frac{h_{melting}V_{melt}}{\Delta t} - \int_{V_m}\frac{|\boldsymbol{J}|^2}{\sigma}dV \quad (10)$$

The equation (10) includes the estimated time $\Delta t$ of melt heating and melting processes.

Estimated value $q_{spot}^{arc} \sim 5.1 \cdot 10^7\ W/m^2$ is obtained using parameters from Tables 1, 2 as well as chosen $\Delta t\ =\ 30\ min$ and $T_{initial} = T_a = 323.15\ K$.

According to performed estimations, the arc is the source of 99.8% of heat supplied to the melt, the rest (0.2%) is *Joule* heat in the melt. More than 89% of supplied heat is necessary for metal heating (71.8%) and melting (17.2%).

Values of the voltage $U_{arc}$ and the resistance $R_{arc}$ of the arc can be calculated from estimated value of the heat $Q_{arc} = q_{spot}^{arc}S_{spot}$ supplied from the arc to the melt

$$U_{arc} = \frac{Q_{arc}}{I_{el}^{top}} \quad R_{arc} = \frac{U_{arc}}{I_{el}^{top}} \quad (11)$$

Estimated value are: $U_{arc}$ ~ 78.2 V; $R_{arc}$ ~ 0.002 Ω; electrical power $P_{arc}$ ~ 3.1 MW.

**Computational results**

Computational results for fine iron ($T_{solidus} = T_{liquidus}$) the heating and melting processes are obtained for mushy zone constant is $A_{mush} \sim 10^3\ kg/(m^3 \cdot s)$.

The mass fraction of liquid phase and the instantaneous velocity vectors for EVF of the melt are shown in Fig. 3 (a,b) for cross-section y = 0. The flow time moments corresponds to parts [in %] of molten metal, chosen from Fig. 2, which illustrate the acceleration of melting process due to intensification of EVF in increasing volume of liquid zone.

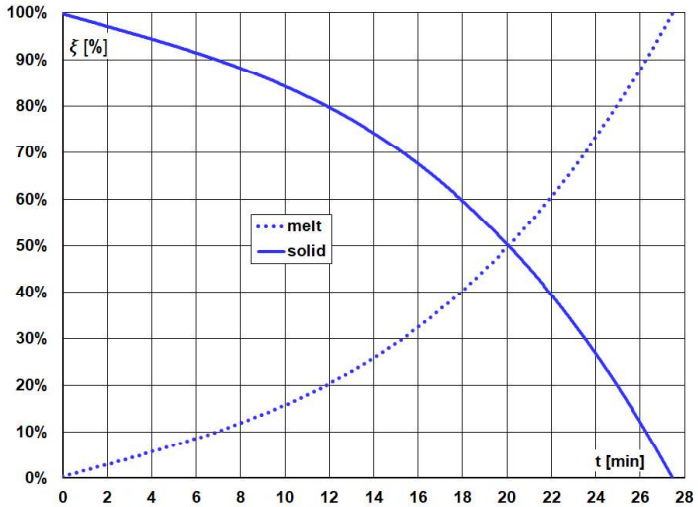


Figure 3. Liquid $\xi_l$ and solid $\xi_s$ mass fraction as function of time $t$

The total time of metal heating and melting, obtained with computations, is $\Delta t$~27.5 min (Fig. 2). This value is very close to $\Delta t$~30 min value, which was used for estimation of heat flux from the arc in equation (10) – the difference is ~7.5%.

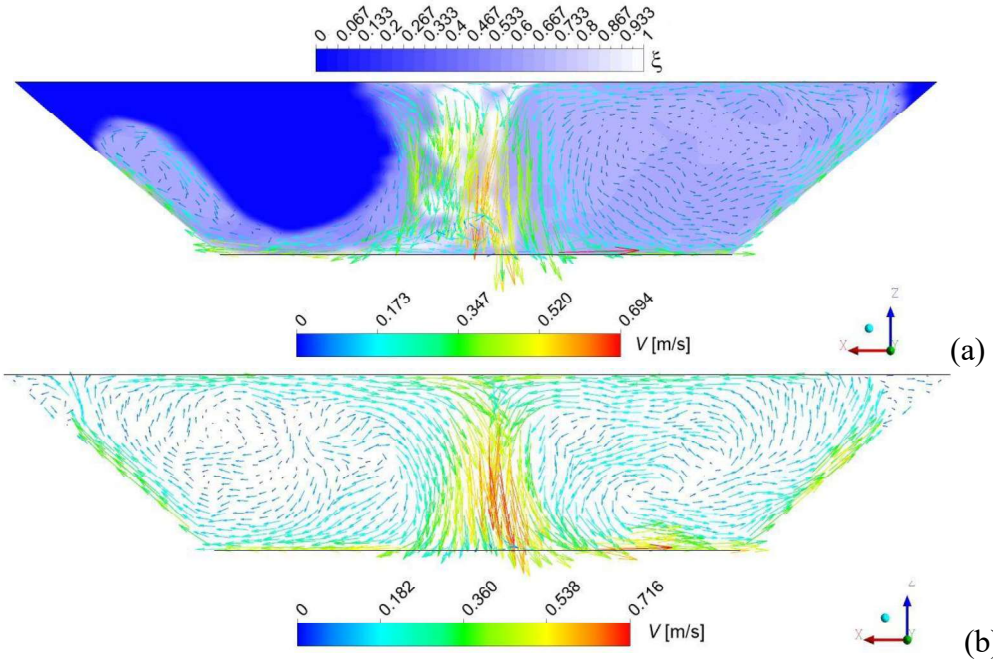


Figure 3. Instantaneous distributions of mass fraction contours of solid/melt (blue/white) and melt velocity vectors: (a) t = 1220 s – 50% of melt; (b) t = 1675 s – 100% of melt

**Unresolved problems of computational model**

The melt temperature distributions near central zone of the arc are not physically correct ($T > T_{boiling}$), because the *Ansys Fluent* module for melting process computations does not cover boiling phenomenon of liquid. According to consideration in [3], the influence of this small volume on whole volume of the melt is vanishingly small.

**Conclusions**

Obtained numerical results illustrate dynamics of heating and melting process as well as make it possible estimations of integral time of metal melting.

The reason for the acceleration of melting process is the intensification of electrovortex flow in a continuously increasing volume of molten metal.

Distribution of liquid zone in metal volume during melting is influenced by molten metal flow structure, which depends on position of bottom electrodes – the offset of axis of bottom electrodes from symmetry plane in industrial DC EAF results the non-symmetry of liquid zone.

**References**

[1] Pavlovs, S., Jakovics, A., Chudnovsky, A., Ivochkin, Yu., Teplyakov, I., Vinogradov D. (2022) Numerical and experimental study of electrovortex flow and temperature field in liquid metal with bifilar power supply. Magnetohydrodynamics, 58 (1–2), 65–79.

[2] Pavlovs, S., Jakovics, A., Chudnovsky, A. (2022) EVF and melt homogenization in the industrial direct current electrical arc furnace. Magnetohydrodynamics, 58 (3), 305–326.

[3] Pavlovs, S., Jakovics, A., Chudnovsky, A. (2023) Numerical modelling of heating and melting of metal in mini industrial direct current electrical arc furnace // Proc. of International Symposium on Heating by Electromagnetic Sources – HES-23, Padua (Italy), ID31:1–8.

[4] Voller, V.R., Prakash, C. (1987) A fixed grid numerical modelling methodology for convection-diffusion mushy region phase-change problems. International Journal of Heat and Mass Transfer, 30 (8), 1709–1719.

# Improving the Ekibastuz coal quality using "dry enrichment" technology

Shaimerdenova K.M.[1], Sakipova S.E.[1], Abdirova N.T.[1], Tussupkhanova A.P.[1], Shunkeev T.[2]

[1]E.A. Buketov University, Karaganda, Kazakhstan, sesaule@mail.ru
[2]LLP Ekibastuz brick factory, Ekibastuz, Kazakhstan

Global climate change, caused by increasing harmful emissions into the atmosphere, necessitates a widespread transition from hydrogen energy to the development of technologies for converting renewable energy sources (RES). Kazakhstan is developing a national strategy for low-carbon development until 2050, aimed at reducing the energy intensity of GDP by 50% compared to 2008 levels. At the state level, voluntary commitments have been made to reduce harmful carbon emissions into the atmosphere. But according to official data, at the end of 2022 in Kazakhstan, 70% of electricity is generated from coal, 20% from gas, about 6% from water energy, and about 3.7% comes from renewable energy sources. Such statistics is due to the fact that Kazakhstan has huge (about 34 billion tons) coal reserves, which are enough for at least 200-300 years. Therefore, along with strategic plans to increase the share of implemented renewable energy projects, develop and actively implement "clean coal" technologies.

This paper discusses the possibility of improving the Ekibastuz coal quality through the use of "dry enrichment" technology. The experiments and calculations carried out made it possible to determine the optimal scheme for enrichment of samples of thermal coals from the Ekibastuzsky open pit of "Angrensor-Energo" LLP. Testing of technical characteristics, such as moisture content, ash content, volatile matter yield) and calculation of energy characteristics of enriched samples of thermal coal was carried out in 3 stages in a coal chemistry laboratory. As a result, it was found that the energy content of the enriched fuel samples increased to 28.5% of the original. This significantly improved consumer properties by obtaining the maximum yield of high quality coal concentrate. Consequently, the developed scheme of enrichment allows to significantly reduce the consumption of electricity, reduce emissions into the atmosphere, reduce the harmful impact on the environment, and expand the markets for coal.

# Power calculation in a 2D axisymmetric centrifugal separator with traveling magnetic field

Rūdolfs Strazdiņš* Lorenzo Terlizzi Linards Goldšteins
Rudolfs.Strazdins@lu.lv Lorenzo.Terlizzi@lu.lv Linards.Goldsteins@lu.lv
*Corresponding author's e-mail: Normunds.Jekabsons@lu.lv

Institute of Physics, University of Latvia,
3 Jelgavas street, LV-1002 Riga, Latvia

***Keywords***— power, centrifugal, magnetic, separator, numerical

**Abstract**

A common problem in metallurgy is that metals often have impurities. The solution is to filter them out, usually using a mechanical filter. However, this approach has several disadvantages such as requiring regular replacement and cleaning as the filter congests.

Another approach is to use centrifugal (inertial) forces created by travelling (rotating) magnetic field fields using e.g. permanent magnets. This centrifugal separator can be modelled as an axisymmetric system 2D system, similarly to a centrifugal electromagnetic pump. Travelling fields will induce currents, which will create forces that will rotate the liquid metal and create inertial forces on particles. Thus, particle impurities will move in the radial direction, creating separate areas of clean and polluted metal.

In this study both analytical and numerical model are created to estimate the required power to drive this system, which is one of the main parameters in the design process of such a device.

## References

[1] A. I. VOLDEK. Induction Magnetohydrodynamic Machines with Liquid Metals as a Working Medium (Energia Publ House, Leningrad, 1970) (in Russian).

[2] I. BUCENIEKS. Perspectives of using rotating permanent magnets for electromagnetic induction pump design. Magnetohydrodynamics, vol. 36 (2000), no. 2, pp. 151–156.

# Ultrasonic Doppler Velocimetry for melt flow in model experiments for Czochralski crystal growth

*I. Tsiapkinis, A. Wintzer, S. Foroushani, K. Dadzis*
Leibniz-Institut für Kristallzüchtung (IKZ), Max-Born-Str. 2, 12489 Berlin, Germany
iason.tsiapkinis@ikz-berlin.de

The Czochralski (CZ) method is used in the industry and research to grow single crystaline materials with high purity. During the growth process, the melt flow has a significant impact on the homogeneity and quality of the crystal. Despite its importance, fundamental questions about typical flow patterns are still unanswered and many numerical models lack sufficient validation. Low-temperature model experiments offer a reliable method for investigating flow phenomena in detail and obtaining data for model validation. The main advantage of such model experiments is easier access for various in-situ measurement techniques. In this work, we design model experiments representing the CZ method as seen in Fig. 1, and measure velocity inside the melt with the non-invasive Ultrasonic Doppler Velocimetry (UDV) technique. As model material, we use tin with a melting point of 232°C. This enables us to study the melt flow during an actual crystal growth process [1], compared to previous studies in the literature where mostly GaInSn without a crystallization process has been used [2]. We address problems of UDV measurements in liquid tin: application of waveguides [3] to withstand high temperatures; acoustic contact with the melt; and furnace access. We discuss the flow patterns and their significance to the CZ growth process and evaluate experimental uncertainties.

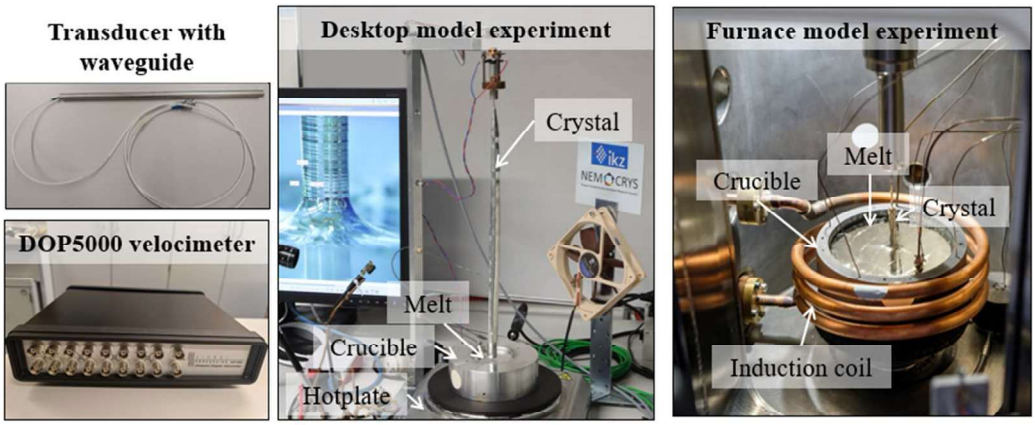


**Fig. 1**: UDV equipment (left), CZ model experiments with tin (middle and right). Velocity profiles are measured through crucible side in desktop model and crucible bottom in furnace model.

**Acknowledgment:** We thank our former colleague Dr. Josef Pal as well as colleagues from the department of Magneto-hydrodynamics at the Helmholtz-Zetrum Dresden-Rossendorf (HZDR) for providing valuable assistance and guidance during the initial testing phase. The NEMOCRYS project has received funding from the European Research Council (ERC) under the European Union's Horizon 2020 research and innovation programme (grant agreement No 851768).

[1] A. Enders-Seidlitz et al. *IOP Conf. Ser.: Mater. Sci. Eng*. 1223 (2022) 012003. DOI: 10.1088/1757-899X/1223/1/012003
[2] O. Pätzold et al. *J. Cryst. Growth*, 588 (2022) 126656. DOI: 10.1016/j.jcrysgro.2022.126656
[3] S. Eckert et al. *Experiments in Fluids*, 35 (2003) 381. DOI: 10.1007/s00348-003-0606-0

# INFLUENCE OF SURFACE WAVES ON LIQUID-TO-GAS MASS TRANSFER IN MOLTEN SILICON

G. Zageris*, V. Geza, S. Pavlovs

Institute of Numerical Modeling, University of Latvia
3 Jelgavas street, Riga, LV-1004, LATVIA
*e-mail: girts.zageris@lu.lv

This paper focuses on the numerical analysis of the mass transfer of impurities from the waved surface of molten silicon to the gas phase. The mathematical model is described herein, with the modeling of a wavy silicon melt surface being done with the moving mesh technique. The model employs assumptions about the mass transfer process on the surface, and they are described as well. The model is verified against limited experimental data for a stationary melt surface, and reasonable agreement is obtained. Thereafter, numerical studies are undertaken for a wavy melt surface. The dependence of impurity removal rate on the wave amplitude, wavelength and frequency is analyzed. It is shown that the waves on the surface of the liquid increase the mass transfer rate in a certain parameter range. Finally, results are analyzed to find an explanation for this increase and to determine technological factors that impact it. A criterion for the minimal wave amplitude required to obtain improved impurity removal is found and discussed.

**Keywords**: *Surface waves, mass transfer, computational fluid dynamics, silicon refinement.*

## 1. INTRODUCTION

The requirement for alternative energy sources, e.g. solar, wind, hydro, etc., is growing because of the exhaustion of fossil fuel resources, with growing energy consumption and global warming. One of the most attractive sources is solar power, which is divided in two types - direct conversion to electricity (photovoltaics - PV) and solar power concentration systems. PV systems are more widely used because they can be used for applications of different scales. As shown in [1], the energy cost for solar power is still higher than for hydro, onshore wind, geothermal and even biomass energy sources. To diminish this cost difference, the reduction of production costs for PV cells is necessary. PV cell costs are directly connected with costs for raw materials, e.g. polysilicon. Reduction of energy consumption during production of polysilicon is one of the key steps towards solar power becoming more accessible.

In 2012, it was shown that production of polysilicon constituted approx. 14% of the total solar cell costs [2]. This number can be reduced by lowering energy consumption during solar grade silicon (SoG-Si) production. Most silicon production starts with reduction of quartzite or sand with carbon materials [3]. Such a process can achieve a purity of up to 99%. To achieve higher purity, there are two ways – the chemical and the metallurgical route. The metallurgical route consumes about 30 kWh/kgSi (kilowatt-hours per kilogram of silicon) of energy. In comparison, the chemical route such as the Siemens process, which is the most widely used refining process nowadays, consumes 65 kWh/kgSi [4].

In the metallurgical route for silicon production, directional solidification is used to remove metallic impurities. The most problematic elements are boron and phosphorus because their removal via the directional solidification method is limited due to their high segregation coefficients. In many investigations, phosphorus removal is found to be the most challenging task, since the purity threshold (<1 ppm) was not reached [5]. Although oxidation and slag refinement is a simple process for removing phosphorus from silicon, it is insufficient to reach the high purity threshold. The most popular approach for phosphorus removal is evacuation. In [6], it was shown that the rate for phosphorus evaporation corresponds to a first order reaction and that

under medium vacuum conditions the evaporation rate is determined by chemical evaporation at the surface and gas phase mass transfer.
For boron removal, a well known approach is blowing oxidizing gas on the free surface of the melt [7]. The highest boron refining rates can be achieved with plasma refining, but it has a high energy demand. In reactive gas refining, the concentration of boron changes according to a first order rate law

$$\ln\left(\frac{C_{\mathrm{B},0}}{C_{\mathrm{B},t}}\right) = k_{\mathrm{B}}\frac{St}{V}\#(1)$$

Here $C_{\mathrm{B}}$ is the boron concentration with indices after comma indicating time, $S$ is the area of interfacial surface between oxidizing gas and silicon melt, $V$ is the volume of silicon melt, $t$ is time, $k_{\mathrm{B}}$ is the boron mass transfer coefficient at the surface, measured in µm/s. In fact, the reaction occuring at the interface is of second order, however, the concentration of the reacting gas is kept constant by continuously supplying gas to the surface, thus the law describing reaction rate becomes first order effectively. $k_{\mathrm{B}}$ is determined experimentally and is dependent on the oxidizing gas supply rate, the type of oxidizing gas, and melt temperature. Typical $k_{\mathrm{B}}$ values found in literature are $6-40$ µm/s [7], [8], [9], and the value for $k_{\mathrm{P}}$ is 2-5 µm/s for phosphorus [6]. The typical melt temperature is ≈1425 °C.
The creation of surface waves would, in principle, increase the S/V ratio, thus speeding up boron removal. Though under normal operating conditions no waves are generated during the purification process, it has been shown that waves on liquid metal surfaces can be generated, for example, by contactless electromagnetic interaction in mercury both experimentally [10] and theoretically [11]. Therefore, it would potentially be of interest to create waves during purification to increase process efficiency.

## 2. MODEL DESIGN AND BOUNDARY CONDITIONS

### 2.1. Problem description

The physical system considered in this study is that of a cylindrical tank which contains molten silicon. The oxidizing gas is introduced via a centrally located cylindrical pipe directly above the melt. The impurities located inside the melt can then evacuate from it via the melt-gas interface and escape the tank together with the gas flow. Then surface waves are introduced on the silicon melt to study the impact of these waves on the overall purification efficiency.
In cases where this study focuses on the diffusion of the impurities on a larger time scale, the entire system (melt + gas) is modeled with a stationary interface. However, when the effects of a wavy surface are studied, only the gas domain is modeled. In this case, the silicon melt is only taken in account in the form of a boundary with a certain harmonic profile and a constant impurity concentration.
To reduce the need for substantial computational resources, the problems are modeled with 2D axi-symmetric geometries.
In this study, the gas blowing above the melt is assumed to have the same viscosity as dry air $\nu = 1.511\cdot10^{-5}$ m$^2$/s [12].

### 2.2. Model equations

To describe this problem, one needs to describe the fluids in motion. The motion of an incompressible fluid is governed by the Navier-Stokes equations (Eq. 2). The additional information necessary to describe fluid flow is the conservation of mass (Eq. 3), expressed by the equation of continuity.

$$\frac{\partial \boldsymbol{u}^*}{\partial t^*} + (\boldsymbol{u}^* \cdot \nabla)\boldsymbol{u}^* = -\nabla p^* + \frac{1}{Re}\nabla^2 \boldsymbol{u}^* \#(2)$$

$$\nabla \cdot \boldsymbol{u}^* = 0 \#(3)$$

$$Re = \frac{UL}{\nu} \#(4)$$

The mass transfer equation is written in the form of

$$\frac{\partial C}{\partial t^*} + \boldsymbol{u}^* \cdot \nabla C = \frac{1}{Pe_m} \nabla^2 C \#(5)$$

$$Pe = \frac{LU}{D} \#(6)$$

These equations implicitly take in account the following assumptions:

- The fluid is incompressible
- The fluids in consideration are Newtonian
- The diffusion coefficient of the impurities $D$ is independent of spatial coordinates

To numerically investigate the role of surface waves on impurity removal from silicon, the open-source toolbox *OpenFOAM* is used. The main algorithm for calculating the flow and impurity diffusion is *pimpleDyMScalarFoam*, which is derived from the default *OpenFOAM* algorithm *pimpleDyMFoam*, which calculates fluid flow for a dynamic mesh by deploying the PIMPLE algorithm. However, *pimpleDyMFoam* does not contain any other scalar diffusion equations, so a concentration diffusion term has been added to the algorithm, renaming it to *pimpleDyMScalarFoam* (the name contains *Scalar*, but it can simulate both thermal and diffusion processes due to the equations being identical).

*pimpleDyMScalarFoam* solves fluid flow and concentration diffusion separately –- first, it recalculates fluid velocity relatively to the moving mesh, then it solves a full PIMPLE cycle (ignoring concentration diffusion), and then calculates one step for diffusion with the newly obtained fluid variables. Therefore, the fluid impacts how concentration diffusion happens but not vice versa. It is thus implicitly stated that the gas above the molten silicon is dilute with respect to the concentration of silicon impurities. The algorithm repeats additional iterations until a residual of $10^{-6}$ is obtained. In this study, the PIMPLE algorithm runs with two outer corrector loops, one inner corrector loop and one non-orthogonal corrector loop. The time domain is discretized with the Euler scheme, divergence terms are discretized with the Gauss upwind scheme and the Laplacian terms are approximated with Gauss linear corrected schemes. Turbulence is modeled with the k-ϵ model.

Boundary conditions must also be set for the problem. In most cases, *OpenFOAM* has keywords for standard boundary conditions. However, in this case, a custom boundary condition was necessary for the deformation of the boundary corresponding to the surface of molten silicon. To do this, a new boundary condition *SineVelocity* was defined, which moves the boundary points according to the law $u_y = A\sin\left(\frac{2\pi x}{\lambda}\right)\sin\left(\frac{2\pi t}{T}\right)$. The free parameters here are amplitude $A$, wavelength $\lambda$ and period $T$. The value of $L$, which corresponds to the length of the moving boundary, is determined automatically. Despite the parameters $\lambda$ and $T$ being free to choose from an implementation standpoint, the dispersion relation for gravity waves is nevertheless used as an approximation for the relation between variables $\lambda$ and $T$. Generally, the dispersion relation for gravity waves is:

$$\omega^2 = gk_\lambda + \frac{\sigma k_\lambda^3}{\rho} \#(7)$$

However, with the characteristic values of $g$=10 m/s$^2$, $\lambda$=5 mm, $\sigma$=0.7 N/m [13] and $\rho$=2550 kg/m$^3$ [14] for molten silicon, the ratio between the first term and second term in Eq. 7 is approximately 140, thus allowing to use only the first term in the dispersion relation. This allows to rewrite the dispersion relation for variables $\lambda$ and $T$:

$$\frac{\lambda}{T} = \sqrt{\frac{g\lambda}{2\pi}} \#(8)$$

Once calculations are complete, the concentration flow field is integrated on the outflow boundary at every time step to obtain the total amount of impurity concentration that has left the domain:

$$\Phi_C = \int C v_n \, dS \, \#(10)$$

The value of $\Phi_C$ serves as the main comparative quantity between different calculations if inlet velocity remains fixed.

2.3. Neglecting chemical reactions

The reaction scheme for partial boron oxidation with the oxidizing gas is described in [7]:

$$\mathrm{Si} + \mathrm{H_2O} = \mathrm{SiO} + \mathrm{H_2} \#(11)$$

$$\mathrm{B} + \mathrm{H_2O} = \mathrm{HBO} + \frac{1}{2}\mathrm{H_2} \#(12)$$

$$\mathrm{B} + \mathrm{SiO} + \frac{1}{2}\mathrm{H_2} = \mathrm{HBO} + \mathrm{Si} \#(13)$$

For this research, reactions at the interface were neglected. Instead, constant concentration of HBO was assumed at the silicon surface. This was done for several reasons. Firstly, Sortland [7] argues that resistance for HBO transport stemming particularly from the reactions at the interface is very small and their influence on boron removal rate is negligible.

Secondly, the supply of $H_2O$ to the surface depends on the concentration of $H_2O$ in the gas and the resistance of diffusion layer:

$$J_{\mathrm{H_2O}} = k_{\mathrm{diff}}^{\mathrm{H_2O}} \left( C_{\mathrm{H_2O}}^{\mathrm{gas}} - C_{\mathrm{H_2O}}^{\mathrm{int}} \right) \#(14)$$

Here $k_{\mathrm{diff}}^{\mathrm{H_2O}}$ is the mass transfer coefficient of the $\mathrm{H_2O}$ from the gas to the interface, $C_{\mathrm{H_2O}}^{\mathrm{int}}$, $C_{\mathrm{H_2O}}^{\mathrm{gas}}$ - concentration of $\mathrm{H_2O}$ in the gas and at the interface respectively. Here only $k_{\mathrm{diff}}^{\mathrm{H_2O}}$ can vary spatially due to a different thickness of the diffusion layer along the silicon-gas interface.

The same principle can be applied to the diffusion of HBO from the interface to the gas. Assuming good mixing in the silicon and slowly changing concentrations of B (characteristic time is several hours), $C_B$ can be assumed to be constant along the surface, hence also $C_{\mathrm{HBO}}^{\mathrm{int}}$ is constant.

$$J_{\mathrm{HBO}} = k_{\mathrm{diff}}^{\mathrm{HBO}} \left( C_{\mathrm{HBO}}^{\mathrm{int}} - C_{\mathrm{HBO}}^{\mathrm{gas}} \right) \#(15)$$

Taking into account those considerations, it is possible to simplify the model to a purely diffusion dominated impurity flux from the silicon to the gas in the boundary layer. Of course, the boron removal rate depends also on the amount of water vapor in the reactive gas, but this is not taken into account here.

2.4. Geometry and meshing

In this simulation, calculations are done for a 2D axisymmetric geometry. In Fig. 1, the geometry and a representative picture of the computational mesh are given. In Fig. 1a the sketch of the geometry is shown. Fig. 1b and 1c show the mesh grid used for calculations. As can be seen, the grid is more refined where deformations of the mesh take place, both to better absorb the mesh deformations and to resolve the diffusion boundary layer.

The computational mesh was created using an open-source program SALOME. The number of elements in the mesh is 15000. To arrive at this number, a mesh independence study was performed. An initial coarse mesh was progressively made finer and finer until no significant difference in the simulation results could be observed. The results obtained with the mesh used in this study differed no more than 1% from the previous calculation, which was deemed precise enough in the scope of this research. A mesh twice as fine (i.e. face size of each element is two times smaller) gave no appreciable improvement to the results as compared to the mesh used in the study (deviations were less than 1%).

Finally, boundary conditions were set. The boundary conditions are summarized in Table 1. It is important to note that the chosen boundary condition for the value of impurity concentration on the surface of the molten silicon being constant $c$=1 is a simplification that neglects the role of

transient chemical reactions and impurity transport within the molten silicon itself. However, within the scope of this research it is an acceptable simplification (see subsection 2.5.). Inlet values for $k$ and $\varepsilon$ were chosen to keep turbulence low at the inlet in order to allow for the system geometry, wave interaction and diffusion at the interface to dominate the effects on all physical processes.

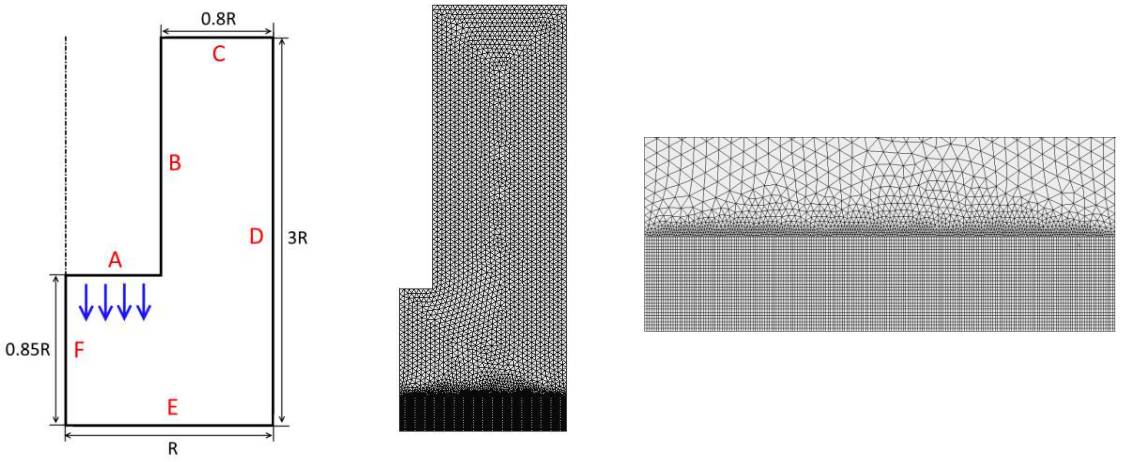


a) Sketch of the geometry, $R$ = 1 m

b) The mesh in the entire domain

c) Zoomed mesh near the surface of the silicon melt

Fig. 1. Problem geometry and computational mesh.

Table 1. Summary of boundary conditions in the simulation. WF – Wall Function, SYMM – Symmetry.

| Boundary | Inlet | Inner wall | Outlet | Outer wall | Si surface | Axis |
|---|---|---|---|---|---|---|
| Label (Fig 1) | A | B | C | D | E | F |
| Quantity | | | | | | |
| $\boldsymbol{u}^*$ | $\boldsymbol{u}_n^* = 0.7$ m/s | $\boldsymbol{u}^* = 0$ | $\frac{\partial \boldsymbol{u}^*}{\partial \boldsymbol{n}} = 0$ | $\boldsymbol{u}^* = 0$ | $\boldsymbol{u}^* = 0$ | SYMM |
| $p$ | $\frac{\partial p}{\partial \boldsymbol{n}} = 0$ | $\frac{\partial p}{\partial \boldsymbol{n}} = 0$ | $p = 0$ | $\frac{\partial p}{\partial \boldsymbol{n}} = 0$ | $\frac{\partial p}{\partial \boldsymbol{n}} = 0$ | SYMM |
| $c$ | $c = 0$ | $\frac{\partial c}{\partial \boldsymbol{n}} = 0$ | $\frac{\partial c}{\partial \boldsymbol{n}} = 0$ | $\frac{\partial c}{\partial \boldsymbol{n}} = 0$ | $c = 1$ | SYMM |
| $\varepsilon$ | $\varepsilon = 10^{-6}$ m$^2$/s$^3$ | WF | $\frac{\partial \varepsilon}{\partial \boldsymbol{n}} = 0$ | WF | WF | SYMM |
| $k$ | $k = 10^{-5}$ m$^2$/s$^2$ | WF | $\frac{\partial k}{\partial \boldsymbol{n}} = 0$ | WF | WF | SYMM |
| Motion | $\boldsymbol{v} = 0$ | $\boldsymbol{v} = 0$ | $\boldsymbol{v} = 0$ | $\frac{\partial \boldsymbol{v}}{\partial \boldsymbol{\tau}} = 0$ | *SineVelocity* | $\frac{\partial \boldsymbol{v}}{\partial \boldsymbol{\tau}} = 0$ |

## 3. RESULTS AND DISCUSSION

### 3.1. Verification of the model

To date, there are no experimental data to use for verifying the numerical model with a wavy surface, thus other methods must be used to determine whether the model gives physically

adequate results and whether the assumptions of subsection 2.3 are adequate. For this purpose, a small separate study was conducted. In this separate study, a 2D axi-symmetrical crucible of radius $R_0 = 0.0031$ m and centrally located inlet radius $r_0 = 0.0031$ m was considered. The height of the crucible was $H = 0.186$ m and was filled up to half height with molten silicon. The top half of the crucible is filled with (initially clean) argon gas. Additionally, there is an inductor placed around the molten silicon that facilitates melt mixing. The current in the inductor was $I = 10$ kA with frequency $f = 50$ Hz, the inductor had 10 turns and a total height $h = 0.082$ m. The material constants were silicon density $\rho_{Si} = 2550$ kg/m$^3$ [14], silicon viscosity $\mu_{Si} = 9.78 \cdot 10^{-4}$ Pa·s [15], argon density $\rho_{Ar} = 1.511$ kg/m$^3$, argon viscosity $\mu_{Ar} = 7.44 \cdot 10^{-5}$ Pa·s [16]. The argon gas introduced through the top inlet was flowing in at a velocity of $v_0 = 2.21$ m/s. The temperature of the crucible was $T = 1500\,°C$. Other boundary conditions are consistent with Table 1, except that the interface between the melt and gas is no longer a boundary in this case. Instead, the silicon melt has an initial impurity concentration $c = 1$, which can diffuse to the gas phase according to Fick's law with a uniform diffusion constant $D_0 = 3.4 \cdot 10^{-4}$ m$^2$/s. This corresponds to the diffusion coefficient for HBO gas [17]. A schematic representation of the model can be seen in Fig. 2 a).

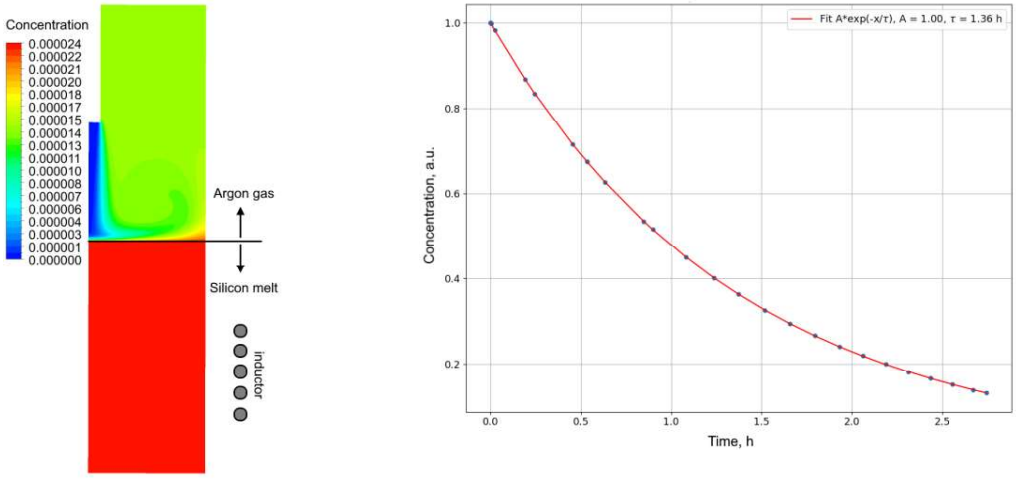


a) Schematic sketch of the verification case

b) Average concentration in the silicon melt over time in the verification case

Fig. 2. Verification case setup and data of impurity concentration over time.

This case was run in *ANSYS Fluent*. Ultimately, an exponential decay was obtained for the average concentration in the silicon melt with a characteristic time of $\tau$=1.36 h (see Fig. 2). This allows the estimation of the coefficient $k_B$ according to Eq. (1), which gives the value $k_B$=1.9·10$^{-5}$ m/s. This value is both in agreement with the range described in Section 1 and also with literature where experimental data is available for similar cases with silicon melt stirring [7] [18]. This agreement with other work appears to justify the assumptions made previously in this paper.

However, a moving silicon melt surface must also be considered, and this will further be modeled with the algorithm *pimpleDyMScalarFoam.* To verify this algorithm, identical cases were studied with the *pimpleDyMScalarFoam* algorithm in *OpenFOAM 4.1.* and in *ANSYS Fluent 18*. The case was set up according to Table 1 with a stationary melt surface and the same computational mesh was deployed in both programs. Upon comparing the results, the flow velocity fields and concentration fields matched, with differences of no greater than 3% across the domain for all physical quantities and for the concentration flux at the outflow. Because the mesh independence study showed a dependence on the mesh no greater that 1%, then from here on out the error of all

results for concentration outflow is assumed to be 3% of the flux value. This is how error bars are calculated later in the paper. This slight disagreement between *ANSYS Fluent* and *pimpleDyMScalarFoam* is most likely due to slightly different implementations of wall functions and numerical schemes.

3.2. Simulations for steady surface

Since it was not clear whether the gas velocity and thus also the turbulization and the thickness of the boundary layer are the main parameters responsible for the removal of boron, an assumption was made that it is the uniform distribution of the incoming (clean) oxidizing gas across the surface which can enhance the purification rate. For this reason, simulations with a steady (flat) free surface were done for a different number of lances of the incoming gas jet. More jets may lead to a more uniform distribution of the incoming gas and the normal gradient of concentration would be equal across the free surface.

Quasi-stationary gas and silicon flow patterns and boron concentration distribution are shown in Fig. 3. Similar distributions are obtained also with a 3D model. The time scale in plots is scaled according to $t^* = D/d^2 t$, where $D$ – diffusion coefficient of HBO in gas, $d$ - crucible diameter. Thus, time scale $t^* = 1$ corresponds to the diffusion time scale.

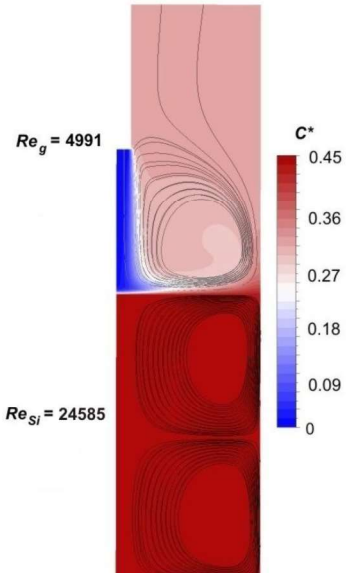


Fig. 3. 2D scheme of boron removal from silicon with gas jet: $Re_{\mathrm{Si}}$ and $Re_{\mathrm{g}}$ – silicon and gas Reynolds numbers and $C^*$ – boron concentration contours where $C^* = \frac{C_{\mathrm{B},t}}{C_{\mathrm{B},0}}$ and $\mathrm{C_{B,0}} = 10^{-5}$, obtained with 2D model for flow time $t^* = 0.022$.

The computed integral boron concentration in silicon during long-time refinement process is shown in Fig. 4 – dotted and solid lines for 2D and axi-symmetrical 3D models with a single lance (n = 1) accordingly. The estimated dimensionless boron mass transfer coefficient values $k_{\mathrm{B}}^* = k_b \cdot \frac{d}{D}$ based on simulation of refinement is $k_{\mathrm{B}}^* = 36.27$ for 2D model; for the axi-symmetrical 3D model the estimated value is by 10% greater – $k_B^* = 39.94$ (see Fig. 4).

The computations are performed for different numbers of lances n = 1, 2, 3, 4, 5, 13. The total flow rate of all gas jets is constant and is equal to the flow rate of the gas jet for the model with a single lance. The coefficient $k_B^*$ as a function of the number of lances n is shown in Fig. 5 (blue scale and triangles). Obtained results show that the largest value of $k_B^*$ corresponds to a single lance system. A possible explanation is connected with the analysis of gas flow patterns in the vicinity of gas–silicon interface:

- The gas flow rate in each single jet for a multiple lance system is lower, hence the turbulization rate is lower;
- Gas jets decelerate each other;
- The inertia of the incoming jet is lower and thus less gas reaches the surface, and the diffusion boundary layer is larger in case of multiple jets.

A very important issue here is the size of the diffusion boundary layer. This is essential in a real process where chemical reactions take place. As already noted, only the diffusion process is taken in account in this paper. A simple way of viewing the influence of the boundary layer is following the path of a single oxygen molecule. Oxygen with a water molecule diffuses through the boundary layer with a mass transfer coefficient $k_{diff}^{H_2O}$, then water reacts with boron (reaction Eq. 12]), and HBO is removed from the system, first through boundary layer with $k_{diff}^{HBO}$, and then with gas in bulk flow. So, for boron removal, two diffusion processes must follow each other.

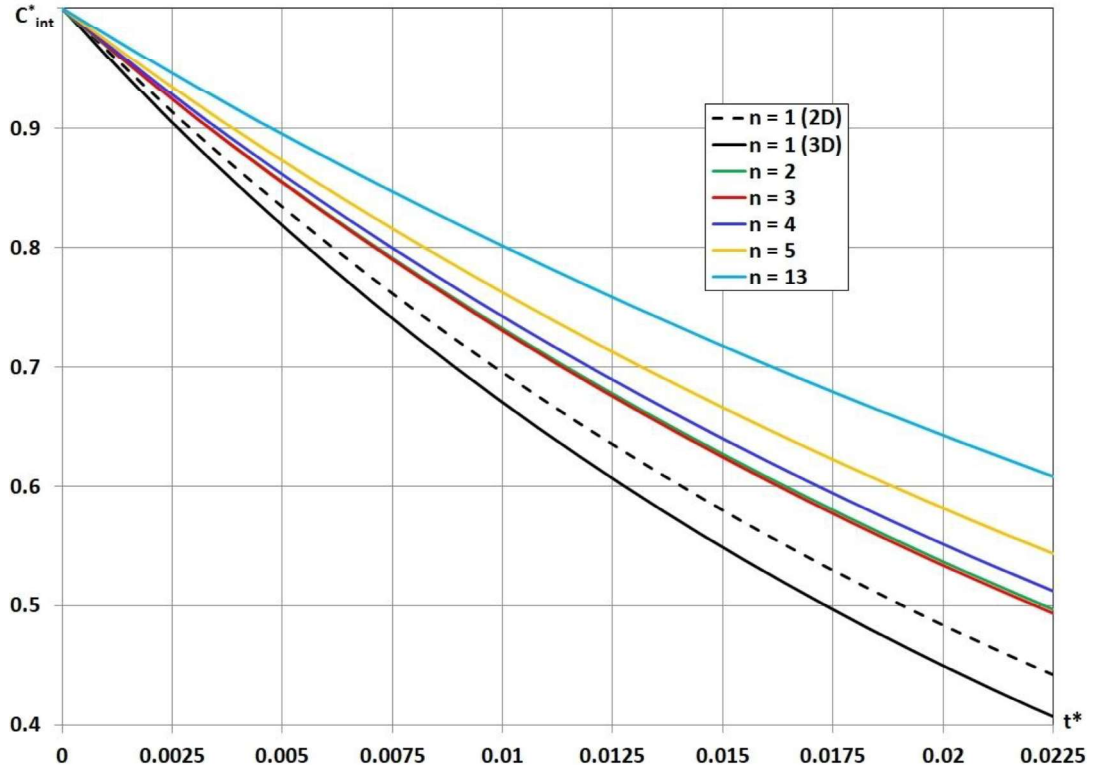


Fig. 4. Boron integral concentration $C_{int}^{*}$ (where $C_{\mathrm{int}}^{*} = \frac{C_{\mathrm{B},t}^{\mathrm{int}}}{C_{\mathrm{B},0}^{\mathrm{int}}}$) in silicon melt as function of silicon refining process time $\mathrm{t}^{*}$ for different numbers (n) of vertical ($\alpha_{\mathrm{lance}} = 0°$) gas lances.

Fig. 5 also shows the dependence of the mass transfer coefficient on the height of the lance (distance from the silicon surface). It is visible that there is a slight enhancement of mass transfer if the lance is moved closer to the surface – an increase of 25% by moving the lance from the distance $h^{*} = h/d = 0.75$ to $h^{*} = 0.05$.

Simulations with slanted lances were also performed, however, the coefficient $k_{\mathrm{B}}^{*}$ decreases by 30% when the angle of the slope $\alpha_{\mathrm{lance}}$ increases by 45° as measured from the vertical line.

This suggests that it is not possible to improve the purification rate by manipulating only the gas flow - different numbers of lances and/or diameters of lances and/or sloping angles of the lances

do not give any improvement when the total mass flow rate of the gas is kept constant and the lance height is kept constant as well.
Therefore, an investigation on the transient free surface parameters is required.

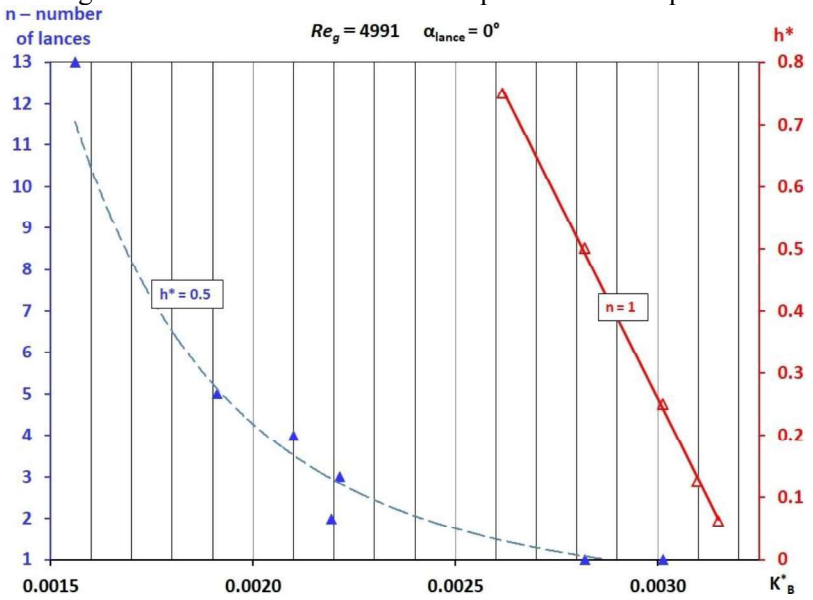


Fig. 5. Boron mass transfer coefficient $k_{\mathrm{B}}^{*}$ at the gas-silicon interface for vertical ($\alpha_{\mathrm{lance}} = 0°$) gas lances: (red scale and triangles) $k_{\mathrm{B}}^{*}$ as function of gas lance height lance-to-melt with linear trend line (solid) (blue scale and triangles) $k_{\mathrm{B}}^{*}$ as a function of the number of lances n for $\mathrm{h}^{*} = 0.5$ with power trend line (dotted).

3.3. Wave parameter impact on HBO diffusion

To study the impact of molten silicon surface waves on impurity diffusion away from the silicon, numerical calculations were performed. The criterion for the quality of impurity diffusion is the concentration flow which flows out of the computational domain $\Phi_C$. Surface wave amplitude, frequency and wavelength are chosen as independent parameters to study the impact on impurity removal. One must note that in further calculations the mass diffusion coefficient for impurities was set as $D_0 = 1.76 \cdot 10^{-5}$ m$^2$/s, which corresponds to water vapor in air [19]. As these wave parameter studies are fundamental in nature, the exact choice of $D_0$ does not matter. Its role on the factors determining impurity evacuation rate will be discussed later in Section 4.5.
In our calculations, no case went above a dimensionless wave amplitude of $A/\lambda > 0.2$. This is because waves larger than that approach the limit at which they would be expected to deform and crash. Furthermore, the obtained data was also normalized by the enlargement of the surface area due to waves to determine whether the improvement in impurity removal is solely due to the surface area enlargement. Since the surface waves are assumed to be harmonic in the scope of this research, one can analytically calculate the surface area of the wavy surface with basic calculus. To obtain the surface area enlargement, one must then divide the enlarged surface with the original surface of the stationary melt. Thus, the average surface area enlargement $q$ over time can be calculated numerically by using:

$$q = \frac{1}{R_0}\int_0^{R_0} \sqrt{1 + \frac{1}{2}\left(\frac{\pi n A}{R_0}\cos\frac{\pi n x}{R_0}\right)}\, dx \quad \#(16)$$

Here, $l$ is the crucible radius, $n$ is the wavenumber of the surface waves.

3.3.1. Effect of frequency

First of all, the effect of wave oscillation frequency on impurity diffusion was studied. It is important to note that in this part of the study, frequency was considered independent of wavelength (that is, only the wave oscillation was changed while the wavelength was kept constant $\lambda = 0.25$ m). Later in the study, the dispersion relation is taken in account to model the relationship between frequency and wavelength. As can be seen in Fig. 6, no change was observed — the mean value of the total impurity concentration flow away from the computational domain was unchanged. Changes could be observed only in small time scale oscillations (at the same order of magnitude as the wave oscillations themselves) which do not affect long-term processes (such as the overall purification of the molten silicon). The frequencies studied were around the base frequency $f_0$ for the chosen base wavelength $\lambda = 0.25m$. According to Eq. 8, $f_0 = 2.52$ Hz. The error bars for Fig. 6 (and further figures from here on out) are calculated as described in Section 3.1.

3.3.2. Effect of amplitude

A series of calculations with fixed wavelength and variable wave amplitudes was computed. In Fig. 7, a clear upward trend with increasing wave amplitude above the error threshold for the impurity concentration outflow can be observed. Furthermore, the normalized data almost agrees with the stationary diffusion rate.

3.3.3. Effect of wavelength

Next, a series of calculations with fixed amplitude and variable wavelengths was computed. In Fig. 8, an upward trend beyond the error threshold is also observable. The data was once again normalized to surface area enlargement. In this case, despite having approximately the same dimensionless amplitudes, the observed concentration outflow values differ significantly.

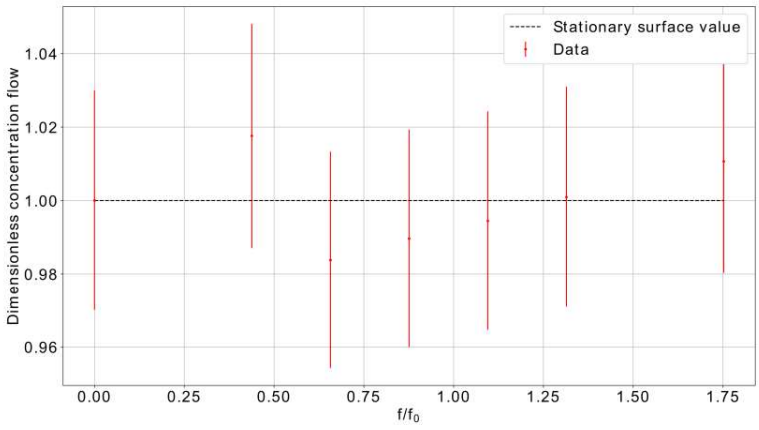


Fig. 6. HBO concentration outflow as a function frequency, $f_0 = 2.52$ Hz.

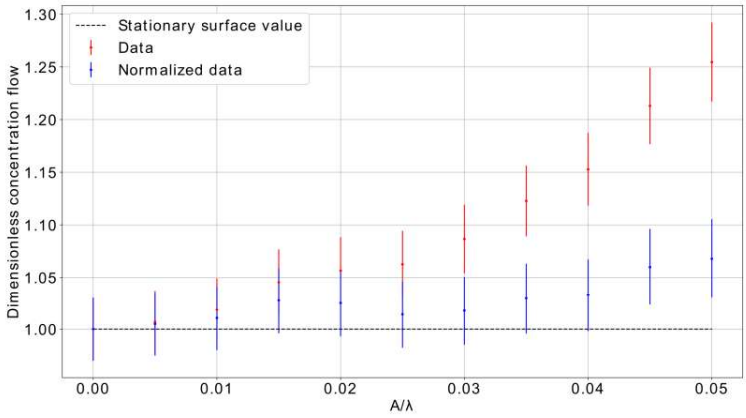


Fig. 7. HBO concentration outflow as a function of dimensionless wave amplitude for variable amplitudes. Amplitude is normalized to $\lambda = 0.25$ m.

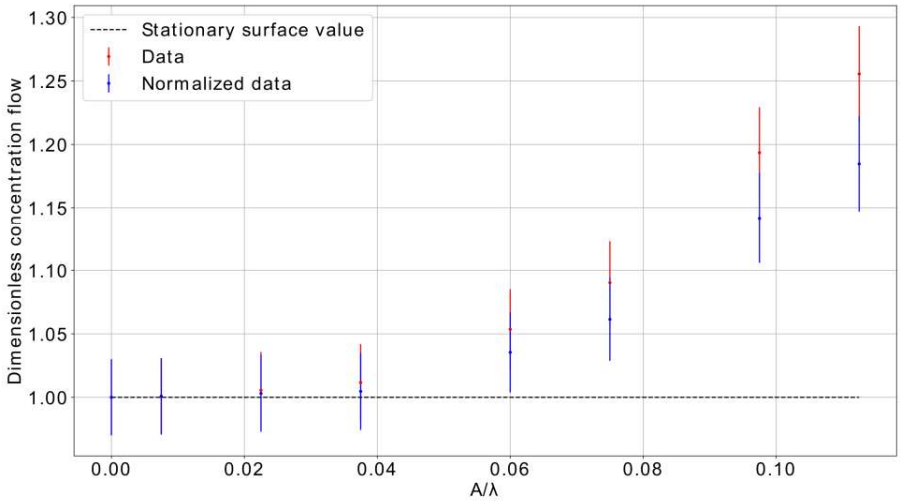


Fig. 8. HBO concentration outflow as a function of dimensionless wave amplitude for variable wavelength. The amplitude is constant $A = 0.015$ m.

## 4. RESULTS AND DISCUSSION

### 4.1. Factor analysis

In both the cases of variable amplitude and variable wavelength, an improvement for integral concentration outflow is observed. There are multiple factors that could contribute to this.

To begin, there is the surface area enlargement due to waves. As diffusion occurs via the surface, a larger surface area would also mean increased diffusion. In the variable amplitude case, this would almost suffice as an explanation – as can be seen in Fig. 7, the normalized data agrees with the original stationary surface diffusion rate within margin of error (except for the final two points). However, this does not explain the data obtained with variable wavelength. Here, the normalized data does not agree with the stationary diffusion rate. Therefore, some other mechanism must be in play.

As [20] has shown, thermal diffusion for inclined plates (with respect to the incoming flow direction) increases with angle of attack. The flow above the surface waves is practically horizontal (consider Fig. 10), so the flow regime is not unlike the one studied by [20]. Therefore, the angle of the surface wave crests with respect to the incoming flow plays a role in the improvement of the diffusion rate. As the value of $A/\lambda$ increases, so does the maximum angle of the wave, thus improving diffusion. This, for example, could contribute to the disparity for the final two points for the normalized data in Fig. 7.

Furthermore, it can also be shown that waves with a larger dimensionless wave amplitude generate greater turbulence in the vicinity of those waves. To support this, additional supportive calculations were performed in ANSYS Fluent, in which the flow close to the waves was studied. In Fig. 9, eddy viscosity $\mu_T$ near the waves is larger for the case when the amplitude is also greater. This has a direct impact for impurity diffusion as well – turbulent diffusion is far greater than molecular diffusion ($D_T/D_0 >> 1$), thus eddy viscosity is a deciding factor for the rate of diffusion at a certain point. For larger wave amplitudes, turbulence near waves is also greater, facilitating better impurity removal from the area immediately next to the waves. This is in accord with a similar study done in [21], where an analogous problem is studied for heat diffusion in wavy channels.

Finally, the flow characteristics above surface waves must also be considered. All of the factors considered thus far affect diffusion uniformly across the whole surface. However, the flow above the waves introduce a certain asymmetry. In Fig. 10, the flow velocity vectors show the flow both near the axis of the geometry (leftmost side) and next to the wall (rightmost side) is stagnant. In these stagnant points, particularly near the wall, a stable concentration gradient can form, as opposed to the waves in the middle, where no stable gradient can form. Because of this, diffusion is more intense where the flow is closer to the waves, and less intense in the stagnant points. Therefore, all the previously discussed effects also have a more pronounced effect for waves in the middle and less so for the waves near the edges of the geometry.

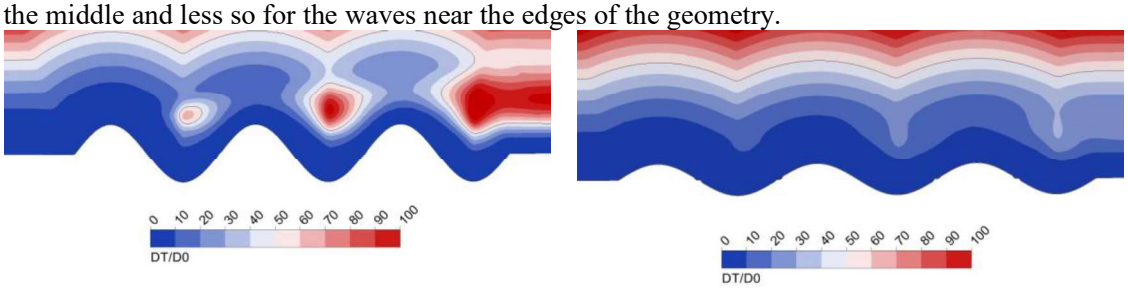


$A/\lambda = 0.2$ $A/\lambda = 0.1$

Fig. 9. Eddy viscosity near waves for different wave heights

This effect allows for illustration of the tendency seen in Fig. 8. Even though values for $A/\lambda$ were the same for both the cases of variable amplitude and variable wavelength, the integral concentration outflow differs significantly. This means that changing amplitude at a fixed wavelength and changing wavelength at a fixed amplitude is not the same in terms of effect produced, even if it is in terms of dimensionless amplitude. This may be explained by the effect just discussed – when the wavelength is shortened, more waves appear in the active diffusion zone, allowing for all the previous mechanisms to have a more pronounced effect, leading to an increase in concentration outflow.

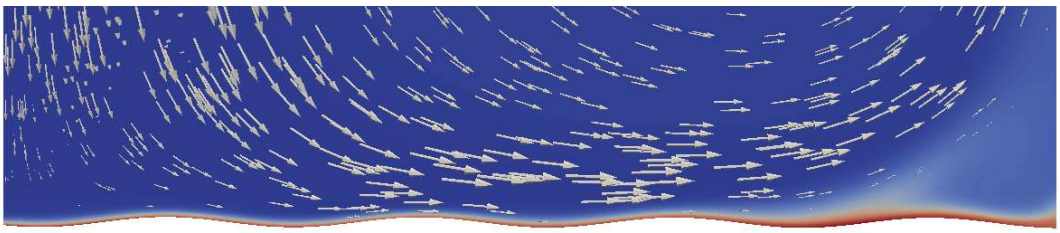

Fig. 10. Flow regime directly above the surface waves. Vectors denote velocity, background coloring denotes concentration of HBO.

4.2. Role of molecular diffusion

Up to this point, the role of molecular diffusion of HBO has been underlooked. Namely, the Peclet number in all cases considered up to this point was nearly the same. A separate study has been done to determine how the Peclet number impacts the results so far discussed. In this study, five otherwise identical cases were simulated with different values of $Pe$. To calculate $Pe$, one must choose a characteristic length and velocity. Because the silicon-gas interface is of interest, the characteristic length is chosen equal to wave amplitude and the characteristic velocity is chosen as the gas velocity directly above the interface. To better understand the factors impacting impurity removal, this study also considers the impact of different $Pe$ numbers near the melt-gas interface.

To determine this, simulations exactly like described in subsection 3.3.3. were run again, but with modified molecular diffusion coefficients for the impurities in order to obtain different $Pe$ numbers. It was found that for certain values of $Pe$, the surface waves had no impact whatsoever on the concentration outflow - it remained the same for all combinations of dimensionless amplitudes and never showed a value larger than for the stationary surface without waves. However, for larger $Pe$, the characteristic impact discussed previously reappeared (see Fig. 12).

The different values of $Pe$ dictate the extent to which impurities can diffuse into the gas phase in a given time. It was empirically determined that if the diffusion length was large with respect to the amplitude of the waves, the waves could no longer impact the diffusion of HBO (see Fig. 12). Clearly, if the impurities quickly diffuse into the gas, then wave phenomena below this characteristic diffusion length have a diminishing impact. A side-by-side comparison of two cases with different values of $Pe$ can be seen in Fig. 11.

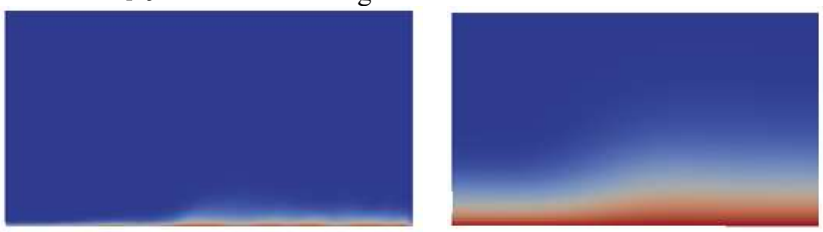

a) $Pe$ = 127 b) $Pe$ = 0.32

Fig. 11. Diffusion length at time $t$ when the air hits the surface for (a) a large value of $Pe$ (b) a small value of $Pe$

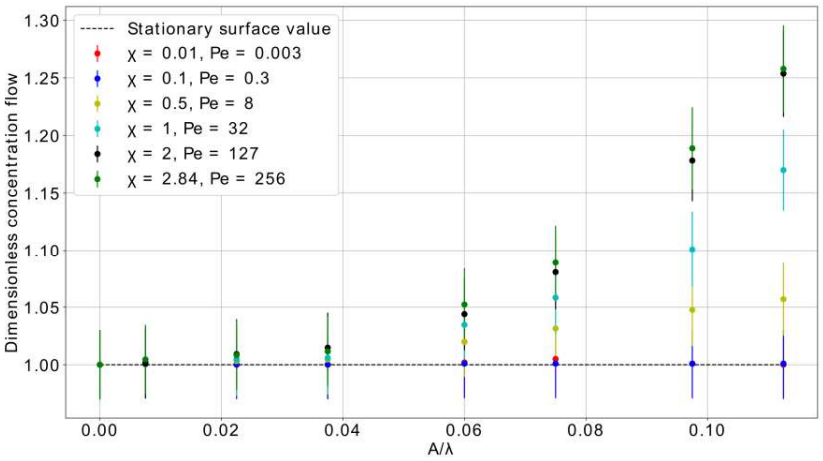


Fig. 12. HBO concentration outflow as a function of dimensionless wave amplitude for variable amplitude at different values of $\chi$, $A = 0.015$ m.

It is hypothesized that a dimensionless parameter $\chi$ that relates the diffusion length to the amplitude of the waves is important for forecasting whether surface waves will have any impact on the overall diffusion of $HBO$ impurities to the gaseous phase. It is defined in the following way:

$$\chi = \frac{A}{2\sqrt{(D_0 T)}} \#(17)$$

Here $A$ is the surface wave amplitude and $T$ is the period of oscillation for these waves. It has been observed that $\chi$ should be at least larger than unity for surface waves to have an effect on the diffusion at the surface (see Fig. 12). This dimensionless number relates the wave amplitude with the characteristic diffusion length over one oscillation period. The reasoning behind choosing such a definition for this number is that the "period" of diffusion is also the wave period - that is to say that the global gas flow removes diffused impurities from the interface once per wave oscillation.

In Fig. 12 one can note that for values of $\chi \ll 1$ the existence of waves does not impact the outflow of HBO at all (at least within the amplitudes considered within the study). The behavior considered previously in this paper, however, is described by the points corresponding to $\chi = 2.84$. One can note that, as $\chi$ approaches 1, the surface waves begin to affect the HBO removal process, but not quite to the extent as previously determined. When $\chi = 2$, practically the same behavior is retained as when $\chi = 2.84$. This is in accord with our hypothesis that there is a requirement for $\chi > 1$ for surface waves to have an impact on the impurity removal phenomenon.

This may be counter-intuitive - greater diffusion of impurities to the gas phase leads to *less* effect from the wavy surface. However, this does not mean that the concentration outflow is less. Take note that in Fig. 12 the value on the vertical axis is the normalized concentration flow, meaning that the absolute concentration flow rates can be different for each case. In fact, total concentration outflow grows with an increasing diffusion coefficient - which is because more impurities can diffuse into the gas phase. However, as diffusion increases, the diffusion length also becomes greater, meaning that the wavy surface has less impact on the process efficiency because it is below the characteristic length of diffusion. For example, in Fig. 11 (a) the value of

$\chi = 2$, and in Fig. 11 (b) the value of $\chi = 0.1$. The first case showed a pronounced effect of surface waves on impurity diffusion, the second displayed none.
In real life applications, of course, it is impossible to impact the molecular diffusion coefficient of some particular substance. However, in practical terms, this allows for the calculation of the minimum wave amplitude required to observe any improvement in diffusion (also in terms of wave frequency $f$ if one assumes that $\chi$ must be larger than unity:

$$A \geq 2\sqrt{D_0 T} = 2\sqrt{\frac{D_0}{f}} \#(18)$$

Thus, for a given system, one must generate waves of at least such an amplitude to expect any meaningful improvement for the molten silicon purification process.

## 5. CONCLUSIONS

In the analyzed surface-to-gas diffusion problem it was shown that the increased number of jets directed at the surface cannot ensure better mass transfer from the surface at the fixed gas flow rate. For this reason, the wavy surface was analyzed and it was found that it increases the diffusion rate from the surface by means of several phenomena:

- waves increase the surface area and also the diffusion rate;
- they alter the flow patterns near the surface and lead to a better diffusion via turbulent mass transfer in the vicinity of the surface;
- a decreased diffusion boundary length due to an angle between the main flow and the surface also improves the impurity removal rate.

However, a limitation for the diffusion from the surface at large diffusion coefficients was found. This limitation is linked to the ratio between the diffusion length and the wave amplitude, making this approach unsuitable for small systems.

*Acknowledgements*

This work was funded by European Regional Development Fund under contract "Refinement of metallurgical grade silicon using smart refinement technologies" (No. 1.1.1.1/16/A/097).

## REFERENCES

1. International Renewable Energy (2017) *Renewable Power Generation Costs in 2017 (report),* Agency (IRENA), January 2018, ISBN: 978-92-9260-040-2
2. Kavlak, G., McNerney, J., Trancik, J.E. (2018) Evaluating the causes of cost reduction in photovoltaic modules. *Energy Policy,* Vol.123, pp. 700-710, ISSN 0301-4215, https://doi.org/10.1016/j.enpol.2018.08.015.
3. Delannoy, Y. Purification of silicon for photovoltaic applications, *Journal of Crystal Growth*, vol. 360, p. 61–67, 2012.
4. Fu, R., James, L. T. and Woodhouse, M. Measurements of polysilicon for the photovoltaic industry: market competition and manufacturing competitiveness, *IEEE Journal of Photovoltaics*, vol. 5, no. 2, p. 515–524, 2015.
5. Khattak, C., Joyce, D. and Schmid, F. A simple process to remove boron from metallurgical grade silicon., *Solar Energy Materials and Solar Cells*, vol. 74, no. 1, p. 77–89, 2002.
6. Galpin, J. and Fautrelle, Y. (1992) Liquid-metal flows induced by low-frequency alternating magnetic fields. *Journal of Fluid Mechanics*, 239, 383-408. doi:10.1017/S0022112092004452

7. Fautrelle, Y., Sneyd, A.D. (2005) Surface waves created by low-frequency magnetic fields, *European Journal of Mechanics - B/Fluids*, vol. 24, issue 1, pages 91-112, https://doi.org/10.1016/j.euromechflu.2004.05.005.
8. Sortland, Ø. and Tangstad, M. (2014) Boron removal from silicon melts by H2O/H2 gas blowing: mass transfer in gas and melt., *Metallurgical and Materials Transactions E*, vol. 1, no. 3, p. 211–225, 2014.
9. Marrero, T.R. and Mason, E.A. (1973), Correlation and prediction of gaseous diffusion coefficients. *AIChE J.*, 19: 498-503. doi:10.1002/aic.690190312
10. Safarian J., Thang K., Hildal K., Tranell G. (2014) *Metallurgical and Materials Transactions E* 1 41
11. Nordstrand E. F., Tangstad M. (2012) *Metallurgical Material Transactions B* 43 814
12. Safarian, J. and Tangstad, M. (2012) Kinetics and Mechanism of Phosphorus Removal from Silicon in Vacuum Induction Refining. *High Temperature Materials and Processes*. 31. 10.1515/htmp.2011.143.
13. Khanjian, A., Habchi, C., Russeil, S. et al. (2018) Effect of the angle of attack of a rectangular wing on the heat transfer enhancement in channel flow at low Reynolds number. *Heat Mass Transfer* (2018) 54: 1441. https://doi.org/10.1007/s00231-017-2244-8
14. Dellil, A.Z., Azzi, A. and Jubran, B.A. (2004) Turbulent flow and convective heat transfer in a wavy wall channel. *Heat Mass Transfer* 40: 793. https://doi.org/10.1007/s00231-003-0474-4
15. Yuan, Z., Mukai, K. and Huang, W., (2002), Surface Tension and Its Temperature Coefficient of Molten Silicon at Different Oxygen Potential. *Langmuir,* 18, 6, 2054-2062. https://doi.org/10.1021/la0112920
16. Sato, Y., Nishizuka, T., Hara, K. et al. (2000) Density Measurement of Molten Silicon by a Pycnometric Method. *International Journal of Thermophysics* 21: 1463. https://doi.org/10.1023/A:1006661511770
17. Kestin, J., Whitelaw, J.H. (1964) The viscosity of dry and humid air, *International Journal of Heat and Mass Transfer*, Volume 7, Issue 11, 1964, Pages 1245-1255, ISSN 0017-9310, https://doi.org/10.1016/0017-9310(64)90066-3
18. Sortland, O.S. (2015) Boron removal from silicon by steam and hydrogen, PhD thesis, Trondheim: Norwegian University of Science and Technology, October 2015
19. Rhim, W.K., Ohsaka, K. (2000) Thermophysical properties measurement of molten silicon by high-temperature electrostatic levitator: density, volume expansion, specific heat capacity, emissivity, surface tension and viscosity, *Journal of Crystal Growth*, Volume 208, Issues 1–4, 2000, Pages 313-321, ISSN 0022-0248, https://doi.org/10.1016/S0022-0248(99)00437-6
20. Guevara, F. A., McInteer, B. B. and Wageman, W. E. (1969) High-Temperature Viscosity Ratios for Hydrogen, Helium, Argon, and Nitrogen, *The Physics of Fluids* 12:12, 2493-2505
21. Bird., R., Stewart, W. and Lightfoot, E. (2002) Transport Phenomena, New York: Wiley & Sons.